



# Kent Academic Repository

**Riesenmey, Marine Caroline Alexandra (2021) *Anatase TiO<sub>2</sub> nanotubes as negative electrodes for Lithium-ion and Sodium-ion microbatteries.* Doctor of Philosophy (PhD) thesis, University of Kent,.**

## Downloaded from

<https://kar.kent.ac.uk/89307/> The University of Kent's Academic Repository KAR

## The version of record is available from

<https://doi.org/10.22024/UniKent/01.02.89307>

## This document version

UNSPECIFIED

## DOI for this version

## Licence for this version

CC BY (Attribution)

## Additional information

## Versions of research works

### Versions of Record

If this version is the version of record, it is the same as the published version available on the publisher's web site. Cite as the published version.

### Author Accepted Manuscripts

If this document is identified as the Author Accepted Manuscript it is the version after peer review but before type setting, copy editing or publisher branding. Cite as Surname, Initial. (Year) 'Title of article'. To be published in *Title of Journal*, Volume and issue numbers [peer-reviewed accepted version]. Available at: DOI or URL (Accessed: date).

## Enquiries

If you have questions about this document contact [ResearchSupport@kent.ac.uk](mailto:ResearchSupport@kent.ac.uk). Please include the URL of the record in KAR. If you believe that your, or a third party's rights have been compromised through this document please see our [Take Down policy](https://www.kent.ac.uk/guides/kar-the-kent-academic-repository#policies) (available from <https://www.kent.ac.uk/guides/kar-the-kent-academic-repository#policies>).

# Anatase TiO<sub>2</sub> nanotubes as negative electrodes for Lithium-ion and Sodium-ion microbatteries

## Abstract:

The aim of this thesis is to gain a deeper understanding of the anatase TiO<sub>2</sub> nanotubes as negative electrodes in lithium-ion and sodium-ion microbatteries by researching their fundamental intercalation processes. The nano-structuring of the anatase TiO<sub>2</sub> electrodes allows to improve their electrochemical behaviour, and thus the batteries capacities. To this end, a DFT study of the lithium and sodium insertions into the anatase bulk, slab and nanotubes has been carried out.

The study shows that the anatase TiO<sub>2</sub> exhibits a higher reactivity towards sodium than towards lithium, resulting in two different insertion mechanisms: Li ions are intercalated via a two-phases equilibrium, while Na ions insertion occurs spontaneously without phase transformation. This high reactivity towards sodium may induce Na trapping, partly explaining the irreversible capacity losses observed during the first cycle.

The sodium ions are favourably adsorbed above all the oxygen atoms of the anatase surface and spontaneously inserted into the surface. However, the surface reconstruction is restricted by the electronic repulsion of the Na ions. This limited stability of the sodiated surfaces can be a possible explanation of their transformation into amorphous structure.

The most favourable intercalation sites of the nanotubes are located in their external wall, stabilizing the *nt*-TiO<sub>2</sub> structure. Li and Na ions are also favourably adsorbed on-top the outermost oxygen atoms, explaining why more external wall exposure exhibit better capacities. Reactivity with the internal wall is spontaneous for Li ions, while the Na ions require low potentials and are associated with rupturing Ti-O bonds in agreement with the formation of amorphous *nt*-TiO<sub>2</sub> below 0.5 V vs Na/Na<sup>+</sup>.

*Thesis submitted in 2020 in the School of Physical Sciences (62565 words, 256 pages).*

**Anatase TiO<sub>2</sub> nanotubes as negative electrodes for  
Lithium-ion and Sodium-ion microbatteries**

by

**Marine Riesenmey**

**Thesis**

Submitted to the University of Kent as part of the  
requirement in the subject of Chemistry for the degree

of

**Doctor of Philosophy**

**School of Physical Sciences**

May 2020

University of  
**Kent**

# Contents

<b>List of Figures</b> .....	<b>iv</b>
<b>List of Tables</b> .....	<b>xv</b>
<b>Acknowledgements</b> .....	<b>xvi</b>
<b>Declaration</b> .....	<b>xvii</b>
<b>Abstract</b> .....	<b>xviii</b>
<b>Chapter 1 Introduction</b> .....	<b>1</b>
1.1 Aims .....	1
1.2 Background .....	4
1.2.1 The Li-ions batteries .....	4
1.2.2 The TiO <sub>2</sub> nanotubes as anode for microbatteries .....	6
1.2.3 The anatase crystal structure .....	12
1.2.4 Theoretical studies of the anatase surfaces .....	15
1.2.5 Modelling of TiO <sub>2</sub> nanotubes.....	18
1.2.6 Modelling of Li intercalation into TiO <sub>2</sub> bulk anatase .....	28
1.2.6.1 The intercalation sites .....	28
1.2.6.2 The phase separation between anatase and Li <sub>0.5</sub> TiO <sub>2</sub> titanate.....	31
1.2.6.3 The Li <sub>0.5</sub> TiO <sub>2</sub> titanate structure .....	32
1.2.6.4 The electron transfer from lithium to the titanate .....	35
1.2.6.5 The Lithium Deintercalation .....	36
1.2.6.6 Lithium intercalation above x= 0.5 .....	37
1.2.7 Modelling of Li intercalation into anatase nanotube.....	39
1.2.8 The sodium ion batteries .....	42
1.2.9 Modelling of Na intercalation into TiO <sub>2</sub> anatase .....	44
1.3 Summary .....	47
<b>Chapter 2 Methodology</b> .....	<b>49</b>
2.1. Hartree Fock and DFT theory .....	49
2.1.1. A brief introduction to computational chemistry .....	49
2.1.2 Fundamentals of the quantum mechanics methods.....	51
2.1.2.1 The Schrödinger Equation .....	51
2.1.2.2 The Born-Oppenheimer approximation .....	51
2.1.2.3 The Hartree Fock approximation .....	53
2.1.2.4 The Density functional theory approximation .....	54
2.1.2.5 The Hartree Fock / DFT hybrid methods.....	56

2.1.3	The basis sets .....	57
2.1.3.1	Slater and Gaussian type orbitals .....	57
2.1.3.2	Basis sets classification .....	60
2.1.4	Modelling of periodic system .....	61
2.1.4.1	Periodic and molecular systems .....	61
2.1.4.2	The self-consistent field approach .....	63
2.1.5	Geometry optimization of a periodic system .....	64
2.2	Modeling of nanotubular TiO <sub>2</sub> .....	65
2.2.1	Basis sets and functional choices .....	65
2.2.2	Self-Consistent Field (SCF) parameters optimization .....	70
2.3	Conclusion.....	72
<b>Chapter 3</b>	<b>Properties of the anatase bulk, slab and nanotube .....</b>	<b>73</b>
3.1	Aims .....	73
3.2	The bulk properties.....	73
3.3	Properties of the (001) terminated slab .....	76
3.4	The nanotubes construction.....	81
3.5	Properties of the 38 Å diameter nanotube .....	85
3.6	Conclusion.....	91
<b>Chapter 4</b>	<b>Lithium intercalation into anatase .....</b>	<b>92</b>
4.1	Aims .....	92
4.2	Choice of Lithium basis set.....	93
4.3	Lithium intercalation into Li <sub>0.5</sub> TiO <sub>2</sub> anatase bulk .....	96
4.4	Lithium intercalation into LiTiO <sub>2</sub> anatase bulk.....	103
4.5	Lithium intercalation into the slab.....	106
4.5.1	Intercalation with lithium capacity of x = 0.33 .....	107
4.5.1.1	The tetrahedral intercalation sites .....	108
4.5.1.2	The octahedral intercalation sites.....	109
4.5.2	Intercalation with lithium capacity of x = 0.5 .....	113
4.5.3	Intercalation with lithium capacity of x = 0.67 .....	114
4.5.4	Intercalation with lithium capacity of x = 1 .....	118
4.5.5	Intercalation voltages .....	127
4.5.6	Intercalation versus lithium metal plating.....	129
4.6	Lithium intercalation into the nanotube .....	130
4.6.1	Intercalation with lithium capacity of x = 0.33 .....	130
4.6.1.1	The tetrahedral intercalation sites .....	131

4.6.1.2	The octahedral intercalation sites.....	133
4.6.2	Intercalation with lithium capacities of $x = 0.67$ and $x = 1$ .....	149
4.6.3	Intercalation versus lithium metal plating.....	150
4.6.4	Intercalation voltages .....	152
4.7	Conclusion.....	154
<b>Chapter 5</b>	<b>Sodium intercalation into anatase .....</b>	<b>157</b>
5.1	Aims .....	157
5.2	Choice of Sodium basis set .....	158
5.3	Sodium intercalation into $\text{Na}_{0.5}\text{TiO}_2$ anatase bulk.....	161
5.4	Sodium intercalation into $\text{NaTiO}_2$ bulk anatase .....	167
5.5	Sodium intercalation into the slab .....	171
5.5.1	Intercalation with sodium capacity of $x = 0.33$ .....	172
5.5.2	Intercalation with sodium capacity of $x = 0.67$ .....	176
5.5.3	Intercalation with sodium capacity of $x = 1$ .....	180
5.5.4	Intercalation voltages .....	183
5.5.5	Intercalation versus sodium metal plating .....	185
5.6	Sodium intercalation into the nanotube.....	188
5.6.1	Intercalation with sodium capacity of $x = 0.33$ .....	189
5.6.1.1	Intercalation into the external wall.....	189
5.6.1.2	Intercalation into the internal wall .....	192
5.6.2.3	Intercalation into the central layer.....	194
5.6.2	Intercalation with sodium capacities of $x = 0.67$ and $x = 1$ .....	195
5.6.3	Intercalation versus sodium metal plating .....	196
5.7	Conclusion.....	199
<b>Chapter 6</b>	<b>Conclusions and future work .....</b>	<b>201</b>
6.1	Lithium intercalation into anatase .....	202
6.2	Sodium intercalation into anatase.....	204
6.3	Comparison of the lithium and sodium insertions.....	208
6.4	Future work .....	210
<b>Appendix A</b>	<b>Titanium basis set .....</b>	<b>212</b>
<b>References</b>	<b>.....</b>	<b>213</b>

# List of Figures

Figure 1.1: Charge and discharge mechanisms of a lithium batteries <sup>8</sup> .....	4
Figure 1.2: Lithium metal <sup>13</sup> (a) and Lithium ion <sup>15</sup> (b) batteries.....	6
Figure 1.3: Schematic of the 2D and 3D thin film microbatteries. ....	7
Figure 1.4: Anatase, rutile and TiO <sub>2</sub> (B) polymorphs where the grey and red spheres represent the titania and oxygen atoms, respectively <sup>25</sup> .....	8
Figure 1.5: Anatase conventional unit cell (a) where the Ti atoms are displayed in grey and the O ones in red; and a polyhedral representation of the anatase structure showing the TiO <sub>6</sub> octahedrons <sup>26</sup> (b). ....	12
Figure 1.6: Splitting of the <i>d</i> orbitals in an octahedral complex.....	13
Figure 1.7: Splitting of titanium <i>d</i> orbitals in going from ideal O <sub>h</sub> to anatase (D <sub>2d</sub> ) <sup>41</sup> . ....	13
Figure 1.8: Density of states (DOS) of bulk anatase TiO <sub>2</sub> <sup>26</sup> . VB and CB represent the valence and conduction bands, respectively. ....	14
Figure 1.9: Unreconstructed anatase (001) surface showing the coordination of the different atoms <sup>50</sup> . Reprinted (adapted) with permission from reference <sup>50</sup> . Copyright 2014 American Chemical Society.....	15
Figure 1.10: Bond lengths of the optimized (001) anatase surface <sup>49</sup> .....	16
Figure 1.11: DOS of the (001) anatase (001) surface, showing the O <sub>2c</sub> and O <sub>3c</sub> contributions <sup>56</sup> .....	18
Figure 1.12: zig-zag (0, <i>n</i> <sub>2</sub> ) and ( <i>n</i> <sub>1</sub> ,0) and armchair ( <i>n</i> <sub>1</sub> , <i>n</i> <sub>2</sub> ) rolling up vectors of a graphene lattice <sup>6</sup> .....	19
Figure 1.13: (12,0) zig-zag, (6,6) armchair and (6,4) chiral single walled carbon nanotubes <sup>65</sup> .....	20
Figure 1.14: Anatase surfaces and the corresponding rolling-up vectors <sup>48</sup> . The Ti atoms are in purple and the O ones in green. Republished with permission of Royal Society of Chemistry, from reference <sup>48</sup> obtained in 2021; permission conveyed through Copyright Clearance Center, Inc.....	21
Figure 1.15: Fluorite armchair TiO <sub>2</sub> nanotube where O <sub>be</sub> and O <sub>bi</sub> refer to the bridging oxygens .....	22

Figure 1.16: (15, 0) <i>nt</i> -TiO <sub>2</sub> generated from a three monolayer thick (100) slab <sup>48</sup> . The O atoms are in green and the Ti ones in purple. Republished with permission of Royal Society of Chemistry, from reference <sup>48</sup> obtained in 2021; permission conveyed through Copyright Clearance Center, Inc. ....	23
Figure 1.17: Two monolayer thick lepidocrocite slab (a) and <i>nt</i> -TiO <sub>2</sub> (b) <sup>48</sup> . The Ti atoms are in purple and the O ones in green. Republished with permission of Royal Society of Chemistry, from reference <sup>48</sup> obtained in 2021; permission conveyed through Copyright Clearance Center, Inc. ....	24
Figure 1.18: 3ML <i>nt</i> -TiO <sub>2</sub> rolled up along the (0, <i>n</i> <sub>2</sub> ) direction (a) or the ( <i>n</i> <sub>1</sub> , 0) direction (b) <sup>86</sup> . The O atoms are in red and the Ti ones in blue. Reprinted (adapted) with permission from reference <sup>86</sup> . Copyright 2010 American Chemical Society. ....	25
Figure 1.19: Non optimized (a) and optimized into a nanotubular structure (b) 3 ML thick anatase slab cut along the (001) direction <sup>86</sup> . The Ti and O atoms are in blue and red, respectively. Reprinted (adapted) with permission from reference <sup>86</sup> . Copyright 2010 American Chemical Society.....	25
Figure 1.20: Calculated strain energies for ( <i>n</i> <sub>1</sub> , 0) <i>nt</i> -TiO <sub>2</sub> built from anatase (001) slab <sup>91</sup> , where D is the diameter of the nanotube.....	26
Figure 1.21: Lithium ion inserted into an octahedral intercalation site of bulk anatase. The Ti atoms are indicated in grey, the O ones in red and the Li one in purple. ....	29
Figure 1.22: The conventional unit cells of the two most stable Li distribution structures for x = 0.5 <sup>40</sup> referred to as structure I ( <i>Pmma</i> ) or structure II ( <i>Imm2</i> ). The Li ions are in purple, while the Ti and O atoms are in grey and red, respectively. ....	30
Figure 1.23: Octahedral packing of bulk anatase <sup>117</sup> (a) and Li <sub>0.5</sub> TiO <sub>2</sub> titanate (b) <sup>118</sup> . The Ti atoms are in blue, the O ones in red and the Li ions in purple. Republished with permission of Royal Society of Chemistry, from reference <sup>117</sup> obtained in 2021; permission conveyed through Copyright Clearance Center, Inc. ....	33
Figure 1.24: Illustration of the electronic structure modification upon lithium intercalation <sup>41</sup> .....	34
Figure 1.25: Top (right) and side (left) views of the four investigated Li intercalation sites in an (101) <i>nt</i> -TiO <sub>2</sub> <sup>138</sup> . The grey, red and purple spheres represent the Ti, O and Li atoms. Republished with permission of Royal Society of Chemistry, from reference <sup>138</sup> obtained in 2021; permission conveyed through Copyright Clearance Center, Inc. ....	40

Figure 1.26: Diffusion pathways between the different Li intercalation sites in an (101) <i>nt</i> -TiO <sub>2</sub> <sup>138</sup> . The grey, red and purple spheres represent the Ti, O and Li atoms. Republished with permission of Royal Society of Chemistry, from reference <sup>138</sup> obtained in 2021; permission conveyed through Copyright Clearance Center, Inc. .	41
Figure 1.27: Total DOS of Li <sub>0.11</sub> TiO <sub>2</sub> (blue), Na <sub>0.11</sub> TiO <sub>2</sub> (red), Mg <sub>0.11</sub> TiO <sub>2</sub> (green) and TiO <sub>2</sub> (black) anatase bulks. The vertical lines represent the respective the Fermi energies <sup>149</sup> .	45
Figure 2.1: Repartition of the different simulation methods according to the space-time scale <sup>151</sup> .	50
Figure 2.2: Comparison of the quality of GTOs up to a 3 <sup>rd</sup> term linear combination to model a plot <i>I</i> <sub>s</sub> -STO orbital <sup>166</sup> .	59
Figure 2.3: Total energies of bulk anatase TiO <sub>2</sub> calculated with different alpha coefficient. Blue rhombus basis set with only <i>4d</i> and orange square is ( <i>4d</i> , <i>5d</i> ) basis set.	69
Figure 2.4: Total energies of bulk anatase TiO <sub>2</sub> calculated for different shrinking factor values.	70
Figure 2.5: Total energies of bulk anatase TiO <sub>2</sub> and calculation durations obtained with different cutoff threshold parameters. Total energy and computational time are displayed with blue rhombus and orange squares, respectively.	71
Figure 3.1: Non-optimized (a) and optimized (b) bulk anatase using computational settings from section 2.2. The Ti and O atoms are in grey and red, respectively.	74
Figure 3.2: DOS of TiO <sub>2</sub> bulk anatase.	75
Figure 3.3: Optimized 3ML anatase slab cut along the (001) surface. Green labels indicate full coordinated while black labels undercoordinated atoms.	76
Figure 3.4: Geometry optimization of the (001) 3ML slab where the Ti atoms are in grey and the O ones in red. The non-optimized slab is displayed in figure a. The changes in bond lengths and the angle modifications are detailed in figures b and c, respectively.	78
Figure 3.5: Mulliken charges of the (001) 3ML slab. Green labels represent Ti and black labels O atoms, respectively.	79
Figure 3.6: DOS of the anatase (001) 3ML slab where the Ti atoms are in grey and the O ones in red. The blue plot stands for the total DOS of the slab, while the red and green colors are related to the <i>p</i> and <i>d</i> orbital contributions of the selected atom (highlighted in green), respectively.	80

Figure 3.7: 3ML <i>nt</i> -TiO <sub>2</sub> rolled up along the (0, <i>n</i> <sub>2</sub> ) direction (a) or the ( <i>n</i> <sub>1</sub> , 0) direction (b). The grey and red spheres represent the Ti and O atoms, respectively. ....	81
Figure 3.8: 3ML <i>nt</i> -TiO <sub>2</sub> rolled up along the ( <i>n</i> <sub>1</sub> ,0) direction having an internal diameter of 8 Å (a) and 66 Å (b). The O and Ti atoms are in red and grey, respectively. ....	82
Figure 3.9: Strain energy of anatase 3ML <i>nt</i> -TiO <sub>2</sub> versus the diameter.....	83
Figure 3.10: 3ML <i>nt</i> -TiO <sub>2</sub> having an internal diameter of 8 Å before (a) and after (b) geometry optimization. The red and grey spheres stand for the O and Ti atoms, respectively. ....	84
Figure 3.11: 38 Å diameter 3ML nanotube before (a) and after (b) geometry optimization. The O and Ti atoms are in red and grey, respectively. ....	84
Figure 3.12: Measures of the Ti-O-Ti chain angles and Ti-O bond lengths of the optimized <i>nt</i> -TiO <sub>2</sub> . The grey and red spheres represent the Ti and O atoms, respectively. Figures a and b detailed the angles while the bond lengths are shown in figures c, d and e. ....	85
Figure 3.13: Localization of the undercoordinated oxygen atoms (highlighted in green) in the anatase slab (a) and nanotube (b). The O atoms are in red and the Ti ones in grey.....	86
Figure 3.14: Labelling of the Ti and O ions constituting the optimized unit cell of the <i>nt</i> -TiO <sub>2</sub> . ....	88
Figure 3.15: DOS of the optimized <i>nt</i> -TiO <sub>2</sub> . Atomic labels are presented in Figure 3.14. The blue plot stands for the total DOS of the nanotube while the red and green plots represent the contributions of the <i>p</i> and <i>d</i> orbitals, respectively.....	90
Figure 4.1: Crystallographic structure of lithium bulk space group <i>Im3m</i> . ....	94
Figure 4.2: Li <sub>0.5</sub> TiO <sub>2</sub> supercell before geometry optimization. The grey, red and purple colours represent the Ti, O and Li ions, respectively.....	95
Figure 4.3: Optimized non-lithiated (a) and lithiated (b) bulk anatase. The Ti atoms are in grey, the O ones in red and the Li ions in purple. The reduced Ti <sup>3+</sup> ions are highlighted in green.....	97
Figure 4.4: Visualization of the Li-O bonds present in the <i>xy</i> plane. The grey, red and purple spheres represent the Ti, O and Li elements, respectively.....	98
Figure 4.5: DOS of the Li <sub>0.5</sub> TiO <sub>2</sub> bulk where VB and CB represent the valence and conduction bands. The blue plot represents the total DOS while the red and green plots stand for the contribution of the <i>p</i> and <i>d</i> orbitals, respectively.....	101

Figure 4.6: Anatase bulk with one Li ion intercalated in a tetrahedral site. The Ti atoms are indicated in grey, the O ones in red and the Li ion in purple. ....	102
Figure 4.7: Optimized fully lithiated anatase bulk $\text{LiTiO}_2$ . The Li ions are in purple while the Ti and O atoms are in grey and red, respectively. ....	103
Figure 4.8: Optimized anatase bulk $\text{LiTiO}_2$ showing the Li-Li interaction. The grey, red and purple colours represent the Ti, O and Li ions, respectively. The Li ion highlighted in blue are not present in the $\text{Li}_{0.5}\text{TiO}_2$ bulk anatase. ....	104
Figure 4.9: DOS of the $\text{LiTiO}_2$ bulk. The blue plot stands for the total DOS of the slab, while the red and green colors are related to the <i>p</i> and <i>d</i> orbital contributions of the indicated atom. VB and CB represent the valence and conduction bands, respectively. ....	105
Figure 4.10: Anatase (001) slabs with lithiated octahedral (a) and tetrahedral (b) intercalation sites. Grey, red and purple spheres represent Ti, O and Li, respectively. ....	107
Figure 4.11: Intercalation of Li ions in the outer (a) and inner (b) tetrahedral sites of the (001) anatase slab. The Ti atoms are in grey, the O ones in red and the Li ions in purple. ....	108
Figure 4.12: Octahedral intercalation sites (black crosses) present in the anatase (001) slab. The grey, and red spheres represent the Ti and O atoms, respectively. ....	109
Figure 4.13: Side (a) and face (b) views of the optimized $\text{Li}_{0.33}\text{TiO}_2$ anatase (001) slab. The Li ions are in purple while the Ti and O atoms are in grey and red, respectively. ....	110
Figure 4.14: Top views of the optimized (001) slab showing the widths of the intercalation sites (in blue) and the Ti-O bond lengths (in black) when one outermost surface is lithiated. The purple, red and grey colours stand for the Li, O and Ti ions. ....	111
Figure 4.15: Lithium intercalation into the inner octahedral sites of the (001) anatase slab. The grey, red and purple spheres represent Ti, O and Li, respectively. ....	112
Figure 4.16: Total DOS of the anatase (001) slab having the external (blue plot) or the internal (red plot) intercalation sites lithiated. VB and CB refer to the valence and conduction bands, respectively. ....	113
Figure 4.17: (001) Anatase supercell slab with Li intercalated in half of the octahedral sites. The grey, red and purple spheres are related to Ti, O and Li, respectively. ...	114

Figure 4.18: Side and face views of optimized anatase (001) slabs with lithium inserted in a single surface layer (a) or in both (b) surface layers. The Ti, O and Li atoms are in grey, red and purple, respectively. ....	114
Figure 4.19: Top views of the optimized (001) slabs showing the widths of the intercalation sites (in blue) and the Ti-O bond lengths (in black) when one (a) or two (b) outermost surfaces are lithiated. The purple, red and grey colours are related to Li, O and Ti, respectively. ....	115
Figure 4.20: Filling of the titania <i>d</i> orbitals of the titania located on the upper (a) and lower (b) outermost (001) surfaces. The purple, red and grey colours are associated with Li, O and Ti, respectively. ....	116
Figure 4.21: DOS of the anatase slabs having one (red plot) or two (green plot) outermost (001) surfaces lithiated. VB and CB stand for the valence and conduction bands, respectively. ....	117
Figure 4.22: Optimized lithiated anatase (001) slab with the maximal capacity of $x = 1$ (a) and non-lithiated slab (b). The Li ions are in purple, while the Ti and O atoms are in grey and red, respectively. ....	118
Figure 4.23: Face view (a) and top view (b) of the optimized fully lithiated (001) slab including the measures of angles and bond lengths of the O-Li-O (blue) and O-Ti-O (black) chains. The Ti ions are in grey, the O ones in red and the Li ones in purple. ....	119
Figure 4.24: Profile of the non lithiated (a) and fully lithiated (b) anatase (001) slab. The grey, red and purple colours are related to Ti, O and Li, respectively. ....	120
Figure 4.25: Measures of the $Ti_{6c}-O_{3c}$ (blue) and $Ti_{5c}-O_{3c}$ (black) bond lengths along the <i>z</i> axis of the fully lithiated anatase (001) slab. The Ti, O and Li ions are indicated in grey, red and purple, respectively. ....	120
Figure 4.26: Measures of the Li-O bond lengths and angles of the octahedral sites located at the centre of the fully lithiated (001) slab. The Li, Ti and O ions are in purple, grey and red, respectively. ....	121
Figure 4.27 : DOS of the atoms constituting the inner wall of the fully lithiated (001) slab. The blue plot represents the total DOS of the slab while the red and green colours refer to the <i>p</i> and <i>d</i> orbital contributions of the selected atom (highlighted in yellow). VB and CB indicate the positions of the valence and conduction bands, respectively. ....	122

Figure 4.28 : DOS of the external atoms of the fully lithiated (001) slab. The total DOS is displayed in blue while the red and green colours are associated with the <i>p</i> and <i>d</i> orbital contributions of the selected atom (highlighted in yellow). VB and CB represent the valence and conduction bands, respectively. ....	123
Figure 4.29: Total DOS of the anatase (001) slabs lithiated only on the external surfaces (green plot) or fully lithiated (magenta plot). VB and CB indicate the positions of the valence and conduction bands, respectively. ....	125
Figure 4.30: Total DOS of the fully lithiated (001) slab (red plot) compared with the half (green plot) and fully (blue plot) lithiated anatase bulk. VB and CB stand for the valence and conduction bands, respectively. ....	126
Figure 4.31: Anatase (001) slabs with lithium adsorbed on fully coordinated (a) or undercoordinated (b) surface oxygen atoms. The purple, red and grey spheres are associated with Li, O and Ti, respectively. ....	129
Figure 4.32: Optimized anatase (36, 0) nanotube with Li ions intercalated into the inward surface of the external wall. The Ti, O and Li elements are represented in grey, red and purple, respectively. ....	131
Figure 4.33: Optimized anatase (36, 0) nanotube with lithium ions inserted at the surface of the external wall. The grey, red and purple spheres represent the Ti, O and Li elements, respectively. The black arrows indicate the displacement of the Li ions upon geometry optimization. ....	132
Figure 4.34: Optimized anatase (36,0) nanotube with lithium intercalated into the external wall before (a) and after (b) the final geometry optimization. The Ti atoms are in grey, the O ones in red and the Li ions in purple. The Ti-O bond lengths are indicated in green.....	135
Figure 4.35: Non-optimized (a) and optimized (b) anatase (36,0) nanotubes with lithium intercalated into the external wall. The purple, red and grey spheres represent the Li, O and Ti elements, respectively.....	136
Figure 4.36: DOS of the titania atoms located on the external wall of the $\text{Li}_{0.33}\text{TiO}_2$ anatase (36,0) nanotube. The blue and green plots are associated with the total DOS and the <i>d</i> orbital contributions of the Ti atoms, respectively. VB and CB represent the valence and conduction bands, respectively. ....	138
Figure 4.37: Previously optimized anatase (36,0) nanotube with lithium intercalated into the internal wall before (a) and after (b) the final geometry optimization. The Li	

ions are in purple while the Ti and O atoms are in grey and red, respectively. The Ti-O bond lengths are indicated in green.....	139
Figure 4.38: Non-optimized anatase (36,0) nanotube with lithium intercalated into the internal wall before (a) and after (b) geometry optimization. The grey, red and purple colours refer to the Ti, O and Li elements, respectively. The Ti-O bond lengths are indicated in green. ....	141
Figure 4.39: DOS of the $Ti^{3+}$ ions of the previously optimized anatase (36,0) nanotube having its internal wall lithiated. The blue and green plots represent the total DOS and the titania d orbital contributions, respectively. VB represents the valence band while CB stands for the conduction band. ....	142
Figure 4.40: DOS of the $Ti^{3+}$ ions of the <i>nt-S2</i> anatase (36,0) nanotube having its internal wall lithiated. The blue and green plots stand for the total DOS and the <i>d</i> orbital contribution of the Ti atoms, respectively. VB and CB represent the valence and conduction bands, respectively. ....	143
Figure 4.41: Optimized anatase (36,0) nanotube with lithium inserted into the central layer. The Li ions are in purple while the Ti and O atoms are in grey and red, respectively. ....	144
Figure 4.42: DOS of the reduced Ti ions located in the central layer and in the external wall of the previously optimized anatase (36,0) nanotube having its central layer lithiated. The total DOS is displayed in blue while the green plots represent the <i>d</i> orbital contributions of the selected titania atom (highlighted in green). VB and CB stand for the valence and conduction bands, respectively. ....	145
Figure 4.43: <i>Nt-S2</i> anatase (36,0) nanotube with lithium inserted into the central layer before (a) and after (b) geometry optimization. The grey, red and purple spheres represent the Ti, O and Li elements, respectively.....	147
Figure 4.44: DOS of the $Ti^{3+}$ ions located on the external wall and the central layer of the <i>nt-S2</i> anatase (36,0) nanotube having its central layer lithiated. The blue and green plots refer to the total DOS and the Ti <i>d</i> orbital contributions, respectively. VB represents the valence band while CB stands for the conduction band. ....	148
Figure 4.45: Non-optimized anatase (36,0) nanotube having both its internal and external walls lithiated. The Li ions are in purple while the Ti and O atoms are in grey and red, respectively.....	150

Figure 4.46: <i>Nt-S2</i> anatase (36,0) nanotube with lithium adsorbed at the surface of the external wall. The purple, red and grey spheres represent the Li, O and Ti elements, respectively. ....	151
Figure 5.1: Primitive unit cell of sodium bulk. ....	159
Figure 5.2: Non-optimized $\text{Na}_{0.5}\text{TiO}_2$ supercell. The Na ions are in blue while the Ti and O atoms are in grey and red, respectively. ....	160
Figure 5.3: Optimized anatase $\text{TiO}_2$ (a), $\text{Na}_{0.5}\text{TiO}_2$ (b) and $\text{Li}_{0.5}\text{TiO}_2$ (c) bulks. The Na and Li ions are in blue and purple, while Ti and O elements are in grey and red, respectively. The reduced $\text{Ti}^{3+}$ ions are highlighted in green. ....	162
Figure 5.4: Measures of the Na-O distances for $\text{Na}_{0.5}\text{TiO}_2$ bulk. The blue, grey and red colours represent the Na, Ti and O elements, respectively. ....	163
Figure 5.5: DOS of the $\text{Na}_{0.5}\text{TiO}_2$ bulk where VB and CB indicate the positions of the valence and conduction bands. The blue plot represents the total DOS while the red and green plots stand for the <i>p</i> and <i>d</i> orbital contributions, respectively. ....	165
Figure 5.6: Total DOS of the $\text{Li}_{0.5}\text{TiO}_2$ and $\text{Na}_{0.5}\text{TiO}_2$ bulks. VB and CB stand for the valence and conduction bands, respectively. ....	166
Figure 5.7: Measures of the Ti-O bond lengths and angle (a) and of the Na-O distances (b) of the optimized $\text{NaTiO}_2$ anatase bulk. The Na ions are in blue while the Ti and O atoms are in grey and red, respectively. ....	168
Figure 5.8: DOS of the $\text{NaTiO}_2$ bulk. The total DOS is represented in blue while the red and green plots stand for the <i>p</i> and <i>d</i> orbital contributions, respectively. VB and CB indicate the positions of the valence band and conduction bands, respectively. ....	169
Figure 5.9 : Total DOS of the $\text{LiTiO}_2$ and $\text{NaTiO}_2$ bulks. VB and CB represent the valence and conduction bands, respectively. ....	170
Figure 5.10: (001) anatase slab having its outermost tetrahedral sites filled with sodium. The blue, red and grey colours represent the Na, O and Ti elements, respectively. ....	172
Figure 5.11: Side (a) and face (b) views of the optimized $\text{Na}_{0.33}\text{TiO}_2$ anatase (001) slab. The blue, red and grey colours represent the Na, O and Ti elements, respectively. ....	173
Figure 5.12: Total DOS of the optimized (001) anatase slab having Na ions intercalated in one outermost surface. VB stands for the valence band while CB represents the conduction band. ....	174
Figure 5.13: Optimized (001) anatase slab with Na ions inserted into the inner octahedral sites. The Na ions are in light blue while the Ti and O are in grey and red,	

respectively. The Na-O distance are indicated in blue while the Ti-O bond length is written in black.....	175
Figure 5.14: Total DOS of the optimized anatase (001) slab having the inner octahedral sites filled with sodium. VB and CB represent the valence and conduction bands, respectively. ....	175
Figure 5.15: Non optimized Na <sub>0.67</sub> TiO <sub>2</sub> (a), optimized Na <sub>0.67</sub> TiO <sub>2</sub> (b) and optimized Li <sub>0.67</sub> TiO <sub>2</sub> (c) (001) slabs. The blue, purple, red and grey colours represent the Na, Li, O and Ti elements, respectively. ....	177
Figure 5.16: Storage of the added charges in the (001) Na <sub>0.67</sub> TiO <sub>2</sub> anatase slab. The blue, red and grey colours stand for the Na, O and Ti elements, respectively.....	178
Figure 5.17: Total DOS of the Na <sub>0.67</sub> TiO <sub>2</sub> (001) anatase slab where VB and CB indicate the positions of the valence and conduction bands, respectively.....	179
Figure 5.18: Side (a) and face (b) views of the optimized NaTiO <sub>2</sub> (001) anatase slab. The Na ions are represented in blue while the Ti and O atoms are in grey and red, respectively. ....	181
Figure 5.19: Total DOS of the optimized NaTiO <sub>2</sub> (001) anatase slab. VB and CB stand for the valence and conduction bands, respectively.....	181
Figure 5.20: Optimized TiO <sub>2</sub> (a) and NaTiO <sub>2</sub> (b) (001) anatase slabs. The Na ions are in blue while the Ti and O atoms are in grey and red, respectively.....	182
Figure 5.21: Optimized (001) anatase slabs with sodium adsorbed above the fully coordinated (a) and undercoordinated (b) surface oxygen atoms. The Na ions are in blue while the Ti and O atoms are in grey and red, respectively. ....	185
Figure 5.22: Total DOS of the anatase (001) slab having sodium adsorbed above its fully coordinated oxygen atoms. VB represents the valence band while CB stands for the conduction band. ....	186
Figure 5.23: Total DOS of the anatase (001) slab having sodium adsorbed above its undercoordinated oxygen atoms. VB and CB indicate the positions of the valence and conduction bands, respectively. ....	187
Figure 5.24: <i>Nt-S2</i> anatase (36,0) nanotube having sodium intercalated into the external wall before (a) and after (b) geometry optimization. The blue, red and grey spheres represent the Na, O and Ti elements, respectively.....	190
Figure 5.25: Total DOS of the anatase (36,0) nanotube having Na intercalated in its external wall. VB and CB represent the valence and conduction bands, respectively. ....	191

Figure 5.26: Sodium intercalation into the internal wall of <i>nt</i> -S1 (a) and <i>nt</i> -S2 (b) anatase (36,0) nanotubes. The blue, red and grey colors represent the Na, O and Ti elements, respectively. ....	192
Figure 5.27: <i>Nt</i> -S1 anatase (36,0) nanotube having sodium intercalated into its internal wall after geometry optimization. The Na are in blue, the O in red and the Ti in grey. ....	193
Figure 5.28: <i>Nt</i> -S2 anatase (36,0) nanotube having sodium intercalated into its central layer. The Na ions are in blue while the Ti and O atoms are in grey and red, respectively. ....	194
Figure 5.29: <i>Nt</i> -S2 anatase (36,0) nanotube having both its internal and external walls sodiated. The blue, red and grey spheres represent the Na, O and Ti elements, respectively. ....	195
Figure 5.30: <i>Nt</i> -S2 anatase (36,0) nanotube having sodium adsorbed above the fully coordinated oxygen atoms of the external wall. The blue, red and grey colors stand for the Na, O and Ti elements, respectively. ....	196
Figure 5.31: Total DOS of the <i>Nt</i> -S2 anatase (36,0) nanotube having sodium adsorbed above the fully coordinated oxygen atoms located on the external wall. VB stands for the valence band while CB represents the conduction band. ....	197
Figure A.1: Hay-Wadt ECP basis set chosen for titanium atom <sup>173</sup> .....	212

# List of Tables

Table 2.1: Lattice constants and band gaps of anatase bulk TiO <sub>2</sub> calculated by Lisovski et al. <sup>91</sup> using different functionals. ....	66
Table 2.2: Calculated and experimental lattice constants and band gaps of bulk anatase TiO <sub>2</sub> . ....	67
Table 2.3: Calculated and experimental lattice constants and band gaps of corundum Ti <sub>2</sub> O <sub>3</sub> . ....	68
Table 3.1: Mulliken charges of the Ti and O ions in optimized anatase bulk, slab and <i>nt</i> -TiO <sub>2</sub> structures. ....	87
Table 4.1: Total bulk energies or single point energy obtained with the different Li basis sets. ....	94
Table 4.2: Lithium intercalation energies and voltages calculated with different basis sets. ....	95
Table 4.3: Lithium intercalation energies and voltages for different (001) slab configurations. ....	127
Table 4.4: Lithium intercalation energies and voltages for different anatase (36,0) nanotube configurations. ....	153
Table 5.1: Total bulk energies or single point energy obtained with the different Na basis sets. ....	159
Table 5.2: Sodium intercalation energies and voltages calculated with different basis sets. ....	160
Table 5.3: Sodium intercalation energies and voltages for different slab and bulk configurations. ....	183
Table 5.4: Intercalation energies and voltages obtained for the sodiated and lithiated bulks. ....	184
Table 6.1: Comparison of the lithium and sodium intercalation energies and voltages in the different TiO <sub>2</sub> structures. ....	209

# Acknowledgements

I would like to thank my supervisor, Dr. Maria Alfredsson for having offered me the opportunity to do this work and for all her help and endless support. She taught me to always stay positive and motivated even when things do not go as planned.

I would like to thank the Alistore European Research Institute for providing the funding that has allowed this research to be possible and for all the rewarding exchanges within its different institutions all over Europe.

I would also like to thank the School of Physical Sciences for providing the resources necessary to carry out this work and express my profound gratitude to its staff for their assistance and willingness to help. I am also fully indebted to Dr. Tim Kinnear for all his help solving the computer issues.

To my friends who accompanied me through this challenging last period of study, I would like to thank you all from the bottom of my heart for always being able to find the right words or things to do to keep my spirits up!

Last but not least, I wish to thank my family for their unwavering love and support, with a special huge thanks to my parents for having awakened my curiosity towards science.

# Declaration

I hereby declare that the work presented in this thesis is totally that of the author, except where due acknowledgment has been made. This work has not been previously submitted, in whole or in part, for any other academic degree.

Candidate: Marine Riesenmey

# Abstract

The aim of this thesis is to gain a deeper understanding of the anatase TiO<sub>2</sub> nanotubes as negative electrodes in lithium-ion and sodium-ion microbatteries by researching their fundamental intercalation processes. The nano-structuring of the anatase TiO<sub>2</sub> electrodes allows to improve their electrochemical behaviour, and thus the batteries capacities. To this end, a DFT study of the lithium and sodium insertions into the anatase bulk, slab and nanotubes has been carried out.

The study shows that the anatase TiO<sub>2</sub> exhibits a higher reactivity towards sodium than towards lithium, resulting in two different insertion mechanisms: Li ions are intercalated via a two-phases equilibrium, while Na ions insertion occurs spontaneously without phase transformation. This high reactivity towards sodium may induce Na trapping, partly explaining the irreversible capacity losses observed during the first cycle.

Lithium ions are intercalated spontaneously with higher capacities into the surface than into the bulk and can explain the capacities exceeding the theoretical bulk value reported for the nanostructured electrodes. The lithium intercalation induces a gradual structural reconstruction, forming a rock salt LiTiO<sub>2</sub> phase, but its inward growth is limited to a few nanometres.

The sodium ions are favourably adsorbed above all the oxygen atoms of the anatase surface and spontaneously inserted into the surface. However, the surface reconstruction is restricted by the electronic repulsion of the Na ions. This limited stability of the sodiated surfaces can be a possible explanation of their transformation into amorphous structure.

The most favourable intercalation sites of the nanotubes are located in their external wall, stabilizing the *nt*-TiO<sub>2</sub> structure. Li and Na ions are also favourably adsorbed on-top the outermost oxygen atoms, explaining why more external wall exposure exhibit better capacities. Reactivity with the internal wall is spontaneous for Li ions, while the Na ions require low potentials and are associated with rupturing Ti-O bonds in agreement with the formation of amorphous *nt*-TiO<sub>2</sub> below 0.5 V vs Na/Na<sup>+</sup>.

# Chapter 1

## Introduction

TiO<sub>2</sub> nanotubes are a promising material as negative electrode for lithium-ion and sodium-ion microbatteries. This three-dimensional (3D) nano-architected electrode improve the areal capacity of the microbatteries by 65% compared to a two-dimensional (2D) thin film<sup>1</sup>. First-principles calculations were carried out in this thesis to gain a deeper understanding of both the chemical and structural changes occurring in this electrode, and hence optimize its performances.

### 1.1 Aims

The miniaturization of portable devices requires the development of power sources at the micrometer scale, which is a huge potential market. Thus, microbatteries are used for remote and nomadic powering of autonomous portable devices, such as microelectromechanical systems (a system where a component, such as a sensor or an actuator, is built directly on a computer chip and powered by its own microbattery), implantable medical devices, RFIDs and many others<sup>2</sup>. Owing to the high energy density, the microbatteries are Li-ion batteries. However, the similar electrochemical properties of sodium, combined with its abundance and low cost, have recently encouraged the scientists to develop Na-ion batteries as a promising and cheaper alternative to the Li-ion ones. The low energy per unit area and the lifetime of actual microbatteries, based on the 2D thin film technology, are holding back the development of the latter applications. Changing the configuration of the electrodes, from 2D to a 3D nano-architecture, is one of the ways to improve the electrochemical performances.

Titania can self-organize into amorphous nanotubes (*nt*-TiO<sub>2</sub>) thanks to a template-free, simple anodization process leading to an increase of the microbattery capacities by 65%. Moreover, the anodization process allows a good electrical contact between the active material and the current collector, excluding the use of additives, such as, carbon blacks or polymer binders<sup>3</sup>. The amorphous *nt*-TiO<sub>2</sub> can then be transformed into anatase ones by annealing.

Recently, polymer electrolyte was successfully electrodeposited inside TiO<sub>2</sub> nanotubes<sup>4</sup>, opening the way to an electrochemically fabricated 3D microbattery. Nevertheless, the fundamental processes involved in *nt*-TiO<sub>2</sub> as negative electrode are still poorly understood while further improvements require a deeper understanding of both the chemical and structural changes occurring in this electrode. Density Functional Calculations (DFT) allows to access information on the electronic structure of the atoms. The development of software like the periodic CRYSTAL<sup>5</sup> code, that fully exploits the helical rototranslational symmetry of the nanotube structure, allows to drastically reduce the computational time<sup>6</sup>. Thus, *nt*-TiO<sub>2</sub> containing several hundreds of atoms are reachable by first principles studies.

The three layers thick (3ML) [001] anatase *nt*-TiO<sub>2</sub> are one of the rare nanotubes models to exhibit a negative strain energy over the whole diameter range, indicating a higher stability of the nanotube compared to the corresponding 3 ML sheet. This result points out the favourable formation of nanotubes and make the 3ML [001] anatase *nt*-TiO<sub>2</sub> a suitable model to acquire a better understanding of *nt*-TiO<sub>2</sub> as negative electrode. This model has never been used before for the study of lithium or sodium intercalation to the best of our knowledges.

The aim of this thesis is to gain a deeper understanding of the lithium and sodium intercalations into the nanotubular anatase electrodes by means of DFT calculations. The identification of the most favourable intercalation sites present in the nanotubes will help to determine the most suitable *nt*-TiO<sub>2</sub> architecture. The length, diameter and wall thickness of the nanotubes produced experimentally can then be designed by changing the electrochemical parameters (potential, time, electrolyte composition) to fabricate microbatteries with enhanced performances.

The first objective of this work is to study the cation intercalations into the bulk at different concentrations using the same geometry constraints as the ones required for the modelling of nanotubes. The results obtained will then be compared with the previous theoretical studies to isolate the influences of these constraints. The bulk studies also allow to constitute a collection of reference data from where the intercalation into the slab and nanotubes can later be compared.

In a second phase, the cation insertions into the slab will be investigated. This part will allow to better understand the role plays by the anatase surface on the cation intercalations, and thus on the battery capacities. Another advantage of the slab calculations is their low computational cost that allows to explore many different configurations. Like for the bulk, the calculations carried out on the slab will form a collection of reference data from where the influence of the strain energy present in the nanotubes will be later be isolated.

The last step will be to study the cation intercalations into the nanotubes using the 3ML [001] anatase *nt*-TiO<sub>2</sub> rolled up along the  $(n_1,0)$  direction as model. The calculations will help to better understand how the narrowing and the widening of the octahedral sites induced by the strain energy affect the cation intercalations. This study will also allow to determine if other phenomena, such as insertion into the tetrahedral sites or favourable cation adsorptions at the surface, are present in the nanotubes.

The lithium and sodium intercalations will be compared throughout the Chapter 5 to describe some phenomena observed experimentally<sup>7</sup>, such as, the absence of potential plateau during the cycling of the sodiated electrodes or the transformation of the anatase nanotubes into amorphous ones when Na ions are intercalated at low voltages.

## 1.2 Background

### 1.2.1 The Li-ions batteries

Batteries are devices made of electrochemical cells that convert electrical energy into chemical energy by means of redox reactions with the potential to store it. Each cell contains an anode or negative electrode, a cathode or positive electrode and an electrolyte that separates the two electrodes assisting ion transfer between them. When these two electrodes are connected, electrons flow spontaneously from the anode that is oxidized to the cathode which is reduced. For a certain number of batteries; i.e. secondary batteries, the electrochemical process can be reversed by applying a current on the opposite direction that restores the chemical composition of the electrodes and thus recharges the cell, as detailed in Figure 1.1.

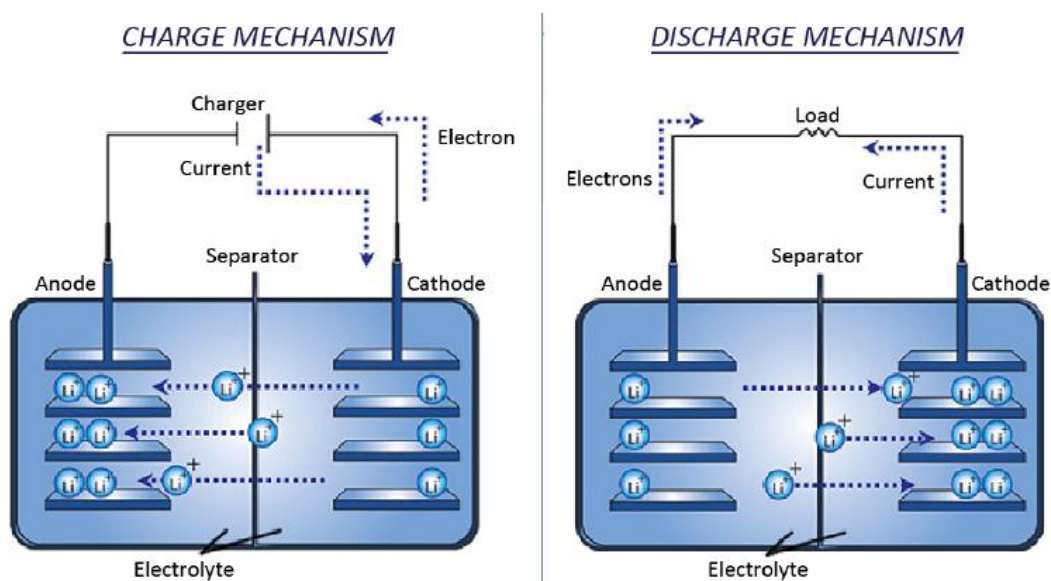


Figure 1.1: Charge and discharge mechanisms of a lithium batteries<sup>8</sup>.

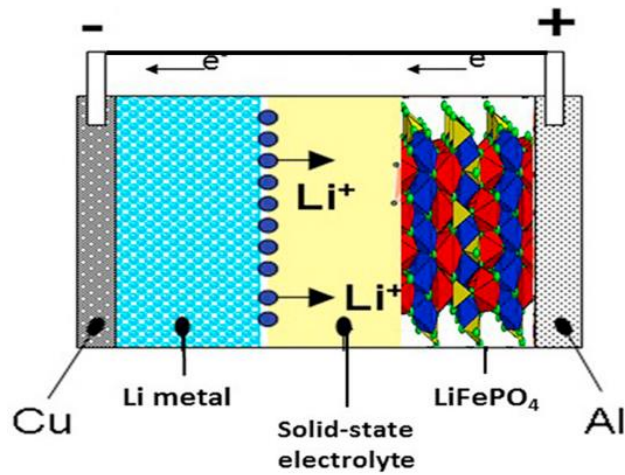
Several parameters that depend on the chemistry of the system allow to define the battery properties. Among them are the cell voltage, expressed in volt, that represents the difference between the potential of each electrode; or the capacity, in ampere-hour per gram, that corresponds to the quantity of electricity that can be stored per gram of active material. This variable can be deduced from the number of exchanged electrons per gram of material and is an intrinsic property of the active material.

Lithium is the lightest solid element of the periodic table, with a molar mass equal to  $6.491 \text{ g}\cdot\text{mol}^{-1}$  and a density equal to  $0.53 \text{ g}\cdot\text{cm}^{-3}$ , as well as the most electropositive metal ( $-3.04 \text{ V}$  versus standard hydrogen electrode). Due to the properties of Li-metal, this element has found attraction as the anode, allowing the design of storage systems with high energy density that aroused the interest of the scientists during the previous century<sup>9</sup>. The first work about lithium batteries was initiated by G.N Lewis in 1912 and the first commercialization occurred in 1970 thanks to the development of insertion cathode materials by S. Whittingham<sup>10</sup>. This first commercialized battery was made of a lithium metal anode, a  $\text{TiS}_2$  cathode and an organic electrolyte. However, the formation of irregular deposits<sup>11</sup> of lithium (dendrites) during the charge lead the metal anode to reach the cathode and short-circuit the electrochemical cell, introducing safety issues.

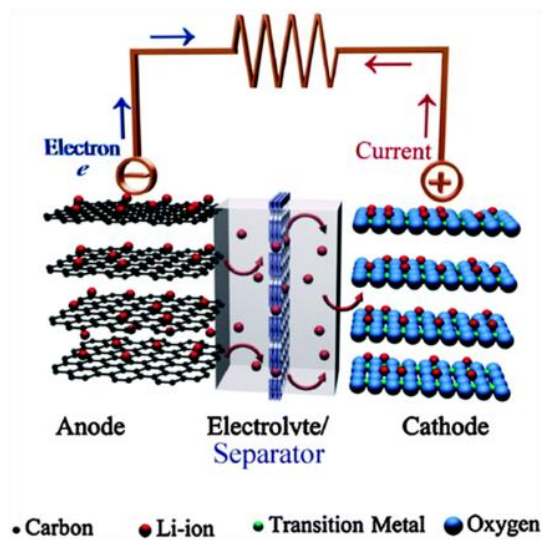
Two main approaches were developed to reduce the growth of dendrites<sup>12</sup>. The first one consists on replacing the liquid electrolyte by a solid one, whose mechanical properties stop the growth of the dendrites avoiding to short circuit the cell. The solid electrolyte can be a polymer, leading to the so-called “lithium polymer battery” technology, or a solid-state inorganic electrolyte as it is illustrated in Figure 1.2a<sup>13</sup>. The other approach is to replace the metallic anode by a low potential insertion material, such as graphite<sup>14</sup> as it is displayed in Figure 1.2b<sup>15</sup>.

The latter solution is referred to as “lithium ion battery” technology because the lithium is only present in its ionic state. The first lithium ion batteries were commercialized by Sony in 1991<sup>16</sup> using graphite as the negative electrode (anode),  $\text{LiCoO}_2$  as the positive electrode (cathode) and a solution of  $\text{LiPF}_6$  dissolved in ethylene carbonate (EC) and diethylene carbonate (DEC) as the electrolyte.

The very low Li intercalation potential exhibited by the graphite facilitates lithium electrodeposition on the electrodes. As a result, even a slight overcharging of the battery can lead to the growth of dendrites that can easily cause short circuits and destroy the battery cell by causing serious runaway exothermic reactions<sup>17</sup>. This problem brought the scientists to look for alternative negative electrode materials.



a



b

Figure 1.2: Lithium metal<sup>13</sup> (a) and Lithium ion<sup>15</sup> (b) batteries.

### 1.2.2 The TiO<sub>2</sub> nanotubes as anode for microbatteries

The high intercalation potential exhibited by the titanium dioxide electrode (1.75 V versus Li<sup>+</sup>/Li redox couple) eliminates the risk of dendrites formation in case of overcharging, and make TiO<sub>2</sub> a promising alternative negative electrode material<sup>18</sup>. Macklin and Neat<sup>19</sup> were the first to report the high capacity and reversibility of lithium insertion into titanium oxide electrodes for battery applications.

The theoretical capacity of graphite is  $379 \text{ mA.h.g}^{-1}$ , while  $\text{TiO}_2$  anatase theoretically reaches  $168 \text{ mA.h.g}^{-1}$ . However, this modest capacity can be improved by moving from a planar (2D) configuration to 3D-nanoarchitected electrode structure exhibiting larger specific area<sup>17</sup>. Thus, the interfacial area between active components of the battery increases while the diffusion distances remain short.

In 1999, Zwilling et al.<sup>20</sup> reported for the first time the possibility to form organized porous  $\text{TiO}_2$  structures by anodization of titanium in an electrolyte containing chromic acid and hydrofluoric acid. The nanotubular titanium oxide (*nt*- $\text{TiO}_2$ ) produced by anodization has then gained significant attention as a material with increased versatility. Among the different applications, it opened up the possibility using nanostructured titania as a possible negative material in Li-ion batteries<sup>21</sup>. The first electrochemical study on lithium storage in self-supported *nt*- $\text{TiO}_2$  obtained by electrochemical anodization was published by Fang<sup>22</sup> et al. in 2008.

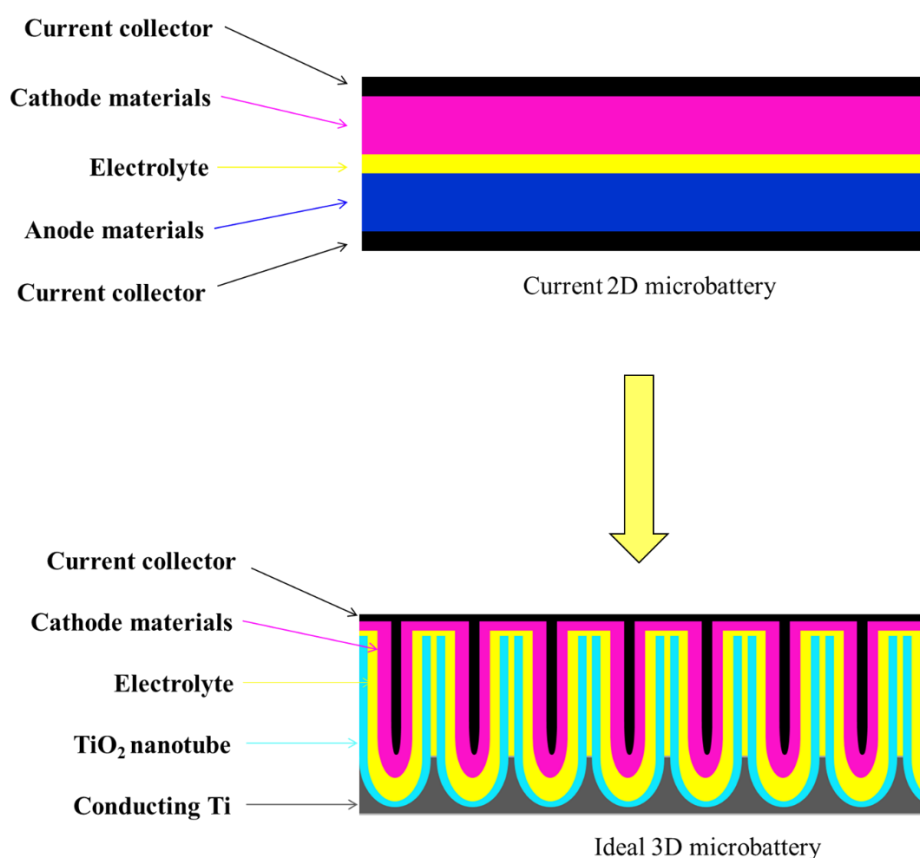


Figure 1.3: Schematic of the 2D and 3D thin film microbatteries.

One of the main advantages of the anodization process is to generate a good electrical contact between the active material and the current collector, excluding the use of additives, such as, carbon blacks or polymer binders that are currently used in composite electrodes, as shown in Figure 1.3. The anodization process generates amorphous *nt*-TiO<sub>2</sub>. However, these amorphous nanotubes can be easily transformed into anatase ones by annealing at 150-500°C temperatures range<sup>23</sup>. The good discharge capacity and cycling stability make *nt*-TiO<sub>2</sub> very promising materials for Li-ion microbatteries.

Among all polymorphs of titania, the anatase structure is a potential candidate due to the good lithium intercalation behaviour associated to enhanced safety, low self-discharge, good capacity retention on cycling and high power<sup>24</sup>. Other polymorphs of TiO<sub>2</sub> have also been studied as the negative electrode in Li-ion batteries. Examples of different starting material include rutile, anatase or TiO<sub>2</sub>-B, as displayed in Figure 1.4 where the titania and oxygen atoms are represented in grey and red, respectively.

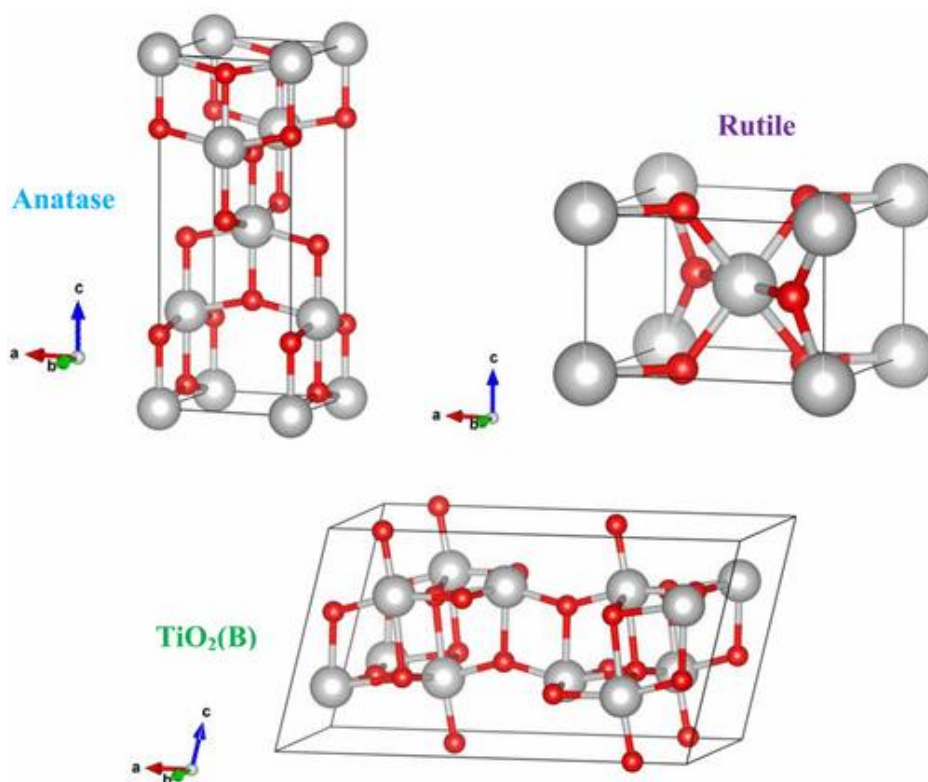


Figure 1.4: Anatase, rutile and TiO<sub>2</sub> (B) polymorphs where the grey and red spheres represent the titania and oxygen atoms, respectively<sup>25</sup>.

The lithium intercalation into rutile is negligible at room temperature<sup>26</sup> while TiO<sub>2</sub> (B) is a very promising intercalation material with a reported capacity of 305 mA.h.g<sup>-1</sup> for electrodes made of TiO<sub>2</sub> (B) nanowires<sup>21</sup>. However, the nanowires require the use of composite electrode. Li<sup>+</sup> ion insertion into the crystalline anatase phase is possible up to 0.5 Li per Ti reaching a theoretical capacity value of 168 mA.h.g<sup>-1</sup><sup>27</sup>. The nanostructured anatase electrodes made of nanosheets<sup>28</sup> or nanotubes<sup>29</sup> exhibit a capacity of 200 mA.h.g<sup>-1</sup>.

The important role played by the anatase surface was highlighted in 1997 by Lindstrom et al.<sup>30</sup> who observed a particularly high capacity for the nanoporous anatase TiO<sub>2</sub> films and attributed it to Li ions adsorption at the surface. Ten years later, Wang et al.<sup>31</sup> studied the pseudocapacitive contributions to electrochemical energy storage in anatase TiO<sub>2</sub> nanoparticles. This study showed that the charge stored at the surface of the TiO<sub>2</sub> from the pseudocapacitance storage mechanism contributes to the total charge storage of the nanoparticles. The effects on capacities become increasingly important for particles sizes under 10 nm.

Zhang et al.<sup>32</sup> reported the pseudocapacitive contribution to the electrochemical energy storage for different nanotubes of TiO<sub>2</sub> including the anatase ones. The importance of this contribution depends on the phase and morphology of the *nt*-TiO<sub>2</sub>. The pseudocapacitive Li ion storage with respect to oriented anatase *nt*-TiO<sub>2</sub> grown by anodization was studied by Zhu et al.<sup>31</sup>. They showed that the anatase *nt*-TiO<sub>2</sub> electrodes have both pseudocapacitive Li<sup>+</sup> storage associated with the nanotube surface and the Li<sup>+</sup> storage within the bulk material.

The relative contribution of the pseudocapacitive and bulk storages depends strongly on the scan rate. At low scan rates, the bulk Li<sup>+</sup> storage dominates the total Li<sup>+</sup> storage. However, at the scan rate of 1 mV/s, the pseudocapacitive storage capacity has a similar value to the bulk storage capacity and even overcome the bulk one at higher scan rates. As a result, the storage of Li<sup>+</sup> associated with the surface, along with the storage in the bulk TiO<sub>2</sub>, could explain the improved Li<sup>+</sup> storage capacity for *nt*-TiO<sub>2</sub>. This study also showed that the pseudocapacitive behaviour is observed between 1.75 and 1.4V. The rate capability of the charge capacity for *nt*-TiO<sub>2</sub> electrodes with different film thickness was also investigated and did not show any thickness dependence.

This result implies that the electron transport across the *nt*-TiO<sub>2</sub> is not the rate-limiting step for Li<sup>+</sup> intercalation/deintercalation process. It also indicates that the electrolyte ion conduction within the *nt*-TiO<sub>2</sub> pores or between the nanotubes is fast enough. Similar investigation were recently conducted by Plylahan et al.<sup>33</sup> using a PEG-MMA electrolyte (instead of EC/DMC). This study showed the pseudocapacitive contribution is still present but less important.

A deeper study of lithium intercalation into anatase surface was carried out by Wagemaker et al.<sup>34</sup> using reflection mode grazing incidence X-ray Absorption Spectroscopy (XAS) in powder samples of anatase. For the largest glancing angle measured, corresponding to a penetration depth of more than 50 nm, the spectrum is recognized as that of Li-titanate (Li<sub>0.5</sub>TiO<sub>2</sub>). The corresponding edge position leads to a Ti oxidation state of +3.4, which is comparable to that of the bulk Li-titanate; +3.5 estimated from X-ray Absorption Near Edge Spectroscopy (XANES) measurements in transmission mode. However, for a smaller glancing angle, corresponding to a penetration depth of about 3-4 nm, the Ti oxidation state results in a value close to +3.

As a result, a thin Ti<sup>3+</sup> layer, with a XANES structure similar to that of Ti<sub>2</sub>O<sub>3</sub> is formed on a Li-titanate layer by the electrochemical intercalation of Li into anatase. Moreover, after the first intercalation/deintercalation cycle, the Ti<sup>3+</sup> top layer is also present in the partly charged and deintercalated state, although the thickness is reduced to a few Ångstroms, meaning that this transformation is not fully reversible, and after the first cycle, structural changes remain present.

The Extended X-Ray Absorption Fine Structure (EXAFS) signal showed that the near neighbour atomic configuration of the first 4 nm, characterized by Ti<sup>3+</sup> states, is comparable with that of the Li-titanate phase. Therefore, it is concluded that Li intercalation into anatase TiO<sub>2</sub> leads to the transformation toward the Li-titanate structure, in addition, a thin film of about 4 nm in thickness has a similar atomic structure compared to Li-titanate but with a Ti valence close to 3+ (like in Ti<sub>2</sub>O<sub>3</sub>).

The effective  $\text{Ti}^{3+}$  valence of the first 4 nm suggests a composition close to  $\text{LiTiO}_2$  in order to preserve local charge neutrality. Assuming a similar crystallographic structure as the orthorhombic Li-titanate ( $\text{Li}_{0.5}\text{TiO}_2$ ), it seems reasonable that in  $\text{LiTiO}_2$  all of the available octahedral sites will be occupied by Li, whereas in the Li-titanate, every second site remains unoccupied. The thickness of the layer is such that the charge cannot be compensated by ions adsorbed at the surface, and additional Li ions are required to intercalate into the material for charge compensation.

A further study was carried out by Wagemaker et al.<sup>35</sup> on anatase nanoparticles. It showed that the lithiation results into the formation of a  $\text{LiTiO}_2$  phase of approximately 4 nm, independent of the particle size. As a result, the particles of 7 nm were completely transformed into the  $\text{LiTiO}_2$  phase.

Anatase transition into  $\text{LiTiO}_2$  phase was reported in the literature<sup>19</sup> under cycling at 120°C where the whole material was converted to composition  $x=1$ . However, the cycle ability at elevated temperatures after the formation of the  $\text{LiTiO}_2$  material is worse compared to the cycle ability up to a maximum composition  $x=0.5$ . This might indicate that the formation of the  $x=1$  material fractures the anatase  $\text{TiO}_2$  electrode material in such a way that it leads to a decrease of the capacity within a few cycles.

Another important study was carried out by Bi et al.<sup>36</sup> who grew *nt*- $\text{TiO}_2$  into Ti foam. The *nt*- $\text{TiO}_2$  grown on foam exhibit much higher capacities than the *nt*- $\text{TiO}_2$  grown from Ti foil. This study was carried out on amorphous *nt*- $\text{TiO}_2$ . The nanotubes grown on the curved foam are more distant from each other, allowing a better contact between the electrolyte and the external wall. They also exhibit a more obvious pseudocapacitive behaviour. On the other hand, Wei et al.<sup>37</sup> reported the fabrication of highly ordered anatase *nt*- $\text{TiO}_2$  via a two steps anodization process. A continuous nano-ring layer is formed at the top of *nt*- $\text{TiO}_2$ , avoiding any contact between the electrolyte and the external wall of the nanotubes. The electrochemical study of this *nt*- $\text{TiO}_2$  shows the absence of Li-intercalation occurring at the surface, meaning that the inner wall of the nanotubes does not exhibit pseudo-capacitive behaviour.

### 1.2.3 The anatase crystal structure

Considering that the nanotubes, when in crystalline form, adopt the anatase crystal structure, a closer understanding of this phase is discussed in more details. Anatase is an insulating, nonmagnetic, and partially covalent crystal<sup>38</sup>. Anatase has a tetragonal symmetry, its space group is  $I(4)1/amd$  (lattice constants:  $a = 3.792 \text{ \AA}$ ,  $c = 9.497 \text{ \AA}$ )<sup>39</sup>. The Ti atoms occupy the  $4e$  positions of the space group whereas the oxygen atoms fill the  $8e$  positions. The rest of the volume consists of empty octahedrons centered at  $4b$  positions and tetrahedrons at  $16f$  special positions<sup>40</sup>. Thus, the anatase structure can also be seen as a chain of distorted  $\text{TiO}_6$  octahedrons sharing four adjacent edges. This stacking, equivalent in the  $a$  and  $b$  directions, leads to empty zigzag channels in the anatase framework<sup>41</sup>.

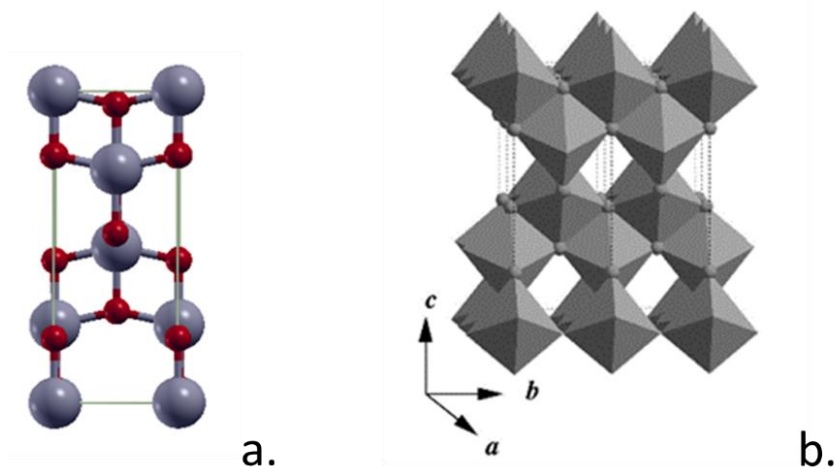


Figure 1.5: Anatase conventional unit cell (a) where the Ti atoms are displayed in grey and the O ones in red; and a polyhedral representation of the anatase structure showing the  $\text{TiO}_6$  octahedrons<sup>26</sup> (b).

In a free ion, all the  $d$  orbitals are degenerate. In an octahedral field, the  $d$  orbitals split into two groups as shown in Figure 1.6:

- The  $d_{xy}$ ,  $d_{xz}$ , and  $d_{yz}$  orbitals are lowered in energy and are collectively referred to as the  $t_{2g}$  orbitals.
- The  $d_{z^2}$  and  $d_{x^2-y^2}$  have higher energy and are labelled the  $e_g$  orbitals.

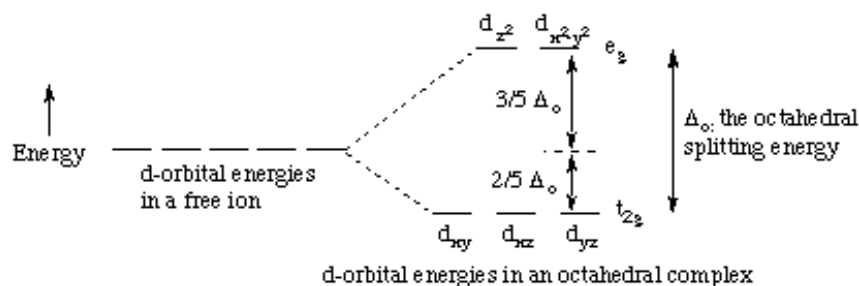


Figure 1.6: Splitting of the  $d$  orbitals in an octahedral complex.

The octahedral crystal field splitting energy is written  $\Delta_o$ . This is the energy difference between the  $t_{2g}$  and  $e_g$  orbitals. In an octahedral field, the  $e_g$  orbitals are destabilized by  $3/5 \Delta_o$  whereas the  $t_{2g}$  orbitals are stabilized by  $2/5 \Delta_o$  compared to the free ion.

Nuspl et al.<sup>41</sup> reported a further splitting of the  $t_{2g}$  set of the titanium  $d$  orbitals in the  $\text{TiO}_2$  anatase structure, attributed to the distorted local  $\text{TiO}_6$  geometry, which is lowered from  $O_h$  in an idealized framework to  $D_{2d}$  (Figure 1.7). The degenerated  $d_{xz}$  and  $d_{yz}$  are higher in energy due to the edge sharing of the octahedra in the  $bc$  and  $ac$  planes. The lowest energy orbitals  $d_{xy}$  are in the  $ab$  planes where there is no edge sharing<sup>26</sup>.

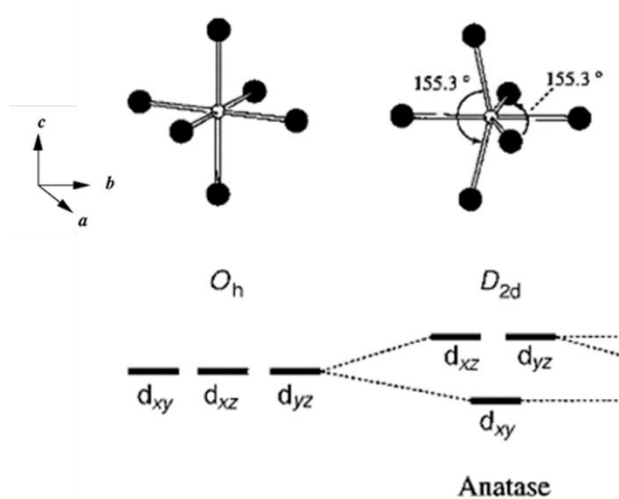


Figure 1.7: Splitting of titanium  $d$  orbitals in going from ideal  $O_h$  to anatase ( $D_{2d}$ )<sup>41</sup>.

This distortion is seen in the calculated density of states (DOS) where the valence band is predominantly of O ( $2p$ ) character while the lower conduction band consists of Ti ( $d_{xy}$ ) orbitals<sup>26</sup>. The observed band gap of anatase is approximately 3.2 eV<sup>42</sup> and the valence bandwidth measured in X-ray photoelectron spectroscopy (XPS) is 4.75 eV<sup>43</sup>. The values calculated computationally are strongly influenced by the functionals and basis sets choices. The anatase DOS computed by Koudriachova et al.<sup>26</sup> is shown in Figure 1.8. It can be noticed that the band gap equals approximately 2 eV and the valence bandwidth 4.83 eV. Lower occupied bands consist of largely O ( $2s$ ) character and lie 10–11 eV below the upper bands.

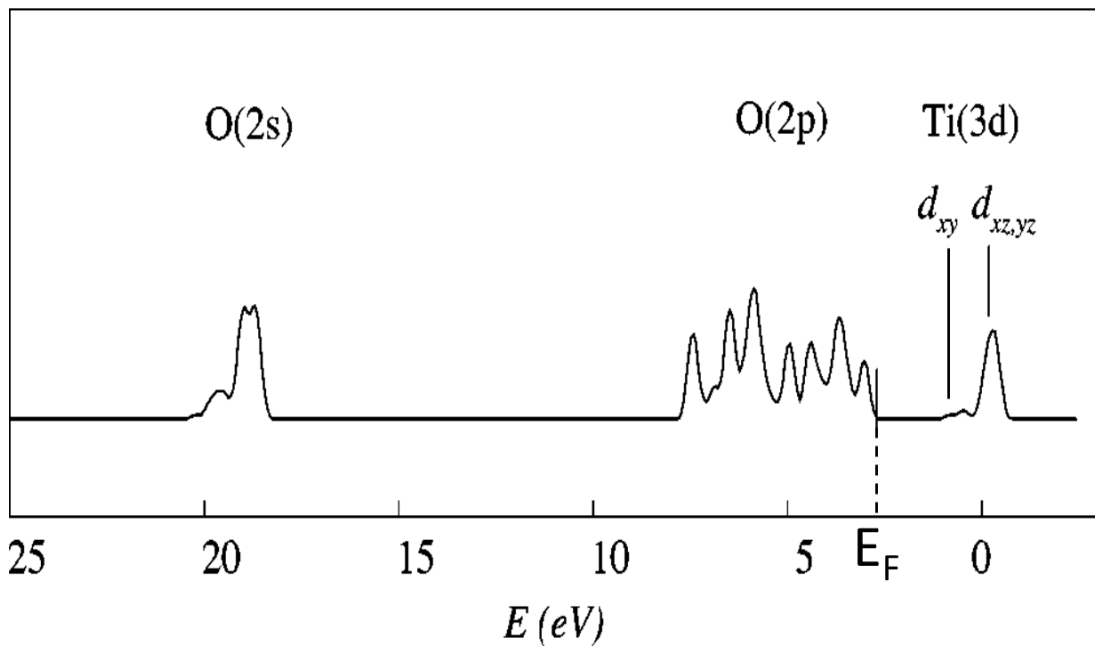


Figure 1.8: Density of states (DOS) of bulk anatase TiO<sub>2</sub><sup>26</sup>. VB and CB represent the valence and conduction bands, respectively.

Mulliken population analyses reported by Stashans<sup>44</sup> and Mackrodt et al.<sup>38</sup> using Hartree Fock methods showed effective cation charges of + 2.3 e and +2.5 e, respectively. Both studies reported that the oxygen has an effective charge equal to -1.15 e.

## 1.2.4 Theoretical studies of the anatase surfaces

In anatase, both experimental<sup>45</sup> and computational<sup>46</sup> studies proved that the (101) surface is the most stable one. As a result, the first theoretical study on lithium intercalation into anatase was performed using a bulk and a (101) surface<sup>44</sup>. The first simulations on *nt*-TiO<sub>2</sub> were also built by rolling up slabs cut along the (101) direction<sup>47</sup>. However, all these nanotubes exhibited a positive strain energy. The only reported 3 monolayer thick *nt*-TiO<sub>2</sub> exhibiting negative strain energies over the whole diameter range were built by rolling up a slab cut along the (001) direction<sup>48</sup>.

The (001) surface is more reactive because of the unsaturated coordination of the Ti atoms that are exclusively fivefold coordinated (Ti<sub>5c</sub>)<sup>49</sup>. The oxygen atoms present at this surface are a mix of fully coordinated threefold oxygens O<sub>3c</sub> and unsaturated twofold O<sub>2c</sub> as displayed in Figure 1.9<sup>50</sup>.

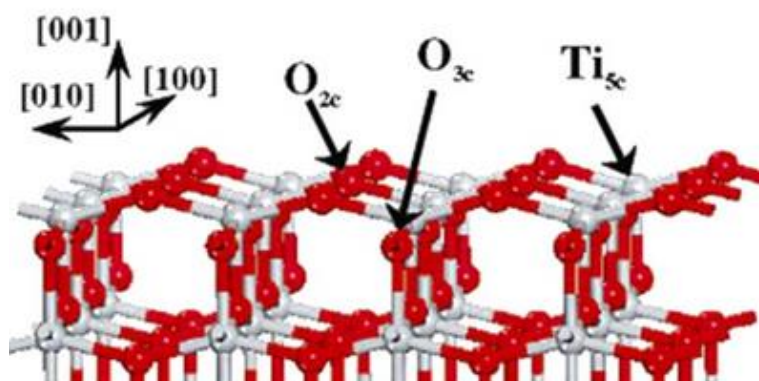


Figure 1.9: Unreconstructed anatase (001) surface showing the coordination of the different atoms<sup>50</sup>. Reprinted (adapted) with permission from reference<sup>50</sup>. Copyright 2014 American Chemical Society.

When the surface is allowed to relax, the bonds of the first four layers are elongated in the *z*-direction, resulting in an increase of the slab thickness<sup>49</sup>. The distance separating two oxygen atoms in the bulk *z*-direction equals 2.37 Å while in the slab this distance varies between 2.52 Å and 2.43 Å depending on the position in the structure (Figure 1.10). The significant elongation of the first layer can be explained by the electronic repulsion between atoms on the surface<sup>51</sup>.

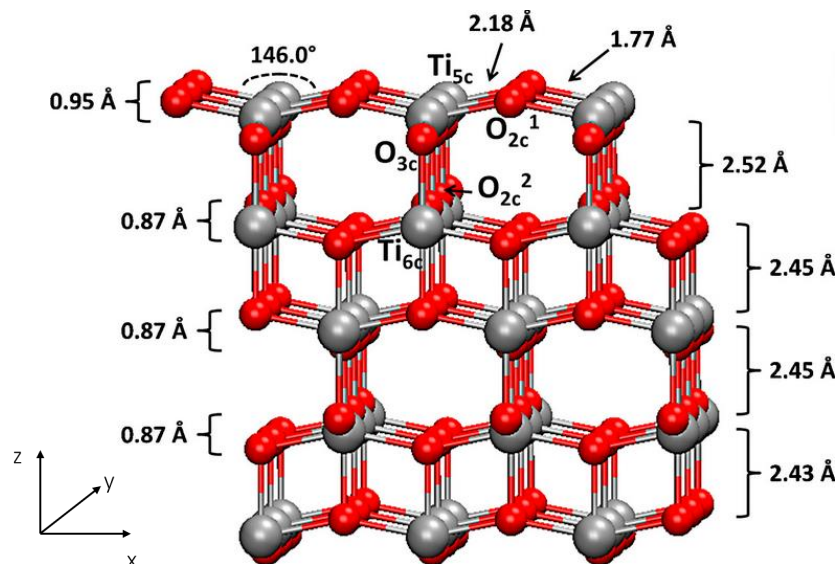


Figure 1.10: Bond lengths of the optimized (001) anatase surface<sup>49</sup>.

Another surface rearrangement is the displacement of the O<sub>2c</sub> atoms closer to one of the neighboring Ti<sub>5c</sub> chains, breaking the symmetry of the structure. Ortega et al.<sup>49</sup> reported that the Ti<sub>5c</sub>-O<sub>2c</sub> bonds that were equivalent in the unrelaxed surface (with a bond length of 1.93 Å) become strongly inequivalent with bond lengths of 2.18 and 1.77 Å as illustrated in Figure 1.10. Vittadini et al.<sup>52</sup> explain this particular modification by the conflicting stabilization criteria of the (001) anatase surface. Usually, the metal oxide surfaces are stabilized by a shortening of the bonds between undercoordinated ions and a particular motion of the ions: the cations are moving inward from the surface whereas the anions move outward from the bulk plane. This symmetry breaking decreases the O<sub>2c</sub>-Ti<sub>5c</sub>-O<sub>2c</sub> angle from 157 to 146°, causing a tensile stress of the surface mentioned in several theoretical studies<sup>53,54</sup>.

Vittadini et al.<sup>52</sup> also showed, using simulations, that the 2 monolayer thick slab, when cut along the (001) surface, spontaneously transforms into a very stable lepidocrocite structure with fully sixfold coordinated Ti atoms. When a third layer is added to this slab, the O<sub>2c</sub>-Ti<sub>5c</sub>-O<sub>2c</sub> chains present at the bottom and at the surface of the structure are running perpendicularly to each other. As a consequence, the inequivalent Ti<sub>5c</sub>-O<sub>2c</sub> bond lengths observed in the relaxed (001) surface can also be interpreted as a frustrated attempt to a lepidocrocite structure.

When the lateral size of the slab is constrained to the bulk lattice constants, it is possible to calculate the surface energy ( $E_S$ )<sup>49,52</sup> by using the formula detailed in Equation 1.1:

$$E_S = \frac{1}{2A} \left[ E_{\text{Slab}} - E_{\text{Bulk}} \left( \frac{n_{\text{Slab}}}{n_{\text{Bulk}}} \right) \right] \quad (1.1)$$

In this equation,  $A$  stands for the surface area,  $n$  represents the number of atoms,  $E_{\text{Slab}}$  and  $E_{\text{Bulk}}$  are the energy of the slab and the bulk, respectively.

Araujo et al.<sup>51</sup> reviewed the (001) surface energies using different theoretical levels, including density functional theory (DFT) functionals. They reported a value of 84 meV when the B3LYP hybrid functional was used to perform the calculations<sup>55</sup>.

When the lateral size of the slab is not constrained, the formation energy of the slab can be calculated using the formula displayed in Equation 1.2 below. This energy was referred to as  $E_{\text{film}}$  by Vittadini et al.<sup>52</sup>

$$E_{\text{film}} = \frac{E_{\text{tot}}(\text{slab})}{n} - E_{\text{tot}}(\text{TiO}_2) \quad (1.2)$$

$E_{\text{tot}}(\text{slab})$  stands for the total energy of the optimized slab,  $n$  is the number of  $\text{TiO}_2$  units used to build the slab and  $E_{\text{tot}}(\text{TiO}_2)$  is the total energy of optimized bulk anatase. By using the PBE functional, Vittadini et al.<sup>52</sup> reported a film energy of 0.44 eV/ $\text{TiO}_2$  for the optimized 3 monolayer thick (001) anatase slab.

The electronic structure of the (001) anatase surface is very similar to the bulk one with a valence band mainly composed of O ( $2p$ ) character and a conduction band essentially made with Ti ( $3d$ ) states. Only the three outmost layers undergoes slight modifications. Zhao et al.<sup>54</sup> mentioned the presence of surface states induced by the undercoordinated Ti atoms. However, it is located at the bottom of the conduction band and does not form an isolated state in the band gap.

Calatayud et al.<sup>56</sup> studied the different contribution of the O<sub>2c</sub> and O<sub>3c</sub> surface oxygen atoms to the valence band. They showed that the O<sub>2c</sub> atom dominates the upper part of the valence band whereas the O<sub>3c</sub> atom is located at a lower energy as displayed in Figure 1.11. The particular location of the undercoordinated oxygen atoms confirms its higher reactivity.

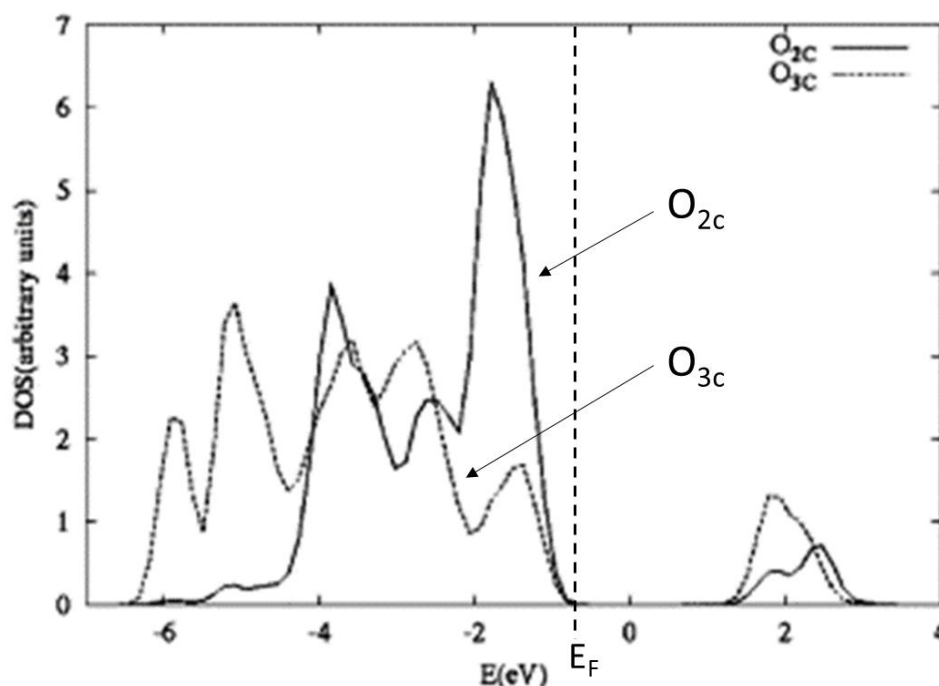


Figure 1.11: DOS of the (001) anatase (001) surface, showing the O<sub>2c</sub> and O<sub>3c</sub> contributions<sup>56</sup>.

### 1.2.5 Modelling of TiO<sub>2</sub> nanotubes

The first synthesis of carbon nanotubes by Iijima<sup>57</sup> in 1991 raised the question about the possible existence of nanotubular forms of other compounds. One year later Tenne et al.<sup>58</sup> reported the synthesis of the first inorganic nanotubes made of WS<sub>2</sub>. This was followed by the synthesis of wide range of inorganic nanotubes<sup>59</sup> including the *nt*-TiO<sub>2</sub>. Due to their chemical inertness, endurance, strong oxidizing power, large surface area, high photocatalytic activity, non-toxicity and lower production cost, they have aroused the interest of the scientists. Their first fabrication was achieved by Hoyer<sup>60</sup> in 1996 using electrodeposition into a polymer mold obtained from a porous aluminum oxide. Two years later, Kasuga et al.<sup>61</sup> reported the first hydrothermal synthesis of *nt*-TiO<sub>2</sub>.

The *nt*-TiO<sub>2</sub> were then fabricated using various routes<sup>62</sup> like sol-gel methods, hydro/solvothermal approaches, electro-chemical means or template-assisted methods. Such a broad range of synthesis methods lead to a large variety of *nt*-TiO<sub>2</sub> morphologies<sup>63</sup>: they can be single-walled or multi-walled nanotubes, having diameters varying from a few nanometers to a hundred nanometers, and exhibit different crystallographic structures.

The single walled carbon nanotubes were the first ones to be modeled. They were built by rolling a graphene sheet<sup>64</sup> as detailed in Figure 1.12.

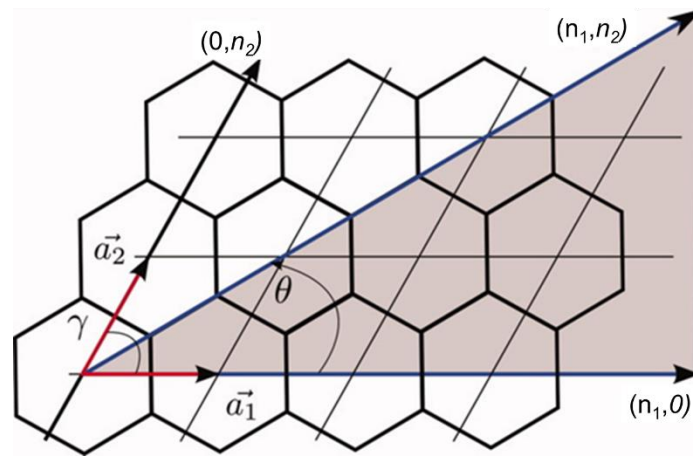


Figure 1.12: zig-zag  $(0, n_2)$  and  $(n_1, 0)$  and armchair  $(n_1, n_2)$  rolling up vectors of a graphene lattice<sup>6</sup>.

The rolling up vector  $\vec{R}$  must be a translation vector of the 2D lattice and will define the nanotube circumference. It is defined as  $\vec{R} = n_1 \vec{a}_1 + n_2 \vec{a}_2$  where  $\vec{a}_1$  and  $\vec{a}_2$  are the slab cell vectors;  $n_1$  and  $n_2$  must be integers. The choice of the  $(n_1, n_2)$  indices allows to define three groups of nanotubes<sup>63</sup>:

- When  $n_1 = n_2$ , the nanotube is known as “armchair”. Historically, the hexagonal lattice of the graphene was forming an armchair pattern along the circumference of the carbon nanotube.
- When  $n_1 = 0$  or  $n_2 = 0$ , the nanotube belong to the so-called “zig-zag” family. The hexagonal lattice of the graphene was forming a zig-zag pattern along the circumference.
- When  $n_1 \neq n_2$ , the nanotube belongs to the “chiral” family.

Zig-zag and armchair nanotubes are both achiral tubes, as a contrary of the chiral ones (Figure 1.13).

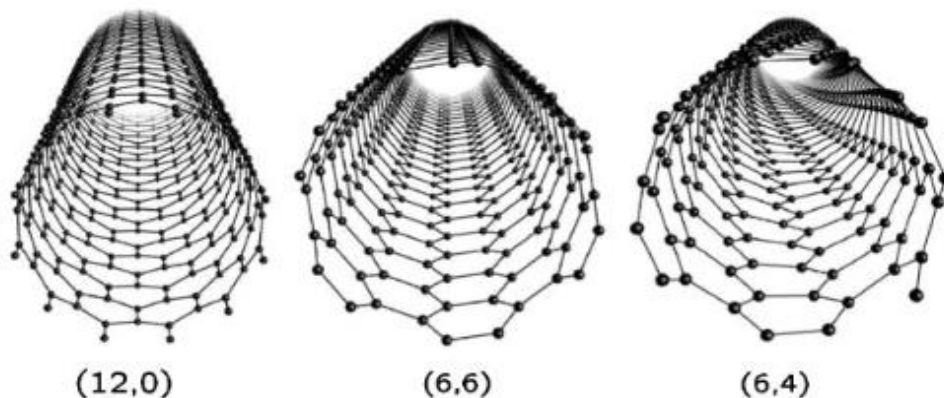


Figure 1.13: (12,0) zig-zag, (6,6) armchair and (6,4) chiral single walled carbon nanotubes<sup>65</sup>.

Nanotubes are characterized by a helical symmetry that reduces drastically the computational time. Thus, *ab initio* calculations can be performed on nanotubes containing several hundreds of atoms<sup>6</sup>. The same rolling up method was used to generate inorganic nanotubes from other 2D slabs. *Ab initio* calculation of the first inorganic nanotubes<sup>66</sup> was carried out on boron nitride (BN) nanotubes by rolling up a BN graphitic sheet.

The first theoretical study of titania nanotubes (*nt*-TiO<sub>2</sub>) was reported by Ivanovskaya et al.<sup>67</sup> in 2003 using tight binding Extended Hückel calculation without performing geometry optimization. Further studies were then performed on single walled *nt*-TiO<sub>2</sub> exhibiting other crystalline structures such as anatase, dititanate<sup>68</sup>, trititanate<sup>47,69</sup>, lepidocrocite<sup>70,71</sup>, rutile<sup>72,73</sup> or hexagonal ABC<sup>74</sup>.

The slabs used to generate anatase *nt*-TiO<sub>2</sub> can be cut from three anatase surfaces: (101), (001) and (100). These surfaces and the rolling-up vectors are shown in Figure 1.14<sup>48</sup> where the titania atoms are indicated in purple and the oxygen ones in green.

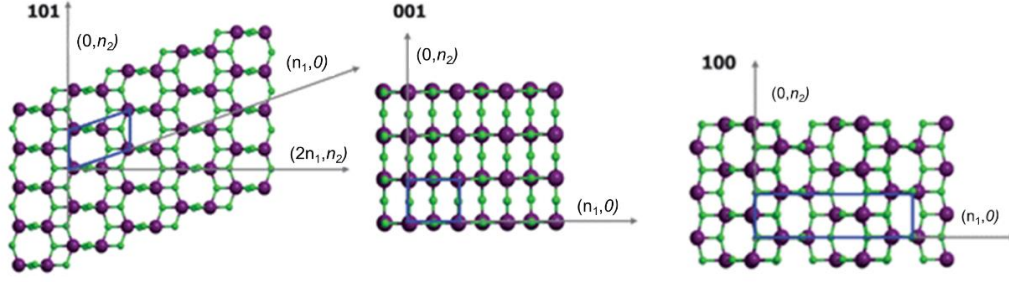


Figure 1.14: Anatase surfaces and the corresponding rolling-up vectors<sup>48</sup>. The Ti atoms are in purple and the O ones in green. Republished with permission of Royal Society of Chemistry, from reference<sup>48</sup> obtained in 2021; permission conveyed through Copyright Clearance Center, Inc.

The nanotubes stability can be evaluated by calculating the so-called strain energy described in Equation 1.3:

$$E_{\text{strain}} = \frac{E_{\text{Slab}}}{n_{\text{Slab}}} - \frac{E_{\text{Nanotube}}}{n_{\text{Nanotube}}} \quad (1.3)$$

where  $E_{\text{Slab}}$  and  $E_{\text{Nanotube}}$  stands for the total energy of the optimized slab and nanotube, respectively, while  $n_{\text{Slab}}$  and  $n_{\text{Nanotube}}$  indicates the number of  $\text{TiO}_2$  unit used to build the primitive cell of the structure.

The strain energy reflects the ability of the system to cope with the strain coming from the surface tensions present at each side of the rolled slab. Thus, a negative strain energy points out the higher stability of the nanotube compared to the corresponding flat structure.

The thickness of the slabs resulting in stable nanotubes is included between one and three monolayers (a monolayer consists of one  $\text{TiO}_2$  unit). Several theoretical<sup>48,75,76</sup> studies have demonstrated that the single walled *nt*- $\text{TiO}_2$  built with four monolayers are not stable. At this critical thickness, the favored structure is a double-walled *nt*- $\text{TiO}_2$  made of a pair of two monolayers.

The first slabs used to build the anatase *nt*- $\text{TiO}_2$  were cut along the (101) direction, probably because both experimental<sup>45</sup> and theoretical<sup>46</sup> studies have shown that the (101) anatase surface is particularly stable. However, the specific symmetry of the (101) surface makes it not possible to generate three monolayers thick slabs<sup>75</sup>.

The first *nt*-TiO<sub>2</sub> considered were one monolayer thick and all exhibited positive strain energies<sup>67,70,72</sup>. Nevertheless, further studies<sup>75,77</sup> proved that the optimization of these *nt*-TiO<sub>2</sub> leads to a spontaneous reorganize into the (111) fluorite TiO<sub>2</sub> structure, as displayed in Figure 1.15 where O<sub>be</sub> stands for the bridging oxygen atoms located on the external surface while the bridging oxygens located on the internal surface are referred as O<sub>bi</sub>.

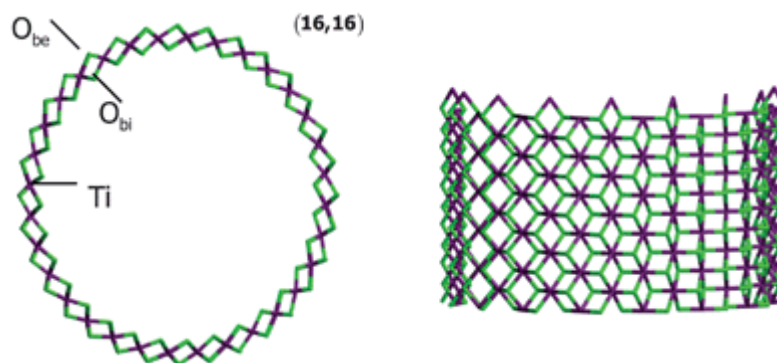


Figure 1.15: Fluorite armchair TiO<sub>2</sub> nanotube where O<sub>be</sub> and O<sub>bi</sub> refer to the bridging oxygens located on the external and the internal surfaces, respectively<sup>48</sup>. Republished with permission of Royal Society of Chemistry, from reference<sup>48</sup> obtained in 2021; permission conveyed through Copyright Clearance Center, Inc.

*Nt*-TiO<sub>2</sub> built by rolling up two monolayers of anatase (101) were then studied by many groups<sup>47,78–83</sup>, especially for their application in photovoltaic<sup>82</sup> or hydrogen adsorption<sup>83</sup>. Although the stability of these *nt*-TiO<sub>2</sub> is enhanced when the diameter increases<sup>81</sup>, the strain energy introduced makes the *nt*-TiO<sub>2</sub> energies higher than the corresponding sheet structures over the entire diameter range<sup>47</sup>.

Only few studies about the *nt*-TiO<sub>2</sub> made from slabs cut along the (100) direction were carried out, probably because of the low geometry exhibited by this structure. The minimum thickness of a slab is two monolayers. Hart et al.<sup>47</sup> found that the nanotubes made from the two monolayer thick (100) slabs of anatase exhibits higher energy than the corresponding *nt*-TiO<sub>2</sub> made from (101) slabs. This result points out the low stability of the (100) anatase *nt*-TiO<sub>2</sub>. Moreover, Ferrari et al.<sup>48</sup> showed that the two monolayer thick (100) slab spontaneously rearranged into a (101) slab when geometry optimization is performed.

$Nt$ -TiO<sub>2</sub> can also be generated from a three monolayer thick (100) slab<sup>48</sup>. This kind of  $nt$ -TiO<sub>2</sub> exhibit a very peculiar structure made of three layers thick blocks connected by one layer thick junctions as illustrated in Figure 1.16, where the titania and oxygen atoms are displayed in purple and green, respectively. Although this structure confers a certain degree of flexibility to the  $nt$ -TiO<sub>2</sub>, they showed a positive strain energy over the whole diameter range.

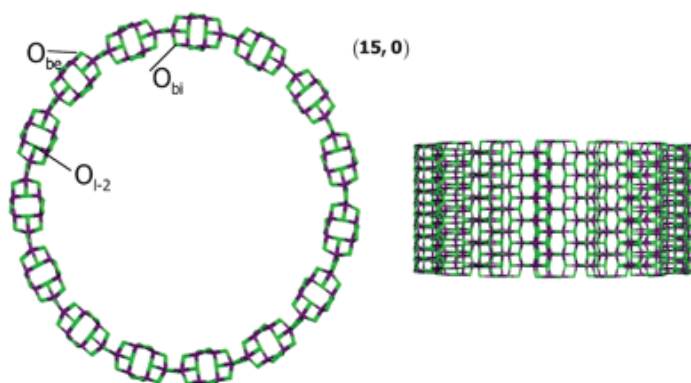


Figure 1.16: (15, 0)  $nt$ -TiO<sub>2</sub> generated from a three monolayer thick (100) slab<sup>48</sup>. The O atoms are in green and the Ti ones in purple. Republished with permission of Royal Society of Chemistry, from reference<sup>48</sup> obtained in 2021; permission conveyed through Copyright Clearance Center, Inc.

The last anatase slabs allowing to generate  $nt$ -TiO<sub>2</sub> are cut along the (001) direction. Evarestov et al.<sup>84</sup> carried out theoretical calculations on one monolayer thick  $nt$ -TiO<sub>2</sub>. They observed that the nanotubes with chirality  $(n,0)$  exhibit a negative strain energy after geometry optimization. This means that this kind of  $nt$ -TiO<sub>2</sub> are more stable than the corresponding slab. However, the reason for this stabilization is not fully understood. The authors also found that the stability of the nanotubes decreases when the diameter increases. This model of  $nt$ -TiO<sub>2</sub> was later used by Pan et al.<sup>85</sup> to build arrays of nanotubes to study the adsorption of gas molecules.

However, further studies by Ferrari et al.<sup>86</sup> suggest that both the two monolayer thick anatase (001) slab<sup>52,87</sup> and the one monolayer thick anatase (001)  $nt$ -TiO<sub>2</sub><sup>77,84</sup> will spontaneously rearrange into a two monolayer thick lepidocrocite structure. From Figure 1.17 it is seen that the lepidocrocite structure demonstrates a layered structure with fully coordinated Ti (purple) and O (green) atoms.

The two reasons mentioned<sup>88</sup> to explain the reconstructions are the change of coordination of the Ti cations from fivefold-coordinated to fully sixfold-coordinated; and the reduction of the bond angle between the oxygen atoms. The corresponding lepidocrocite *nt*-TiO<sub>2</sub> exhibit a positive strain energy over the entire diameter range<sup>77</sup>, which is what was predicted by Ferrari et al<sup>48</sup>.

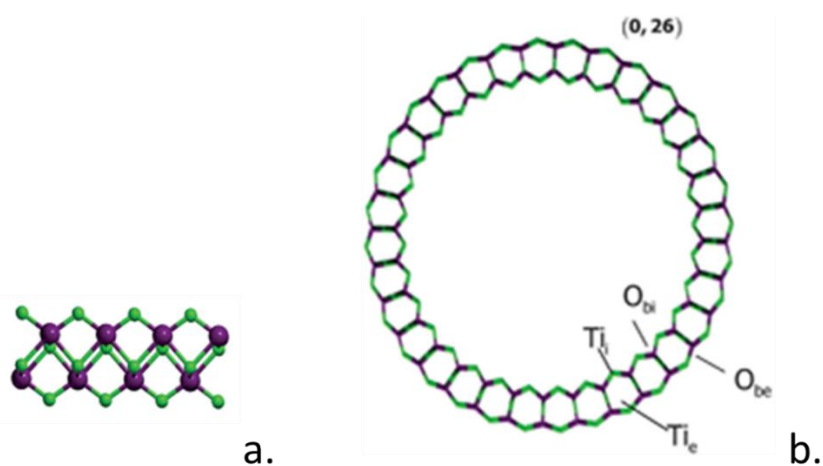


Figure 1.17: Two monolayer thick lepidocrocite slab (a) and *nt*-TiO<sub>2</sub> (b)<sup>48</sup>. The Ti atoms are in purple and the O ones in green. Republished with permission of Royal Society of Chemistry, from reference<sup>48</sup> obtained in 2021; permission conveyed through Copyright Clearance Center, Inc.

The  $(n_1, 0)$  *nt*-TiO<sub>2</sub> generated from a three monolayer thick (001) slab exhibit a negative strain energy for all the diameters above 8 Å<sup>86</sup>, meaning that the nanotubular structure is more stable than the corresponding thin film. Other studies<sup>48,77</sup> showed that the  $(0, n_2)$  nanotubes built from the same slab are less stable than the corresponding  $(n_1, 0)$  ones. All the  $(0, n_2)$  *nt*-TiO<sub>2</sub> exhibit a positive strain energy. The  $(0, 60)$  and the  $(60, 0)$  nanotubes having a diameter of 37.1 Å are shown in Figure 1.18<sup>86</sup> where the titania atoms are in blue and the oxygen ones in red. It can be noticed that the stress induced by the rolling up is more consequent for the  $(0, n_2)$  nanotubes where the bonds located on the external wall undergo an important extension while the bonds located on the internal wall are significantly compressed. As a result, the  $(0, n_2)$  nanotubes are less stable than the  $(n_1, 0)$  nanotubes and exhibit positive strain energies over the whole diameter range<sup>86</sup>.

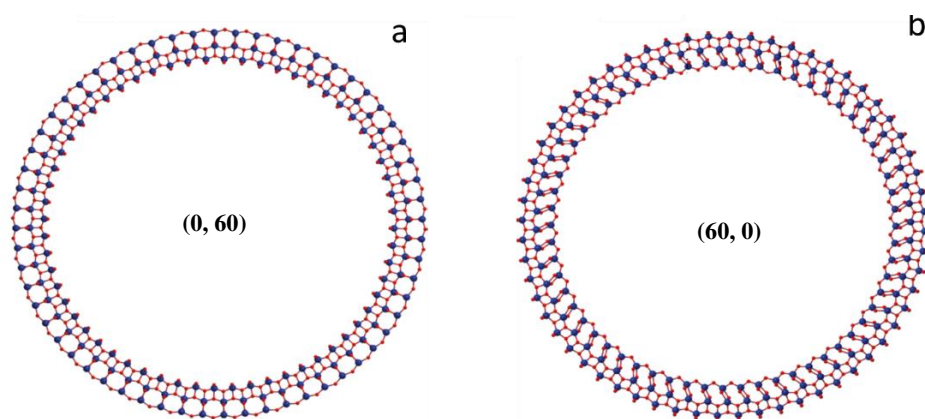


Figure 1.18: 3ML *nt*-TiO<sub>2</sub> rolled up along the (0,  $n_2$ ) direction (a) or the ( $n_1$ , 0) direction (b)<sup>86</sup>. The O atoms are in red and the Ti ones in blue. Reprinted (adapted) with permission from reference<sup>86</sup>.

Copyright 2010 American Chemical Society.

The negative strain energy exhibited by the ( $n_1$ , 0) *nt*-TiO<sub>2</sub> can be explained by the particular structure of the corresponding slab: it contains two rows of bi-coordinated oxygen atoms, located at the top and at the bottom of the sheet, which are perpendicularly oriented to each other. This particular orientation creates a directional asymmetry on both sides of the slab, as illustrated in Figure 1.19a<sup>86</sup> where the bi-coordinated oxygen atoms are identified as O<sub>2c</sub>. In this figure, the titania and oxygen atoms are in blue and red, respectively.

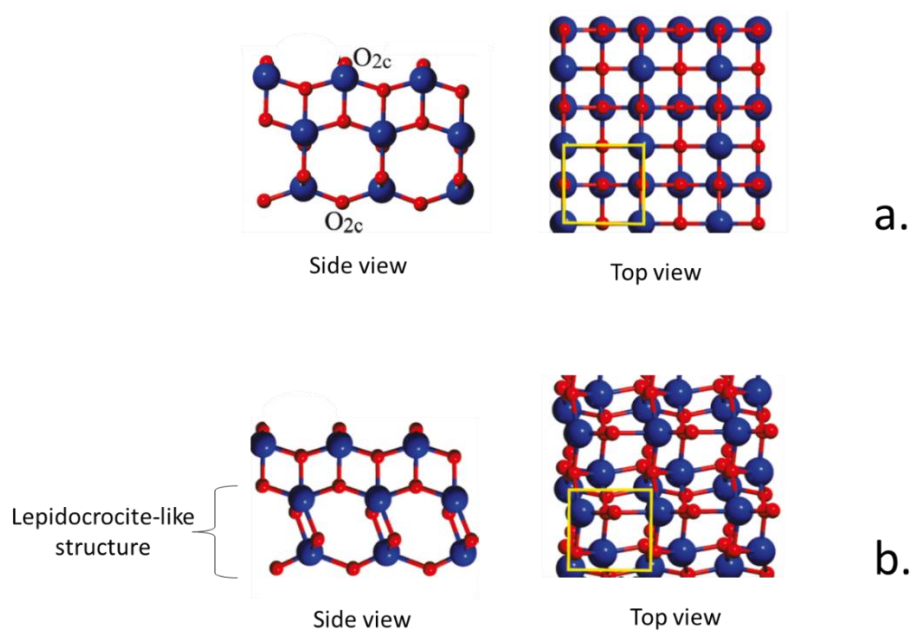


Figure 1.19: Non optimized (a) and optimized into a nanotubular structure (b) 3 ML thick anatase slab cut along the (001) direction<sup>86</sup>. The Ti and O atoms are in blue and red, respectively. Reprinted (adapted) with permission from reference<sup>86</sup>. Copyright 2010 American Chemical Society.

When the *nt*-TiO<sub>2</sub> geometry is optimized, the internal and external walls are running perpendicularly to each other, the internal wall being subjected to a larger stress than the external one<sup>50</sup>. The final structure of the *nt*-TiO<sub>2</sub> is made of two perpendicular layers, the bottom one being a lepidocrocite-like structure, as displayed in Figure 1.19b. The asymmetry of the two sides of a slab was already identified as a possible driving force for the formation of nanotubular structure. This phenomena was encountered in several nanotubular crystals such as imogolite<sup>89</sup> that also exhibits a negative strain energy. Although they showed a positive strain energy, the titanate (hydrated TiO<sub>2</sub>) *nt*-TiO<sub>2</sub> were claimed to roll up as a consequence of the asymmetry caused by hydrogen deficiency at the top of H<sub>2</sub>Ti<sub>3</sub>O<sub>7</sub> thin plates<sup>90</sup>.

The strain energy of the (*n*<sub>1</sub>, 0) *nt*-TiO<sub>2</sub> having different diameters were calculated<sup>91</sup> and are displayed in Figure 1.20.

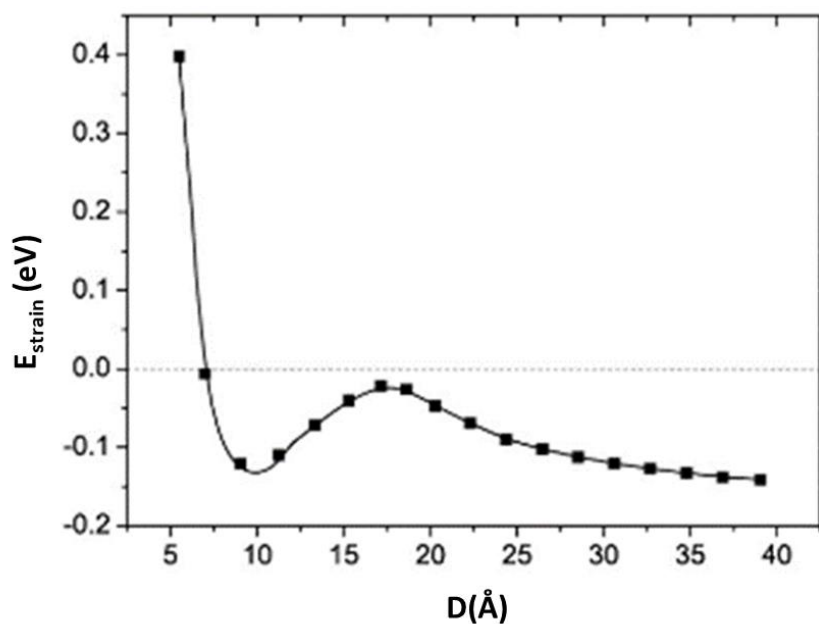


Figure 1.20: Calculated strain energies for (*n*<sub>1</sub>, 0) *nt*-TiO<sub>2</sub> built from anatase (001) slab<sup>91</sup>, where D is the diameter of the nanotube.

Ferrari et al.<sup>86</sup> showed that the strain energy is increasing again for diameters above 60 Å, indicating a preferred nanotube size in the 40–60 Å diameter range. This result is in agreement with the internal diameter of 4–5 nm exhibited by the multi-layered (001) anatase nanotubes obtained by hydrothermal synthesis<sup>92</sup>. Moreover, XANES analysis have confirmed the presence of 40% of five-coordinated titanium atoms in nanotubular structures<sup>92,93</sup>.

The band gap width of the (001) anatase *nt*-TiO<sub>2</sub> depends on the chosen computational method. Generally, these anatase nanotubes are semi-conductor exhibiting band gaps slightly higher than the bulk<sup>84</sup>. This can be explained by the increase of the strain energy that induces structural changes in the nanotube walls.

The (*n*<sub>1</sub>, 0) *nt*-TiO<sub>2</sub> exhibiting negative strain energy were the model chosen by the group of Lisovski et al.<sup>94</sup> to study the effect of different substitution doping for water splitting hydrogen generation. The *nt*-TiO<sub>2</sub> selected was the (36, 0) nanotube as it is the smallest nanotube exhibiting similar properties to those of *nt*-TiO<sub>2</sub> with larger diameters.

The (36,0) nanotubes exhibit an internal diameter of 38 Å and agree with the size of the multi-layered nanotubes synthesized by hydrothermal methods<sup>92</sup>. As a result, the (36,0) nanotubes appear as a good compromise for the modelling of big systems with acceptable calculations requirements. The first study carried out by this group concerned the sulphur doped *nt*-TiO<sub>2</sub><sup>91</sup>. They subsequently extend their research to the effect of oxygen substitution by carbon or nitrogen and the effect of titanium substitution by iron. They found that the most favourable atom positions for oxygen substitution are located in the outer wall of the *nt*-TiO<sub>2</sub><sup>95</sup>, and identified the co-doped nanotubes with nitrogen and sulphur as the most favourable ones for water splitting<sup>96</sup>.

## 1.2.6 Modelling of Li intercalation into TiO<sub>2</sub> bulk anatase

### 1.2.6.1 The intercalation sites

Li intercalation into anatase does not require large lattice distortions. Both empty sites, octahedral and tetrahedral, are in principle candidates to host a Li ion. Experimental studies found Li ions residing in the octahedral sites<sup>97,98,99</sup>. Theoretical studies confirmed this tendency: Li intercalation into the tetrahedral sites lead to serious problems of convergence<sup>40</sup> or to a spontaneous drift of the Li to the octahedral site<sup>100</sup>.

The most favourable lithium intercalation sites present can also be determined by comparing the lithium intercalation energies. The more negative is the energy, the more favourable is the lithium intercalation site. This intercalation energy can be calculated following the Equation 1.4<sup>101</sup>:

$$E_{\text{Li Intercalation}} = \frac{E_{\text{Li}_x\text{TiO}_2} - (E_{\text{TiO}_2} + x E_{\text{Li}})}{x} \quad (1.4)$$

where  $E_{\text{Li Intercalation}}$  defines the intercalation energy per lithium ion into the TiO<sub>2</sub> structure,  $E_{\text{Li}_x\text{TiO}_2}$  is the total energy of the lithiated structure,  $E_{\text{TiO}_2}$  stands for total energy of the optimized system without lithium,  $x$  is the number of lithium per TiO<sub>2</sub> unit and  $E_{\text{Li}}$  defines the total energy of the optimized bulk structure of metallic lithium.

Thus, Koudriachova et al.<sup>102</sup> reported a preference for intercalation into the octahedral site by 0.45 eV compared to the tetrahedral one. Belak et al.<sup>103</sup> explained that the adjacent tetrahedral sites between neighboring Li octahedra share faces with two Ti containing octahedra. The strong electrostatic repulsion from these face-sharing Ti renders the tetrahedral sites unstable. Consequently, Li ions will sit exclusively in noticeably distorted octahedral sites (due to the presence of Ti<sup>4+</sup>) with edge lengths (O–O interatomic distance) varying between 3.08 Å and 3.77 Å<sup>103</sup>.

Various concentration of Li has been intercalated to follow the structural and energetical effects into anatase. The amount of Li-ions is represented as  $\text{Li}_x\text{TiO}_2$ , where  $x$  varies between  $x = 0$  to 1. The Li ions intercalated at the center of the octahedral sites will be fourfold coordinated, as it shown in Figure 1.21 where the Li ion is in purple while the Ti and O atoms are indicated in grey and red, respectively. This kind of intercalation was reported only for very low Li concentration ( $x < 1/16$ )<sup>102,104</sup>.

For  $x < 1/4$ , Tielens et al.<sup>40</sup> reported a small shift of about 0.1 Å above the symmetry plane of the oxygen octahedron but the Li ions remain four-fold coordinated.

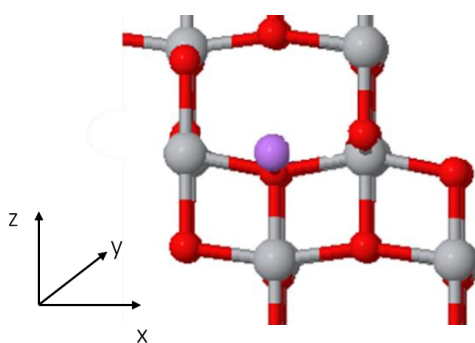


Figure 1.21: Lithium ion inserted into an octahedral intercalation site of bulk anatase. The Ti atoms are indicated in grey, the O ones in red and the Li one in purple.

For higher concentrations, both experimental<sup>39,105</sup> and theoretical studies<sup>106,107,108,109,110</sup> showed that the Li ions will be shifted up or down the  $c$  axis, leading to fivefold-coordinated cations. If the geometry of the cell is constrained, the anatase structure is maintained and the displacement distances up and down from the center, as well as the repartition of the Li ions between the two positions are equivalent. This can be explained by the fact that all the octahedral sites are equidistant from each other<sup>105</sup>. If the cell parameters are allowed to relax during geometry optimization, the lithiated anatase will be transform into  $\text{Li}_{0.5}\text{TiO}_2$  titanate whose structure will be detailed below. In titanate, the shift from the center and the repartition of the Li ions between the two positions are different. This is a result of the orthorhombic distortion of anatase. The lithium located more toward the center of the octahedron will suffer less Li–Li coulomb repulsion<sup>105</sup>. Moreover in this position, Li–O distances range from 1.97 to 2.05 Å and are close to the Li–O distance of 1.996 Å observed in  $\text{Li}_2\text{O}_2$ <sup>26</sup>.

Experimentally, the maximum Li insertion ratio for bulk anatase commonly reported is  $x = 0.5$ <sup>99</sup>. The  $\text{Li}_{0.5}\text{TiO}_2$  unit cell consists of two Li ions that can be distributed over the four available octahedral positions. The most stable Li distributions reported by Koudriachova et al.<sup>26</sup> consist of half-filled  $c$ -channels and are detailed in Figure 1.22. In this figure, the Ti atoms are in grey, the O atoms in red and the Li ions in purple. Li can be placed either at (0.5, 0.0, 0.25) position and give form to a  $Pmma$  symmetry unit cell (structure I), or at (0.5, 0.5, 0.0) position forming an  $Imm2$  symmetry unit cell (structure II).

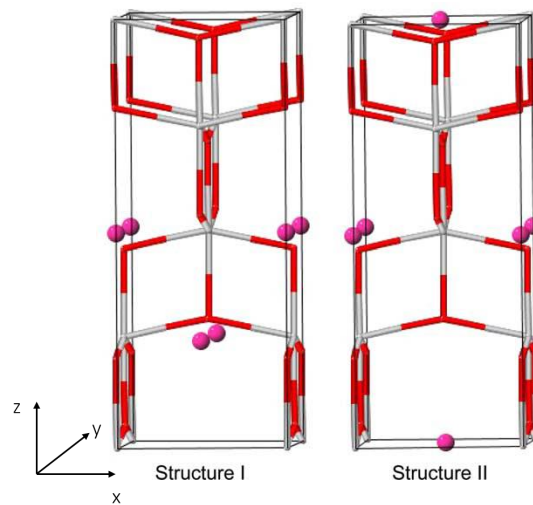


Figure 1.22: The conventional unit cells of the two most stable Li distribution structures for  $x = 0.5$ <sup>40</sup> referred to as structure I ( $Pmma$ ) or structure II ( $Imm2$ ). The Li ions are in purple, while the Ti and O atoms are in grey and red, respectively.

Koudriachova et al. reported an energy difference between these two structures which equals 0.001 eV per formula unit at room temperature. Consequently, a mixture of these two distributions is expected. Averaging structural parameters over the A and B structures results in a system with orthorhombic  $Imma$  symmetry in agreement with the crystallographic data obtained by neutron diffraction analysis<sup>98</sup>. A Density functional theory (DFT) study carried out later by Tielens et al.<sup>40</sup> using a plane wave pseudopotential approach confirmed the very small difference of 30meV in total energy between the two configurations.

### 1.2.6.2 The phase separation between anatase and $\text{Li}_{0.5}\text{TiO}_2$ titanate

Though no significant expansion is required to accommodate Li-ions into anatase, experimental and theoretical studies both show that serious structural changes are involved in the Li-intercalation process. The in situ X-ray diffraction carried out by Van de Krol et al.<sup>111</sup> showed that Li intercalation into anatase occurs as a single phase reaction up to  $x = 0.05$ . Further intercalation leads to a phase separation between a Li-poor phase that exhibit a tetragonal anatase structure having a Li fraction of  $x \approx 0.01$ <sup>99</sup> and a Li-rich phase made of  $\text{Li}_{0.5}\text{TiO}_2$  titanate. The separation occurs with sub-micron domain sizes and only the relative phase proportions vary upon Li intercalation until the whole structure can be considered as a single Li-rich phase at  $x = 0.5$ <sup>112</sup>. The ratio between the two phases does not change significantly as a function of temperature<sup>105</sup>. This two-phase thermodynamic equilibrium allows to maintain a constant electrical potential over a wide range of Li concentrations<sup>103,113</sup>. The intercalation potential of  $\text{TiO}_2$  equals 1.75 V versus  $\text{Li}^+/\text{Li}$  redox couple<sup>18</sup> and can be calculated using Equation 1.5<sup>114</sup>:

$$V(x) = \frac{-\Delta G}{xF} \quad (1.5)$$

where  $\Delta G$  is the free energy change in joule per mole,  $x$  stands for the number of intercalated lithium per  $\text{TiO}_2$  unit and  $F$  is the Faraday constant that equals 96485.33 C/mol. Nevertheless, the free energy change can be approximated by the lithium intercalation energy  $E_{\text{Li intercalation}}$  as the contribution of the entropy to the cell voltage is small enough to be ignored<sup>115</sup>. As a result, most of the lithium intercalation voltages are calculated using Equation 1.6:

$$V(x) = - \frac{E_{\text{Li intercalation}}}{xF} \quad (1.6)$$

Open circuit voltage calculated in different theoretical studies are close to this value depending on the kind of calculations performed<sup>104,110,116</sup>.

Nuclear Magnetic Resonance (NMR) measurements carried out by Wagemaker et al.<sup>99</sup> showed that the diffusion coefficient for Li ions inside each of the two phases ( $4.7 \times 10^{-12}$  cm<sup>2</sup>/s for anatase and  $1.3 \times 10^{-11}$  cm<sup>2</sup>/s for lithium titanate Li<sub>0.5</sub>TiO<sub>2</sub>) is several order of magnitude higher than the overall diffusion coefficient previously determined using electrochemical techniques ( $\approx 10^{-15}$  cm<sup>2</sup>/s)<sup>30,111</sup>. As a result, the diffusion rate must be limited by the diffusion of Li ions between phases (or by the movement of the phase boundary) and not by the diffusion within the phases.

### 1.2.6.3 The Li<sub>0.5</sub>TiO<sub>2</sub> titanate structure

The Li-rich phase is known as lithium titanate with composition Li<sub>0.5</sub>TiO<sub>2</sub>. This phase results from an orthorhombic distortion of the anatase structure made by an anisotropic expansion in the *ab* plane (by 1% in the *a*-direction and about 8% in the *b*-direction) accompanied by a contraction along the *c*-direction by 5%<sup>26</sup> compared to the anatase structure. Expansion in the *b*-direction is limited by the Ti-O and Li-O bonds that would be stretched above common values. The volume of the unit cell increases by about 4%<sup>99</sup>.

The dimensional changes reduce the tetragonal symmetry of the anatase to the *Imma* orthorhombic space group (No. 74, lattice constants: *a* = 3.819 Å, *b* = 4.084 Å, *c* = 9.066 Å)<sup>39</sup>. Lithium titanate exhibits more regularly shaped TiO<sub>6</sub> octahedra than anatase<sup>99</sup>. The contraction along the *c*-direction is explained by a change in the octahedral packing (the expansion in the *ab* plane allow the layer above to penetrate more deeply) rather than a modification of the octahedra height. The difference in octahedral packing between the bulk anatase and the Li<sub>0.5</sub>TiO<sub>2</sub> titanate is shown in Figure 1.23 where the titania atoms are in blue, the oxygen ones in red and the lithium ions in purple.

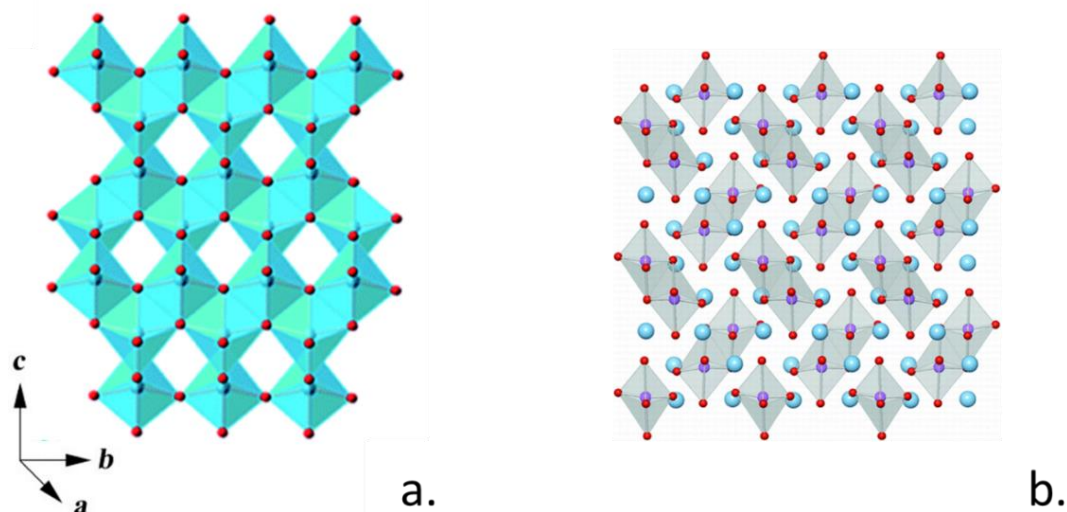


Figure 1.23: Octahedral packing of bulk anatase<sup>117</sup> (a) and Li<sub>0.5</sub>TiO<sub>2</sub> titanate (b)<sup>118</sup>. The Ti atoms are in blue, the O ones in red and the Li ions in purple. Republished with permission of Royal Society of Chemistry, from reference<sup>117</sup> obtained in 2021; permission conveyed through Copyright Clearance Center, Inc.

The formation of zig-zag Ti-Ti bonds along the *b*-direction was the first mechanism proposed by Nuspl et al.<sup>41</sup> in 1997 to explain the orthorhombic distortion. Later Mulliken analysis carried out by Koudriachova et al.<sup>26</sup> showed no significant population of these Ti-Ti bonds, indicating that the formation of Ti-Ti close contact is induced by the structure deformation but is not the driving mechanism. The latter proposed the localization of the charge donated by Li ion as the governing mechanism for the orthorhombic distortion. Indeed, anatase Ti *3d* orbitals exhibit highly localized nature. Lithium having a very low ionization energy, each Li-ion donates 0.86 e to the lattice (equivalent to 1.7 e per anatase unit cell).

Though the  $d_{xy}$  orbital is the lowest in energy, this orbital is a shallow acceptor as the corresponding Ti-O bonds are not coplanar. Insertion of electrons into this orbital leads to additional repulsions resulting in a further and unfavourable elongation of the Ti-O bonds. Moreover, no  $\pi (d_{xy}^{\text{Ti}} - d_{xy}^{\text{Ti}})$  bonds can be formed as the nearest Ti neighbor for an interaction is 3.784 Å apart.

Consequently, for  $x > 0.0625$ , occupancy of anti-bonding orbitals begins, leading to a destabilization of the framework balanced by spontaneous Jahn–Teller-like orthorhombic distortion of the lattice leading to the formation of the  $\text{Li}_{0.5}\text{TiO}_2$  lithium titanate phase. The degeneracy of the orbitals is lifted and the additional charge will be located exclusively in the  $d_{yz}$  orbitals, the  $d_{xy}$  states being empty, as shown in Figure 1.24. The  $d_{yz}$  orbitals split slightly from the conduction band and form gap states. The  $d_{yz}$  orbitals were reported to be located 1.74 eV above the valence band edge with a width of 1.5 eV<sup>26</sup>.

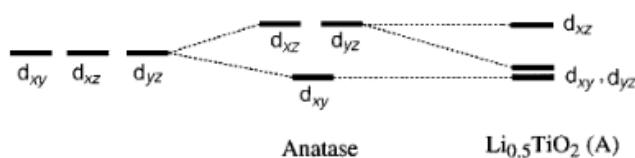


Figure 1.24: Illustration of the electronic structure modification upon lithium intercalation<sup>41</sup>.

The elongation of the Ti–O bond length observed along the  $b$ -direction (from 1.93 Å to 2.02 Å) is typical of the  $\text{Ti}^{3+}$ –O distances observed in  $\text{Ti}_2\text{O}_3$  (2.02 Å), whereas no significant bond length modification occurs in the  $a$ -direction. As a result, the Ti–O–Ti chains parallel to the  $b$ -direction are almost flat. Moreover, the  $\text{Li}^+$ –O and  $\text{Ti}^{3+}$ –O distances being very similar, the broadening in the  $b$ -direction creates ideal off-center positions for the Li ions. Nearly co-linear Li–O–Li contacts are also formed along  $b$ , leading to five-fold coordinated Li-ions.

The similarity of the  $\text{Li}^+$  and  $\text{Ti}^{3+}$  ionic radius also plays a role in the stability of the structure<sup>26</sup>. Morgan and Watson<sup>118</sup> showed later that the addition of electrons to the anatase structure does not lead to the formation of an orthorhombic cell. The presence of the intercalated lithium is needed to stabilize the orthorhombic titanate phase. The specific Li–O distances enhances the Coulomb stabilization of the Li. By trying different configurations, the authors showed that the intercalation energy per lithium is a minimum of  $x = 0.5$ .

Consequently, for  $0.01 < x < 0.5$ , structures are unstable with respect to a mixture of lithium titanate and Li-poor anatase. The low energy of specific lithium configurations for  $x = 0.5$  is the origin of the anatase–titanate phase separation identified by these authors. The formation of short Li-O valence bonds were later confirmed by Raman investigations<sup>119,120</sup>.

Belak et al.<sup>103</sup> claimed that the structure transformation has much in common with the martensitic phase transformations occurring in shape memory alloys. The restricted dimensional changes (occurring only in the *bc* plane) results in planes that are common to both TiO<sub>2</sub> anatase and Li<sub>0.5</sub>TiO<sub>2</sub> with zero misfit strain. Consequently, the strain invariant interface separating the two phases is parallel to any of the strain invariant planes.

#### 1.2.6.4 The electron transfer from lithium to the titanate

Lithium has a very low ionization energy. The energy level of its 2*s* electron is located well above the Ti 3*d* levels that make up the conduction band<sup>121</sup>. Consequently, the 2*s* electrons will enter the lowest unoccupied energy levels, which are located in the conduction band<sup>107</sup>.

X-ray Photoelectron Spectrometry (XPS) measurements<sup>122</sup> indicate the formation of Ti<sup>3+</sup> species upon Li<sup>+</sup> intercalation. XANES studies<sup>123</sup> shows a Ti oxidation state of +3.4 in Li-titanate. Theoretical studies shows a binding energy for the [Li<sub>i</sub><sup>•</sup>-Ti<sub>Ti</sub><sup>•</sup>] neutral pair which equals  $-0.5$  eV<sup>107</sup>, indicating that it is energetically favourable for a Li<sup>+</sup> interstitial to bind to a Ti<sup>3+</sup> ion. Thus, the intercalation potential of titania is determined by the change of oxidation state of the Ti ions and not by the O ions as it is assumed to be the case for transition metal oxides<sup>124</sup> such as LiCoO<sub>2</sub> or LiMn<sub>2</sub>O<sub>4</sub><sup>125</sup>. XAS studies<sup>112,126</sup> showed that Li intercalation results in the occupation of the Ti 3*d* orbitals rather than the other possibility Ti 4*s*. The electrons become trapped in localized states situated in the band gap and well separated from the bottom of the conduction band.

GGA + U<sup>104</sup> calculations predict a defect state located 0.96 eV below the conduction band edge in agreement with XPS studies. It is known that GGA cannot be used for this type of calculations due to the inherent self-interaction error. When GGA is used, the charge is delocalized over all atoms, leading to a metallic state in contradiction with experimental conductivity measurements and XPS<sup>118</sup>. GGA + U is also reported to be subjected to band gap error that can be corrected by using a sX functional<sup>110</sup>.

The formation of a defect state in the band gap can be explained by the Mott-Hubbard theory: the occupancy of some Ti *3d* state leads to strong intra-atomic d-d Coulomb repulsion, inducing a splitting between the occupied and the unoccupied Ti *3d* states<sup>100</sup>. Only one Ti *3d* state is occupied upon Li intercalation<sup>127</sup>. Morgan et al.<sup>104</sup> reported that the occupied *3d* states are strongly localized on single Ti atoms adjacent to the inserted lithium. They explain that this localization of the charge breaks the crystalline symmetry: the structure is distorted to accommodate the larger radius of Ti<sup>3+</sup> cations. The electrons that occupy this *3d* level and that are bound to the Ti cation are reported to be trapped as polarons<sup>100</sup>. Short range and weak interactions between the localized electron and the inserted lithium were also reported<sup>104,107,108</sup>. Small change in the valence bandwidth<sup>26</sup> and a decrease of the O2*p* –Ti *3d* interaction<sup>128</sup> were reported upon Li insertion.

#### **1.2.6.5 The Lithium Deintercalation**

During the extraction of Li ions from the electrode, the orthorhombic cell is maintained until  $x = 0.25$ <sup>129</sup>. Chronopotentiometric measurements carried out by Kavan et al.<sup>130</sup> showed that the intercalation process is three time slower than the deintercalation.

This can be explained by four different phenomena:

- a solvent effect (during the intercalation, an extra activation energy is required to remove the lithium from the solvent)<sup>130</sup>.
- a large difference in the mobility of Li ions between anatase and titanate<sup>40,111</sup>.
- the lattice relaxation accompanying the accommodation of lithium that is an activated process<sup>130</sup>
- the overall diffusion during insertion is limited by the motion of Li ions between the two phases (or by the movement of the phase boundaries)<sup>99</sup>.

The first insertion/extraction cycle will shorten the  $c$  axis by 2 %<sup>129,131</sup> whereas the  $a$  and  $b$  axis will not be modified. A two-fold decrease in the conductivity is also observed and can be attributed to chemical changes occurring at the electrode surface<sup>121</sup>.

#### 1.2.6.6 Lithium intercalation above $x=0.5$

Li intercalation above 0.5 Li ion per  $\text{TiO}_2$  unit has been reported in the literature using chemical synthesis. Intercalation with  $n$ -butyllithium leads to a ratio of  $x = 0.7$ <sup>132</sup>. Electrochemically, higher ratio can be obtained by cycling the battery at an elevated temperature of  $120^\circ\text{C}$ <sup>131</sup> but the electrodes age quickly<sup>133</sup>. Another possibility to increase the lithium ratio without damaging the electrode, and thus being able to cycle the battery for a long time period, is to use nanostructured anatase electrodes. Capacities up to  $x = 0.75$  were reported for 3-4 nm nanorods<sup>134</sup>. Nanoparticles smaller than 7 nm can be fully lithiated ( $x = 1$ )<sup>135,136</sup>.

This high ratio insertion occurs via a two-phase equilibrium between the  $\text{Li}_{0.5}\text{TiO}_2$  titanate and a rich  $\text{Li}_1\text{TiO}_2$  phase<sup>103,118</sup>. The  $\text{Li}_1\text{TiO}_2$  rich phase has a tetragonally distorted rock salt structure<sup>40,102</sup> similar to the anatase structure ( $I41/amd$ ) but with different lattice parameters ( $a = 4.043 \text{ \AA}$ ,  $c = 8.628 \text{ \AA}$ )<sup>99</sup>.

The shortening of the  $c$ -direction can be attributed to an increase of the Madelung field induced by a better alternation of opposite charged ions. Li–O bonds ( $2.026 \text{ \AA}$ ) and Ti–O bonds ( $2.120 \text{ \AA}$ ) have very similar bond lengths in the rock salt structure<sup>40</sup>.

Increasing the lithium ratio above  $x = 0.5$  leads to a progressive filling and a strengthening of the Ti–Ti  $3d_{yz}$  bonding bands, resulting in a very small decrease of the bond lengths (from 2.8914 Å to 2.8878 Å)<sup>41,123</sup>. The Ti valence changes from  $4^+$  to  $3^+$ <sup>103</sup> and the orbitals are fully hybridized<sup>137</sup>.

By carrying out UHF calculations on  $\text{LiTiO}_2$  (and considering only isotropic variation of the unit cell), Mackrodt et al.<sup>38</sup> showed that the electron transfer is confined almost exclusively to the oxygen sublattice closest to the lithium with less than 10% to the cation sites. Electron transfer leads to the creation of occupied titanium and oxygen states above the upper valence band edge with weights on both sublattices. These new states are strongly reminiscent of the gap states which have been identified in oxygen deficient  $\text{TiO}_2$ . The increase in conductivity for  $x$  values above 0.5 reported by Van de Krol et al.<sup>121</sup> can be attributed to the filling of higher band with good conduction properties.

The  $\text{TiO}_6$  octahedra exhibit regular geometry with uniform and noticeably smaller length<sup>103</sup> and the Li ions are now six fold coordinated<sup>137</sup>. The octahedral distortions that open up the path for Li diffusion in  $\text{Li}_{0.5}\text{TiO}_2$  titanate disappeared. The diffusion becomes isotropic with higher migration barriers (it becomes more difficult for the Li ions to pass between the two oxygen atoms forming the octahedra edges)<sup>103</sup>. Moreover, higher Li ratio induces stronger Li-Li repulsion. In  $\text{Li}_{0.5}\text{TiO}_2$  titanate, the average Li–Li distance is 2.54 Å<sup>98</sup> in the  $a$ -direction and 3.50 Å in the  $b$ -direction. Consequently, each Li is surrounded by two empty sites in the  $a$ -direction to minimize the Coulomb interaction. An increase of the Li concentration above  $x = 0.5$  will lead to more and more adjacent Li-Li neighbours at 2.54 Å introducing unfavourable repulsive interactions<sup>41</sup>.

Diffusion will be the main factor limiting the Li intercalation above 0.5 Li per TiO<sub>2</sub> unit. Theoretical studies<sup>102,103</sup> reported Li insertion energy barriers equal to 1 eV and 1.37 eV for  $x = 0.75$  and  $x = 1$  respectively (compared to 0.5 eV for  $x = 0.5$ ). This leads to a several orders of magnitude drop in the chemical diffusion coefficient. Belak et al.<sup>103</sup> reported a diffusion coefficient value of  $6 \times 10^{-26}$  cm<sup>2</sup>/s for the fully lithiated phase. The same authors also showed that the LiTiO<sub>2</sub> rich phase will firstly be formed at the surface of the electrode with an inward growth towards the bulk. XANES studies<sup>123</sup> confirmed that the Ti oxidation state is close to 3<sup>+</sup> for a 3-4 nm depth below the surface.

Further lithiation will require additional Li ions from the electrolyte to diffuse through the LiTiO<sub>2</sub> phase and reach the two-phase reaction front. Nevertheless, the very low diffusion coefficients exhibited by LiTiO<sub>2</sub> will prevent further Li supply once a thin layer of LiTiO<sub>2</sub> has covered the electrode surface. Thus, the capacity of anatase is limited to half of its theoretical value for non-nanostructured electrodes. Full lithiation was reported only for the smallest nanoparticles ( $< 7$  nm) where the distance are too small to be limited by diffusion<sup>135,136</sup>. Although intercalation with  $x > 0.5$  have been reported for non-nanostructured electrodes at elevated temperatures (diffusivity increases with the temperature), the electrodes age quickly because of the strong local distortions of the structure<sup>102</sup>.

### 1.2.7 Modelling of Li intercalation into anatase nanotube

Liang et al.<sup>138</sup> investigated lithium intercalation and diffusion into anatase *nt*-TiO<sub>2</sub> using the two monolayers thick anatase (101) nanotubes as model. They performed *ab initio* calculation on the (9, 0) nanotube to determine the most favourable lithium intercalation sites. The lithium ions were inserted in one repeated unit of the nanotube to avoid any Li-Li interactions. Consequently, the Li concentration was relatively low. Four intercalation sites were considered and are displayed in Figure 1.25<sup>138</sup> where the grey, red and purple spheres stand for the Ti, O and Li atoms.

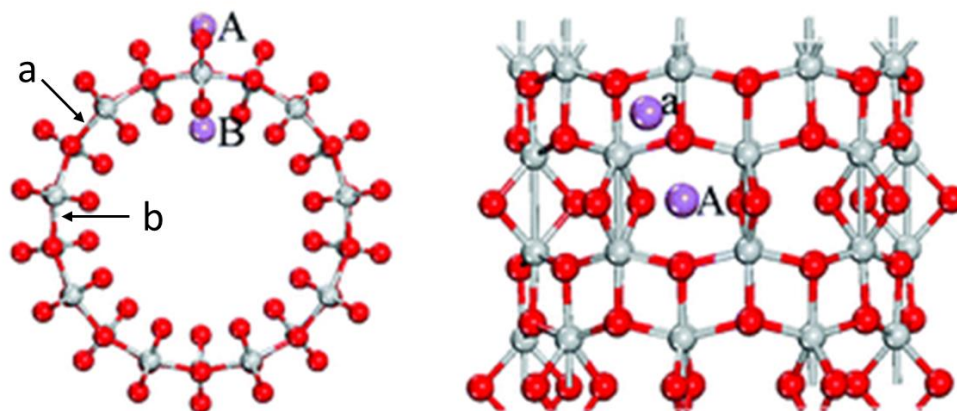


Figure 1.25: Top (right) and side (left) views of the four investigated Li intercalation sites in an (101) *nt*-TiO<sub>2</sub><sup>138</sup>. The grey, red and purple spheres represent the Ti, O and Li atoms. Republished with permission of Royal Society of Chemistry, from reference<sup>138</sup> obtained in 2021; permission conveyed through Copyright Clearance Center, Inc.

The “a” and “A” sites are located on the outermost wall while the “b” and “B” sites are located on the innermost wall. The ions intercalated in the “A” and “B” sites were surrounded by eight atoms unlike the Li inserted in the “a” and “b” positions that were encircled by only four atoms. It is interesting to note that the “A” and “B” positions look very similar to the octahedral intercalation sites encountered in the bulk anatase. Similarly, the “a” and “b” sites can be the equivalent of the tetrahedral intercalation sites.

When geometry optimization was performed, the Li ions located in the “a” and “b” positions moved spontaneously to the “A” and “B” sites, respectively. This indicates that the “a” and “b” locations are not stable. Theoretical calculations<sup>127</sup> have shown a similar phenomenon in the anatase bulk: the Li intercalated in the tetrahedral sites spontaneously changed position to the octahedral ones.

Liang et al.<sup>138</sup> found that the intercalation of the Li ions is 0.32 eV (energetically) more stable in the B-sites located on the inner surface than on the A-sites located on the outer one for the (9, 0) *nt*-TiO<sub>2</sub>. However, they showed that this energy difference is gradually reduced when the *nt*-TiO<sub>2</sub> diameter increases. The same authors also studied several diffusion pathways that are displayed in Figure 1.26 where the titania atoms are in grey, the oxygen ones in red and the lithium ions in purple.

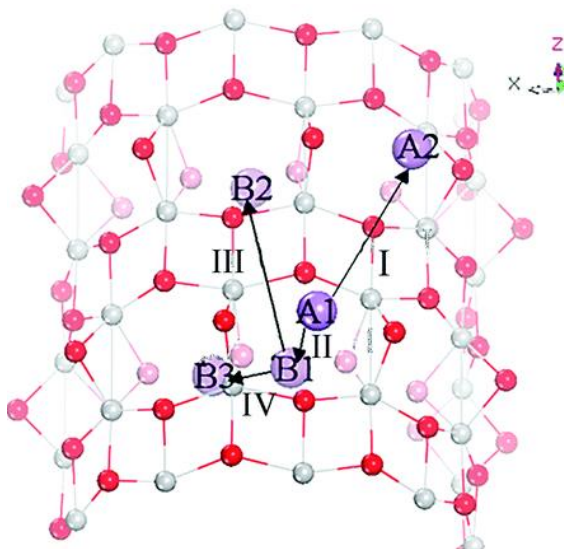


Figure 1.26: Diffusion pathways between the different Li intercalation sites in an (101) *nt*-TiO<sub>2</sub><sup>138</sup>. The grey, red and purple spheres represent the Ti, O and Li atoms. Republished with permission of Royal Society of Chemistry, from reference<sup>138</sup> obtained in 2021; permission conveyed through Copyright Clearance Center, Inc.

The pathway exhibiting the lowest energy barrier is the one denoted IV because of the very short distance separating the two “B” intercalation sites. The second lowest energy barrier was calculated for the path II. However, the A1 → B1 diffusion has a lower activation barrier than the B1 → A1, indicating that it is more favourable for the Li ions to move from the outer side to the inner one than to do the opposite. The paths labelled I and III exhibit the highest activation energies, suggesting that diffusion within the layer is higher than diffusion along the nanotube. The effect of the oxygen vacancies on the Li diffusion was also investigated. The most stable oxygen vacancies are created by removing the two-fold coordinated oxygen atoms located in the inner surface. When these vacancies are present, the diffusion barriers along path II (from the outer surface to the inner one) is reduced from 0.8 eV to 0.53 eV.

## 1.2.8 The sodium ion batteries

The electrochemical properties of sodium have aroused the scientist's interest to build sodium ion batteries. This element is much more abundant than lithium and have a redox potential that equals -2.71 V versus the hydrogen electrode<sup>139</sup>, only 0.3 V above that of lithium. Consequently, the sodium ion batteries can be a promising and cheaper alternative to the lithium ones.

The first Na cells based on TiO<sub>2</sub> electrodes were built by Xiong et al.<sup>140</sup> in 2011. They used amorphous TiO<sub>2</sub> nanotubes and reported a self-improved capacity of 150 mA.h.g<sup>-1</sup> after 15 cycles. The initial capacity equalled 75 mA.h.g<sup>-1</sup> after the first cycle and slowly increases to almost double after 15 cycles. The authors also noticed that sodium ions can be intercalated only on nanotubes having a diameter wider than 80 nm. They explained this phenomenon by the inability of the sodium ions to infiltrate within *nt*-TiO<sub>2</sub> exhibiting smaller diameters. Two years later, Bi et al.<sup>36</sup> reported a similar self-improving behaviour of amorphous *nt*-TiO<sub>2</sub> grown on Ti foam. They observed a continual improvement of the capacity, that triples its initial value after 100 cycles, and explained this enhancement by a transformation of the amorphous *nt*-TiO<sub>2</sub> into a face-centred cubic crystalline structure.

Sodium ions were then successfully intercalated into anatase nanoparticles<sup>141-143</sup>, nanorods<sup>144</sup> and nanotubes<sup>7,145</sup>. Wu et al.<sup>141</sup> showed that anatase nanoparticles can be cycled for more than 1000 cycles retaining the same capacity. However, they noticed that the anatase structure completely disappeared after the first sodium intercalation to form a mixture of amorphous sodium titanate, metallic titanium and sodium superoxide NaO<sub>2</sub>. On the other hand, Li et al.<sup>143</sup> reported that anatase nanoparticles underwent a phase transformation into a rhombohedral O3-type layered structure once fully sodiated. By cycling anatase nanoparticles at 90°C, Ding et al.<sup>142</sup> noticed that a Na<sub>2</sub>Ti<sup>II</sup>Ti<sup>IV</sup>O<sub>4</sub> solid solution was formed after the first sodium intercalation. The deintercalation process reversibly transformed the solid solution into a mixture of amorphous TiO<sub>2</sub>, amorphous Na<sub>2</sub>TiO<sub>3</sub> and crystalline TiO.

Kim et al.<sup>144</sup> used anatase nanorods as electrode material in sodium ion batteries. They carried out *Ex Situ* XRD characterization indicating that the anatase structure is maintained during the Na intercalation/deintercalation cycles for a voltage range of 3–0 V vs Na/Na<sup>+</sup>. The XAS studies of the electrode showed that the Na insertion induces a reversible Ti<sup>4+</sup>/Ti<sup>3+</sup> redox reaction. The authors also demonstrated that the capacity and rate capability of anatase nanorods can be improved by carbon coating.

Gonzales et al.<sup>145</sup> used anatase nanotubes in sodium ion batteries. They reported a capacity of 190 mA.h.g<sup>-1</sup> after 800 cycles for nanotubes having an inner diameter of 92 nm. However, irreversible capacity losses were observed in the first cycle whatever was the cycling condition. The XRD analysis performed by the authors showed that the anatase structure is retained, even for potential equal to 0.0 V vs Na<sup>+</sup>/Na. These results agree with the XRD measurements carried out by Bella et al.<sup>146</sup> indicating that the crystallinity of the anatase *nt*-TiO<sub>2</sub> is not modified by Na intercalation for potential included between 0.3 and 2.5 V vs Na<sup>+</sup>/Na. However, the electrochemical tests reported by Gonzales et al. indicates the presence of irreversible faradic processes, associated with both electrolyte decomposition and sodium intercalation into the nanotubes, for potentials below 0.3 V vs Na<sup>+</sup>/Na. Consequently, the best cycling behaviours were observed for 2.6-0.5 V of potential limits.

Moreover, by comparing the results obtained with those reported for equivalent lithium ion batteries, the authors noticed that the accommodation in the surface of the *nt*-TiO<sub>2</sub> is more important for the Na ions than for the Li ones. As a result, the capacity of 190 mA.h.g<sup>-1</sup> observed for the Na-ion batteries based on anatase nanotubes is close to the one observed for the equivalent Li-ion batteries<sup>29</sup> that equals 200 mA.h.g<sup>-1</sup>.

Three years later, Li et al.<sup>7</sup> performed XANES analysis of both amorphous and anatase *nt*-TiO<sub>2</sub> at different charge/discharge potentials in Na-ion batteries. Their study suggests that the irreversible loss of capacity observed during the first cycle for both phases can be explained by an irreversible phase transformation of both the surface and the near surface regions into amorphous sodium titanate. Moreover, the same regions are partially reduced to metallic Ti during the next charge/discharge cycles. The shapes of sodium discharging/charging curves do not show potential plateaus, indicating that the Na<sup>+</sup> ions rather adsorb than diffuse inside the nanotubes.

The XANES measurements carried out for the anatase nanotubes indicates that the *nt*-TiO<sub>2</sub> retain their anatase structure only for potential above 0.5 V vs Na/Na<sup>+</sup>. An irreversible transformation into an amorphous structure is then observed for lower potential. The authors explained this structural change by the stress caused by the accommodation of large Na<sup>+</sup> that will induce a distortion of the local structure of the TiO<sub>6</sub> octahedron, as well as a modification of their long-range connectivity. The authors also reported the reversible formation of flower-like structures made of Na<sub>2</sub>CO<sub>3</sub> at the top surface of *nt*-TiO<sub>2</sub> once discharged to 0.01 V.

### **1.2.9 Modelling of Na intercalation into TiO<sub>2</sub> anatase**

Several theoretical studies about sodium intercalation into bulk anatase were carried out. All these studies identified the octahedral sites as the most favourable ones for sodium insertion. The first study was performed by Lunell et al.<sup>106</sup> using DFT in a Na<sub>0.5</sub>TiO<sub>2</sub> cell where half of the octahedral sites were filled with sodium. The geometry modifications generated by the sodium insertion were an elongation of the Ti-O bonds located in the *xy* plane by 0.31 Å whereas the Ti-O bonds parallel to the *z* axis were shortened by 0.41 Å. Similar structures changes were observed in the Li<sub>0.5</sub>TiO<sub>2</sub> cell but the bond length modifications were less important<sup>147</sup>.

By comparing two anatase bulks doped with 0.9 % of lithium or sodium, Kortados et al.<sup>148</sup> confirmed that the Na ions generate bigger lattice distortions than the Li ones. Lunell et al.<sup>106</sup> were the first ones to observe that the sodium ions are not located at the centre of the octahedral site but are shifted by 0.06 Å along the *c* direction. This particular location of the Na ions was later confirmed by other theoretical studies<sup>25,143,149</sup>. As a result, both the Na and Li ions are five-fold coordinated when they are intercalated into a bulk anatase.

Lithium and sodium intercalations into anatase bulk induce similar modifications to the electronic structure<sup>25,148,149</sup>. The added electron is given to one of the nearest Ti neighbours, reducing it to Ti<sup>3+</sup>. The extra charge is stored in a single Ti *3d* state, generating strong intra-atomic coulombic repulsions between the different *d* orbitals. According to the Mott–Hubbard theory, the coulombic repulsions will be balanced by a splitting between the occupied and unoccupied Ti *3d* states. Thus, the occupied Ti *3d* states create a defect state in the band gap, while the unoccupied Ti *3d* states stay in the conduction band.

The total DOS of the Na<sub>0.11</sub>TiO<sub>2</sub> anatase bulk is displayed in red in Figure 1.27<sup>149</sup>. For comparison, the total DOS of the TiO<sub>2</sub>, Li<sub>0.11</sub>TiO<sub>2</sub> and Mg<sub>0.11</sub>TiO<sub>2</sub> anatase bulks are also displayed in black, blue and green. The vertical lines in the Figure represent the Fermi energies.

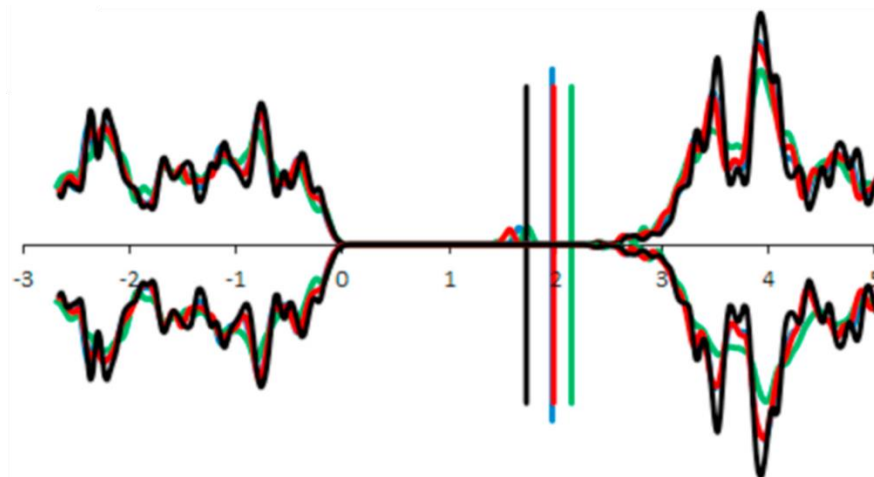


Figure 1.27: Total DOS of Li<sub>0.11</sub>TiO<sub>2</sub> (blue), Na<sub>0.11</sub>TiO<sub>2</sub> (red), Mg<sub>0.11</sub>TiO<sub>2</sub> (green) and TiO<sub>2</sub> (black) anatase bulks. The vertical lines represent the respective the Fermi energies<sup>149</sup>.

The sodium intercalation energies reported in the literature all indicate that the sodium insertion into anatase bulk is favourable. Their values depend on both the computational parameters and the sodium concentration. Thus, Legrain et al.<sup>149</sup> found an intercalation energy of  $-0.27$  eV per  $\text{TiO}_2$  unit for  $\text{Na}_{0.11}\text{TiO}_2$  bulk. The same authors also compare the intercalation energies into the  $\text{Na}_{0.11}\text{TiO}_2$  and  $\text{Li}_{0.11}\text{TiO}_2$  bulks and noticed that the lithium insertion is much more favourable with an intercalation energy that equals  $-1.85$  eV per  $\text{TiO}_2$  unit. In addition, Bella et al.<sup>146</sup> reported a sodium insertion energy of  $-0.14$  eV per  $\text{TiO}_2$  unit when the capacity is  $x = 0.03$  while Li et al.<sup>143</sup> calculated an energy of  $-0.08$  eV for a capacity of  $x = 0.008$ . The relatively low intercalation energies reported for the sodium can be explained by the rigidity of the anatase structure that limits the distortions of the lattice<sup>146</sup>.

Li et al.<sup>143</sup> studied two fully sodiated  $\text{NaTiO}_2$  bulks having a rhombohedral layered structure ( $R\bar{3}m$  space group) and a tetragonal anatase structure ( $I(4)1/amd$  space group). They reported sodium intercalation energies of  $-1.247$  eV and  $-0.975$  eV per  $\text{TiO}_2$  unit for the rhombohedral and tetragonal structures, respectively. These results suggest that the anatase structure may not be retained with high sodium ratio.

The sodium intercalation into anatase  $\text{TiO}_2$  surfaces and nanotubes has not been considered computationally to the best of our knowledge.

## 1.3 Summary

- The miniaturization of portable devices requires the development of batteries at the micrometer scale. Most of the microbatteries are based on the lithium ion technologies because of the high energy density exhibited by this element.
- The nano-structuring of the anatase  $\text{TiO}_2$  improves its capacity and makes it a promising material as anode for Li-ion microbatteries. Moreover, anatase nanotubes can be easily produced by a simple and template-free anodization process. These nanotubes have a good electrical contact with the current collector and do not need to be mixed with carbon blacks or polymer binders.
- Electrochemical measurements carried out on anatase *nt*- $\text{TiO}_2$  indicate the presence of a pseudocapacitive  $\text{Li}^+$  storage occurring at the nanotube surface. Moreover, XANES analysis showed the formation of a thin film of about 4 nm in thickness with a Ti valence close to  $3^+$  at the surface of the *nt*- $\text{TiO}_2$ . The external wall of the *nt*- $\text{TiO}_2$  seems to play a major role in the storage of the  $\text{Li}^+$  ions at the surface while the internal walls do not store lithium at their surfaces.
- The helical symmetry of the nanotubes allows to drastically reduce the computational time and to perform *ab initio* calculations on nanotubular structures containing several hundreds of atoms. The  $(n_1, 0)$  anatase *nt*- $\text{TiO}_2$  generated from the 3 ML (001) slab exhibit a negative strain energy and were already chosen as a suitable model to study the water splitting hydrogen generation or different doping of the anatase *nt*- $\text{TiO}_2$ .

- Both experimental and computational studies confirmed a maximum Li intercalation ratio of  $x = 0.5$  into anatase bulk. The lithiated anatase undergoes an orthorhombic distortion and is transformed into a  $\text{Li}_{0.5}\text{TiO}_2$  titanate structure where the lithium ions occupy half of the octahedral intercalation sites. The Li intercalation occurs through a two-phase equilibrium between a Li-poor phase having a Li fraction of  $x \approx 0.01$  and a Li-rich phase made of  $\text{Li}_{0.5}\text{TiO}_2$  titanate.
- The computational studies confirmed the existence of a  $\text{LiTiO}_2$  rich phase exhibiting a tetragonally distorted rock salt structure. Nevertheless, the disappearance of the octahedral distortions in this rich phase limits the Li diffusion and increases the migration barriers. As a result, the  $\text{LiTiO}_2$  rich phase will firstly be formed at the surface of the electrode but its inward growth towards the bulk will be limited to a few nanometers.
- The abundance and electrochemical properties of sodium have encouraged the scientists to develop sodium ion batteries as a cheaper alternative to the lithium ones. Anatase *nt*- $\text{TiO}_2$  were recently used in Na-ion microbatteries. However, irreversible capacity losses were reported for the first cycle, independently of the cycling conditions. The anatase *nt*- $\text{TiO}_2$  surface is more reactive towards sodium than towards lithium and is irreversibly transformed into amorphous sodium titanate where the  $\text{Ti}^{4+}$  ions are partially reduced to metallic Ti.
- The theoretical studies carried out about sodium intercalation into bulk anatase indicate that the  $\text{Na}^+$  ions are inserted into the octahedral sites. The sodium insertion generates lattice distortions similar to the lithium one, but the bond length modifications are more important. As a result, the intercalation energies into bulk anatase are less favourable for sodium than for lithium. No computational study of sodium intercalation into anatase surfaces or nanotubes has been carried out to the best of our knowledges.

# Chapter 2

## Methodology

### 2.1. Hartree Fock and DFT theory

#### 2.1.1. A brief introduction to computational chemistry

Computational chemistry began around 1950 and gradually increased with the computer power over time. It gained further recognition in 1998 after John Pople and Walter Kohn won the Nobel Prize in Chemistry<sup>150</sup> for their work on computational methods in quantum chemistry and density functional theory, respectively.

Nowadays, computational chemistry is widely used to study the fundamental properties of atoms and molecules. It is a valuable tool to identify the reaction pathways and predict the most likely products, allowing the development of more productive and efficient synthesis processes. Thus, the financial and time constraints associated with laboratory trials are considerably reduced. It can also be used to explore the physical processes involved in phenomena, such as, phase changes, corrosion or energy storage. Computational chemistry becomes particularly pertinent to predict the properties of expensive or harmful substances. In this thesis, it is employed to help understanding complex results obtained by experimental techniques.

The simulations can be performed over a broad space-time scale as illustrated in Figure 2.1<sup>151</sup>.

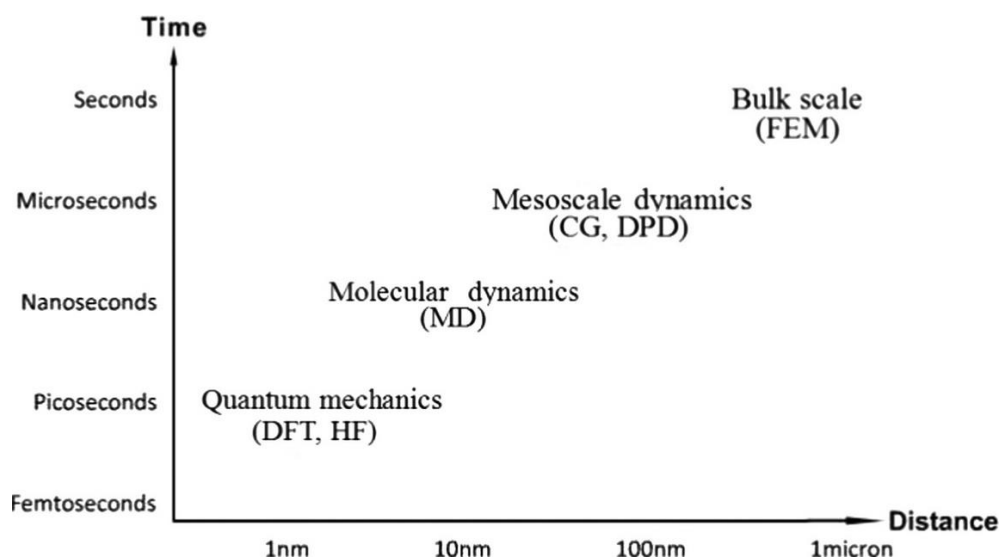


Figure 2.1: Repartition of the different simulation methods according to the space-time scale<sup>151</sup>.

Quantum mechanics allows to perform simulations at an atomic scale. Thus, information about the electronic structure e.g. band structure and the chemical bonds (for example bond strengths and lengths) can be obtained. Density functional theory (DFT) or hybrids between DFT and the Hartree-Fock (HF) approximation are currently the most common methods to perform quantum mechanics calculations<sup>152</sup>. Most DFT based calculations are performed at zero Kelvin, excluding atomic motion, i.e. zero point energy (ZPE).

Instead, molecular dynamics is used to study the interactions between atoms as they are translated in Hubbard space. It simulates the natural motion of the molecular system, according to Newton's law. This method is widely employed to study the conformations of large molecules, for example proteins. Simulations at a mesoscopic scale requires methods, such as coarse grained or dissipative particle dynamics methods. Phenomena describing structural analysis, fluid flow or heat transfer can be studied using finite element method.

The choice of the simulation methods depends on the space-time scale of interest. The aim of this thesis is to get a better understanding of energetics, i.e. intercalation voltages, as well as structural information of the Li<sup>+</sup> and Na<sup>+</sup> intercalation into nanotubes of anatase TiO<sub>2</sub>. The modifications are mainly occurring at the atomic scale and quantum mechanics based on DFT/ hybrid methods were the most suitable choice.

## 2.1.2 Fundamentals of the quantum mechanics methods

### 2.1.2.1 The Schrödinger Equation

Electrons are much lighter than atoms or molecules and they can only be described by quantum mechanics. In contrast to classical mechanics that is deterministic, quantum mechanics is probabilistic. As a result, quantum mechanics allows only to calculate the probability of a particle to be at a certain place at a certain time. Indeed, Heisenberg's uncertainty principle avoids determining simultaneously the place and the time. The probability of finding a particle at a certain place at a certain time is described by the Schrödinger Equation<sup>152</sup>. Thus, by solving or finding an approximate solution of this equation, it is possible to access the properties of a molecule, such as its energy. The time-independent Schrödinger Equation is defined by Equation 2.1.

$$\hat{H}\Psi(\mathbf{R}, \mathbf{r}) = E\Psi(\mathbf{R}, \mathbf{r}) \quad (2.1)$$

In this equation,  $\hat{H}$  is the Hamiltonian operator,  $\psi$  is the wave function and  $E$  is the energy of the state described by the wave function. The wave function is defined by the location of the nucleus ( $\mathbf{R}$ ) and an electron ( $\mathbf{r}$ ). This equation is used in wave function theories, such as the Hartree-Fock approximation.

### 2.1.2.2 The Born-Oppenheimer approximation

The mass difference between the electron and the nuclei is very important. For example, in the hydrogen atom, the nucleus is 1800 times heavier than the electron. This mass difference then gradually grows with the atomic number of the element. The mass difference will induce a velocity difference: the electrons move considerably faster than the nuclei. Consequently, they can adjust very fast if the nuclei position changes. The Sun-Earth system can be used as an analogy, where the planets are rotating around the stationary sun. A good approximation is, therefore, to consider that the electrons are moving around a fixed nucleus.

This simplification is referred to as the Born-Oppenheimer<sup>153</sup> approximation, allowing the wave function  $\psi(\mathbf{R}, \mathbf{r})$  to be factorized in two independent terms as described in Equation 2.2:

$$\Psi(\mathbf{R}, \mathbf{r}) = \Phi(\mathbf{R})\varphi_{\mathbf{R}}(\mathbf{r}) \quad (2.2)$$

where  $\Phi(\mathbf{R})$  represents the nuclear term (the nuclei are free to move and the electrons are fixed) whereas  $\varphi_{\mathbf{R}}(\mathbf{r})$  stands for the electronic term (the electrons are free to move around fixed nuclei). As a result, the electronic wave function  $\varphi_{\mathbf{R}}(\mathbf{r})$  contains all the information about the electrons present in the system. The total energy of a particular electronic wave function can be calculated using the Hamiltonian operator as displayed in Equation 2.3:

$$\hat{H}\varphi_{\mathbf{R}}(\mathbf{r}) = E\varphi_{\mathbf{R}}(\mathbf{r}) \quad (2.3)$$

The Hamiltonian operator contains kinetic ( $\hat{T}$ ) and potential ( $\hat{V}$ ) operators as described in Equation 2.4:

$$\hat{H} = \hat{T} - \hat{V}_{\text{ext}} + \hat{V}_{\text{int}} \quad (2.4)$$

In Equation 2.4,  $\hat{T} = -\sum_{i=1}^N \frac{\hbar^2}{2m} \nabla_i^2$  represents the kinetic energy of the system,  $\hat{V}_{\text{ext}} = \sum_{i,l} \frac{Z_l}{|\mathbf{r}_i - \mathbf{R}_l|}$  stands for the external potential of the nuclei on the electrons, and  $\hat{V}_{\text{int}} = \frac{1}{2} \sum_{i/j} \frac{1}{|\mathbf{r}_i - \mathbf{r}_j|}$  expresses the potential between two separate electrons. This last  $\hat{V}_{\text{int}}$  operator will make the Schrödinger Equation impossible to solve exactly for systems containing more than one electron. Consequently, mathematical approximations were developed to find approximations allowing for this issue.

### 2.1.2.3 The Hartree Fock approximation

One of the most common approximations is the Hartree-Fock (HF) method<sup>150</sup> that concerns the  $\hat{V}_{\text{int}}$  operator. For many-electron systems, it will be very complicated to take into account the interaction between each individual electron. The HF approximation assumes that the N-electron wave function can be replaced by an antisymmetric product of N one-electron wave functions. This antisymmetric product is known as the Slater determinant. The HF approximation will then make all the electrons indistinguishable. As a consequence, one electron will not interact with the other electrons individually, but with an average potential representing a “cloud” of electrons present in the system. Thus, the HF approximation does not take into account the electron correlation but calculates an exact exchange term corresponding to the interaction between one electron and an average potential of all of the other electrons.

As a result, the one-electron wavefunctions can be obtained as solutions of the HF equation (Equation 2.5):

$$\hat{F} \Psi_i(x_i) = \varepsilon_i \Psi_i(x_i) \quad (2.5)$$

where  $\hat{F}$  is the Fock operator.

Although the HF method allows to calculate the total electronic energy of the system, the value obtained will often differ from the exact solution of the Schrödinger equation. The Hartree Fock limit is defined as the energy calculated using a complete basis set (see section 2.1.3). The energy difference between the exact solution and the HF limit defines the correlation energy. The name “correlation energy” originates from the fact that HF does not take into account the influence of individual electrons in the system. As the electrons are repelling each other, the position of one electron will affect the positions of the other ones and they will be localized as far apart as possible.

#### 2.1.2.4 The Density functional theory approximation

Another well-known approximation to the Schrödinger equation is the density functional theory (DFT) method. In the same way as the HF method, the DFT approximation is based on a single-electron function. The DFT originates from a study carried out by Hohenberg and Kohn in 1964<sup>154</sup>, showing that it is possible to describe the ground state properties of a real system, such as its ground state energy, uniquely with its electron charge density  $\rho(\mathbf{r})$ . The electron charge density depends only on three spatial variables, whatever is the number of electrons present in the system. As a result, the energy of a system can be described by a functional of its electron charge density  $E[\rho(\mathbf{r})]$  as displayed in Equation 2.6<sup>155</sup>.

$$E[\rho(\mathbf{r})] = F[\rho(\mathbf{r})] + \int V_{\text{ext}}\rho(\mathbf{r})d\mathbf{r} \quad (2.6)$$

This functional, describing the energy of the system, is the sum of two terms: the first one  $F[\rho(\mathbf{r})]$  is a universal functional taking into account the kinetic energy of the electrons and the electron-electron interactions. The second term represents the interaction of an external potential  $V_{\text{ext}}(\mathbf{r})$  with the electrons.

However, the universal functional  $F[\rho(\mathbf{r})]$  remained unknown until Kohn and Sham<sup>156</sup> proposed to approximate it as the sum of three terms described by in Equation 2.7:

$$F[\rho(\mathbf{r})] = E_{\text{KE}}[\rho(\mathbf{r})] + E_{\text{H}}[\rho(\mathbf{r})] + E_{\text{XC}}[\rho(\mathbf{r})] \quad (2.7)$$

$E_{\text{KE}}$  represents the kinetic energy of a non-interactive electron gas exhibiting the same electronic density  $\rho(\mathbf{r})$  as the real (interacting) one.  $E_{\text{H}}$  stands for the electron-electron interaction energy and  $E_{\text{XC}}$  is the exchange-correlation energy that cannot be solved exactly but needs to be approximated.

The first approximation applied to the exchange correlation functional  $E_{XC}[\rho(\mathbf{r})]$  is referred to as the Local Density Approximation (LDA). It is based on the assumption that the electron density is homogeneous throughout the space<sup>157</sup>. Thus, the exchange correlation energy  $E_{XC}$  can be calculated by integrating the uniform electron gas over all space described in Equation 2.8.

$$E_{XC}^{LDA}[\rho(\mathbf{r})] = \int \rho(\mathbf{r}) \varepsilon_{xc}(\rho(\mathbf{r})) d\mathbf{r} \quad (2.8)$$

In this equation,  $\varepsilon_{xc}(\rho(\mathbf{r}))$  is the exchange correlation energy of the uniform electron gas as a function of the density  $\rho(\mathbf{r})$ .

The LDA functional was the only approximation available for many years. Although this method was working well to describe metals, it failed to describe correctly anisotropic systems<sup>158</sup>. This issue gave rise to the development of other functionals based on the Generalized Gradient Approximation (GGA).

The GGA functionals take into account the possible inhomogeneous repartition of the electron charge density. They contain the same exchange correlation functional as the one used in the LDA method, but a second term depending on the gradient of the density, is added as displayed in Equation 2.9<sup>157</sup>.

$$E_{XC}^{GGA} = E_{XC}^{LDA}[\rho, \nabla\rho] \quad (2.9)$$

A large variety of GGA functionals were developed and are still employed today. Among them are the Becke-Lee-Yang-Parr (BLYP)<sup>159,160</sup> and the Perdew-Burke-Ernzerhof (PBE)<sup>161</sup> functionals used in this thesis.

### 2.1.2.5 The Hartree Fock / DFT hybrid methods

Although the development of the LDA and GGA approximations was a major breakthrough for the DFT method, the materials having highly localized electrons (such as transition metal oxides, including  $\text{TiO}_2$ ) cannot be described correctly. This is due to the so-called self-interaction error present in the Kohn-Sham approximated functional. The classic coulomb term, included in the electron-electron interaction energy  $E_H[\rho(\mathbf{r})]$ , contains the spurious interaction of the electron with itself. Consequently, the orbitals having strongly localized electrons will be destabilized, and their electrons will be improperly delocalized to minimize the self-interaction<sup>155</sup>. However, this issue is not present in the HF method where the exchange term between the electrons is exact. One approach to compensate for the self-interaction error when studying transition metal oxides is to use hybrid functionals.

Hybrid functionals will use a combination (mixture) of HF and DFT exchange contributions. Reintroducing the HF exchange term in the DFT method allows to compensate for the self-interaction error while keeping the correlation energy from DFT<sup>162</sup>. The exchange-correlation energy  $E_{XC}$  present in the Kohn-Sham approximated functional becomes a sum of two terms detailed in Equation 2.10.

$$E_{XC}[\rho(\mathbf{r})] = E_X^{\text{HF+KS}} + E_C^{\text{KS}} \quad (2.10)$$

In this equation,  $E_X^{\text{HF+KS}}$  is the exchange energy defined by a sum of the Kohn-Sham and some fraction of the HF exchange.  $E_C^{\text{KS}}$  is the correlation energy defined in the Kohn-Sham functional.

One of the most commonly employed hybrid functionals is the B3LYP<sup>163</sup> one. It was developed by Becke who used a functional described by three parameters (B3) for the exchange energy, to which he added the Lee-Yang-Parr (LYP)<sup>160</sup> correlation functional. The proportions of HF and DFT were determined by fitting experimental data for a small set of elements. Based on this fitting, Becke proposed a mixing of 20% HF with 80% of DFT (Becke) exchange.

The PBE0<sup>164</sup> is another well-known hybrid functional, built similarly to the B3LYP, by mixing 25% of HF with 75% of PBE (DFT) exchange. The PBE0 was developed for solids while the B3LYP was originally used to represent molecular systems.

As detailed in section 2.2.1, the B3LYP and PBE0 functionals appeared to be the most suitable choice to describe TiO<sub>2</sub><sup>165</sup>. The B3LYP functional was preferred in this thesis for its more accurate description of the band gap.

## 2.1.3 The basis sets

### 2.1.3.1 Slater and Gaussian type orbitals

The Schrödinger Equation can be solved exactly only for one-electron systems like the hydrogen atom or the H<sub>2</sub><sup>+</sup> molecule. Contrary to classical mechanics where all the energies are allowed, the number of solutions in quantum mechanics is not infinite, resulting in discrete energy levels (eigenvalues). The wave functions, singular or plural, and associated energies, are said to be quantized.

When solving the Schrödinger Equation for the hydrogen atom, it is easier to use spherical coordinates, as the electrons are moving in the three dimensions.

The exact solutions of the Schrödinger Equation for the hydrogen atom are referred to as the hydrogenic orbitals and depend on the three spatial variables  $r$ ,  $\theta$  and  $\varphi$ . They are classified by three quantum number  $n$ ,  $l$  and  $m$ , corresponding to  $r$ ,  $\theta$  and  $\varphi$ , respectively. Consequently, the  $n$  quantum number will describe the size of the orbital, the  $l$  quantum number its shape, and the  $m$  quantum number its orientation relative to a fixed coordinate system. The orbitals can be visualized by plotting the corresponding wave function<sup>152</sup>  $\Psi_{n, l, m}(r, \theta, \varphi)$ .

Mathematically, the orbitals can be written as a product of a *radial* function (representing the behavior according to the  $r$  distance between the electron and the nucleus), and *spherical harmonic* functions that will describe the angular part as a function of  $\theta$  and  $\varphi$ .

Theoretically, all kind of basis functions, including exponential, Gaussian, plane waves, polynomial or cube functions can be used, as long as their behavior agrees with the physics of the system. Thus, this set of basis function is often called atomic orbitals whereas it is generally not a solution of any atomic Schrödinger Equation.

Two kind of basis functions are commonly used: the Slater Type Orbitals (STO) and the Gaussian Type Orbitals (GTO). STOs were the first ones to be developed. They exhibit a similar structure to the hydrogenic orbitals where the dependence on the  $r$  distance is described by an exponential function. The STOs allow to obtain very accurate results for atomic and diatomic systems.

However, from a computational point of view, exponential functions are difficult to handle, especially for molecular systems where the atomic orbitals can be centered on different nuclei. The general form of the STOs is displayed in Equation 2.11<sup>152</sup>.

$$\chi^{\text{STO}} = N \cdot Y_{l,m}(\varphi, \theta) r^{n-1} \exp(-\alpha r) \quad (2.11)$$

It was later shown that STOs can be approximated by a linear combination of GTOs that are easier to handle computationally. GTOs can be written in Cartesian coordinates as described in Equation 2.12:

$$X^{\text{GTO}} = N x^l y^m z^n \exp(-\alpha r^2) \quad (2.12)$$

In both equations 2.11 and 2.12,  $N$  is a normalization factor and  $\alpha$  is the exponent. The main difference between the STOs and the GTOs is the variable  $r$  in the exponential function that is squared in Gaussian functions. Consequently, a single Gaussian function will start with a curve, whereas the STOs begin with a straight downward line. This explains why the STOs cannot be replaced by a single GTO (Figure 2.2).

However, using the advantage that a product of two Gaussian functions can be expressed as a single Gaussian, the STOs are approximated by a linear combination of GTOs as displayed in Equation 2.13.

$$\phi_{\mu} = \sum_{i=1}^L d_{i\mu} \phi_i(\alpha_{i\mu}) \quad (2.13)$$

Where L is the number of primitive Gaussian functions  $\phi_i$  used in the linear combination. Each GTOs is then defined by its coefficient  $d_{i\mu}$  and its exponent  $\alpha_{i\mu}$ . As shown in Figure 2.2, the fit of the GTOs compared with the STO description is improved when the number of Gaussian functions used in the linear combination increases<sup>166</sup>.

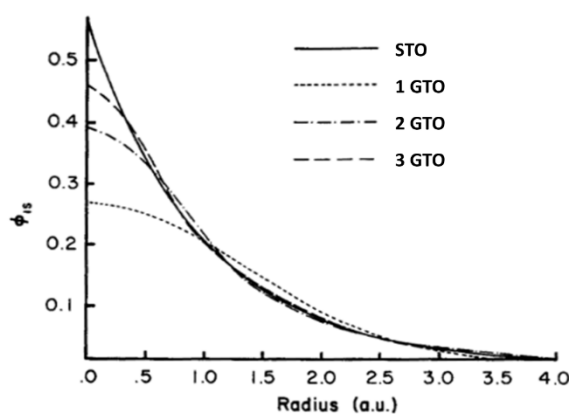


Figure 2.2: Comparison of the quality of GTOs up to a 3<sup>rd</sup> term linear combination to model a plot  $1s$ -STO orbital<sup>166</sup>.

A general rule says that three times as many GTOs as STOs are required to reach a certain level of accuracy.

### 2.1.3.2 Basis sets classification

Once the type of functions (STO/GTO) is determined, it is possible to build the basis set for the system. Most of the GTOs available in the literature are centered at the nuclei. However, for particular calculations for example, where the Van der Waals interactions have to be considered, basis functions centered at a bond or between two non-bonded atoms may be used. GTOs centered at the nuclei were chosen in this thesis.

The basis sets containing the minimum number of functions are known as “*minimal basis sets*”. Only the minimum amount of functions necessary to contain all the electrons of a neutral atom are used in the basis set description<sup>152</sup>. This kind of basis set are thus ignoring the unoccupied orbitals. Severe drawbacks will also be encountered when modeling simple organic molecules: the contracted  $\sigma$ -bonds and more diffuse  $\pi$ -bonds will be defined with the same and unique exponent, as only a single set of  $p$  orbitals is available.

The next improvement is the development of the so-called *double zeta* basis sets where all the basis functions are doubled. Thus, simple organic molecules for example, can be modelled using a double set of  $p$  orbitals. The  $\sigma$ -bonds will be described by the function having a large exponent whereas the other function (having a smaller exponent) will be used for the  $\pi$ -bonds.

When studying the chemical properties of a system, it is possible to simplify the basis set (and thus reduce the computational cost of the calculation) by taking into account that the chemical bonding occurs between valence orbitals. The core orbitals, being independent of the chemical environment, will not fluctuate considerably from one molecule to another. Thus, doubling the basis functions describing the core orbitals will not improve the accuracy of the calculations. The basis sets where only the valence orbitals are doubled are known as *split valence basis*<sup>152</sup>.

Although the *split valence basis* allow an improved representation of the chemical bonding, higher angular momentum functions, known as *polarization functions*, play a major role to correctly describe the shapes of the orbitals.

This can be explained by taking the simple example of a C-H bond. The atomic orbitals involved are the hydrogen 1s, and the carbon 2s and 2p orbitals. However, if the hydrogen atom is defined only by s atomic orbitals, the C-H bond will not be correctly described. By adding a set of p orbitals to the hydrogen atom, some component of the p orbitals can be used to improve the description of the chemical bond. In other words, the presence of polarization functions allows the valence orbitals to distort from their original shape and to conform better to the molecular environment. Generally, the first set of polarization functions (p-functions for hydrogen atoms and d-functions for heavier elements) is sufficient to describe most of the polarization effects.

When the system studied includes atoms located below the first two rows of the periodic table, it is possible to reduce the computational cost by replacing the basis functions representing the numerous core electrons by a single potential. This function is usually called *Effective Core Potential (ECP)*<sup>152</sup> or *Pseudopotential (PP)*<sup>167</sup>.

When GTOs are used to describe the valence orbitals, the ECP is generally made of Gaussian functions as well. The quality of an ECP depends on the proportion of electrons chosen to be described by an ECP. The best compromise between the accuracy of the calculations and the computational cost is obtained when the next lower shell below the valence orbitals is described by normal GTOs. In this thesis, the Ti atoms are described by a small core ECP where the orbitals having a quantum number,  $n$ , equal to 1 and 2 are represented by an ECP function.

## **2.1.4 Modelling of periodic system**

### **2.1.4.1 Periodic and molecular systems**

When a system containing several atoms is studied, the atomic orbitals will be modified by their interaction with other atoms. Thus, the probability of finding an electron in a specific location in a molecule is described by the molecular orbitals. These molecular orbitals are obtained by a linear combination of the atomic orbitals (LCAO) as detailed in Equation 2.14:

$$\Psi_i = \sum_{i=1}^n c_i \varphi_i \quad (2.14)$$

where  $\Psi$  is the molecular orbital,  $\varphi$  stands for the atomic orbital and  $c$  corresponds to the coefficient indicating the weight of the atomic orbital contribution. The molecular orbitals are used to describe the finite system, such as the molecule.

When the system studied is an infinite crystal, it will be described by crystalline orbitals. The general procedure is the same as for the molecular orbitals, but the periodicity of the lattice and the space group symmetry are fully exploited.

The *nt*-TiO<sub>2</sub> studied in this thesis were built by repeating a primitive unit cell in the three dimensions of space. The periodicity of the system can be described by crystalline orbitals where the functions have the same periodicity, i.e. Bloch functions. These particular wave functions enable the user to model periodic systems containing hundreds or thousands of atoms as they only consider the orbitals within the given unit cell. However, the solutions obtained depend on the reciprocal space (i.e. the Brillouin zone). Consequently, a grid of  $k$  points, sampling the reciprocal space, has to be generated, generally according to the Pack-Monkhorst method<sup>168</sup>.

In a three-dimensional crystal, the sampling points belong to a lattice called the “Pack-Monkhorst net” that is defined by three basis vectors (Equation 2.15):

$$\frac{\vec{b}_1}{is_1} ; \frac{\vec{b}_2}{is_2} ; \frac{\vec{b}_3}{is_3} \quad (2.15)$$

$\vec{b}_1$ ,  $\vec{b}_2$  and  $\vec{b}_3$  being the reciprocal lattice vectors; and  $is_1$ ,  $is_2$ ,  $is_3$  representing the integers "shrinking factors" (IS). Their values are input as  $IS = is_1 = is_2 = is_3$ . A second shrinking factor defining the sampling of  $k$  points within the “Gilat net”<sup>169,170</sup> is needed for the calculation of the density matrix. The values of the shrinking factors depend on the system studied and need to be optimized, as detailed in section 2.2.2.

The other parameters that control the accuracy of the calculations are the cutoff parameters for the bielectronic integrals. The bielectronic integrals are used in the CRYSTAL program to describe the Coulomb contributions to the total energy (Equation 2.16):

$$E = \frac{1}{2} \sum_{12} \sum_g P_{1,2}^g \sum_{34} \sum_n P_{3,4}^n \sum_h [\varphi_1^0 \varphi_2^g | \varphi_3^h \varphi_4^{h+n}] \quad (2.16)$$

where the indices 1, 2, 3 and 4 refers to the atomic orbitals of the unit cell while the indices g, n and h define the infinite set of translation vectors. P is the density matrix and  $\varphi$  is the Gaussian distribution defining the electron density.

The cutoff threshold parameters are based on the overlap between two atomic orbitals. When the overlap is smaller than  $10^{-\text{threshold}}$ , the corresponding integral is neglected. There are several values to define:

- the overlap threshold for Coulomb integrals,
- the penetration threshold for Coulomb integrals,
- the overlap threshold for HF exchange integrals,
- the pseudo-overlap for HF exchange series.

The optimization of these truncation criteria for the modelling of the titania nanotubes is detailed in section 2.2.2.

#### 2.1.4.2 The self-consistent field approach

The CRYSTAL code<sup>5</sup> employed in this thesis will use Gaussian basis sets to generate the electron charge density of the system studied, and then calculate its corresponding energy. The crystalline orbitals (CO) will be determined and optimized by using an iterative approach known as the Self-Consistent Field (SCF) procedure. The SCF approach can be applied to both the HF and DFT methods. Following its procedure, the program will take into account the atomic orbitals input as basis set to guess a set of approximated orbitals coefficients to describe the molecular and crystalline orbitals and calculate the corresponding energy of the system.

The new set of crystalline orbitals obtained allow to derive a new set of coefficients and to calculate the corresponding energy. This new energy is compared with the previous one. The whole process is then repeated until the difference in energies differs by less than a given threshold<sup>162</sup> that has to be defined in the input file. In this thesis, the cut-off value is the default one of the CRYSTAL program:  $10^{-6}$  Hartree of the total energy.

### **2.1.5 Geometry optimization of a periodic system**

A crystal structure is described by a space group, the cell parameters and the coordinates of the atoms within the unit cell. These parameters are defined in the input file and correspond to the crystalline unit cell. The CRYSTAL program will then transform the crystalline cell into a primitive cell to optimize the efficiency of the calculation. A primitive cell is a cell of minimum volume that contains only the irreducible atoms. This primitive cell can then be expanded in the three dimensions of the space by symmetry. An extended primitive cell is called a supercell, the size of the supercell is defined in the input file by a matrix indicating how many times the primitive unit cell should be repeated in the different directions, creating a larger primitive cell.

The geometry of a crystal can be optimized to determine the most stable configuration. When a geometry optimization is performed, it concerns only the atoms of the primitive unit cell, the other atoms being symmetric. The choice of primitive units, allowing for a full geometry optimization (space group P1) or a higher symmetry. This means that the geometry of crystals containing several hundreds of atoms can be optimized but also that structures available in higher energy states than ground state at 0°K can be studied. The CRYSTAL software will locate the minima and saddle points on the potential energy surface (PES) by using analytical gradient-based algorithms. The software evaluates the gradient each time the energy is computed and updates the second derivative matrix by using the Broyden-Fletcher-Goldfarb-Shanno (BFGS) algorithm.

The geometry optimization is an iterative process where the root-mean-square, and the absolute value of the largest component of both the gradients and the estimated displacements, are evaluated at the end of each optimization cycle. When the differences in values differs by less than a given threshold, the optimization has converged. For example, in CRYSTAL, the default threshold value is  $\Delta E$  equal to  $10^{-7}$  Hartree between two geometries.

## 2.2 Modeling of nanotubular TiO<sub>2</sub>

### 2.2.1 Basis sets and functional choices

In order have a better understanding of the *nt*-TiO<sub>2</sub> behavior when used as anode in microbatteries, we performed hybrid Density Functional Calculations (DFT). This *ab initio* method allows to access information on the electronic structure of the atoms. The software chosen was the periodic CRYSTAL<sup>5</sup> code that fully exploits the helical rototranslational symmetry of the nanotube structure to drastically reduce the computational time<sup>6</sup>, using 1 Dimensional (1D) symmetry. Thus, *nt*-TiO<sub>2</sub> exhibiting large unit cells (108 to 540 atoms depending on the diameter) are reachable by first principles studies. The symmetry is used for the calculation of one and two-electron integrals, and for the Fock-matrix diagonalization.

Labat et al.<sup>165</sup> compared the performances of different functionals to study the structural and electronic properties of anatase and rutile. They found that both PBE0<sup>164</sup> and B3LYP<sup>163</sup> functionals are in good agreement with the experimental binding energies and band structure. Based on this results, Ferrari et al.<sup>48</sup> chose the PBE0 functional to perform DFT analysis of anatase *nt*-TiO<sub>2</sub> exhibiting negative strain energies. However, the calculated band gap was equal to 4.3 eV for bulk anatase. Later, Lisovski et al.<sup>91</sup> carried out calculations to determine the most favorable functional allowing to investigate the effect of sulphur doping into this negative strain energy *nt*-TiO<sub>2</sub>. They calculated the lattice parameters and band gaps of anatase bulk TiO<sub>2</sub> using various functionals and obtained the results summarized in Table 2.1.

Although the band gap value calculated using B3LYP is around 0.5 eV larger than the experimental one, the B3LYP functional is the one allowing to model the most accurate band gap. As a result, Lisovski et al.<sup>91</sup> chose this hybrid functional but modified the admixture coefficient for the non-local Hartree Fock exchange to obtain a band gap value of 3.16 eV. This modified functional was later used by the same group to study other doped anatase *nt*-TiO<sub>2</sub> structures<sup>94,96</sup>.

Table 2.1: Lattice constants and band gaps of anatase bulk TiO<sub>2</sub> calculated by Lisovski et al.<sup>91</sup> using different functionals.

$E_{xc}$	a, Å	c, Å	$\Delta\varepsilon_g$ , eV
B3PW	3.785	9.580	3.667
PBE0	3.778	9.545	4.109
B3LYP	3.800	9.647	3.641
SOGGAXC	4.449	9.539	0.669
LDA	3.766	9.353	1.999
PBE	3.821	9.597	2.019
PWGGA	3.817	9.595	2.023
HF	3.777	9.643	12.357
Experiment	3.784	9.507	3.18

These two research groups made different basis set choices. Ferrari et al.<sup>48</sup> used a 411-31 Hay-Wadt<sup>171</sup> small core effective core potential (ECP) and an all-electron 8-411G (d) basis sets for titanium and oxygen atoms, respectively. These two basis sets were taken from the CRYSTAL website basis sets library<sup>172</sup>. On the other hand, Lisovski et al.<sup>91</sup> chose the ECP-411sp-311G (d), a Hay-Wadt basis set optimized by Piskunov et al.<sup>173</sup>, for Ti atoms; and a full electron 6s-311sp-1d basis set that they optimized themselves for the oxygen atoms.

By looking at the basis sets library<sup>172</sup> available on CRYSTAL website, we selected four of them:

- a Ti-86-51G (3d) and a O-8-411 basis sets<sup>174</sup>, both used to study the adsorption properties of TiO<sub>2</sub> surface.
- the Hay-Wadt 411sp-311G (d)<sup>173</sup> used by Lisovski et al. for Ti atoms.
- an oxygen atom 8-411d1<sup>175</sup> basis set optimized for BaTiO<sub>3</sub> crystal.

We then used both PBE0 and B3LYP functionals to calculate the lattice constants and the band gaps of bulk anatase TiO<sub>2</sub> using different combinations of these four basis sets. Full geometry optimization was performed: relaxation of both the cell parameters and the atomic coordinates were allowed. The results obtained (Table 2.2) were then compared with experimental data<sup>42</sup>.

Considering both the band gap value as well as lattice parameters, the most accurate values compared to the experimental ones were obtained when using the B3LYP functional, the all-electron 8-411(d) basis set for O and the Hay-Wadt small core ECP with a 411-311G (d) basis set for Ti atoms. Moreover, this Hay-Wadt functional allowed us to reduce the computational cost of the calculations by taking into account only the valence electrons.

As the intercalation of lithium ions into the *nt*-TiO<sub>2</sub> leads to the reduction of the titanium ions from Ti<sup>4+</sup> to Ti<sup>3+</sup>, the same approach was repeated for the bulk of Ti<sub>2</sub>O<sub>3</sub>, which exhibit the corundum crystal structure. The results are displayed in Table 2.3. Again, the combination of computational parameters highlighted in bold appears to be a suitable compromise.

Table 2.2: Calculated and experimental lattice constants and band gaps of bulk anatase TiO<sub>2</sub>.

Ti Basis set	O Basis set	Functionals	Band gap (eV)	Lattice parameters (Å)	
				<b>a</b>	<b>c</b>
86-51G(3d)	8-411	B3LYP	4.71	3.735	9.974
86-51G(3d)	8-411	PBE0	5.22	3.71	9.898
<b>411-311G(d)</b>	<b>8-411(d)</b>	<b>B3LYP</b>	<b>3.77</b>	<b>3.791</b>	<b>9.768</b>
411-311G(d)	8-411(d)	PBE0	4.41	3.776	9.599
411-311G(d)	8-411	B3LYP	4.09	3.755	8.987
411-311G(d)	8-411	PBE0	4.56	3.731	8.878
<b>Experimental values<sup>42</sup> for anatase TiO<sub>2</sub></b>			<b>3.2</b>	<b>3.785</b>	<b>9.514</b>

Table 2.3: Calculated and experimental lattice constants and band gaps of corundum Ti<sub>2</sub>O<sub>3</sub>.

Ti Basis set	O Basis set	Functionals	Band gap (eV)	Lattice parameters (Å)	
				a	c
86-51G(3d)	8-411	B3LYP	1.095	5.247	13.068
86-51G(3d)	8-411	PBE0	1.529	5.218	12.921
<b>411-311G(d)</b>	<b>8-411(d)</b>	<b>B3LYP</b>	<b>0.863</b>	<b>5.247</b>	<b>13.428</b>
411-311G(d)	8-411(d)	PBE0	1.182	5.203	13.307
411-311G(d)	8-411	B3LYP	0.94	5.254	13.304
411-311G(d)	8-411	PBE0	1.28	5.21	13.18
<b>Experimental values<sup>176</sup> for corundum Ti<sub>2</sub>O<sub>3</sub></b>			<b>0.1</b>	<b>5.157</b>	<b>13.61</b>

An ECP basis set was chosen for titanium atom using only the valence electrons to carry out the calculations. This basis set takes into account only the most external *s*, *p* and *d* atomic orbitals because the core electrons are described by an effective core potential (ECP). The *3s*, *3p*, *4s* and *3d* atomic orbitals are filled with electrons. However, to describe the system more accurately, the *4d* and *5d* orbitals have been considered in this basis set. Previous theoretical studies have shown that only the *3d* orbitals are occupied upon Li intercalation<sup>127</sup>. Consequently, the *4d* and *5d* atomic orbitals are added to improve polarization phenomena. This Hay-Wadt basis set is displayed in Appendix A.

To reduce the computational cost of the calculations, the *5d* orbitals were omitted and the titanium basis set was optimized by adjusting the alpha exponent of the Gaussian function defining the *4d* orbitals. For this, we calculated the total energy of bulk anatase TiO<sub>2</sub> for different alpha values, starting with the initial one of 0.8310327. The alpha coefficient was then gradually decreased until an energy minimum was found. The results obtained are presented as a graph in Figure 2.3.

## Hay-Wadt Ti basis set optimization

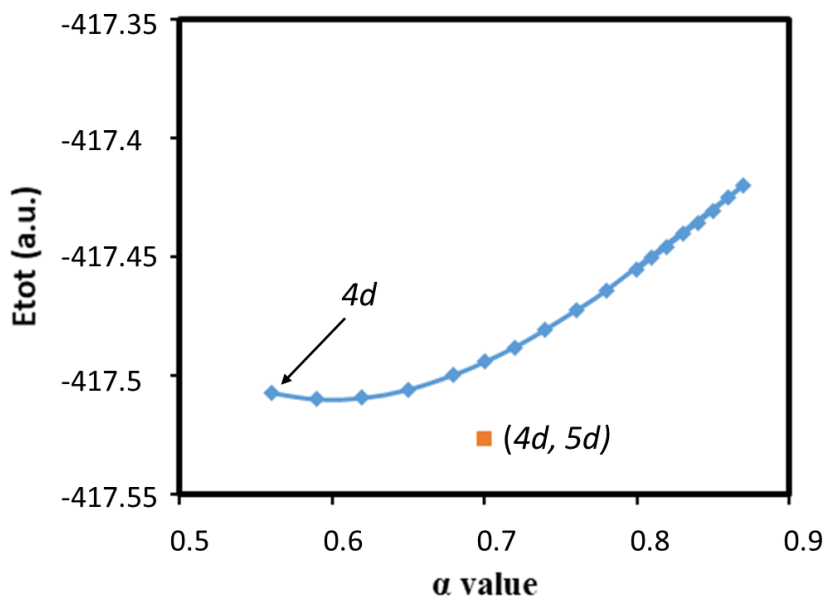


Figure 2.3: Total energies of bulk anatase  $\text{TiO}_2$  calculated with different alpha coefficient. Blue rhombus basis set with only  $4d$  and orange square is  $(4d, 5d)$  basis set.

The total energies, obtained with the modified  $4d$  Gaussian functions and without  $5d$  orbitals, are displayed with blue rhombus. For comparison, the total energy obtained with the original basis set is represented on the graph by an orange square.

Although an energy minimum was reached when the alpha coefficient was around 0.6, the corresponding total energy is still higher than the one obtained when the original basis set is used. This means that our optimization of the basis set leads to a less stable system. As a result, we chose to keep the original basis set (as displayed in Appendix A) to perform all the calculations reported in this thesis.

## 2.2.2 Self-Consistent Field (SCF) parameters optimization

After determining the most suitable basis sets and functional, we optimized the shrinking factor IS by modifying the k-point grid in the reciprocal space as detailed in section 2.1.3.

We calculated the total energy of optimized anatase bulk TiO<sub>2</sub> with different IS integer values to determine the most suitable one. The results are presented as graph in Figure 2.4.

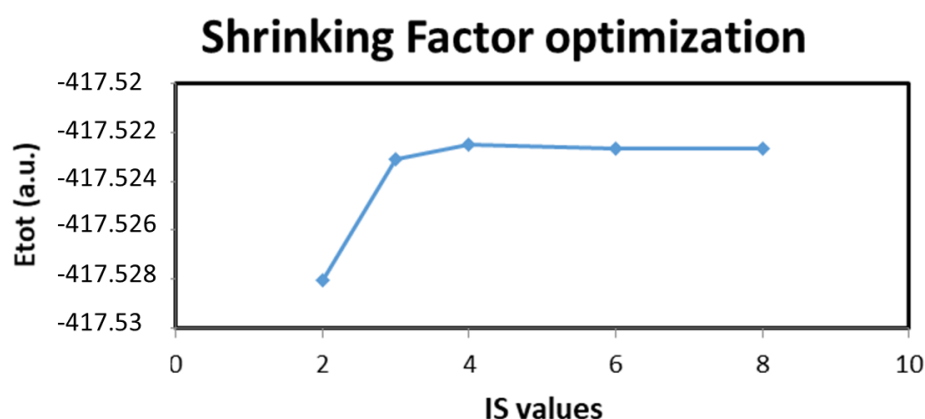


Figure 2.4: Total energies of bulk anatase TiO<sub>2</sub> calculated for different shrinking factor values.

The best compromise between the precision of the results obtained and the computational cost was found for the shrinking factor 6. The same values were chosen by Ferrari et al.<sup>86</sup> to study anatase *nt*-TiO<sub>2</sub>.

The last parameters to optimize are the cutoff threshold parameters for Coulomb and exchange integrals evaluation that are detailed in section 2.1.3. They are defined by five integers in the input that set up the smallest order of magnitude for Coulomb overlap tolerance, Coulomb penetration tolerance, exchange overlap tolerance, exchange pseudo overlap tolerance  $f(g)$  and exchange pseudo overlap tolerance  $p(g)$ .

The results displayed in Figure 2.5 were obtained following the same approach: the total energy of bulk anatase TiO<sub>2</sub> were calculated using different truncation criteria, starting with the default ones 6 6 6 6 12. The values were then gradually increased (7 7 7 14; 8 8 8 8 16; etc.).

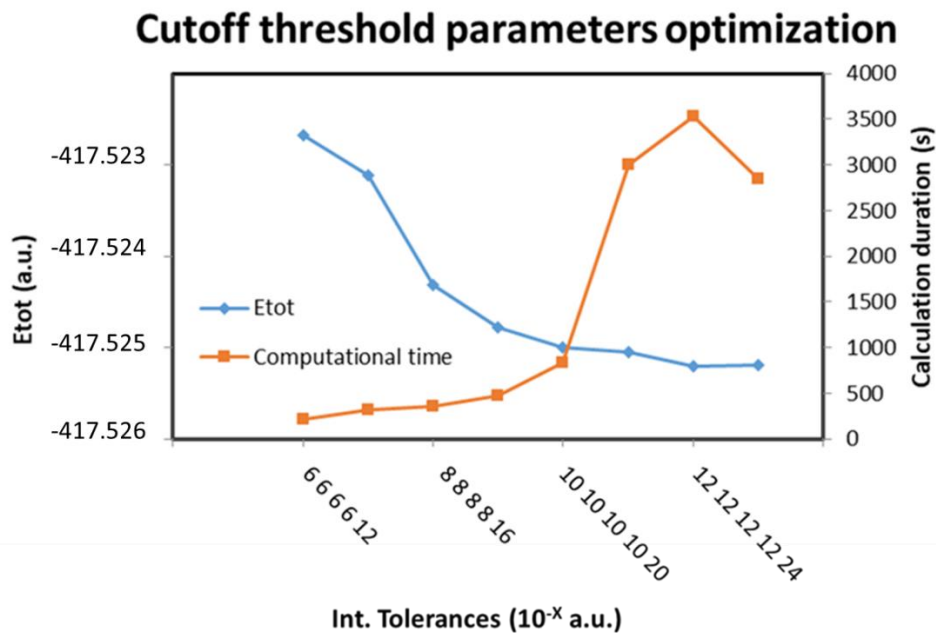


Figure 2.5: Total energies of bulk anatase  $\text{TiO}_2$  and calculation durations obtained with different cutoff threshold parameters. Total energy and computational time are displayed with blue rhombus and orange squares, respectively.

The total energy calculated is displayed with blue rhombus and the corresponding calculation duration is represented by orange squares. A compromise between the accuracy of the calculation and the computational cost was chosen, and all calculations have been done using the 8 8 8 16 setting.

## 2.3 Conclusion

To summarize this part:

- the calculations of the lattice parameters and band gaps, of both bulk anatase  $\text{TiO}_2$  and bulk corundum  $\text{Ti}_2\text{O}_3$ , enabled us to choose the B3LYP functional, a Hay-Wadt small core ECP with a 411-311G (d) basis set for Ti atoms, and an all-electron 8-411(d) basis set for the oxygen atoms.
- the comparison between the bulk anatase  $\text{TiO}_2$  total energies and the calculation durations allowed us to optimize the SCF parameters. Shrinking factors of 6 6 and a '8 8 8 8 16' setting as cutoff threshold for Coulomb and exchange integrals seem to be a good compromise between the accuracy of the calculations and the computational cost.

# Chapter 3

## Properties of the anatase bulk, slab and nanotube

### 3.1 Aims

The aim of this section is to carry out a complete study of the properties exhibited by the anatase bulk, slab and nanotube to understand how the symmetry affects the electronic structure. The results obtained were compared with previous studies reported in the literature to confirm the suitability of the basis sets and functional chosen in this thesis. Moreover, the optimized geometries, electronic structures and total energies calculated for the three systems are used as references in the next chapters when cations ( $\text{Li}^+$  and  $\text{Na}^+$ ) are intercalated into the different structures. The comparison of the slab properties with the bulk ones facilitates the understanding of the surface behavior towards cation intercalation. The slab properties are also compared with the nanotube ones to understand the influence of the “rolling up” on the surface reactivity. Nanotubes described by different roll vector and diameters are also studied in this section to determine the most suitable nanotube model.

### 3.2 The bulk properties

As described in section 1.2.3, anatase is a crystal exhibiting a tetragonal symmetry and belonging to the  $I(4)1/amd$  space group. In the bulk structure, all the atoms are fully coordinated with sixfold Ti atoms ( $\text{Ti}_{6c}$ ) and threefold oxygen atoms ( $\text{O}_{3c}$ ).

The bulk crystal was built using the lattice constants reported in the literature:  $a = 3.792 \text{ \AA}$ ,  $c = 9.497 \text{ \AA}$ <sup>39</sup>. In this crystal, the Ti-O bonds are  $1.94 \text{ \AA}$  long in the  $x$  and  $y$  directions and  $1.97 \text{ \AA}$  long in the  $z$ -direction. The O-Ti-O angles equal  $155^\circ$ . These values confirm that the  $\text{TiO}_6$  octahedra exhibit a low  $D_{2d}$  symmetry (instead of the ideal  $O_h$  one)<sup>41</sup>. This low symmetry will induce a split of the  $t_{2g}$  orbitals: the  $d_{xy}$  orbitals will have a lower energy than the  $d_{xz}$  and  $d_{yz}$  ones because no octahedra edges are shared in the  $ab$  plane.

A full geometry optimization was performed using the B3LYP functional and the basis sets detailed in the previous chapter (lattice parameters are presented in Table 2.2). This optimization leads to an extension of the bonds by  $0.03 \text{ \AA}$  along the  $z$ -direction whereas the extension is very small in the  $xy$  plane. The O-Ti-O angles slightly decrease to  $153.6^\circ$ . The modifications can be explained by the higher energy of the  $d_{xz}$  and  $d_{yz}$  orbitals, compared to the  $d_{xy}$  ones. The structure modifications are displayed in Figure 3.1 where the titanium atoms are in grey and the oxygen ones in red.

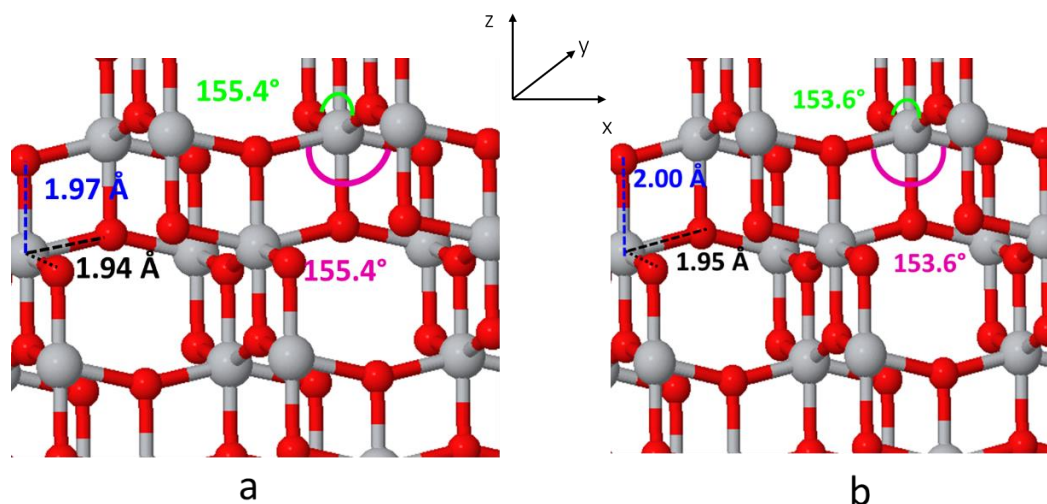


Figure 3.1: Non-optimized (a) and optimized (b) bulk anatase using computational settings from section 2.2. The Ti and O atoms are in grey and red, respectively.

The Mulliken analysis showed a Z charge of 9.685 for the titanium atoms and 9.158 for the oxygen atoms, confirming the partially covalent character of the anatase. Partial charges on the ions can be calculated as the difference between Ti  $12e^-$  and O  $8e^-$ , respectively. Thus, the effective charges are  $+2.32e$  for the titanium atoms and  $-1.16e$  for the oxygen ones. These values are similar to the ones reported in previous theoretical studies<sup>44</sup>.

The Density of States (DOS) of the bulk anatase is displayed in Figure 3.2. It shows a band gap formed by the  $p$  orbitals of the oxygen atoms in the valence band, and the  $d$  orbitals of the titania atoms in the conduction band. Its value is 3.77 eV.

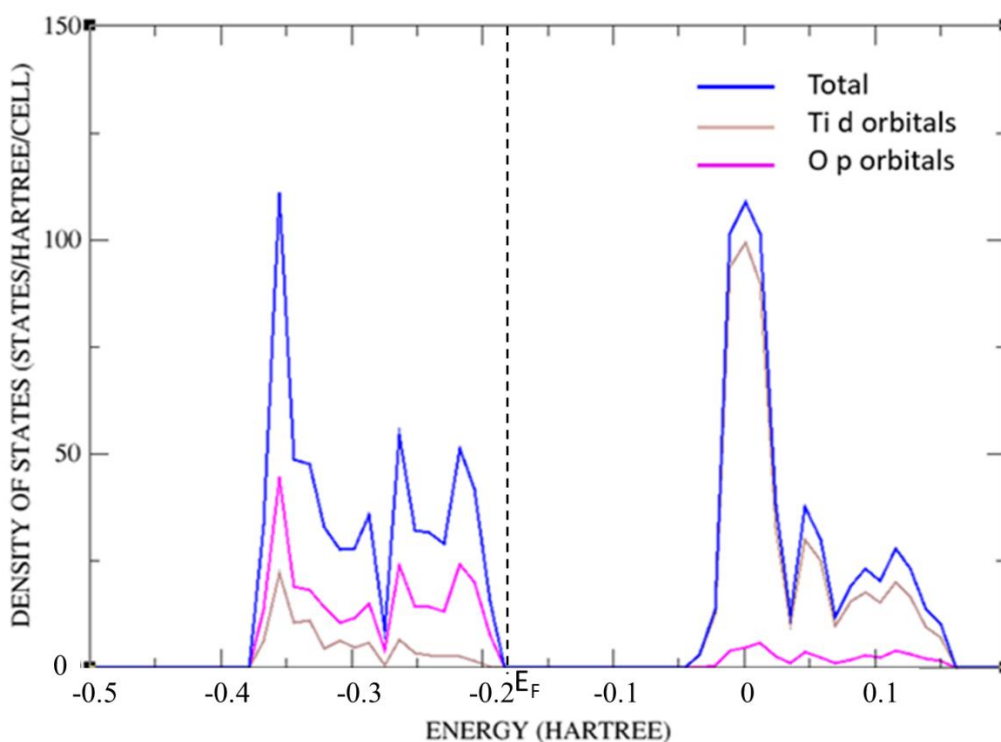


Figure 3.2: DOS of TiO<sub>2</sub> bulk anatase.

### 3.3 Properties of the (001) terminated slab

To study the behavior of the anatase nanotubes as anode, we chose to work with the 3 monolayer (ML) thick nanotube exhibiting a negative strain energy over the whole diameter range that was reported by Ferrari et al<sup>86</sup>. The slab is cut along the (001) surface, as displayed in Figure 3.3 where the Ti and O atoms are displayed in grey and red, respectively.

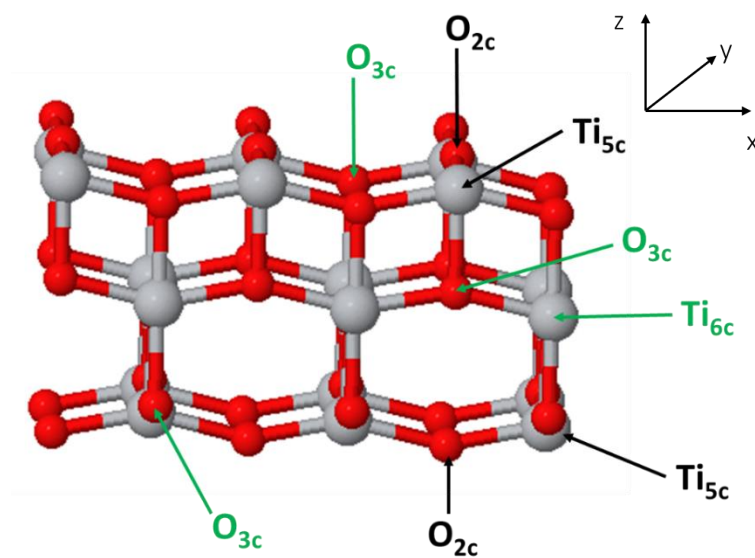


Figure 3.3: Optimized 3ML anatase slab cut along the (001) surface. Green labels indicate full coordinated while black labels undercoordinated atoms.

The coordination of the atoms are detailed in Figure 3.3 where the fully coordinated atoms are indicated with green arrows and the undercoordinated atoms are pointed out with black arrows. The two most external layers are made of undercoordinated fivefold Ti atoms ( $Ti_{5c}$ ) and contain a mix of fully coordinated threefold oxygen atoms ( $O_{3c}$ ) and undercoordinated twofold oxygen atoms ( $O_{2c}$ ), as discussed in section 1.2.4. These two layers are equivalent but the chain of undercoordinated  $O_{2c}$  atoms are running perpendicularly to each other. The internal layer is only made of fully coordinated atoms: sixfold Ti atoms ( $Ti_{6c}$ ) and threefold oxygen atoms ( $O_{3c}$ ).

When a full geometry optimization is performed (both atomic coordinates and cell parameters are allowed to relax), the slab is stretched in the  $z$ -direction and shrunk in the  $x$  and  $y$  directions. The structure modifications are detailed in Figure 3.4 where the non-optimized slab is shown in Figure 3.4a while the modifications in bond lengths and angles are displayed in Figures 3.4b and 3.4c. It is found that the Ti-O bonds parallel to the  $z$ -direction are elongated from 1.97 Å to 2.05 Å. The elongation of the outermost layer of the (001) anatase surface was already mentioned in the study by Ortega et al<sup>177</sup> and was explained by the electronic repulsion of the surface atoms. However, the elongation observed in the 3 ML slab is 0.07 Å less than the one reported in the literature<sup>177</sup> where a single anatase surface was studied. One contributing factor to this difference is explained by the reduction of the dipole moment in the slab, where the presence of a symmetrical mirror plane in the center of the slab removes the dipole moment over the slab. Another reason can be associated with differences in the computational setup.

In the  $xy$  plane, the Ti-O<sub>2c</sub> bonds are slightly shorter (0.02 Å) than the Ti-O<sub>3c</sub> bonds. The O<sub>2c</sub> anions are moving outward from the surface, leading to Ti-O<sub>2c</sub>-Ti chains with an optimized angle of 140°. The shortening of the bonds between undercoordinated ions and the displacement of the anions outward from the surface are regularly mentioned<sup>178</sup> as an usual reconstruction stabilizing the metal oxide surface.

The symmetry breakage observed in the  $xy$  plane of the slab is less pronounced than the ones reported for single anatase surfaces<sup>179</sup> where the O<sub>2c</sub> atoms move closer to one of the neighboring Ti<sub>5c</sub> chains. In the single anatase surface, the Ti-O<sub>2c</sub> bonds exhibit strongly inequivalent bond lengths of 1.77 Å and 2.18 Å, as it was displayed in Figure 1.10. The absence of this kind of reconstruction in the slab can be explained by the two O<sub>2c</sub>-Ti-O<sub>2c</sub> chains that are running perpendicularly to each other at each side of the slab and limit the surface reconstruction.

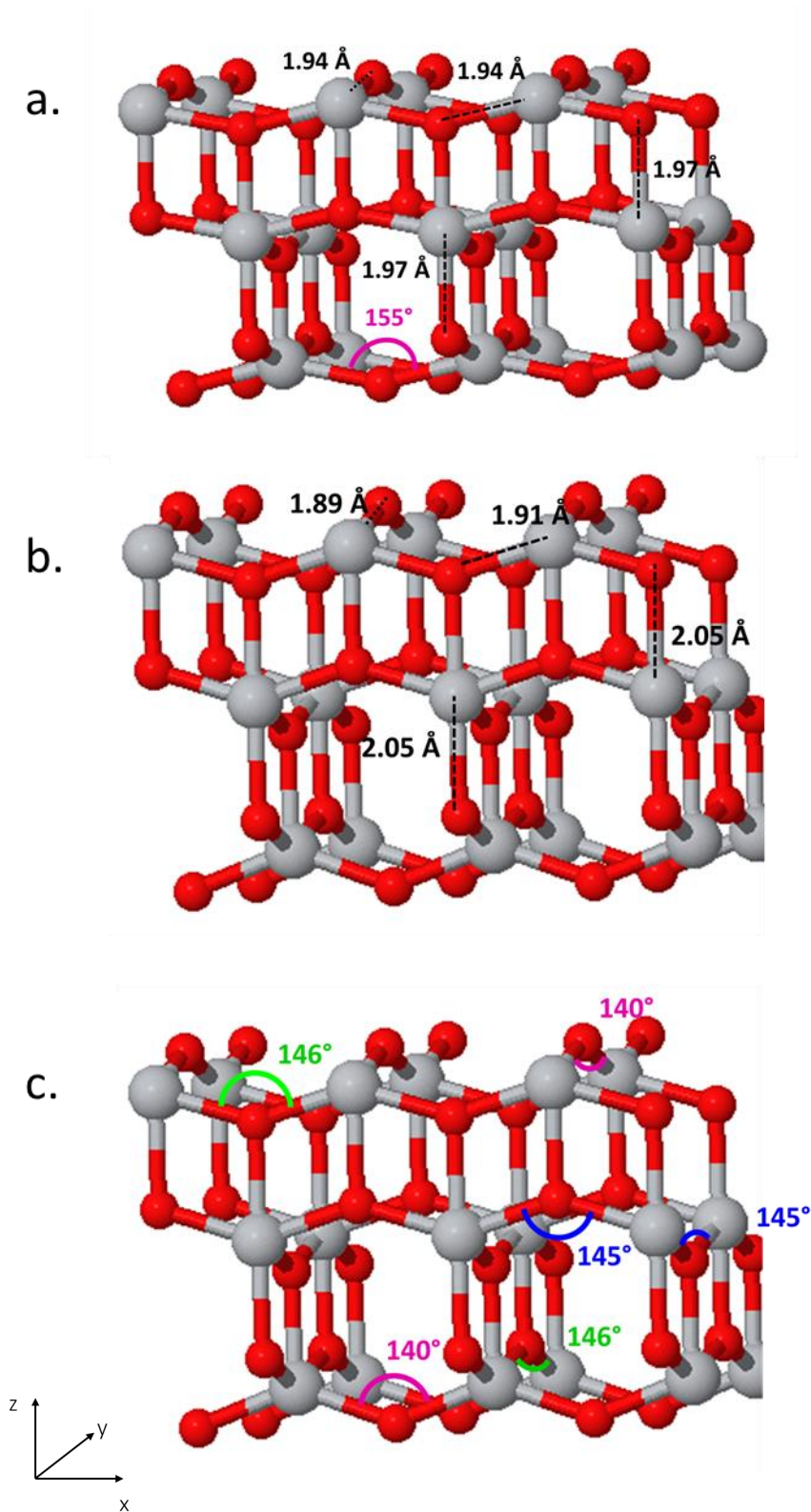


Figure 3.4: Geometry optimization of the (001) 3ML slab where the Ti atoms are in grey and the O ones in red. The non-optimized slab is displayed in figure a. The changes in bond lengths and the angle modifications are detailed in figures b and c, respectively.

The Mulliken analysis is displayed in Figure 3.5 where the charges are indicated in green for the Ti atoms and in black for oxygen ones. In anatase bulk, the charges of the ions were  $+2.32e$  for the titanium and  $-1.16e$  for the oxygen. Thus, a slight decrease of the oxygen charges, as well as a small increase of the Ti charges, are observed overall, indicating a more covalent character in the slab than in the bulk. This result confirms the limited electronic repulsion of the surface atoms and explains the restricted extension of the slab along the  $z$ -direction. The decrease of the partial charge observed for the undercoordinated  $O_{2c}$  ions agrees with the shorter length exhibited by the Ti- $O_{2c}$  bonds.

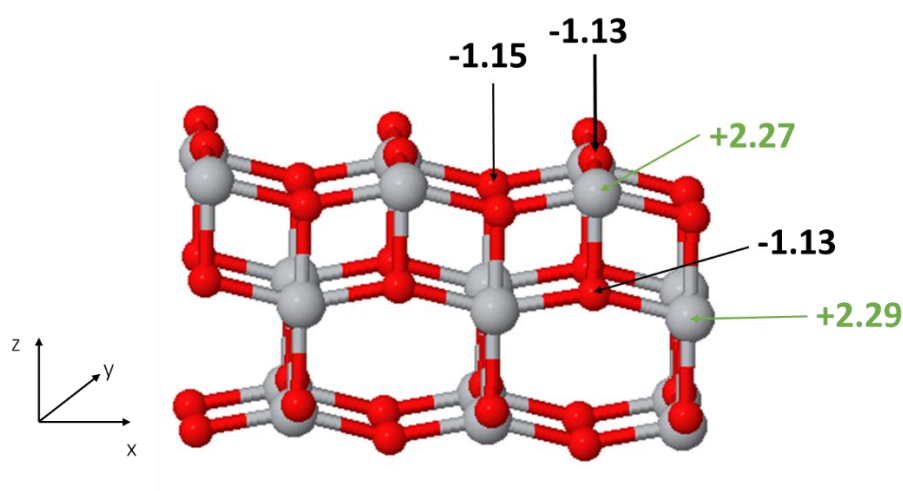


Figure 3.5: Mulliken charges of the (001) 3ML slab. Green labels represent Ti and black labels O atoms, respectively.

The DOS of the anatase slab is displayed in Figure 3.6 where the blue plot refers to the total DOS of the slab, while the black, red and green colors are related to the  $s$ ,  $p$  and  $d$  orbital contributions of the selected atom, respectively. The selected atoms are highlighted in green.

The DOS for the slab is not significantly different from the bulk one. However, it is noticed that the undercoordinated  $O_{2c}$  atoms are located higher in the valence band than the fully coordinated ones. As a result, they contribute to upper part of the valence band and are more reactive. These results are in agreement with a previous study carried out by Calatayud et al.<sup>56</sup>.

The band gap of the slab equals 3.97 eV and is 0.2 eV larger than in the bulk. The valence and the conduction bands are also shifted to lower energies compared to the values reported for the bulk (Figure 3.2). Such results were already reported in the literature<sup>48,180</sup> and are explained by the presence of undercoordinated  $O_{2c}$  and  $Ti_{5c}$  ions. Before the relaxation of the surface, dangling bonds between the  $O_{2c}$  and the  $Ti_{5c}$  ions will be formed, generating surface states located near to the valence band top and close to the conduction band bottom. The relaxation will allow electron transfers that will partially saturate the dangling bonds and remove the surface state from the band gap. As a result, the surface electronic structure will exhibit a larger band gap with a shift of both the valence and conduction bands.

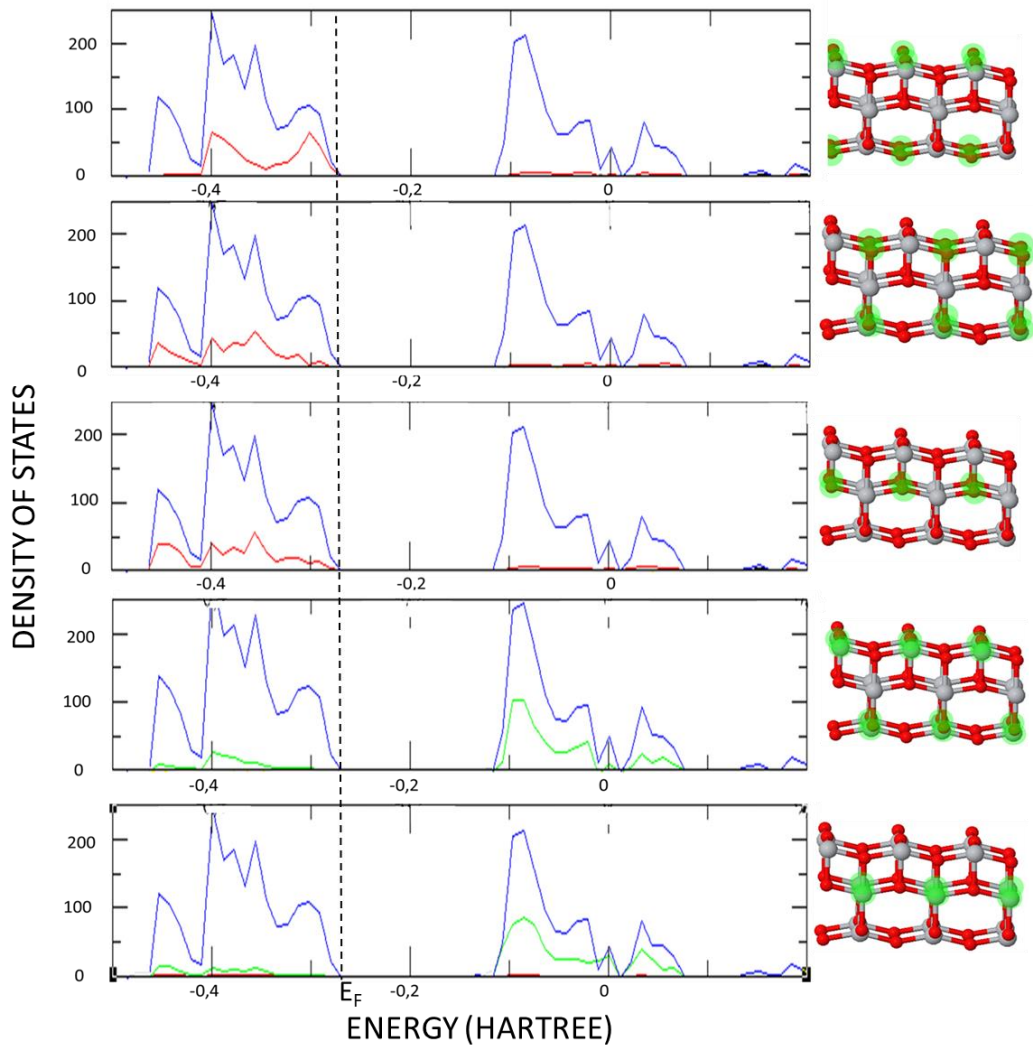


Figure 3.6: DOS of the anatase (001) 3ML slab where the Ti atoms are in grey and the O ones in red. The blue plot stands for the total DOS of the slab, while the red and green colors are related to the  $p$  and  $d$  orbital contributions of the selected atom (highlighted in green), respectively.

The surface energy can be calculated according to the Equation 1.2. As the lateral size of the slab was not constrained in this thesis, its formation is based on a fully relaxed structure when considering  $E_{\text{tot}}(\text{slab})$ . This equation was already used by Vittadini et al.<sup>178</sup> to characterize different slabs of  $\text{TiO}_2$ . The slab used to build the  $nt\text{-TiO}_2$  in this thesis exhibits a formation energy of  $0.61 \text{ eV/TiO}_2$ . This positive value indicates that the slab is less stable than the bulk, because of the tensile stress and the electronic repulsion present on the surfaces, as well as the presence of undercoordinated atoms.

### 3.4 The nanotubes construction

The three layer thick [001] anatase nanotubes were reported by Ferrari et al.<sup>86</sup> to exhibit a negative strain energy over the whole diameter range, indicating a higher stability of the nanotube compared to the 3 ML slab. The nanotubes can be built by “rolling up” the slab along the  $(n_1, 0)$  or the  $(0, n_2)$  direction, as detailed in Figure 3.7 below.

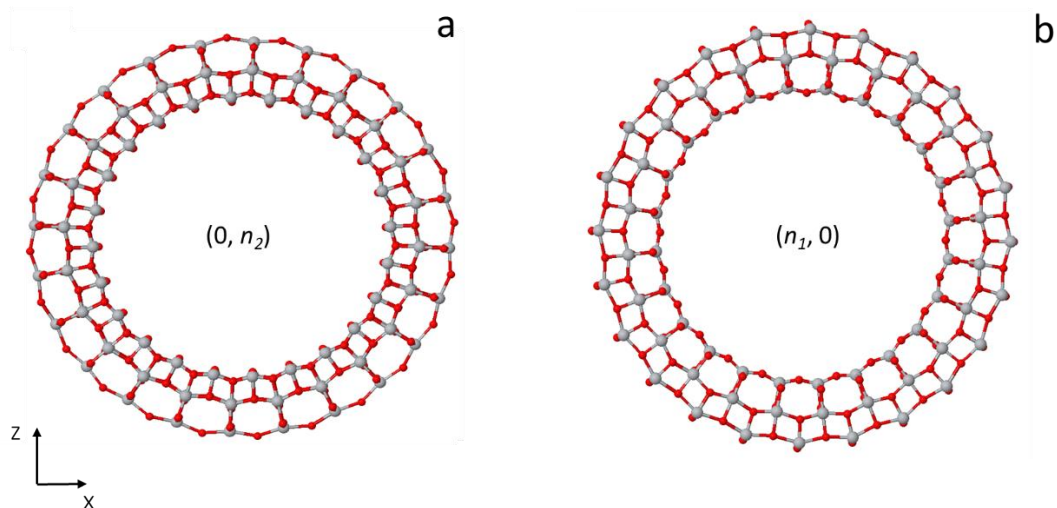


Figure 3.7: 3ML  $nt\text{-TiO}_2$  rolled up along the  $(0, n_2)$  direction (a) or the  $(n_1, 0)$  direction (b). The grey and red spheres represent the Ti and O atoms, respectively.

The *nt*-TiO<sub>2</sub> rolled up along the (0, *n*<sub>2</sub>) direction showed a particularly unstable structure (Figure 3.7a) with a lot of bonds breaking during the geometry optimization resulting in a positive strain energy. This result is in agreement with the literature<sup>91</sup> and can be explained by the important stress applied on the bonds during the “rolling up”: the ones located inside the nanotubes undergo a significant compression whereas the ones situated on the external wall are widely stretched.

When the *nt*-TiO<sub>2</sub> is rolled along the (*n*<sub>1</sub>, 0) direction, the bond lengths are slightly modified, thus the stress applied on the structure is less damaging. This “rolling-up” looks more “natural” for the anatase structure and the calculations converge easily. As a result, only the nanotubes rolled up along the (*n*<sub>1</sub>, 0) direction were considered in this thesis.

The next step was to calculate and compare the strain energy (*E*<sub>s</sub>) of *nt*-TiO<sub>2</sub> considering different diameters of the nanotubes in order to determine the most stable one, and then the best compromise between the computational time and the size of the nanotubes (the bigger ones being closer to the experimental system discussed in section 1.2.2). Thus, *nt*-TiO<sub>2</sub> with internal diameters in the range of 8 to 66 Å were optimized. The smallest and the largest nanotubes are displayed in Figure 3.8 below.

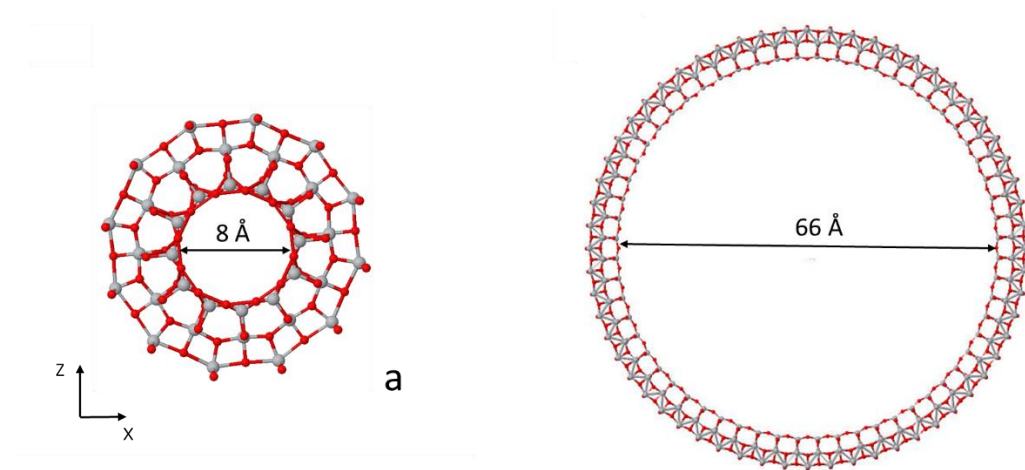


Figure 3.8: 3ML *nt*-TiO<sub>2</sub> rolled up along the (*n*<sub>1</sub>,0) direction having an internal diameter of 8 Å (a) and 66 Å (b). The O and Ti atoms are in red and grey, respectively.

The strain energies of the nanotubes were then calculated using Equation 1.3 (described in section 1.2.5). The results are shown in Figure 3.9 and confirm that the strain energy is negative over the whole diameter range.

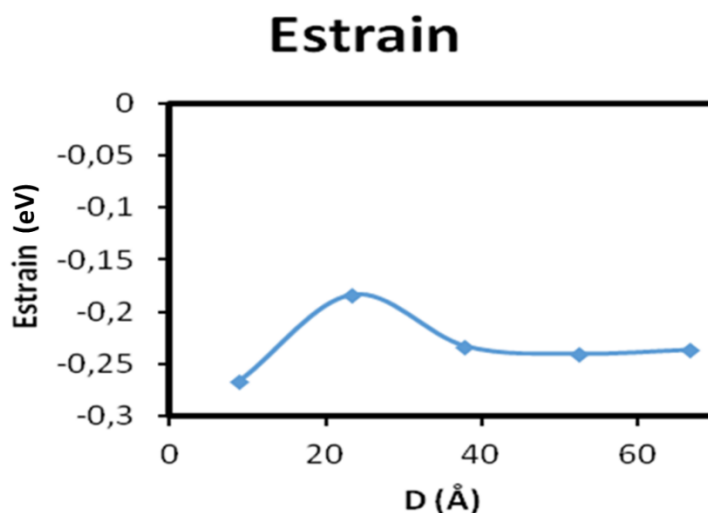


Figure 3.9: Strain energy of anatase 3ML *nt*-TiO<sub>2</sub> versus the diameter.

The most negative strain energy is observed for the smallest diameter (8.9 Å). However, this *nt*-TiO<sub>2</sub> underwent an important reconstruction during the geometry optimization as shown in Figure 3.10. The final structure is too different from the anatase crystal and can not be considered as a suitable model for the *nt*-TiO<sub>2</sub> electrode. This is explained by the symmetry restrictions imposed during geometry optimization. The strain energies calculated are similar to the ones reported by Ferrari et al.<sup>86</sup> and Lisovski et al.<sup>91</sup>.

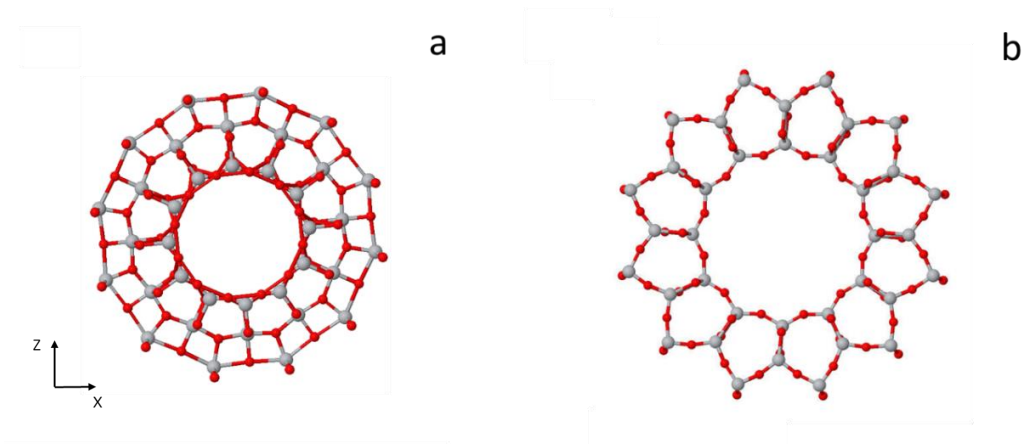


Figure 3.10: 3ML *nt*-TiO<sub>2</sub> having an internal diameter of 8 Å before (a) and after (b) geometry optimization. The red and grey spheres stand for the O and Ti atoms, respectively.

The *nt*-TiO<sub>2</sub> having a diameter of 23 Å conserved its anatase structure during geometry optimization. The higher strain energy shown for this diameter (Figure 3.9) can be explained by the important modification of both the bond length and the angles between the bonds during the “rolling up” process around such a small diameter.

The nanotubes having diameters between 38 Å and 66 Å exhibit almost the same strain energy and show similar rearrangements during their optimization. For computational time saving, the 38 Å diameter *nt*-TiO<sub>2</sub> was chosen in this thesis. The structure modifications occurring during geometry optimization are displayed in Figure 3.11 and will be analyzed in detail in the next section.

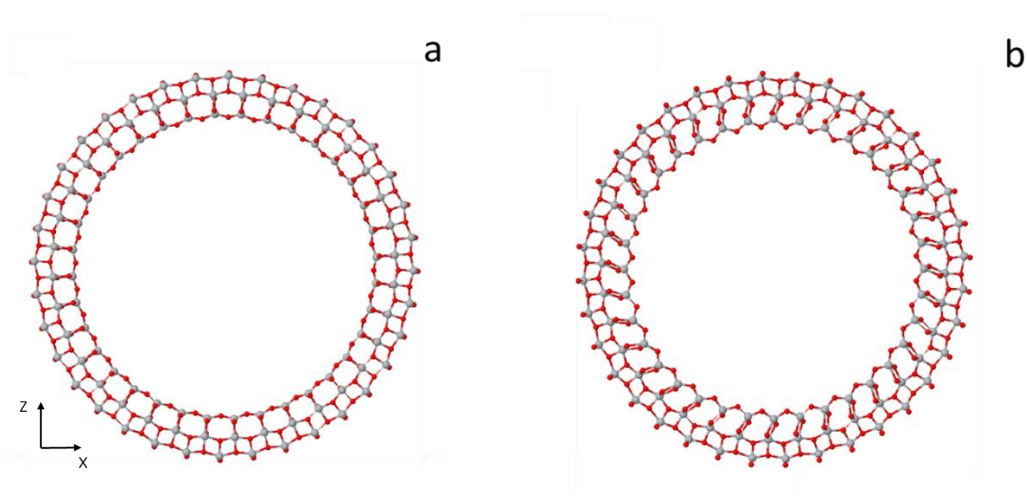


Figure 3.11: 38 Å diameter 3ML nanotube before (a) and after (b) geometry optimization. The O and Ti atoms are in red and grey, respectively.

### 3.5 Properties of the 38 Å diameter nanotube

The bond lengths and the angles of the Ti-O-Ti chains of the 38 Å diameter optimized nanotube are displayed in the Figure 3.12. The angles are detailed in Figures 3.12a and b, while the bond lengths perpendicular to the nanotube axis are indicated in Figures 3.12c and d. The bond lengths parallel to the nanotube axis are displayed in Figure 3.12e.

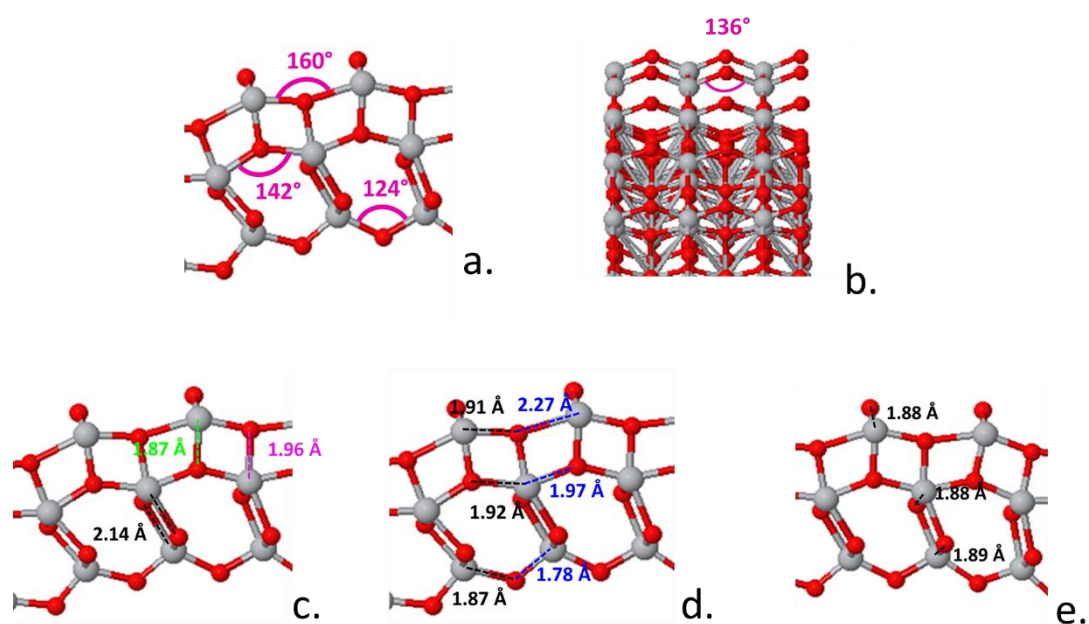


Figure 3.12: Measures of the Ti-O-Ti chain angles and Ti-O bond lengths of the optimized *nt*-TiO<sub>2</sub>. The grey and red spheres represent the Ti and O atoms, respectively. Figures a and b detailed the angles while the bond lengths are shown in figures c, d and e.

When the geometry of the nanotube is optimized, several geometrical reconstructions occur, including a breaking of the nanotube symmetry. Several Ti-O bonds that had the same lengths before the geometry optimization are no longer equivalent, resulting in a distorted structure. The reconstruction seems to be driven by the displacement of the titania inward and the oxygens outward displacements of the surface walls. These particular motions of the cations and anions represent the expected displacements for metal oxide surface stabilization<sup>178</sup>.

The undercoordinated  $O_{2c}-Ti_{5c}-O_{2c}$  chains located on each outermost layer are running perpendicularly to each other, thus only the internal one will be modified by the rolling-up as displayed in Figure 3.13 where the undercoordinated oxygen atoms are highlighted in green.

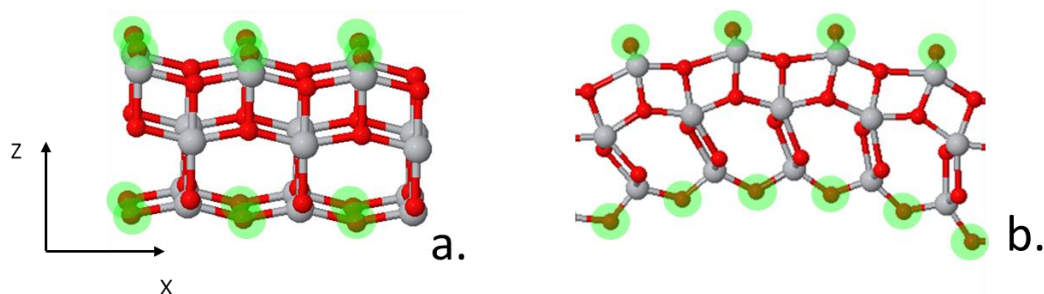


Figure 3.13: Localization of the undercoordinated oxygen atoms (highlighted in green) in the anatase slab (a) and nanotube (b). The O atoms are in red and the Ti ones in grey.

The  $O_{2c}-Ti_{5c}-O_{2c}$  chains that are parallel to y axis in the slab, will be parallel to the nanotube axis, and will not be affected by the rolling-up stress. Thus, the  $Ti-O_{2c}$  bonds located on the external wall of the nanotube will not be modified whereas the  $Ti-O_{3c}$  bonds located on the same wall will be widened. The situation is different for the internal wall where the  $Ti-O_{2c}$  bonds are shortened whereas the  $Ti-O_{3c}$  ones remain unchanged.

As expected, the internal wall is more affected than the external one by the reconstruction, as the stress introduced by the “rolling up” of the surface slab in this layer is higher than in the outermost wall. As a result, the ionic displacements are more pronounced, leading to an important decrease the  $O_{2c}-Ti_{5c}-O_{2c}$  angle from  $155^\circ$  in the slab to  $124^\circ$  in the optimized *nt*- $TiO_2$ , generating a tensile stress of the inner wall surface. In addition, the shortening of the undercoordinated  $Ti_{5c}-O_{2c}$  bonds supports the stabilization of the structure. Consequently, the tensile stress caused by the smaller angles is probably compensated by the translations of the ions, considering the shorter undercoordinated  $Ti_{5c}-O_{2c}$  bonds.

The ionic displacements observed in the optimized *nt*-TiO<sub>2</sub>, were also reported as a frustrated attempt to form a lepidocrocite structure<sup>50</sup>. Such a reconstruction was already observed for the two monolayer thick anatase (001) slab<sup>87</sup>. This sheet will spontaneously rearrange into a stable lepidocrocite structure where the Ti ions are fully coordinated and the bond angles around the oxygen atoms smaller.

As a conclusion, the stress caused by the “rolling up” is absorbed by breaking the symmetry and can be interpreted as a frustrated attempt to form a lepidocrocite structure. This reorganization leads to a stable structure with shorter undercoordinated bonds. Moreover, the displacements of the cations inward from the surface and the anions outward from it reduce the electronic repulsion between surface ions. Thus, the *nt*-TiO<sub>2</sub> are more stable than the corresponding slabs and exhibit a negative strain energy. As expected, only slight modifications of the angles and bond lengths occur along the nanotube axis where no stress associated with the “rolling up” of the slab is applied. This structure is similar to the work presented by Ferrari et al.<sup>86</sup> despite using a slightly different functional.

The Mulliken charges of the titania and oxygen ions in bulk, slab and nanotube structures are compared in Table 3.1 below. As the geometry optimization of the *nt*-TiO<sub>2</sub> broke the symmetry of the unit cell, the ions have been labelled as displayed in Figure 3.14.

Table 3.1: Mulliken charges of the Ti and O ions in optimized anatase bulk, slab and *nt*-TiO<sub>2</sub> structures.

Ion	Charges in bulk	Charges in slab	Charges in <i>nt</i> -TiO <sub>2</sub>
O1	-1.158	-1.134	-1.114
Ti2	2.315	2.269	2.270
O3	-1.158	-1.146	-1.165
O4	-1.158	-1.131	-1.131
Ti5	2.315	2.285	2.298
O6	-1.158	-1.131	-1.178
O7	-1.158	-1.146	-1.199
Ti8	2.315	2.269	2.245
O9	-1.158	-1.134	-1.027

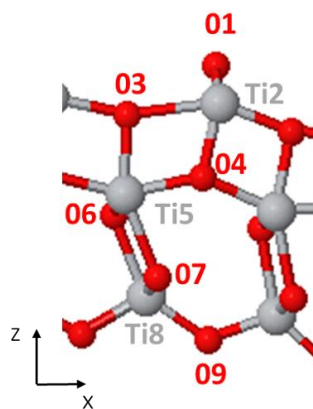


Figure 3.14: Labelling of the Ti and O ions constituting the optimized unit cell of the *nt*-TiO<sub>2</sub>.

The changes of the charge distribution in the nanotubes are more pronounced in the internal wall where the undercoordinated titania and oxygen ions (labelled *Ti8* and *O9*) exhibit a more covalent interaction compared to the outermost wall. This can be explained by the shorter undercoordinated Ti-O bonds. On the other hand, the fully coordinated oxygen ions *O7* and *O6* that are bonded to the *Ti8* cation show higher Mulliken charges than in the slab, possibly indicating a more ionic character. It would appear that the *Ti8* cation is sharing more electrons with the undercoordinated oxygen than with the fully coordinated ones, resulting in an electron redistribution leading to a more delocalized electronic structure at the surface than in the central layer of the tube wall.

In the external wall, the modifications are smaller than in the innermost wall and any electron redistribution concern only the oxygen ions *O1* and *O3*. The charge of the undercoordinated *Ti2* and fully coordinated *O4* ions are not modified. The fully coordinated oxygen *O3* shows a more ionic character, probably caused by the increase of the Ti-O bond length, whereas the undercoordinated oxygen *O1* is slightly more covalent. On the other hand, the fully coordinated *Ti5* ion located in the middle of the structure exhibits a more ionic character, probably induced by the ionic behavior of the bonded *O7* and *O6* ions.

As a conclusion, the Mulliken analysis shows that the undercoordinated ions exhibit a more covalent character, as a contrary of the fully coordinated ones that are more ionic. As a result, the nanotube exhibits a more delocalized electronic structure at the surface than in the central layer. Moreover, the undercoordinated ions located in the internal wall exhibit a more covalent interaction than the ones located in the outermost wall. These changes in electronic structure are similar to the ones reported by Ferrari et al.<sup>48</sup> and Piskunov et al.<sup>181</sup>, and are emphasized by the modifications of the bond lengths.

The DOS of the *nt*-TiO<sub>2</sub> was computed for each of the atoms constituting the irreducible unit cell of the nanotube (all the other atoms are related by symmetry) and is displayed in Figure 3.15. The blue plot represents the total DOS of the *nt*-TiO<sub>2</sub> while the red and green colors are associated with the *p* and *d* orbital of the selected atom, respectively. The *s* orbitals are plotted in black but do not appear on the Figure 3.15 as they are not present in the conduction or the valence band.

The states close to the top of the valence band are almost exclusively represented by the *2p* states of the O1 and the O3 atoms. These two atoms are located on the external wall. These results are in agreement with previous theoretical studies<sup>48,95</sup> and point out the higher reactivity of the external wall compared to the internal one. Thus, the electrochemical reaction should more likely occur on the external wall.

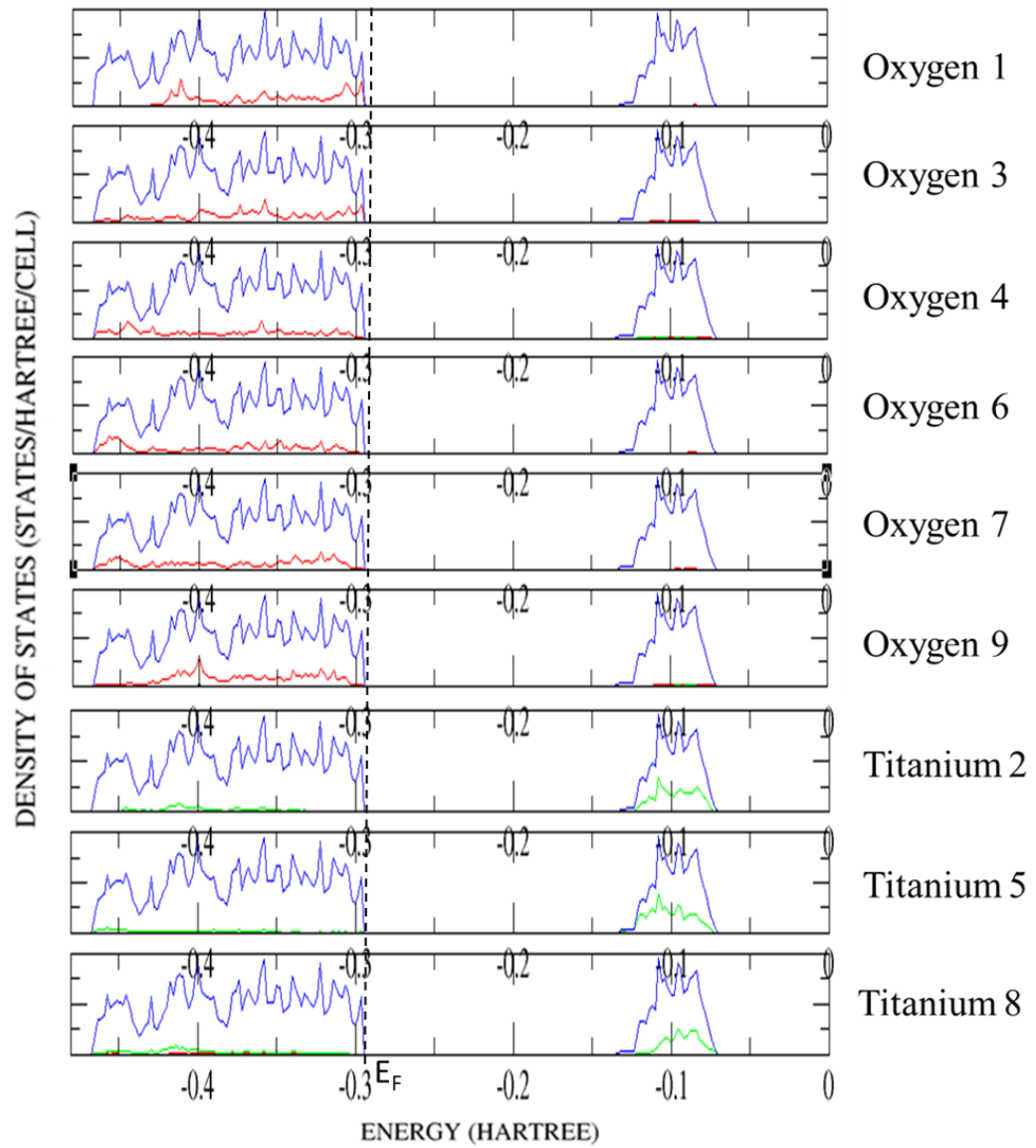


Figure 3.15: DOS of the optimized *nt*-TiO<sub>2</sub>. Atomic labels are presented in Figure 3.14. The blue plot stands for the total DOS of the nanotube while the red and green plots represent the contributions of the *p* and *d* orbitals, respectively.

The band gap of the nanotube is 4.44 eV. This value is higher than the values of the bulk and the corresponding slab. It can be explained by the structural changes in the walls of nanotube caused by the strain. Lisovski et al.<sup>77</sup> and Ferrari et al.<sup>48</sup> both showed that the smaller the nanotube, the larger is the band gap.

## 3.6 Conclusion

- The anatase bulk is elongated along the  $z$ -direction during geometry optimization. This structure change can be explained by the splitting of the titania  $d$  orbitals, resulting in the  $d_{xy}$  orbitals having a lower energy than the  $d_{xz}$  and  $d_{yz}$  ones.
- The band gap of the anatase bulk is 3.77 eV large and is formed by the  $p$  orbitals of the oxygen atoms in the valence band and the empty  $d$  orbitals of the titania atoms in the conduction band.
- The surface reconstruction observed in the slab is smaller than the one reported for a single anatase surface.
- The slab exhibits a slightly more covalent character than the bulk. Its band gap is 0.2 eV higher than the bulk one, and its valence and conduction bands are located 0.7 eV lower in energy compared to the ones reported for the bulk. The undercoordinated  $O_{2c}$  atoms of the slab contribute to the upper part of its valence band while the titania empty  $d$  orbitals are located in the conduction band.
- The nanotube chosen in this thesis is rolled up along the  $(n_1, 0)$  direction and is 38 Å diameter.
- The geometry optimization of the nanotube leads to a distorted structure that can be interpreted as a frustrated attempt to form a lepidocrocite structure.
- The undercoordinated atoms of the nanotube exhibit a more covalent interaction than the fully coordinated ones. Thus, the electronic structure is more delocalized at the surface than in the central layer of the nanotube wall. Moreover, the undercoordinated atoms located on the internal wall are slightly more covalent than the ones located on the external wall.
- The band gap of the nanotube is 4.44 eV. The value is higher than both the bulk (3.77 eV) and the slab (3.97 eV). The states close to the top of the valence band are almost exclusively represented by the oxygen atoms located on the external wall.
- The results are comparable to the study carried out by Ferrari et al. using the PBE0 functional.

# Chapter 4

## Lithium intercalation into anatase

### 4.1 Aims

The main goal of this section is to carry out a comparative study of the lithium intercalation into the anatase bulk, slab and nanotube. The calculations performed on the  $\text{Li}_{0.5}\text{TiO}_2$  bulk anatase is partly used to choose the most suitable Li basis set to study the lithium intercalation process into anatase. Moreover, *ab initio* calculations performed on big systems like nanotubes require the use of geometry constraints. Thus, the comparison of the results obtained for the  $\text{Li}_{0.5}\text{TiO}_2$  bulk using these constraints with previous studies reported in the literature is useful when judging the results introducing such an approximation to be aware of its influences.

Anatase surfaces were reported to exhibit higher lithium capacities than the corresponding bulk<sup>34,103</sup>. Thus, lithium is also inserted with a concentration of  $x = 1$  into both the bulk and slab anatase in order to make a comparable study between the bulk and slab using the results obtained to better understand the role played by surface reconstruction towards lithium intercalation. Moreover, the slab possesses two symmetric outermost surfaces which can be used to study the influence of the polarization by inserting lithium ions into only one or the two outermost surfaces.

The calculations on the lithium insertion into the slab and the nanotube are also used to estimate and to isolate the influence of the strain energy. The different intercalation sites present in the nanotube are studied separately as several experimental studies<sup>36,37</sup> highlighted the major role of the external wall with respect to lithium intercalation. Moreover, the high surface area of the nanotubes results in good contact between the electrolyte and the external wall reported to lead to a higher capacitive behaviour<sup>36</sup> than observed in the bulk. Thus, lithium will also be added above the outermost surfaces of the slab, as well as above the internal and external walls of the *nt*- $\text{TiO}_2$  to confirm an eventual lithium metal plating.

## 4.2 Choice of Lithium basis set

The first step consisted of finding a suitable lithium basis set to study its intercalation into the different systems of  $\text{TiO}_2$ . The most favourable lithium intercalation sites can be determined by comparing the different lithium intercalation energies calculated using the Equation 1.4 (defined in section 1.2.6.1). As a result, the lithium basis set must be able to define both the energy of the lithium in a metallic bulk as well as an ionic species intercalated inside the  $\text{TiO}_2$  structure. However, while most of the basis sets are able to determine the properties of the lithium as an intercalated ion (derived as  $\text{Li}^+$ ), they fail to describe metallic bulk but lead to basis set linear dependencies. When the calculations are performed using this kind of basis set, the bulk lithium energy ( $E_{\text{Li}}$ ) mentioned in Equation 1.4 needs to be replaced by a single point calculation performed on one lithium atom. The comparison of the lithium intercalation energies will still allow to correctly determine the most favourable intercalation sites. Nonetheless, the intercalation voltage associated may not be correct.

Four lithium basis set<sup>182–185</sup> were tested in this thesis. They were firstly used to calculate the total energy of a lithium metallic bulk (when it was not possible because of the basis set linear dependencies mentioned above, a single point calculation was performed instead). The basis sets were then used to study the lithium intercalation into a  $\text{TiO}_2$  bulk. The different lithium intercalation energies and intercalation voltages were compared to determine the most suitable basis set. All the calculations were performed using the same B3LYP functional, shrink factor and cut-off threshold, as for the *nt*- $\text{TiO}_2$ .

The metallic lithium exhibits a body centred cubic structure at room temperature<sup>186</sup>. It belongs to the space group ( $Im\bar{3}m$ ) and its lattice parameter equals 3.48 Å. The lithium bulk lattice is displayed in Figure 4.1.

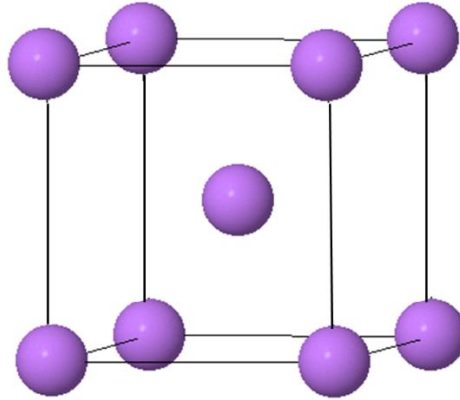


Figure 4.1: Crystallographic structure of lithium bulk space group  $Im\bar{3}m$ .

A full geometry optimization of the lithium bulk was performed using the different basis sets. The energies obtained are shown in Table 4.1. The only basis set that did not allow a bulk energy calculation was the Li\_6\_11G<sup>182</sup> for which the calculation was based on a single point. The lowest bulk energy is obtained with the Li\_POB\_TZVP<sup>184</sup> basis set.

A TiO<sub>2</sub> bulk supercell (1 x 1 x 2) was then built to compare the lithium intercalation energy. The lithium ions were intercalated every second octahedral intercalation site to respect the experimental concentration<sup>99</sup> of 0.5 Li ion per TiO<sub>2</sub> unit. The non-optimized Li<sub>0.5</sub>TiO<sub>2</sub> supercell is shown in Figure 4.2.

Table 4.1: Total bulk energies or single point energy obtained with the different Li basis sets.

Basis set	Lithium bulk energy (eV)	Single point energy (eV)
Li_6_11G <sup>182</sup>		-198.002
Li_6_11G <sup>183</sup>	-204.288	
Li_POB_TZVP <sup>184</sup>	-204.655	
Li_3s2p <sup>185</sup>	-204.691	

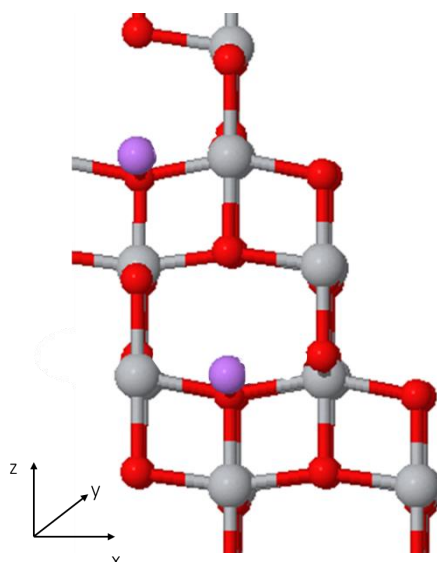


Figure 4.2:  $\text{Li}_{0.5}\text{TiO}_2$  supercell before geometry optimization. The grey, red and purple colours represent the Ti, O and Li ions, respectively.

The structure was then fully optimized and the total energies of both the lithiated and non-lithiated  $\text{TiO}_2$  bulks were calculated. The values obtained, combined with the lithium bulk energies reported in Table 4.1, were used to calculate the lithium intercalation energies for each basis set.

The lithium intercalation energies and intercalation voltages (calculated using Equations 1.4 and 1.6<sup>114</sup>) obtained with the different basis sets are reported in Table 4.2.

Table 4.2: Lithium intercalation energies and voltages calculated with different basis sets.

\* Note  $\text{Li}_6_{11\text{G}}^{182}$  is based on single point calculation.

Basis set	Lithium intercalation energy (kJ/mol)	Lithium intercalation voltage (V)
$\text{Li}_6_{11\text{G}}^{182}$ *	-799.8989461	33.16
$\text{Li}_6_{11\text{G}}^{183}$	-199.6884317	4.14
$\text{Li}_{\text{POB\_TZVP}}^{184}$	-158.9592606	3.29
$\text{Li}_{3\text{s}2\text{p}}^{185}$	-162.5367926	3.37

The experimental intercalation potential of lithium into titanium dioxide equals 1.75 V<sup>187</sup>. One of the closest value was obtained with the Li\_3s2p basis set. Moreover, this basis set is computationally efficient, an important criteria for modelling of big system such as *nt*-TiO<sub>2</sub>, and was reported by Doll et al<sup>185</sup>. to be robust. As a result, this Li\_3s2p basis set was chosen to study the Li intercalation into anatase *nt*-TiO<sub>2</sub> in this thesis.

### 4.3 Lithium intercalation into Li<sub>0.5</sub>TiO<sub>2</sub> anatase bulk

In order to have a better understanding of the *nt*-TiO<sub>2</sub> as an anode in lithium microbatteries, a detailed study of the Li intercalation into bulk anatase was first carried out. There were two goals following this approach. The first one was to compare our model with the previous theoretical studies on lithium intercalation. The second one was to constitute a set of reference data from where the differences between the intercalation into a bulk and into a nanostructure can be studied.

The experimental lithium intercalation ratio into an anatase bulk equals 0.5 Li ion per TiO<sub>2</sub> unit. Following this result, the most stable Li distribution was reported<sup>137</sup> to be associated with half of the octahedral intercalation sites occupied. Previous theoretical studies<sup>26,118</sup> reported an orthorhombic distortion of the lattice and the formation of a titanate structure belonging to the *Imma* space group<sup>26</sup> upon lithium intercalation. However, the modelling of such a phase transformation requires either the use of supercells containing several dozens of independent atoms,<sup>25,149</sup> or a several steps optimization procedure in which the restrictions are released one by one<sup>40</sup>. The theoretical studies of *nt*-TiO<sub>2</sub> are possible at an *ab initio* scale only thanks to the symmetry operators, that reduce the size of the unit cell below ten atoms, combined with a simple optimization procedure. As a result, the lithiated anatase bulk was optimized following the same conditions as for the *nt*-TiO<sub>2</sub> ones: the unit cell chosen was as small as possible and fully optimized in a single step.

A (1 x 1 x 2) supercell containing 14 atoms (4 TiO<sub>2</sub> unit and 2 intercalated Li) was built. The lithium atoms were inserted under their reduced form (with three electrons) in half of the octahedral sites available along the *z*-direction. A full geometry optimization (both the atomic positions and the cell parameters were relaxed) was then performed. The number of symmetry operators was kept constant during the optimization procedure as this condition is compulsory for the modelling of *nt*-TiO<sub>2</sub>. Consequently, no anisotropic modification of the unit cell can be observed because the number of symmetry operators can not be reduced. The changes occurring in the bulk anatase upon lithium intercalation are shown in Figure 4.3.

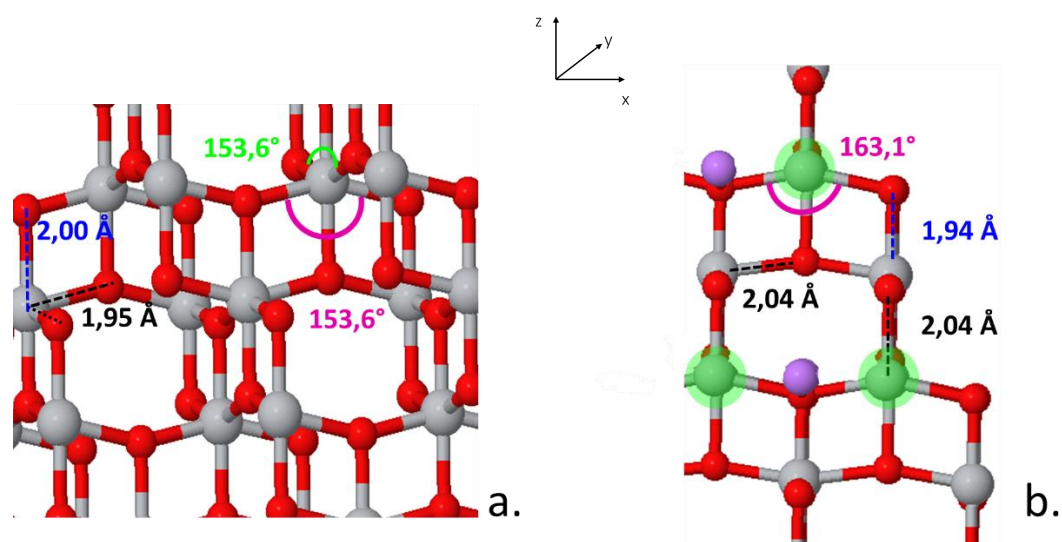


Figure 4.3: Optimized non-lithiated (a) and lithiated (b) bulk anatase. The Ti atoms are in grey, the O ones in red and the Li ions in purple. The reduced Ti<sup>3+</sup> ions are highlighted in green.

The lithium intercalation induces an elongation from 1.95 Å to 2.04 Å of all the Ti-O bonds present in the *x* and *y* directions. Consequently, the O-Ti-O angles present in the *xy* plane are also increased by 10°. The modifications occurring in the *z*-direction are quite different: the Ti-O bond lengths depend on the degree of oxidation of the titania ions. The Ti<sup>3+</sup>-O bonds exhibit a very similar length as the one observed in Ti<sub>2</sub>O<sub>3</sub> (2.04 Å for the former and 2.02 Å for the latter). Instead, the Ti<sup>4+</sup>-O bonds are shortened to 1.94 Å. As a result, the lithiated anatase contains an alternance of short and long Ti-O bonds along the *z*-direction. The size of the conventional unit cell is also modified by the Li intercalation.

By comparing the cell parameters of the two optimized structures before and after the Li intercalation, it can be observed that the  $c$  parameter is reduced from 9.77 Å to 9.39 Å in the lithiated structure. On the contrary, the  $a$  and  $b$  cell parameters are increased from 3.79 Å to 3.99 Å upon Li intercalation. By taking into account the fact that the symmetry operators avoid any anisotropic modification in the  $xy$  plane, the optimized lithiated bulk structure is coherent with the previous theoretical studies<sup>26</sup>.

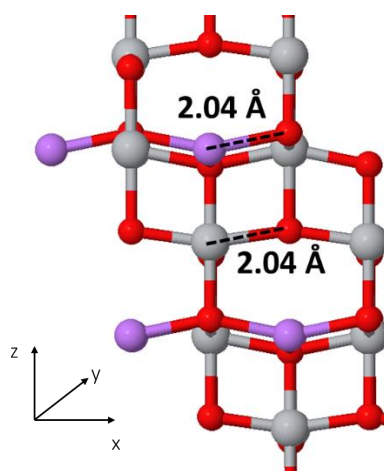


Figure 4.4: Visualization of the Li-O bonds present in the  $xy$  plane. The grey, red and purple spheres represent the Ti, O and Li elements, respectively.

The Li position inside the octahedra intercalation sites is shown in Figure 4.4. The oxygen atoms located in the  $xy$  plane are not all at the same height but stand above and below a centred plane, leading to the formation of distorted octahedra. Similar results were reported by Tielens et al.<sup>40</sup> or Legrain et al.<sup>149</sup> performing *ab initio* calculations. In our model, the lithium stays at the middle of the octahedron and is fourfold coordinated, no shift along the  $c$ -direction was observed.

The previous theoretical studies do not agree with each other concerning the size of the shift of Li along the *c*-direction, the values reported varying between 0.15 Å and 0.6 Å<sup>25,40,149</sup>. Moreover, Dawson et al.<sup>25</sup> showed that the shifted position is only 0.01 eV more stable than the centred one. As a result, the shift of the Li ions along the *c*-direction seems to be strongly influenced by the computational method chosen. Thus, the small size of the unit cell chosen in this thesis, combined with a full geometry optimization performed in a single step, can explain the absence of shift observed for the lithiated bulk. Another explanation for the absence of shift might be the location of the Li ion in a high symmetry point, representing a local minimum.

A possible explanation for the modifications of the bond lengths upon Li intercalation is linked to the filling of the anti-bonding  $d_{yz}$  orbitals. The destabilization of the electronic structure was balanced by a Jahn–Teller-like orthorhombic distortion of the lattice. However, Morgan and Watson<sup>118</sup> proved later that the added electrons were not enough to induce such a distortion. They pointed out the key role played by the intercalated lithium to stabilize the distorted structure. They noticed that the Li-O distances were close to the ones observed in Li<sub>2</sub>O<sub>2</sub>, enhancing the Coulomb stabilization of the Li.

In our model, the symmetry constraints avoid an orthorhombic distortion of the lattice. As a result, all the Ti<sup>4+</sup>–O and Li-O bonds located in the *xy* plane are parallel to each other and exhibit the same length of 2.04 Å. This value is close to the Li-O distance of 1.996 Å observed in Li<sub>2</sub>O<sub>2</sub><sup>26</sup> but stretches the Ti<sup>4+</sup>–O bonds above their equilibrium position equal to 1.93 Å. Consequently, the Coulomb stabilization of the lithium seems to be one of the main driving mechanisms for the reorganization of the lattice, as proposed by Morgan and Watson<sup>118</sup>.

The Mulliken population analysis showed that the lithium gives 0.8e to the lattice when intercalated. This extra charge is localized in the  $d_{xy}$  orbital of the adjacent titanium ion, reducing it to Ti<sup>3+</sup> (Figure 4.3) in agreement with XAS results<sup>112,126</sup>. The  $d_{xz}$  and  $d_{yz}$  orbitals stay empty, confirming that no Jahn-Teller distortion of the lattice can be observed. Similar results were reported by the most recent theoretical studies<sup>118,149</sup>.

The DOS of the lithiated bulk is displayed in Figure 4.5 where the blue plot represents the total DOS of the structure while the black, red and green colors are related to the  $s$ ,  $p$  and  $d$  orbital contributions of the selected atom, respectively. The  $2p$  orbitals of the oxygen atoms constituting the valence band are slightly affected by the Li intercalation. The main modification concerns the  $d_{xy}$  orbitals of the titania ions that were initially empty and located in the conduction band of the anatase bulk. These orbitals are now occupied for the  $\text{Ti}^{3+}$  ions and form a localized state in the band gap situated 0.62 eV below the conduction band edge.

This phenomenon is in agreement with the previous studies<sup>104,149</sup> and can be explained by the Mott-Hubbard theory. Indeed, the occupancy of a single Ti  $3d$  state generates important intra-atomic Coulomb repulsions between the different  $d$  orbitals and induces a splitting of the occupied orbital below the conduction band. The lithium orbitals are not visible in the DOS plotted in Figure 4.5 as they do not contribute to the band gap, the  $\text{O}2s$  orbitals being located above the Ti  $3d$  ones<sup>188</sup>.

As mentioned in the previous part of this chapter, the lithium is intercalated with an energy of -1.68 eV per  $\text{TiO}_2$  unit, corresponding to an intercalation voltage of 3.37 V.

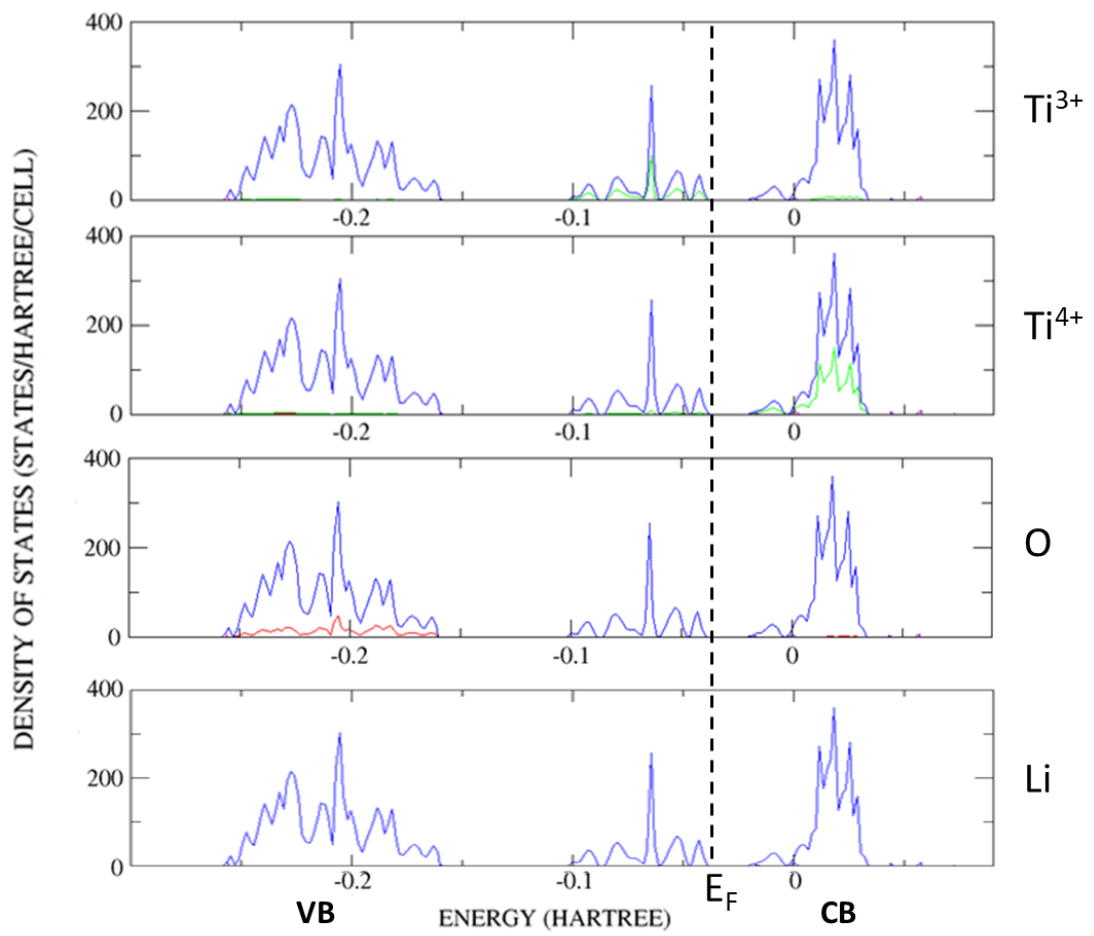


Figure 4.5: DOS of the  $\text{Li}_{0.5}\text{TiO}_2$  bulk where VB and CB represent the valence and conduction bands. The blue plot represents the total DOS while the red and green plots stand for the contribution of the  $p$  and  $d$  orbitals, respectively.

The previous theoretical studies<sup>103,149</sup> pointed out the instability of the tetrahedral intercalation sites caused by the electrostatic repulsion of the Ti ions. In order to compare the behaviour of our model with the previous studies, Li ions were also intercalated in different tetrahedral sites of the anatase bulk, the concentration being the same as for the octahedral sites. The aim of this study is to obtain reference results that can be then compared with the lithium intercalation into the slab and nanotube tetrahedral sites that will be discussed in the next sections. Indeed, the tetrahedral sites located near the surface of the slabs or the nanotubes can exhibit less electrostatic repulsions as only half of the Ti ions are present. Moreover, the sites located on the external wall of the nanotubes are widened by the strain energy.

In our model, all the Li ions inserted in a bulk tetrahedral site spontaneously moved to the nearest octahedral site when the structure is allowed to relax. An example of the Li behaviour is illustrated in Figure 4.6 where the black arrow indicates the displacement of the lithium ion during geometry optimization. Similar results were observed by Legrain et al.<sup>149</sup>.

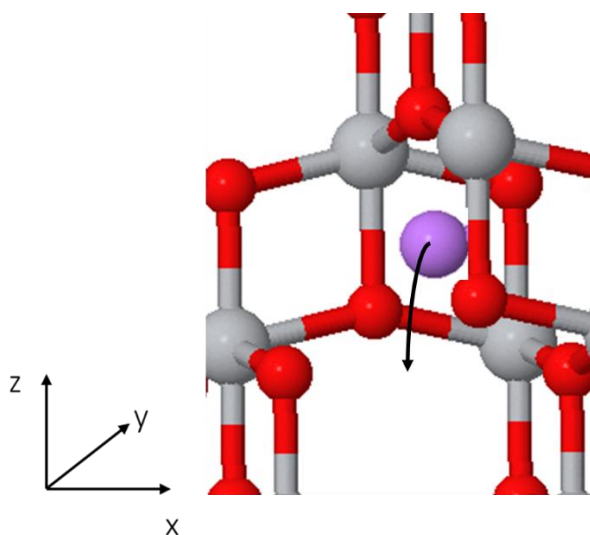


Figure 4.6: Anatase bulk with one Li ion intercalated in a tetrahedral site. The Ti atoms are indicated in grey, the O ones in red and the Li ion in purple.

## 4.4 Lithium intercalation into LiTiO<sub>2</sub> anatase bulk

The nanostructured TiO<sub>2</sub> electrodes exhibit higher capacities because of their larger surface. XANES studies<sup>123</sup> indicates a Ti oxidation state close to 3<sup>+</sup> for the first four nanometers of TiO<sub>2</sub> present below the surface. Further theoretical study carried out by Belak et al.<sup>103</sup> confirmed the formation of a LiTiO<sub>2</sub> rich phase at the surface of the electrode. The slabs and nanotubes studied in this thesis both exhibit favorable Li intercalation for capacities superior to  $x = 0.5$ . In order to have a deeper understanding of their behavior with this high concentration of lithium, a fully lithiated LiTiO<sub>2</sub> anatase bulk was studied. The optimized structure is shown in Figure 4.7.

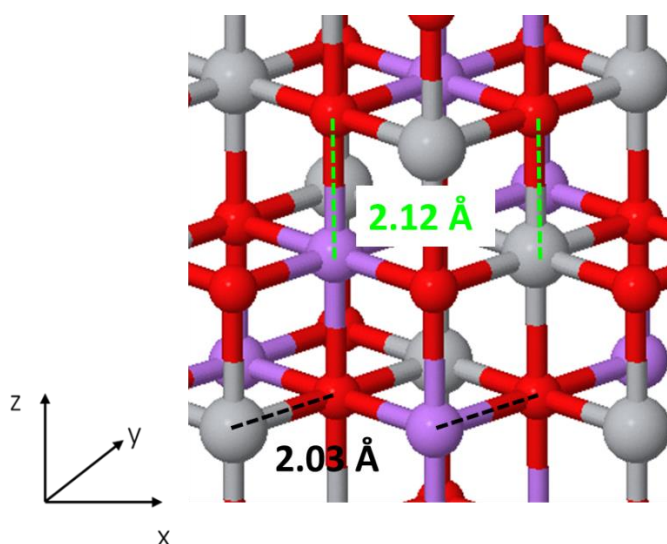


Figure 4.7: Optimized fully lithiated anatase bulk LiTiO<sub>2</sub>. The Li ions are in purple while the Ti and O atoms are in grey and red, respectively.

The LiTiO<sub>2</sub> exhibits a slightly distorted rock salt structure. The Li-O and Ti-O bonds present in the  $xy$  plane exhibit the same length of 2.03 Å whereas the bonds located along the  $z$  axis are 0.1 Å longer. All the angles of the unit cell equal 90°, meaning that the bonds are either colinear or perpendicular to each other. The lattice parameters of the conventional unit cell are  $a = 4.06$  Å and  $c = 8.51$  Å in agreement with previous studies<sup>40,99,189</sup>.

All the octahedral intercalation sites are now occupied by six-fold coordinated Li ions. Consequently, each intercalated lithium is coordinated by four other ones located  $2.94 \text{ \AA}$  away. The unfavorable Li-Li repulsive interactions are displayed in Figure 4.8. For comparison, the octahedra sites that stay empty in the  $\text{Li}_{0.5}\text{TiO}_2$  are highlighted in blue. Thus, the Li-Li repulsions can explain the less favorable lithium intercalation energy exhibited by the  $\text{LiTiO}_2$  compared to the  $\text{Li}_{0.5}\text{TiO}_2$  bulk anatase. The lithium is intercalated with an energy of  $-1.27 \text{ eV}$  per  $\text{TiO}_2$  unit in the  $\text{LiTiO}_2$  whereas this value equals  $-1.68 \text{ eV}$  when the capacity is lowered to  $x = 0.5$ .

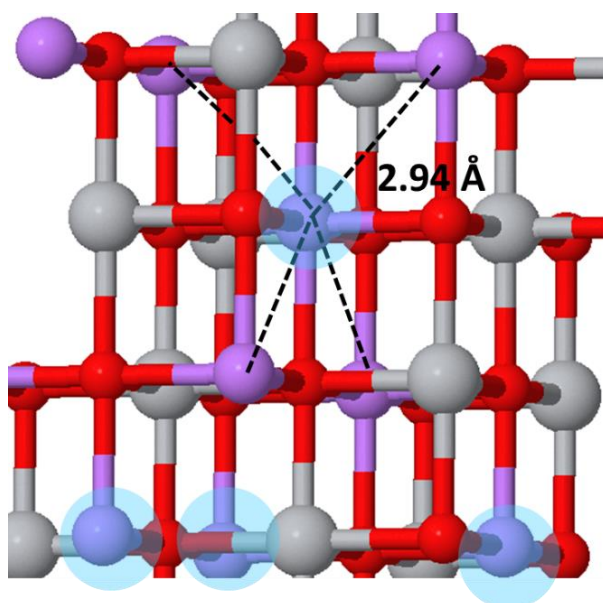


Figure 4.8: Optimized anatase bulk  $\text{LiTiO}_2$  showing the Li-Li interaction. The grey, red and purple colours represent the Ti, O and Li ions, respectively. The Li ion highlighted in blue are not present in the  $\text{Li}_{0.5}\text{TiO}_2$  bulk anatase.

The DOS of the  $\text{LiTiO}_2$  is shown in Figure 4.9 where the blue plot represents the total DOS of the unit cell while the green and red plots stand for the  $d$  and  $p$  orbitals of the indicated atom, respectively. The Fermi level that is normally drawn on top of occupied bands cannot be plotted in this Figure because the conduction band is partially filled with electrons.

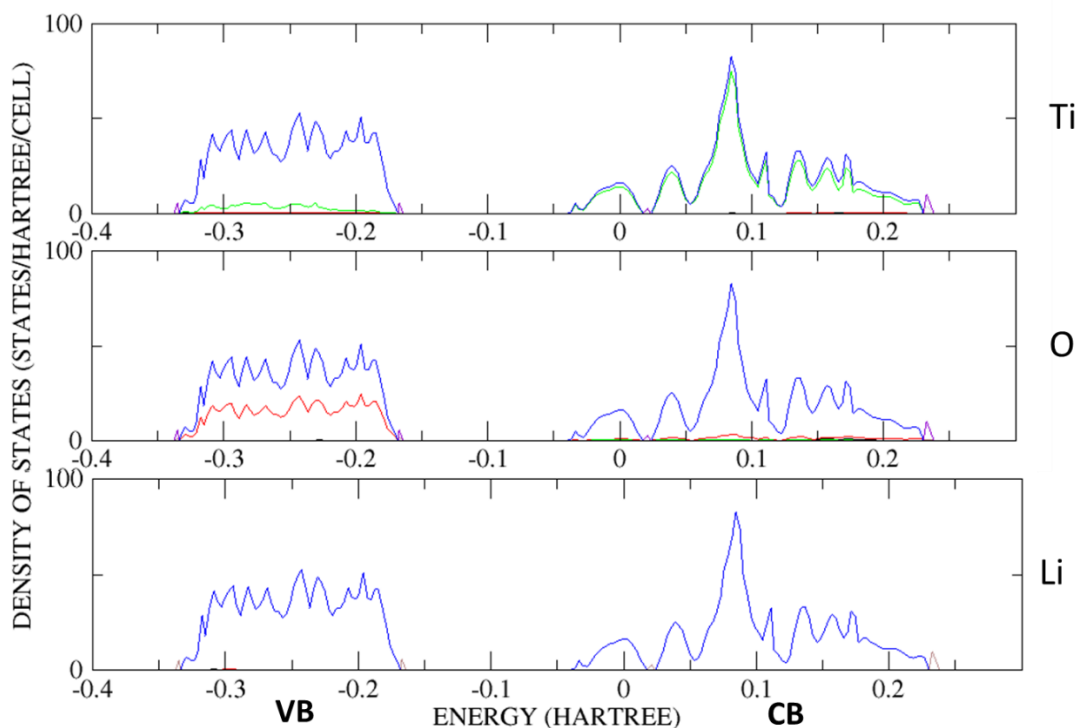


Figure 4.9: DOS of the  $\text{LiTiO}_2$  bulk. The blue plot stands for the total DOS of the slab, while the red and green colors are related to the  $p$  and  $d$  orbital contributions of the indicated atom. VB and CB represent the valence and conduction bands, respectively.

From Figure 4.9, it is seen that the conduction band exhibits a main sharp peak surrounded by smaller ones. This shape is typical of the  $\text{Ti}^{3+}$  ions and was already observed in  $\text{Li}_{0.5}\text{TiO}_2$  titanate. Nonetheless, the  $\text{Ti}^{3+}$  peaks do not form a localized state in the band gap as it was the case in the  $\text{Li}_{0.5}\text{TiO}_2$  titanate but all states are described by the conduction band. The explanations to the differences in the band structure can be associated with the mixed oxidation state of  $\text{Li}_{0.5}\text{TiO}_2$ , where both  $\text{Ti}^{3+}$  and  $\text{Ti}^{4+}$  ions are present, leading to occupied ( $\text{Ti}^{3+}$ ) and unoccupied ( $\text{Ti}^{4+}$ )  $d$  orbitals. The  $\text{Ti}^{3+}$  have the  $d_{xy}$  orbital filled with an electron forming a localized state in the band gap, instead the conduction band of the titanate is formed by the empty  $d$  orbitals of the  $\text{Ti}^{4+}$  ions. In  $\text{LiTiO}_2$  only  $\text{Ti}^{3+}$  ions are present and the three lowest  $d_{xy}$ ,  $d_{xz}$  and  $d_{yz}$  orbitals of the  $\text{TiO}_2$  are occupied with the electrons given by the lithium, in agreement with previous studies<sup>103,137</sup>. Consequently, there is no single occupied orbital available and thus, no localized state can be formed in the band gap.

The DOS indicates a higher population of the valence band compared to the  $\text{TiO}_2$  and the  $\text{Li}_{0.5}\text{TiO}_2$  titanate. The main contribution comes from the  $2p$  orbitals of the oxygen atoms. The Mulliken population predicts that the lithium ions give 0.97 e per  $\text{TiO}_2$  unit compared to 0.8 e in  $\text{Li}_{0.5}\text{TiO}_2$ . The extra charge of 0.17e is located in the  $2p$  orbitals of the oxygens, in agreement with the results reported by Mackrodt et al.<sup>190</sup>. The DOS also confirms that the Li ions do not contribute to the band gap as their  $2s$  orbitals are located above the conduction band.

As a conclusion, the electron transfer affects both the oxygen and the titania sublattices and leads to a 0.2 eV smaller band gap than the one observed in bulk anatase, indicating a higher electronic conductivity. Van de Krol et al.<sup>188</sup> point out the enhancement of the  $\text{LiTiO}_2$  electronic conductivity induced by the filling of the  $d$  orbitals present in the conduction band. However, the experimental conductivity exhibited by the  $\text{LiTiO}_2$  is higher than the one of the  $\text{Li}_{0.5}\text{TiO}_2$  titanate.

## 4.5 Lithium intercalation into the slab

In chapter 3, it was concluded that the oxygen terminated (101) surface was the energy most favourable surface, but only from the oxygen terminated (001) is it possible to construct nanotubes with a negative strain energy. To compare lithium intercalation in the surface structure and the nanotubes, only the (001) oxygen terminated surface for anatase is considered in this study.

The main goal was to gain a deeper understanding of the intercalation into the surface structure and to compare with both the bulk and the nanotubes. It is also worth mentioning that the calculations carried out on a slab are computationally far less expensive than the ones performed on the nanotubes. Thus, the number of tests can be multiplied to explore a large number of configurations. Some calculations were difficult to converge or showed structural breakdown, mainly because of a polarization or an interatomic repulsion that dominated the interactions. It is expected that this surface will exhibit similar behaviour in  $nt\text{-TiO}_2$ . Thus, the nanotube calculations that were identified to be difficult to converge were optimized using low truncation criteria to confirm the similar behaviour and save computational time.

Another reason to study lithium insertion into the slab was to isolate the influence of the strain by comparing the surface intercalation energies with the *nt*-TiO<sub>2</sub> ones. To determine the energetically most favourable site in the structure, both octahedral and tetrahedral sites have been considered in the outermost surface layer as well as in the centre of the slab. For completeness, different Li ion concentrations ranging from  $x = 0.33$  to  $x = 1$  have been considered and the insertion voltage calculated. When the lithium ions were intercalated in the sites located near the surface, only one side of the slab was considered as the two surfaces are symmetric.

#### 4.5.1 Intercalation with lithium capacity of $x = 0.33$

Initially, a low concentration of intercalated lithium was considered. Only one Li ion per slab primitive unit cell was inserted, corresponding to a stoichiometry of Li<sub>0.33</sub>TiO<sub>2</sub>. The first step was to determine which of the tetrahedral or the octahedral intercalation sites were the most favourable. The location of these two kinds of intercalation sites is shown in Figure 4.10. The inner octahedral intercalation sites are filled with lithium in the picture a, while some tetrahedral sites located near the outermost surface are lithiated in the slab displayed in Figure 4.10b.

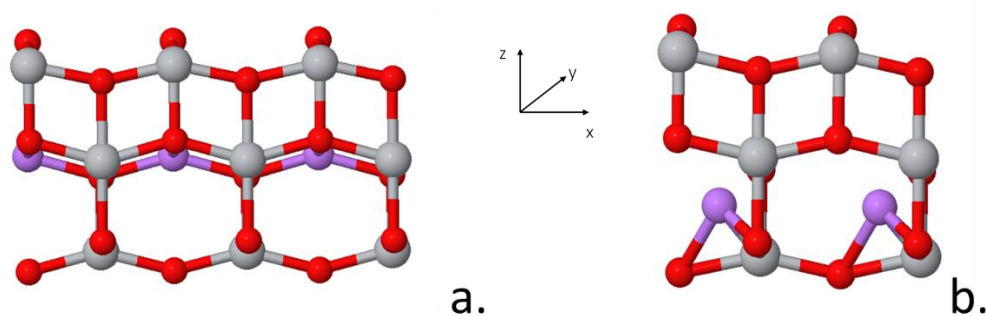


Figure 4.10: Anatase (001) slabs with lithiated octahedral (a) and tetrahedral (b) intercalation sites. Grey, red and purple spheres represent Ti, O and Li, respectively.

#### 4.5.1.1 The tetrahedral intercalation sites

For the bulk structure of anatase, it was concluded that the tetrahedral intercalation sites were not favourable because of the Coulombic repulsion of the four surrounding Ti atoms. Nonetheless, when the bulk is cut to build the slab, new tetrahedral sites with only 2 Ti atoms are formed at the surface of the slab. These sites exhibit less electrostatic repulsions and can potentially host Li ions.

Thus, lithium was intercalated at the surface of the slab as displayed in Figure 4.11a. However, when the geometry was optimized, the lithium moved spontaneously to the nearest octahedral sites as indicated by the black arrow. As a result, the tetrahedral intercalation sites present at the surface are not the most favourable ones and will not host Li ions.

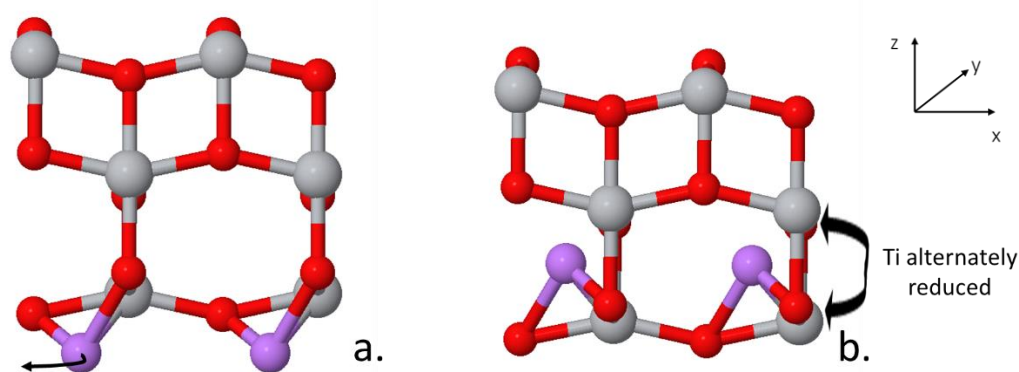


Figure 4.11: Intercalation of Li ions in the outer (a) and inner (b) tetrahedral sites of the (001) anatase slab. The Ti atoms are in grey, the O ones in red and the Li ions in purple.

The tetrahedral sites located at the inner part of the surface were also filled with lithium as displayed in Figure 4.11b. The reactivity of these sites might have been influenced by the undercoordinated surface atoms. Nonetheless, the calculations did not converge because the surrounding Ti atoms were alternately reduced. As a conclusion, the tetrahedral intercalation sites present in the slab behave in the same way as the bulk ones and cannot host Li ions. Thus, only the octahedral sites present in the slab will be considered in the next part of this section.

#### 4.5.1.2 The octahedral intercalation sites

The primitive unit cell of the slab contains three octahedral intercalation sites whose locations are indicated by black crosses in Figure 4.12.

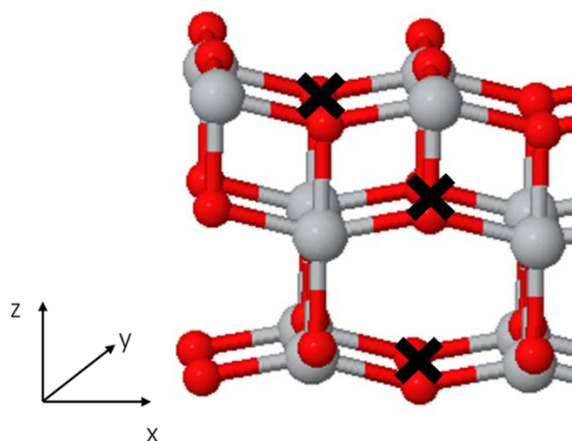


Figure 4.12: Octahedral intercalation sites (black crosses) present in the anatase (001) slab. The grey, and red spheres represent the Ti and O atoms, respectively.

The lithium is intercalated with a capacity of  $x = 0.33$  when a single Li ion is added to the slab primitive unit cell. Thus, the lithium can be inserted in the centre of the slab or on one of its outermost surfaces. The surfaces being symmetric, it is not necessary to carry out two separate studies of the Li insertions at the top and at the bottom of the slab. However, this intercalation breaks the slab symmetry, resulting in the creation of a dipole moment over the slab that can influence the results obtained. This is not the case when the lithium is inserted in both of outermost surface layers, corresponding to a capacity of  $x = 0.67$  that will be discussed in section 4.5.3.

When only one of the surfaces is filled with lithium, the slab is polarized leading to large structural rearrangements to reduce the induced dipole moment as displayed in Figure 4.13.

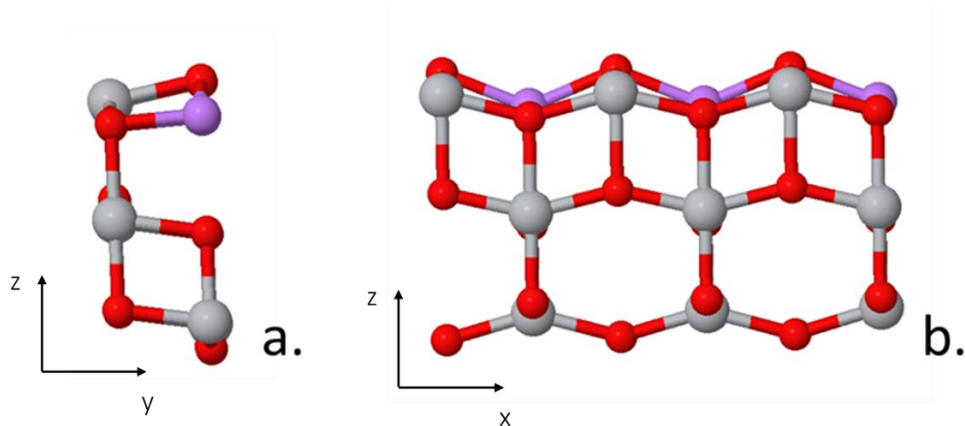


Figure 4.13: Side (a) and face (b) views of the optimized  $\text{Li}_{0.33}\text{TiO}_2$  anatase (001) slab. The Li ions are in purple while the Ti and O atoms are in grey and red, respectively.

The lithium will move inward from the surface in an attempt to reduce the dipole moment. Consequently, the oxygen anions move outward from the surface to enhance the stabilization of the slab. Moreover, the Mulliken population indicates that all the titania atoms located on the lithiated surface are reduced to  $\text{Ti}^{3+}$  storing the additional charge from lithium in their  $d_{xy}$  orbitals, the other  $d$  orbitals stay empty. Similar results were observed for bulk  $\text{Li}_{0.5}\text{TiO}_2$  titanate. The  $d_{xy}$  orbitals exhibiting the lowest energy in  $\text{TiO}_2$ , they will be the first ones to host the added electrons. However, the Mulliken population also indicates that the overlap population between the  $\text{Ti}^{3+}$  and its neighbouring surface atoms is more consequent with the fully coordinated oxygens than with the undercoordinated ones.

The localized filling of the  $d_{xy}$  orbitals, will limit the elongation of the  $\text{Ti}^{3+}$ -O bond distances present in the  $xy$  plane as displayed in Figure 4.14. As discussed in section 4.3, all the  $\text{Ti}^{3+}$ -O bonds parallel to the  $xy$  plane increased to 2.04 Å upon lithium intercalation in the  $\text{Li}_{0.5}\text{TiO}_2$  bulk titanite. Moreover, the higher overlap population between the  $\text{Ti}^{3+}$  and the fully coordinated oxygen atoms will reduce the extension of the  $\text{Ti}^{3+}$ - $\text{O}_{3c}$  bonds that are parallel to the  $x$  axis. Consequently, the lithiated octahedral intercalation sites are shorter and more distorted than the one observed in the bulk. The inserted lithium ions are four-fold coordinated with Li-O distances varying between 2.02 Å and 1.95 Å as displayed in Figure 4.14. These values are close to the ones observed in  $\text{Li}_2\text{O}_2$  bulk. On the contrary, the  $\text{Ti}^{3+}$ -O bonds parallel to the  $z$  axis are extended. A similar behaviour was also observed for the non-lithiated slab that was elongated in the  $z$ -direction.

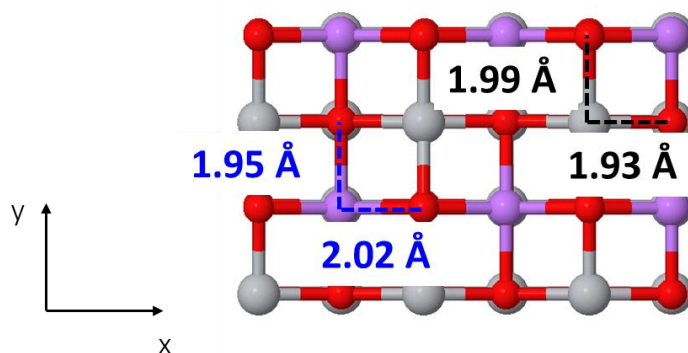


Figure 4.14: Top views of the optimized (001) slab showing the widths of the intercalation sites (in blue) and the Ti-O bond lengths (in black) when one outermost surface is lithiated. The purple, red and grey colours stand for the Li, O and Ti ions.

Thus, the Li intercalation in a single surface layer despite creating a dipole moment leads to a stable system exhibiting a negative intercalation energy of -1.57 eV. This intercalation energy is less negative than the one calculated for the bulk  $\text{Li}_{0.5}\text{TiO}_2$  titanate that equals -1.68 eV per  $\text{TiO}_2$  unit. Thus, the lithium intercalation is less favourable in a single outermost surface of the slab than in bulk titanate. However, the dipole moment generated in the slab is increasing the intercalation energy value.

The lithium was also intercalated in the inner octahedral sites as it is shown in Figure 4.15. The Mulliken population confirms that all the central titania atoms are reduced to  $\text{Ti}^{3+}$  and host the extra charge in their  $d_{xy}$  orbitals. So, the charge repartition is the same as the one observed for the lithiated outermost surface. However, the overlap population between the  $\text{Ti}^{3+}$  and the oxygen atoms is equivalent in the  $x$  and in the  $y$ -direction as the centre of the slab does not contain undercoordinated atoms. As a result, the intercalation sites are not distorted along the  $xy$  plane as displayed in Figure 4.15. The lithium ions are located in the middle of the octahedron, coordinated by four oxygen atoms with a bond distance of 1.96 Å.

The geometry optimization performed after the lithium intercalation into the centre of the slab leads to a different structure from the one observed for the lithiation of the outermost surface. These results point out the major role played by the undercoordinated surface atoms in the geometry changes that facilitate the lithium intercalation.

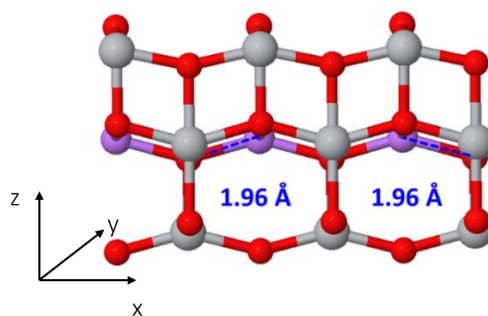


Figure 4.15: Lithium intercalation into the inner octahedral sites of the (001) anatase slab. The grey, red and purple spheres represent Ti, O and Li, respectively.

The corresponding intercalation energy equals  $-0.91$  eV per  $\text{TiO}_2$  unit and is less favourable than the ones exhibited when inserted on the outer surface layer. Moreover, by comparing this slab intercalation energy with the one exhibited by the bulk  $\text{Li}_{0.5}\text{TiO}_2$  titanate, it can be seen that the intercalation energy in the centre of the slab is less favourable than the  $\text{Li}_{0.5}\text{TiO}_2$  bulk structure (which corresponds to  $-1.68$  eV per  $\text{TiO}_2$  unit). In anatase bulk, the lithium intercalation occurs through a two-phase thermodynamic equilibrium<sup>112</sup> between a Li-poor phase exhibiting a capacity of  $x = 0.01$ <sup>99</sup> and a Li-rich phase made of  $\text{Li}_{0.5}\text{TiO}_2$  titanate. When lithium is inserted into the inner octahedron of the slab, all the other octahedron along the  $z$ -direction stay empty and exhibit a geometry influenced by surface reconstruction. Thus, the changes in geometry allowing to stabilize the lithium intercalation are more constrained in the slab than in the bulk and can explain the differences observed in intercalation energies.

The DOS of the slabs corresponding to a capacity of  $\text{Li}_{0.33}\text{TiO}_2$  are presented in Figure 4.16. The blue plot corresponds to the lithiation of the octahedral sites located in the centre of the slab, while the red plot stands for the lithiation of one outermost surface. In both cases, no localized state is generated in the band gap. By comparing the two valence bands of this figure, it appears that the undercoordinated oxygen atoms are slightly higher in energy, and thus more reactive, when they are neighbouring with lithium. The conduction band is located at higher energy when the lithiation is performed on the outermost surface than when it is performed into the internal octahedral sites. This phenomenon can be explained by the weaker stability of the undercoordinated titania atoms once the surrounding lithium reduced them to  $\text{Ti}^{3+}$ . Moreover, the generated dipole moment will also destabilize the  $\text{Ti}^{3+}$  ions.

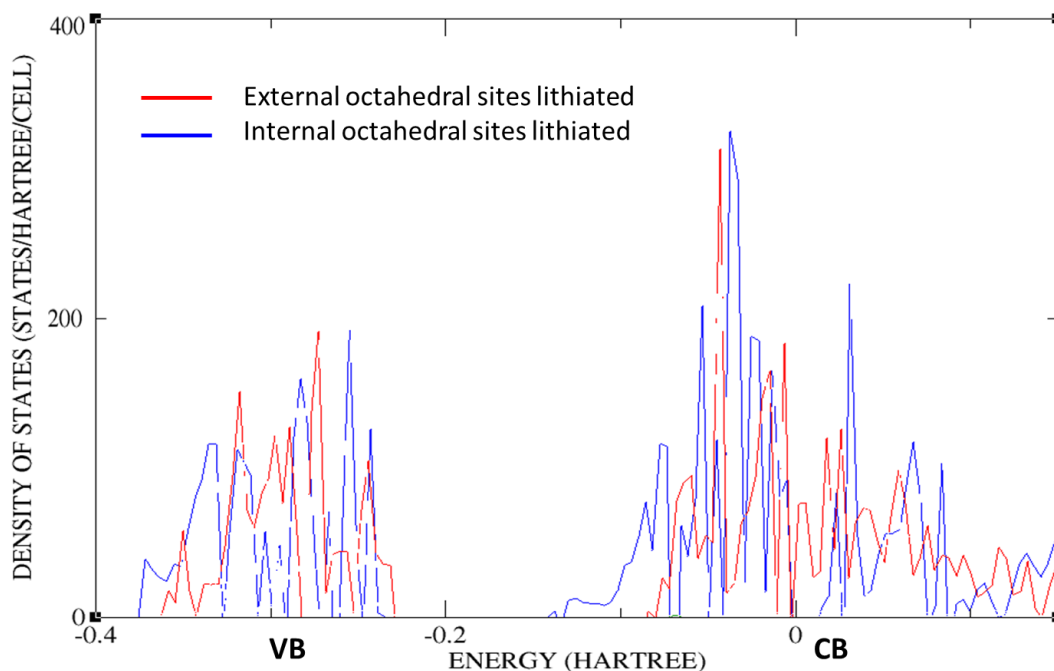


Figure 4.16: Total DOS of the anatase (001) slab having the external (blue plot) or the internal (red plot) intercalation sites lithiated. VB and CB refer to the valence and conduction bands, respectively.

#### 4.5.2 Intercalation with lithium capacity of $x = 0.5$

The most favourable lithium intercalation into the bulk anatase was observed when half of the octahedral sites were empty, corresponding to a capacity of  $x = 0.5$ . However, the primitive unit cell of the slab contains three  $\text{TiO}_2$  units, meaning that inserting lithium with the same capacity requires the use of a supercell containing six  $\text{TiO}_2$  units. This unit cell is shown in Figure 4.17 but the calculations did not converge. The surrounding Ti atoms are alternately reduced as was already observed for the tetrahedral sites. This result points out the instability of this kind of intercalation. Moreover, both experimental and theoretical studies<sup>103,191</sup> indicate that the lithium is intercalated with capacities close to  $x = 1$  at the surface of the  $\text{TiO}_2$  electrodes. Thus, the instability of the supercell, combined with the results of the previous studies, do not make it necessary to study lithium intercalation into the slab for lower capacities than  $x = 0.33$ . As a result, no supercell slabs were used anymore in this thesis.

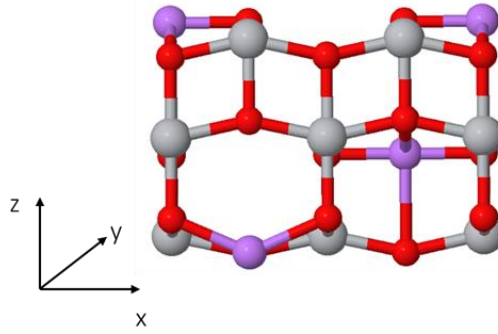


Figure 4.17: (001) Anatase supercell slab with Li intercalated in half of the octahedral sites. The grey, red and purple spheres are related to Ti, O and Li, respectively.

### 4.5.3 Intercalation with lithium capacity of $x = 0.67$

An intercalation ratio of  $x = 0.67$  is obtained when both the outermost surfaces are lithiated. In this configuration, the two surfaces are symmetric, and no dipole moment will be generated by lithium intercalation. Thus, the surface reconstruction is different from the one exhibited by the singly lithiated surface that was driven by the reduction of the dipole moment. The differences in geometry induced by the lithiation of the second surface are displayed in Figures 4.18 and 4.19.

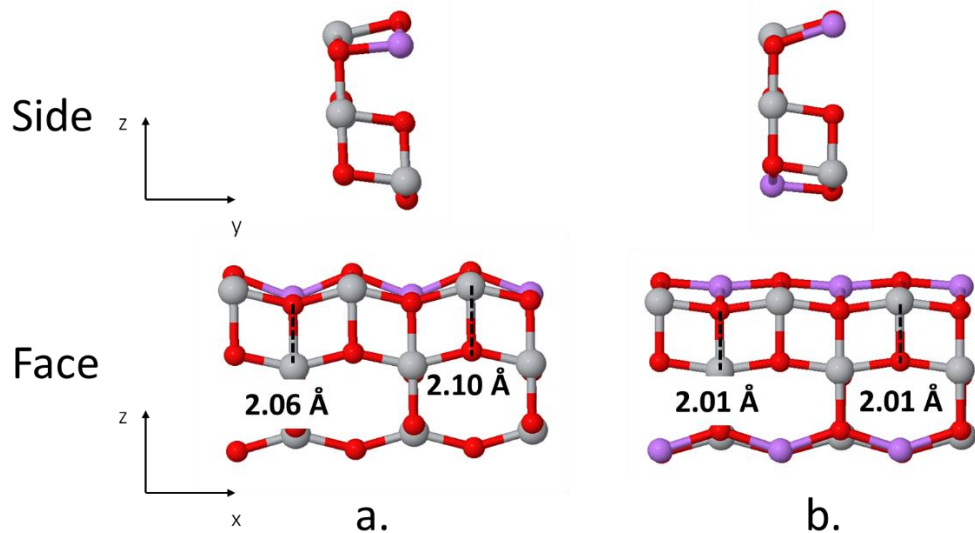


Figure 4.18: Side and face views of optimized anatase (001) slabs with lithium inserted in a single surface layer (a) or in both (b) surface layers. The Ti, O and Li atoms are in grey, red and purple, respectively.

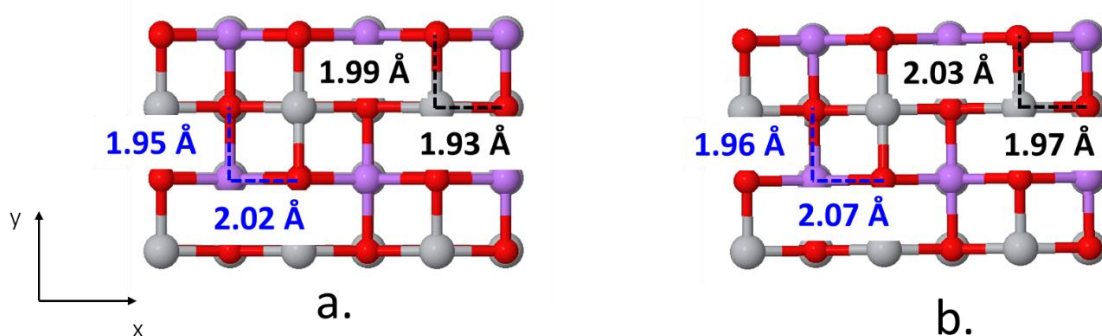


Figure 4.19: Top views of the optimized (001) slabs showing the widths of the intercalation sites (in blue) and the Ti-O bond lengths (in black) when one (a) or two (b) outermost surfaces are lithiated.

The purple, red and grey colours are related to Li, O and Ti, respectively.

When the second outermost surface is lithiated, the lithium ions are not displaced inward in the surface but stay in the outermost surface layers as the polarization of the slab is reduced. The lithiation of the second external surface also modified the  $\text{Ti}^{3+}$ -O bond lengths by shortening all the bonds parallel to  $z$  axis to 2.01 Å, as displayed in Figure 4.18. On the contrary, the  $\text{Ti}^{3+}$ -O bonds present in the external surfaces are widened by 0.4 Å in both  $x$  and  $y$  directions as it is shown in Figure 4.19.

The Li-O bonds are extended from 2.02 Å to 2.07 Å along the  $x$  axis whereas their lengths are slightly modified along the  $y$  axis. As a result, the lithiation of the second surfaces leads to more distorted octahedral intercalation sites. These changes can be explained by the displacement of the Li ions in the outermost surface layers.

The modification of the Ti-O bond lengths can be explained by the electronic structure of the titania atoms located on the outermost surface. The Mulliken population indicates that all the external titania atoms are reduced to  $\text{Ti}^{3+}$  and exhibit now hybridized  $d$  orbitals. Nevertheless, the filling of the hybridized  $d$  orbitals is different depending on which outermost surface the  $\text{Ti}^{3+}$  ions are located, as it is detailed in Figure 4.20.

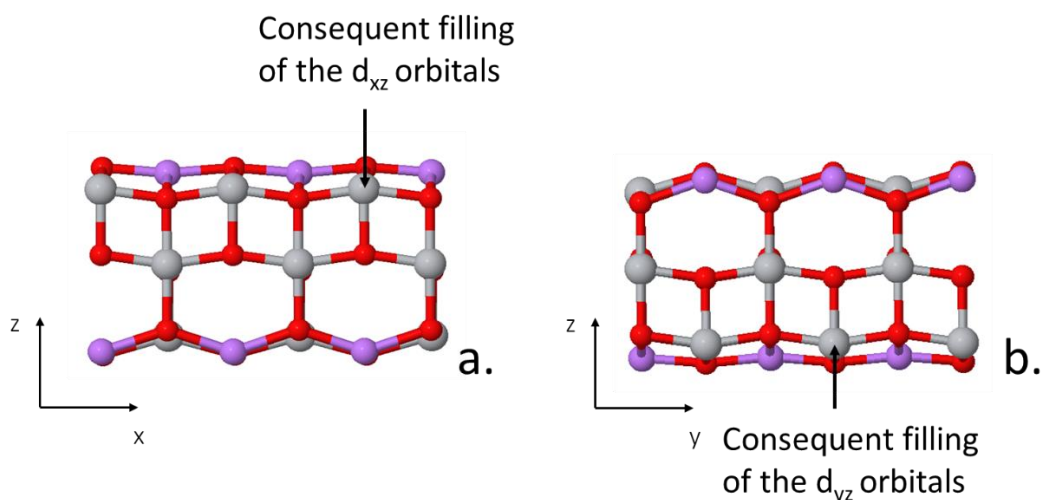


Figure 4.20: Filling of the titania  $d$  orbitals of the titania located on the upper (a) and lower (b) outermost (001) surfaces. The purple, red and grey colours are associated with Li, O and Ti, respectively.

The  $O_{3c}$ -Ti- $O_{3c}$  chains present in the outermost surfaces are running perpendicularly to each other as shown in Figure 4.20. Thus, the  $O_{3c}$ -Ti- $O_{3c}$  chains located on the upper outermost surface are parallel to the  $x$  axis whereas the ones situated on the lower external surface are parallel to the  $y$  axis. The  $Ti^{3+}$   $d_{xy}$  orbitals are not empty but get hybridized with the  $d$  orbitals parallel to the  $O_{3c}$ -Ti- $O_{3c}$  chains. Thus, the  $Ti^{3+}$  located on the upper outermost surface shows a consequent filling of their  $d_{xz}$  orbitals, their  $d_{yz}$  orbitals staying empty. The situation is reversed for the titania present on the lower outermost surface: the added charges are hosted by the  $d_{yz}$  orbitals whereas the  $d_{xz}$  orbitals are empty. Thus, the  $Ti^{3+}$ -O bonds are shortened along the  $z$ -direction as the  $d_{xz}$  and  $d_{yz}$  titania orbitals are now hosting electrons. The electronic repartition will also increase the  $Ti^{3+}$ -O bond lengths in the  $xy$  plane as the  $d_{xy}$  orbitals contain less charges. The Mulliken population analysis of the outermost bonds parallel to the  $xy$  plane confirms that the overlap population is higher in the  $Ti^{3+}$ - $O_{3c}$  bonds than in the  $Ti^{3+}$ - $O_{2c}$  ones. A similar overlap population was observed when only one outermost surface was lithiated. As a result, the Ti-O bonds forming the outermost surfaces does not exhibit the same lengths, the  $Ti^{3+}$ - $O_{2c}$  bonds being longer than the  $Ti^{3+}$ - $O_{3c}$  ones.

There are several possible explanations to the hybridization of the orbitals. The first one being the intercalation ratio whose value is  $x = 0.67$ . Previous studies<sup>118,147</sup> mentioned the hybridization of the titania  $d$  orbitals when the lithium capacities overcome  $x = 0.5$ . The particular geometry of the structure can also destabilize the  $d_{xy}$  orbitals when the two outer surfaces are lithiated. As discussed in section 4.5.1, the lithiation of a single external surface leads to an anisotropic extension of the  $\text{Ti}^{3+}$ -O bonds present in the outermost  $xy$  planes, enhancing the stabilization of the  $d_{xy}$  orbitals. As a result, the Ti-O bonds forming the upper outermost surface are elongated along the  $y$  axis when lithium is intercalated. However, the external  $\text{O}_{3c}$ - $\text{Ti}^{3+}$ - $\text{O}_{3c}$  chains are running perpendicularly to each other. Thus, if the lower outermost surface gets lithiated as well, the extension of the outermost Ti-O bonds forming this surface will be more pronounced along the  $x$  axis. As a result, when the two external surfaces are lithiated, the stabilization criteria are conflicting. All the  $\text{Ti}^{3+}$   $d_{xy}$  orbitals will be destabilized, facilitating the hybridization and the filling of the other titania  $d$  orbitals.

For a better understanding of the changes in electronic structure upon lithium intercalation, the DOS of the slabs having only one or both the outermost surfaces lithiated are shown in Figure 4.21. The red plot stands for the lithiation of one of the outermost surfaces while the green plot corresponds to the lithiation of both external surfaces.

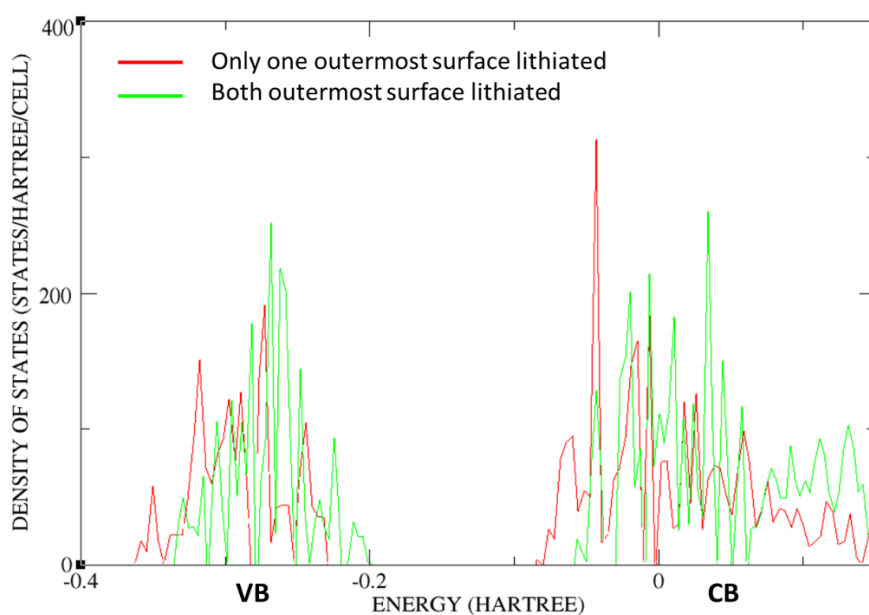


Figure 4.21: DOS of the anatase slabs having one (red plot) or two (green plot) outermost (001) surfaces lithiated. VB and CB stand for the valence and conduction bands, respectively.

The lithium intercalation into the second outermost surface does not generate a localized state in the band gap but generates some modifications to the DOS. Both the valence and the conduction bands are shifted to a slightly higher energy. This can be explained by the increase of the number of undercoordinated atoms neighbouring with lithium. The conduction band also exhibit a less localized character induced by the hybridization of the titania  $d$  orbitals.

The  $\text{Li}_{0.67}\text{TiO}_2$  slab exhibits a lithium intercalation energy of  $-1.91$  eV per  $\text{TiO}_2$  unit, representing the most negative value calculated for the slabs in this thesis. This result points out the particularly favourable intercalation exhibited by the  $\text{TiO}_2$  surface towards high lithium capacities.

#### 4.5.4 Intercalation with lithium capacity of $x = 1$

The lithium was then intercalated with the maximal capacity of  $x = 1$ , corresponding to a fully lithiated slab. This capacity was the one reported in the literature<sup>103,191</sup> for the lithium intercalation into the anatase surface. As a result, the fully lithiated slab was studied in detail in this thesis.

To better understand the effects of high lithium concentration into the slab geometry, the structural modifications induced by lithium intercalation are displayed in Figure 4.22. The optimized non-lithiated slab is shown in Figure 4.22b for comparison and points out that the lithium intercalation “flattens” all the bonds located in the outermost  $xy$  planes and elongates Ti-O bond lengths. Thus, the lithium insertion results in visible surface reconstruction leading to a mix geometry between the  $\text{Li}_{0.5}\text{TiO}_2$  titanate and the  $\text{LiTiO}_2$  rock salt structures.

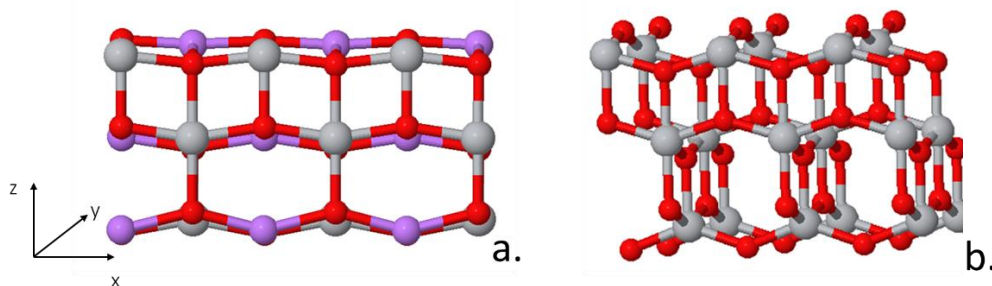


Figure 4.22: Optimized lithiated anatase (001) slab with the maximal capacity of  $x = 1$  (a) and non-lithiated slab (b). The Li ions are in purple, while the Ti and O atoms are in grey and red, respectively.

The main modifications of the geometry occur on the outer surface layers where the undercoordinated oxygen atoms seems to play a major role. The measures of angles and bond lengths are displayed in Figure 4.23 where the blue values refer to the Li-O bonds, while the black ones are related to the Ti-O ones.

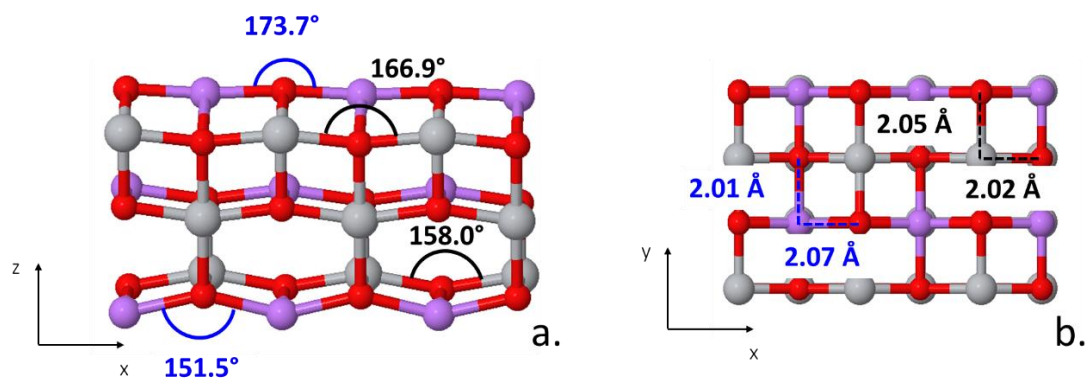


Figure 4.23: Face view (a) and top view (b) of the optimized fully lithiated (001) slab including the measures of angles and bond lengths of the O-Li-O (blue) and O-Ti-O (black) chains. The Ti ions are in grey, the O ones in red and the Li ones in purple.

Both the Ti-O and Li-O bonds involving the undercoordinated oxygen atoms are longer than the bonds involving the fully coordinated ones. Similar bond length differences were observed in section 4.5.3 ( $x = 0.67$ ) where the two outermost surfaces were lithiated. Moreover, the Li-O<sub>2c</sub>-Li chains exhibit a higher angle of 173.7°, indicating that the undercoordinated oxygens build almost flat bonds with the neighbouring Li ions, as in the rock salt structure.

In the non lithiated slab, it was observed that the O<sub>2c</sub> atoms moved outward from the surface. This phenomenon is regularly observed for the metal oxide surfaces and enhances their stabilization<sup>178</sup>. However, when the lithium is intercalated with a capacity of  $x = 1$ , the O<sub>2c</sub> atoms move inward from the surface. They seem to be attracted by the Li ions inserted into the octahedral sites located at the centre of the slab. The Figure 4.24 shows the profile of the slab where a decrease of the O-Ti-O angle by 9° can be observed. The undercoordinated oxygen atoms are located 2.71 Å away from the lithium inserted in the inner intercalation site.

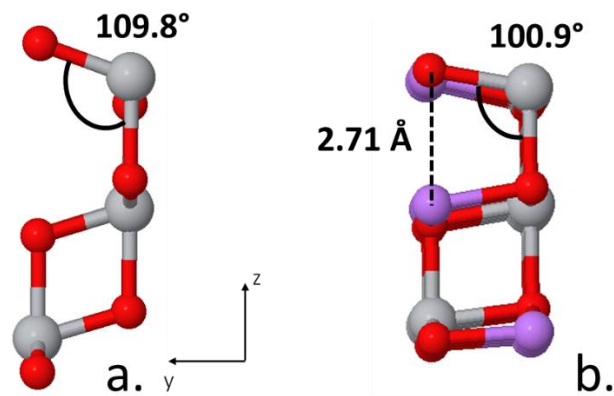


Figure 4.24: Profile of the non lithiated (a) and fully lithiated (b) anatase (001) slab. The grey, red and purple colours are related to Ti, O and Li, respectively.

The Ti-O bonds along the  $z$ -direction do not all exhibit the same lengths as it is displayed in Figure 4.25 where the  $\text{Ti}_{6c}\text{-O}_{3c}$  bond length is indicating in blue while the  $\text{Ti}_{5c}\text{-O}_{3c}$  one is shown in black. Thus, the  $\text{Ti}_{5c}\text{-O}_{3c}$  bonds are  $0.09 \text{ \AA}$  shorter than the  $\text{Ti}_{6c}\text{-O}_{3c}$  ones. The filling of the titania  $d$  orbitals upon lithium intercalation can explain this difference. The undercoordinated  $\text{Ti}_{5c}$  titania located at the outermost surfaces will host the added charge in their  $d_{xz}$  and  $d_{yz}$  orbitals, leading to a shortening of the  $\text{Ti}_{5c}\text{-O}_{3c}$  bonds. On the contrary, the fully coordinated titania atoms located at the centre of the slab accommodate the added charge in their  $d_{xy}$  orbitals, their  $d_{xz}$  and  $d_{yz}$  orbitals staying empty. Thus, the electronic structure of the fully coordinated titania facilitates the displacement of the  $\text{O}_{3c}$  atoms outward from the surface. The Mulliken population of the titania atom will be discuss in detail with the DOS below.

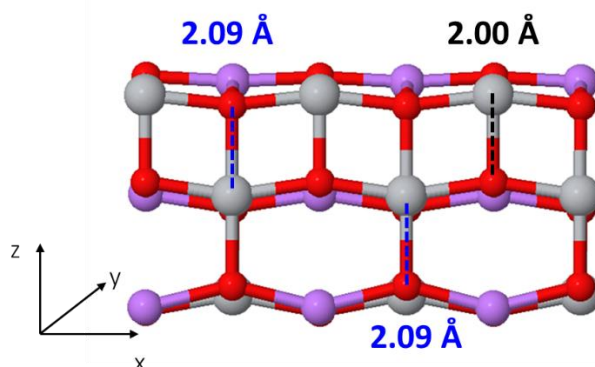


Figure 4.25: Measures of the  $\text{Ti}_{6c}\text{-O}_{3c}$  (blue) and  $\text{Ti}_{5c}\text{-O}_{3c}$  (black) bond lengths along the  $z$  axis of the fully lithiated anatase (001) slab. The Ti, O and Li ions are indicated in grey, red and purple, respectively.

The octahedral intercalation sites located at the center of the slab exhibit some differences with the ones located at the outermost surfaces, i.e. all the Ti-O and Li-O bonds located in the inner  $xy$  plane are parallel to each other and exhibit the same length of 2.03 Å. Thus, the Li-O-Li and Ti-O-Ti angles are equal and measures 162°. These values are similar to the ones observed for the optimized  $\text{Li}_{0.5}\text{TiO}_2$  titanate bulk. As it is illustrated in Figure 4.26, the lithium intercalated in the middle of the slab are four-fold coordinated and sit at the center of an octahedral site that is not distorted in the  $xy$  plane.

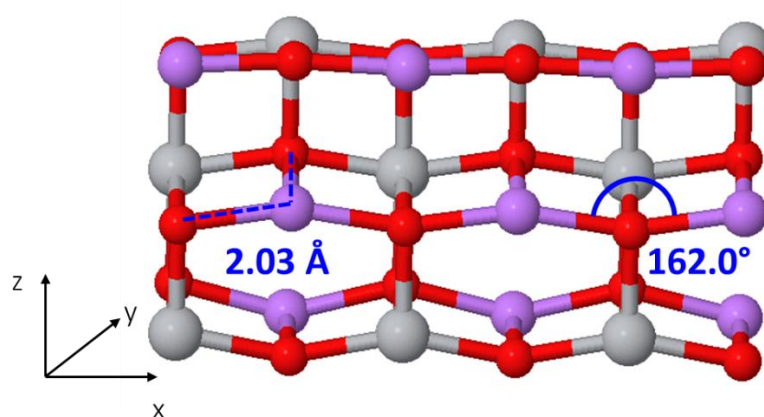


Figure 4.26: Measures of the Li-O bond lengths and angles of the octahedral sites located at the centre of the fully lithiated (001) slab. The Li, Ti and O ions are in purple, grey and red, respectively.

To summarize this part, it can be noticed that the three octahedral sites present in the slab are not equivalent once they are occupied by lithium ions. The two intercalation sites present at each side of the slab shows a different geometry from the ones located in the centre. The lithium intercalation seems to induce a “flattening” of the outermost surface layers, mainly influenced by the undercoordination of the atoms. Consequently, the outermost surfaces of the slab exhibit a structure close to the rock salt structure of  $\text{LiTiO}_2$ , whereas the geometry changes occurring in the inner slab is closer to the one observed for  $\text{Li}_{0.5}\text{TiO}_2$  titanate. As a conclusion, the changes in the geometry controlled by the undercoordinated surface atoms is acting as one of the driving mechanisms for the formation of the rich  $\text{LiTiO}_2$  phase observed at the surface of the anatase electrodes.

The DOS and Mulliken populations were analysed to have a better understanding of the electronic structure of the lithiated slab. The lithium inserted in the external octahedra gives 0.68 e to the lattice and is slightly less ionic than the one intercalated in the middle of the slab that donates 0.71 e to the surrounding atoms. The Mulliken population confirms that all the Ti ions are reduced to  $\text{Ti}^{3+}$ , the extra charge being accommodated by their  $d$  orbitals. A slight part of the lithium charge is also given to the oxygen sublattice but in a less apparent way than for the rock salt  $\text{LiTiO}_2$  bulk.

The DOS of the inner atoms of the slab is displayed in Figure 4.27 while the Figure 4.28 shows the DOS of the atoms constituting the external surface layers. In both figures, the red and green plots refer to the  $p$  and  $d$  orbitals of the indicating atom, respectively. The total DOS of the unit cell corresponds to the blue plot.

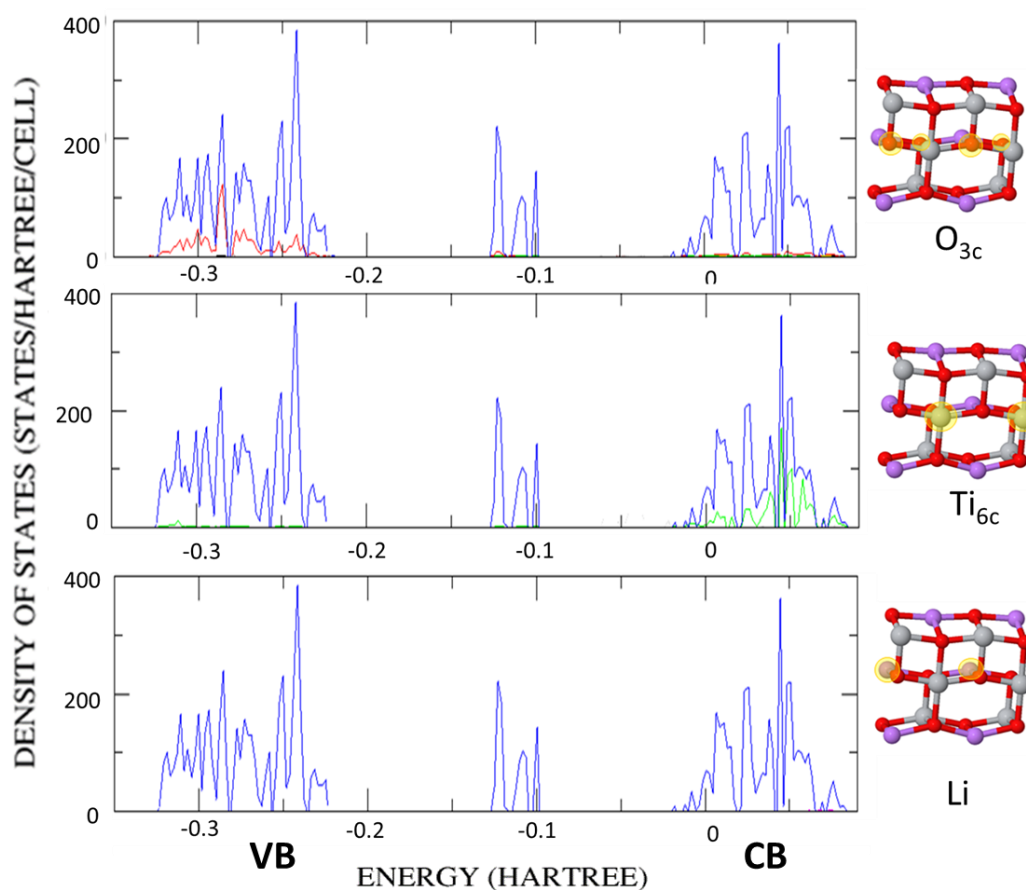


Figure 4.27 : DOS of the atoms constituting the inner wall of the fully lithiated (001) slab. The blue plot represents the total DOS of the slab while the red and green colours refer to the  $p$  and  $d$  orbital contributions of the selected atom (highlighted in yellow). VB and CB indicate the positions of the valence and conduction bands, respectively.

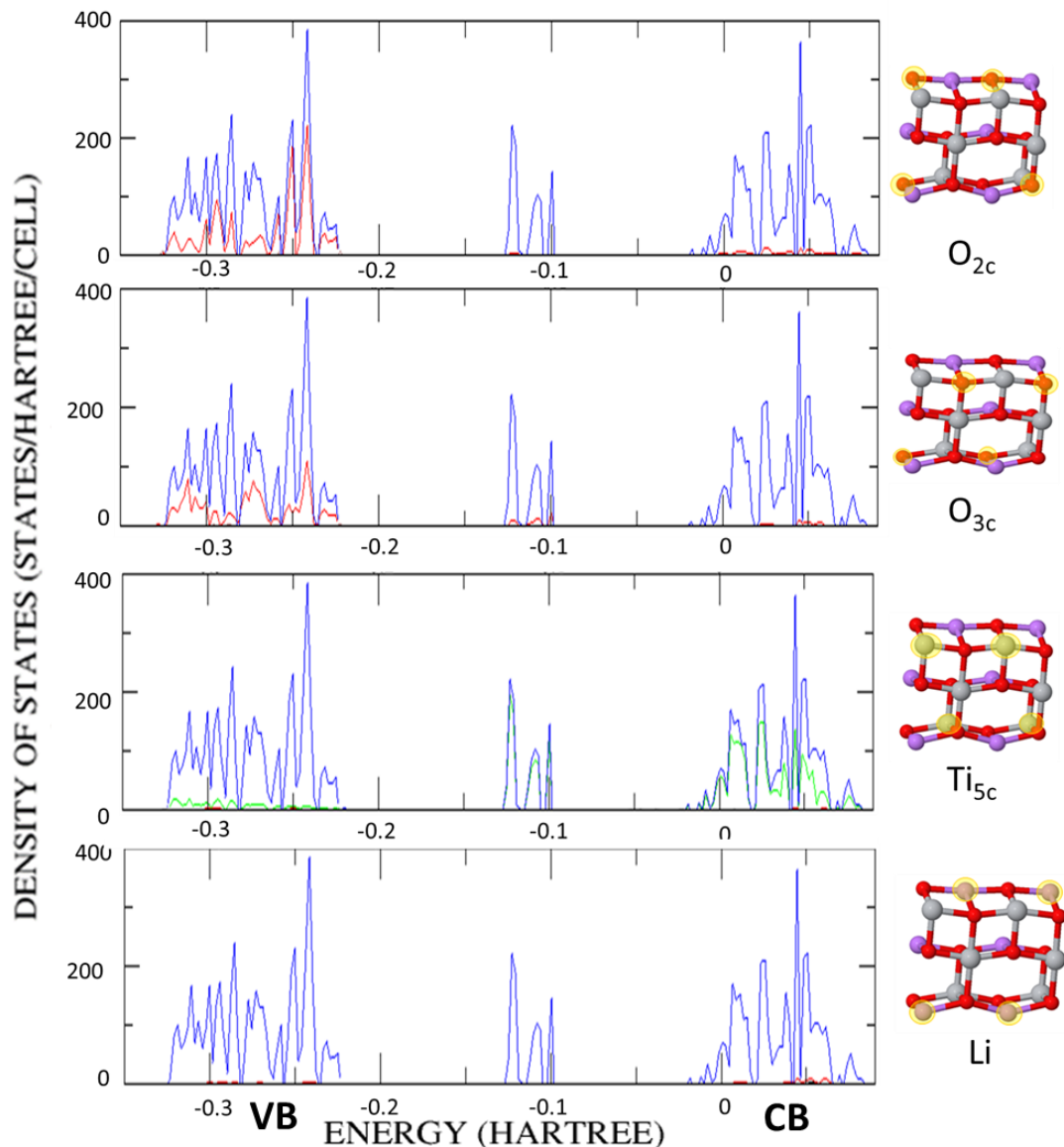


Figure 4.28 : DOS of the external atoms of the fully lithiated (001) slab. The total DOS is displayed in blue while the red and green colours are associated with the  $p$  and  $d$  orbital contributions of the selected atom (highlighted in yellow). VB and CB represent the valence and conduction bands, respectively.

It is clear from Figures 4.27 and 4.28 that the contribution of the titania atoms to the band gap and DOS depends on their position in the slab. Indeed, the DOS indicates that the undercoordinated  $\text{Ti}_{5c}$  atoms located on the external surface layers will lead to the formation of a local state in the band gap. Instead, the  $d$  orbitals of the fully coordinated Ti-atoms ( $\text{Ti}_{6c}$ ) are all located in the conduction band and do not contribute to the localised surface state.

The formation of a localized state in the band gap is explained by the Mott-Hubbard theory. In the fully lithiated slab, all the titania atoms are reduced to  $\text{Ti}^{3+}$  and host the extra charge in their  $d$  orbitals, resulting in consequent Coulomb repulsions between the different  $\text{Ti}^{3+}$   $d$  orbitals. Thus, the splitting of the surface atoms orbitals below the conduction band allows to balance the repulsions

The repartition of the extra charge in the Ti  $d$  orbitals is different from the one observed in the rock salt  $\text{LiTiO}_2$  bulk, where the  $d$  orbitals were hybridized. In the slab, the accommodation of the added charge depends on the position of the Ti ion in the structure. The Mulliken population indicates that there is no hybridization of the  $d$  orbitals in the fully lithiated slab, the extra charge is accommodated in single  $d$  orbitals. The fully coordinated Ti ions located in the central layer store the charge in their  $d_{xy}$  orbitals. Similar behaviour was observed in the  $\text{Li}_{0.5}\text{TiO}_2$  bulk titanate. Moreover, the  $\text{Ti}^{3+}$ -O bonds that are parallel to the  $xy$  plane in the bulk titanate, and the ones located in the central  $xy$  plane of the slab, exhibit similar length.

The situation is different for the external  $\text{Ti}_{5c}$  ions where the extra charges fill exclusively the  $d_{xz}$  orbitals of the titania present on the upper outermost surface, or the  $d_{yz}$  orbitals of the titania located on the lower external surface. These mentioned orbitals were already partially filled and hybridized with the  $d_{xy}$  ones when both the outermost surfaces were lithiated, as it was reported in section 4.5.3. However, when the slab is fully lithiated, the orbitals are not hybridized and the  $d_{xy}$  orbitals stay empty. The filling of the  $d_{xz}$  and  $d_{yz}$  orbitals can be explained by the orientation of the  $\text{Ti}^{3+}$ - $\text{O}_{3c}$  bonds that are parallel to the filled orbitals. The external  $d_{xy}$  orbitals are empty when the slab is fully lithiated because of the electronic repulsion of the parallel  $d_{xy}$  orbitals located at the centre of the slab that are filled with electrons. This electronic repartition may explain the geometry of the lithiated slab by shortening the  $\text{Ti}_{5c}$ -O bonds parallel to the  $z$  axis. Thus, the external  $\text{Ti}_{5c}$  cations are displaced inward from the surface, giving to the outermost layers a geometry close to the  $\text{LiTiO}_2$  rock salt structure as it was displayed in Figure 4.22.

The differences in electronic structure between the  $\text{Li}_{0.67}\text{TiO}_2$  and the  $\text{LiTiO}_2$  slabs can be visualized by comparing their respective DOS as displayed in Figure 4.29. In this figure, the green plot stands for the  $\text{Li}_{0.67}\text{TiO}_2$  slab having the two external surfaces lithiated while the magenta plot is related to the fully lithiated slab  $\text{LiTiO}_2$ .

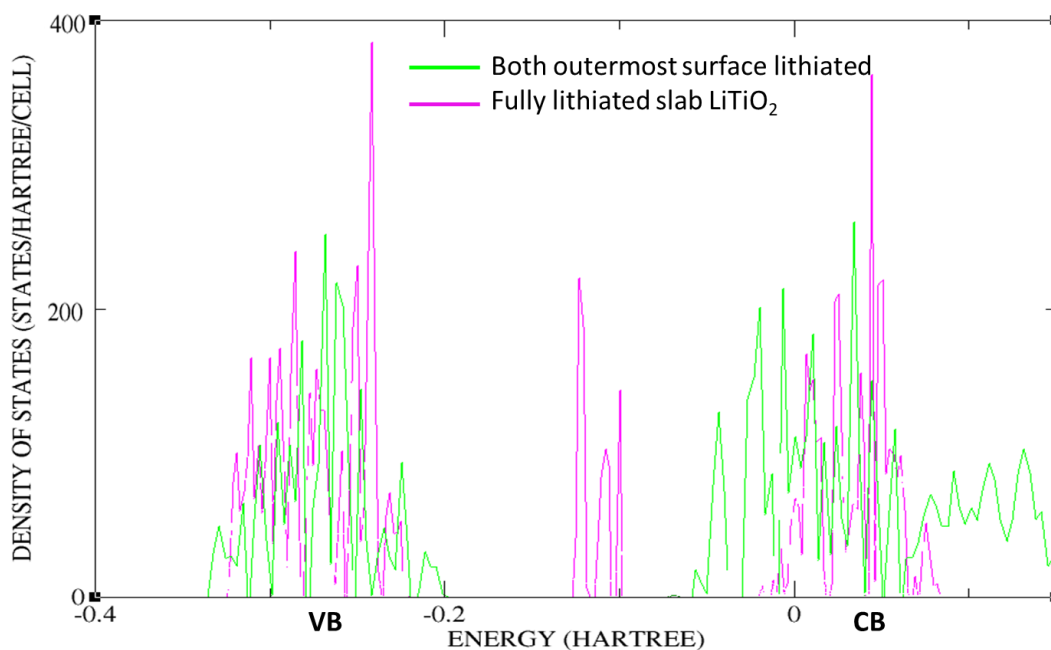


Figure 4.29: Total DOS of the anatase (001) slabs lithiated only on the external surfaces (green plot) or fully lithiated (magenta plot). VB and CB indicate the positions of the valence and conduction bands, respectively.

The absence of hybridization as well as the splitting of the Ti *d* orbitals exhibited by the fully lithiated slab can be clearly seen from the Figure 4.29. Moreover, the valence band of the LiTiO<sub>2</sub> slab is slightly lower in energy than the Li<sub>0.67</sub>TiO<sub>2</sub> one. Thus, the undercoordinated oxygen surface atoms are more stable when their neighbouring Ti<sup>3+</sup> cations do not exhibit hybridized *d* orbitals.

In order to have a better understanding of the electronic structure and conductivity induced by the lithium intercalation, the total DOS of the fully lithiated slab, the bulk Li<sub>0.5</sub>TiO<sub>2</sub> titanate and the rock salt LiTiO<sub>2</sub> were plotted on the same graph (Figure 4.30).

The DOS of the lithiated slab presents more similarities with the Li<sub>0.5</sub>TiO<sub>2</sub> titanate structure than with the rock salt structure of LiTiO<sub>2</sub>. This can be explained by the absence of orbital hybridization. Instead both structures give rise to localized states in the band gap, representing a doped system with conductivity.

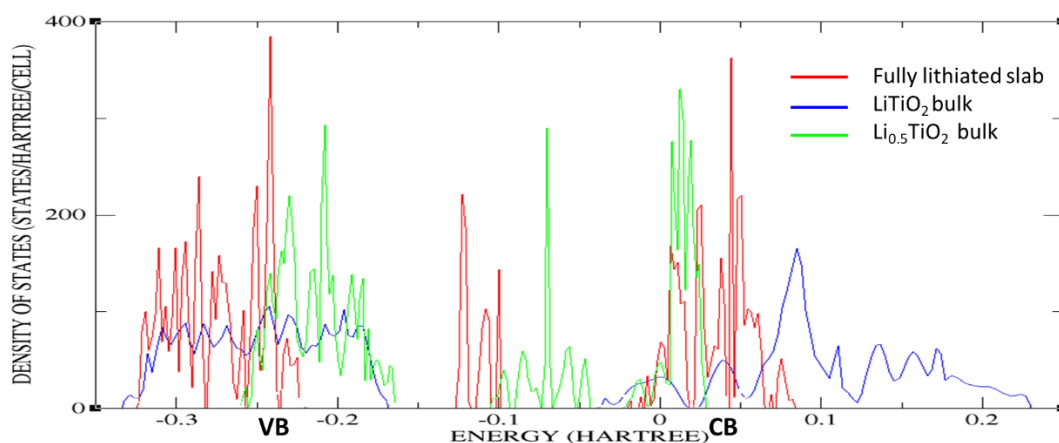


Figure 4.30: Total DOS of the fully lithiated (001) slab (red plot) compared with the half (green plot) and fully (blue plot) lithiated anatase bulk. VB and CB stand for the valence and conduction bands, respectively.

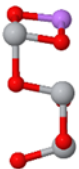
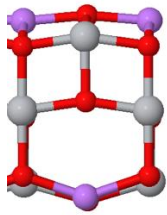
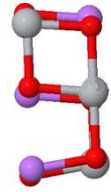
The fully lithiated slab and the Li<sub>0.5</sub>TiO<sub>2</sub> titanate bulk exhibit similar conduction bands, although the slab one contains more charges as all the slab titania atoms are reduced to Ti<sup>3+</sup>. The localized Ti *d* state present in the band gap and the valence band of the slab are lower in energy, and thus more stable, than the bulk structure ones. This can be related to the geometry of the system that is less constrained in the slab where all the Ti and O atoms are neighbouring with lithium. The Coulombic stabilization of the lithium was identified as one the main causes of the geometry changes occurring upon intercalation. However, in titanate, only half of the octahedral sites are filled with lithium, leading to a more constrained and less favourable optimized geometry for the lithium ions.

The fully lithiated LiTiO<sub>2</sub> slab exhibit a lithium intercalation energy of  $-1.86$  eV per TiO<sub>2</sub> unit. This value is 0.05 eV less negative than the one shown by the Li<sub>0.67</sub>TiO<sub>2</sub> slab, probably because of the Li-Li repulsion as it will be discussed in detail in the next section.

### 4.5.5 Intercalation voltages

When designing novel electrode materials for application in Li-ion batteries and to interpret electrochemical measurements, the voltage of the intercalation process linked to the structural changes is of great assistance. Hence, the lithium intercalation energies per  $\text{TiO}_2$  unit and the corresponding intercalation voltages were calculated for all the lithiated slabs and compared with the bulk values. The results obtained are summarized in Table 4.3.

Table 4.3: Lithium intercalation energies and voltages for different (001) slab configurations.

Li position	x (number of Li per $\text{TiO}_2$ unit)	$E_{\text{Li}}$ Intercalation (eV)	Intercalation voltage (V)
	0.33	-1.57	4.7
	0.33	-0.91	2.73
	0.66	-1.91	2.86
	1	-1.86	1.86
Titanate $\text{Li}_{0.5}\text{TiO}_2$ <b>bulk</b>	0.5	-1.68	3.37
Rock salt $\text{LiTiO}_2$ <b>bulk</b>	1	-1.27	1.27

The lowest intercalation energy equals -1.91 eV per  $\text{TiO}_2$  unit and is observed when Li ions are intercalated in both the outermost layers of the slab. This result can be explained by the geometry close to the rock salt  $\text{LiTiO}_2$  exhibited by the fully lithiated surfaces. The lithium intercalation is 0.05 eV less favourable in the fully lithiated slab because of the Li-Li repulsions that were also observed in the  $\text{LiTiO}_2$  bulk structure. These two slab intercalation energies are more negative than the ones exhibited by the  $\text{Li}_{0.5}\text{TiO}_2$  titanate and the  $\text{LiTiO}_2$  rock salt bulk structures. This result points out the particularly favourable lithium intercalation with high capacities occurring into the anatase surface.

Lithium intercalation into a singly outermost surface induces a dipole moment that will destabilize the slab and make the lithium intercalation less favourable compared to the previously mentioned  $\text{Li}_{0.67}\text{TiO}_2$  and  $\text{LiTiO}_2$  slabs. However, by comparing the two  $\text{Li}_{0.33}\text{TiO}_2$  slabs, it appears that the intercalation energy is considerably more negative when the lithium is intercalated in the outermost surface than when it is intercalated in the inner sites. This comparison highlights the favourable lithium insertion into the surface intercalation sites despite creating a dipole moment.

The corresponding intercalation voltages are displayed in the right column of the Table 4.3. The voltages being calculated versus lithium, they do not correspond to a full battery where the titania electrode is usually the anode, but to a half cell made of a titania and a lithium metal electrode. In such a half cell, the titania is the cathode while the lithium metal is the anode. Thus, the lowest intercalation voltages correspond to the highest lithium capacities, because the insertion of lithium into  $\text{TiO}_2$  corresponds to the discharge curve.

## 4.5.6 Intercalation versus lithium metal plating

The study of lithium adsorption at the surface of the slab will allow to complete this section. Lithium ions were added above the oxygen atoms located on the outermost surfaces. Both the fully coordinated and the undercoordinated oxygen atoms were alternately neighbored with lithium and the corresponding lithium intercalation energies were calculated. If the lithium is added on a single outer wall, it generates a consequent polarization of the slab that avoids any calculation convergence. Thus, the lithium must be added on both the outermost surfaces as it is displayed in Figure 4.31.

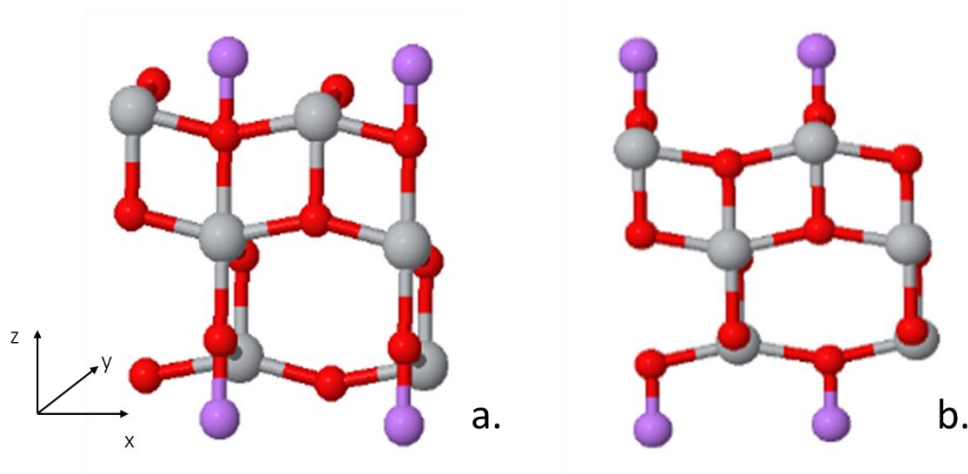


Figure 4.31: Anatase (001) slabs with lithium adsorbed on fully coordinated (a) or undercoordinated (b) surface oxygen atoms. The purple, red and grey spheres are associated with Li, O and Ti, respectively.

When the lithium ions are added above the fully coordinated oxygen, the corresponding intercalation energy equals 0.33 eV. The positive value indicates that this kind of insertion is not favourable and will destabilize the system. It was not possible to calculate the intercalation energy when the lithium ions were added above the undercoordinated oxygen atoms as the calculations did not converge. One of the reasons may be the locations of the lithium ions that are further away from the surface when they are added above the undercoordinated oxygens, and thus induce a bigger polarization of the slab.

As a result, the calculations do not show any favourable adsorption of lithium ions above the surface. Thus, the lithium will be inserted straight away to the outer octahedral intercalation sites of the slab.

## 4.6 Lithium intercalation into the nanotube

In chapter 3, the 38 Å diameter *nt*-TiO<sub>2</sub> rolled up along the  $(n_1,0)$  direction was determined as one of the most suitable models to study lithium intercalation. The study of the lithium intercalation into this nanotube has been guided by the results obtained with the corresponding slab. Thus, the lithium capacities exhibiting negative intercalation energies and easy convergences for the slab were the only ones studied in detail and with high truncation criteria for the nanotubes. Consequently, the calculations concerning the tetrahedral intercalation sites and the lithium metal plating were firstly carried out using low truncation criteria to confirm the lack of convergence, and thus the instability of the configuration, already observed for the slab. However, when the intercalation was favourable, as it was the case for lithium metal plating, the calculations were run a second time using the truncation criteria defined in chapter 2. Likewise, no supercell of the nanotube has been built as this configuration was particularly unstable for the slab.

There are two ways to intercalate lithium into the nanotube. The first one consists of firstly optimize the non-lithiated nanotube as detailed in chapter 3, and then to insert lithium in the already optimized *nt*-TiO<sub>2</sub>. This system is referred to as *nt*-S1. The second way consists of inserting the Li ions into the slab as it was described in the previous section (4.5), and then to roll up the slab to form the lithiated nanotube. This system is referred to as *nt*-S2. As discussed in section 3.5, the geometry optimization of the *nt*-TiO<sub>2</sub> generates several atomic displacements in the inner layer that break the symmetry of the structure. Thus, the intercalation sites present in the *nt*-S1 and in the *nt*-S2 do not exhibit the same geometry and need to be studied separately.

In both *nt*-S1 and *nt*-S2 systems, the curvature breaks the symmetry of the surfaces. As a result, the octahedral intercalation sites located in the internal and in the external walls of the nanotube are not equivalent and need to be studied separately.

### 4.6.1 Intercalation with lithium capacity of $x = 0.33$

The lithium is intercalated into the nanotube with a capacity of  $x = 0.33$  when only one layer of the *nt*-TiO<sub>2</sub> is lithiated.

#### 4.6.1.1 The tetrahedral intercalation sites

In section 4.5, it has been concluded that none of the tetrahedral intercalation sites present in the slab were favourable for lithium intercalation because of the electronic repulsion of the surrounding Ti atoms.

However, the Ti-O bonds located on the external wall of the nanotube have been elongated by the strain energy. Moreover, the atomic displacements occurring in the inner layer of the *nt*-TiO<sub>2</sub> during the geometry optimization increases some of the external Ti-O bonds up to 2.27 Å as discussed in section 3.5. Consequently, the space between the titania atoms of the external wall becomes more important, making the tetrahedral intercalation sites located on this wall potentially favourable to host lithium ions. As a result, lithium ions have been intercalated into the tetrahedral sites located on the external layer of the *nt*-S1.

The first tetrahedral sites to be lithiated were the ones present in the inward surface of the external wall, as shown in Figure 4.32. However, like for the slab the calculations did not converge, confirming the instability of this configuration.

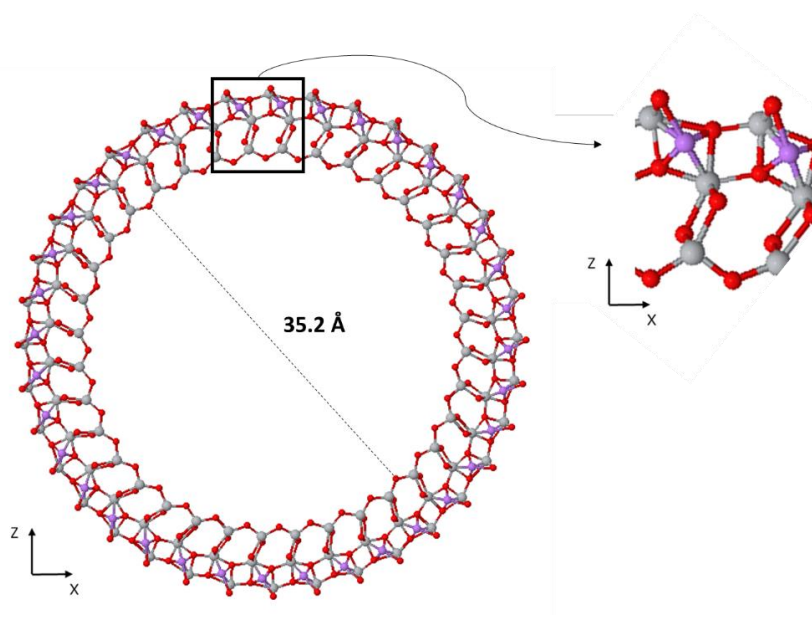


Figure 4.32: Optimized anatase (36, 0) nanotube with Li ions intercalated into the inward surface of the external wall. The Ti, O and Li elements are represented in grey, red and purple, respectively.

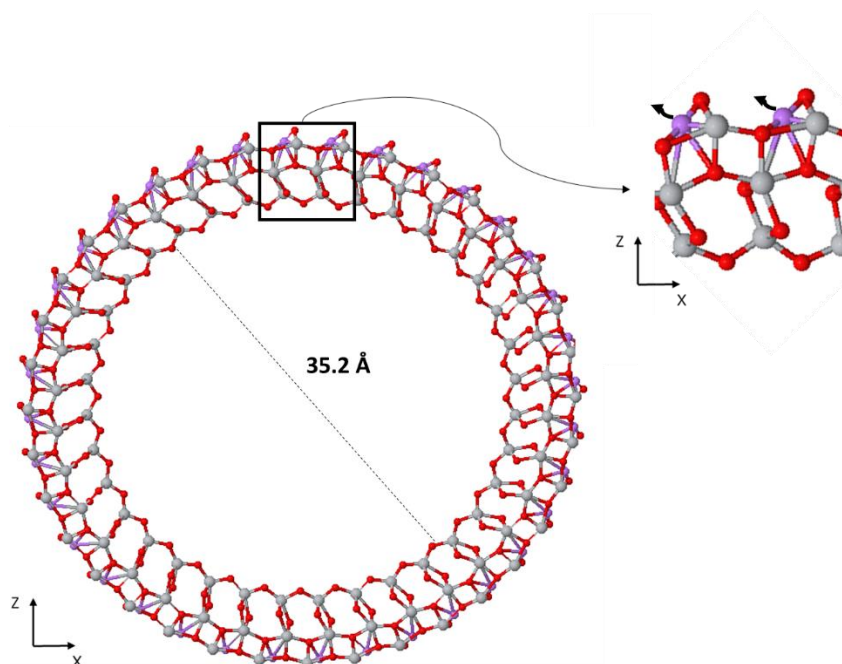


Figure 4.33: Optimized anatase (36, 0) nanotube with lithium ions inserted at the surface of the external wall. The grey, red and purple spheres represent the Ti, O and Li elements, respectively. The black arrows indicate the displacement of the Li ions upon geometry optimization.

The lithium ions were then inserted at the surface of the external wall, where the electrostatic repulsions of the titania atoms are less consequent, as shown in Figure 4.33. However, the lithium ions move to the nearest octahedral sites when the geometry is optimized as indicated by the black arrows in Figure 4.33. A similar behaviour was observed for the slab and points out the preferable lithium intercalation into the octahedral sites. As a conclusion, *nt*-TiO<sub>2</sub> do not exhibit any favourable lithium intercalation into the tetrahedral sites despite elongated Ti-O bonds in the external wall.

#### 4.6.1.2 The octahedral intercalation sites

All the lithium insertion carried out into the octahedral intercalation sites of the slab were favourable. Moreover, the lithium intercalated in the outermost layer of the slab show a more favourable intercalation energy than the ones inserted in the middle of the slab, despite the dipole moment. This was explained by the consequent surface reconstruction that stabilizes the slab.

- **The octahedral intercalation sites located on the external wall**

The first lithium intercalation into the *nt*-TiO<sub>2</sub> was carried out on the external wall of the nanotube. Lithium was inserted into both the *nt*-S1 and the *nt*-S2 nanotubes. Although these lithiated nanotubes both exhibit very similar geometry and electronic structure once they have been optimized, starting from different geometries allows a deeper understanding of the surface reconstruction induced by the lithium intercalation.

The lithium was firstly intercalated into the *nt*-S1. The octahedral sites located on the external wall are highly distorted, as it is shown in Figure 4.34a. Thus, Li-O bond lengths varying from 1.75 Å along the tube axis to 2.89 Å in the *xz* plane.

The geometry of the nanotube was then optimized a second time once the lithium ions have been intercalated. The optimized structure is displayed in Figure 4.34b. It can be observed that the second optimization considerably reduce the distortion of the octahedral sites. The Li-O bonds become equivalent in the *xz* plane and exhibit the same length of 2.14 Å. The thickness of the nanotube also increases, leading to Li-O bonds that measure 1.98 Å along the *y* axis. As a result, the lengths exhibited by all the Li-O bonds are close to the ones observed in the Li<sub>2</sub>O<sub>2</sub> bulk, highlighting the main role played by the Coulombic stabilization of the lithium ions. The lithium ions are intercalated outward of the surface and not inward as it was observed for the slab. This result indicates that the reduction of the dipole moment, induced by the lithium intercalation in a single outermost layer, is not the main driving mechanism for the external surface reconstruction of the nanotube.

Moreover, all the atomic displacements that were present in the inner layer of the *nt-S1* to absorb the strain energy disappear when the external wall is lithiated. This result indicates that the lithium intercalation seems to absorb a part of the strain energy and helps to stabilize the whole nanotube. This tendency is confirmed by the evolution of the nanotube diameter. In chapter 3, it has been observed that the diameter of the non-lithiated nanotube was reduced by 2.6 Å during the optimization. This may have been caused by the elongation of the Ti-O bonds located on the external wall up to 2.27 Å, as indicated in green in Figure 4.34a. This Ti-O bond length is far above the equilibrium value of 1.94 Å observed in the bulk. However, the second optimization of the nanotube, carried out after the lithiation, induces an increase of the nanotube diameter from 35.2 Å to 36.4 Å. Thus, the lithium intercalation, by removing the different atomic displacements present in the inner layer of the optimized nanotube, decrease the lengths of the Ti-O bond present in the external wall to 2.09 Å. As a result, the nanotube can expand to relieve the strain stress applied to the bonds located on the internal wall.

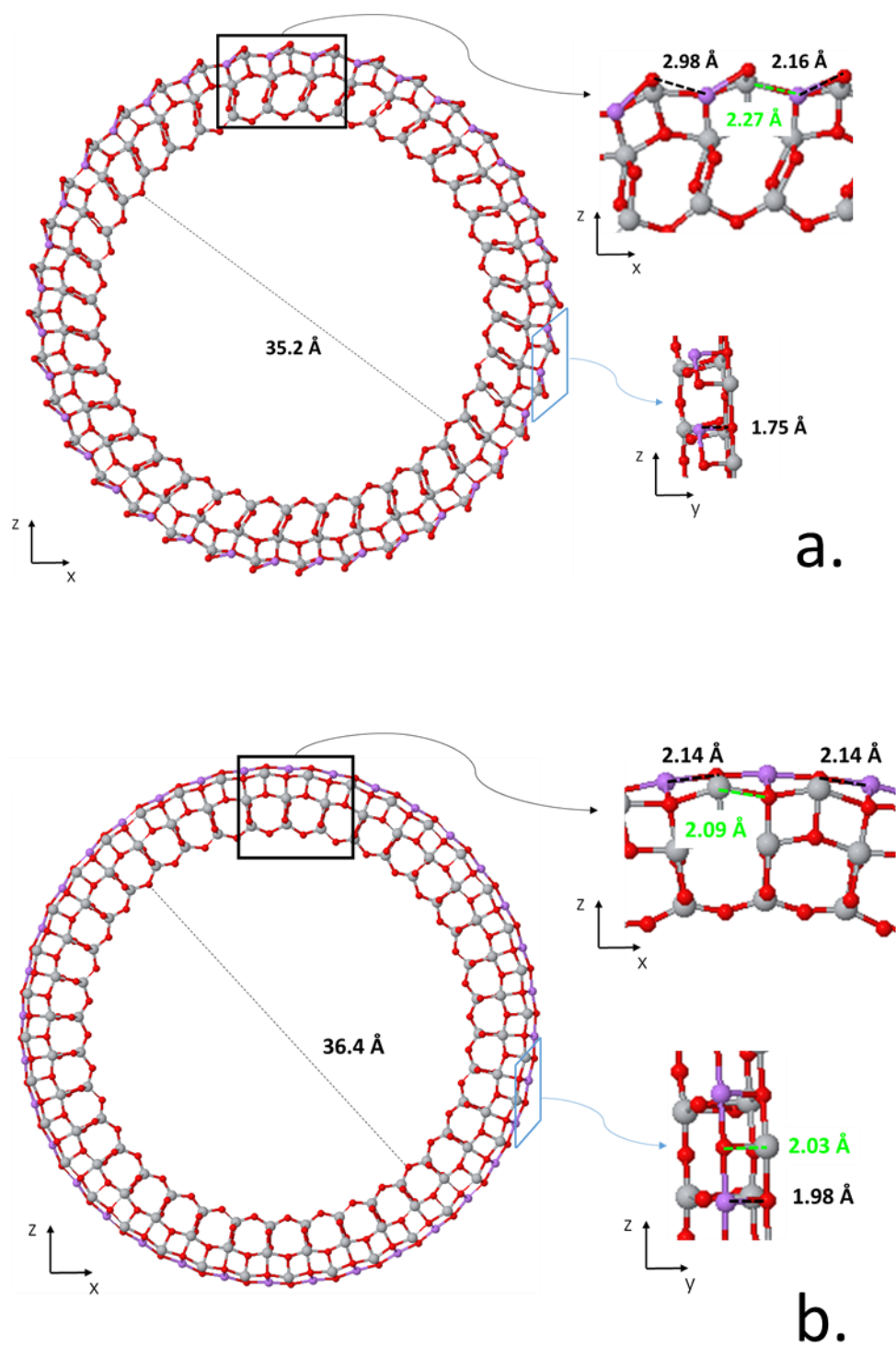


Figure 4.34: Optimized anatase (36,0) nanotube with lithium intercalated into the external wall before (a) and after (b) the final geometry optimization. The Ti atoms are in grey, the O ones in red and the Li ions in purple. The Ti-O bond lengths are indicated in green.

The lithium ions were also inserted into the *nt*-S2 for comparison, as it is displayed in Figure 4.35.

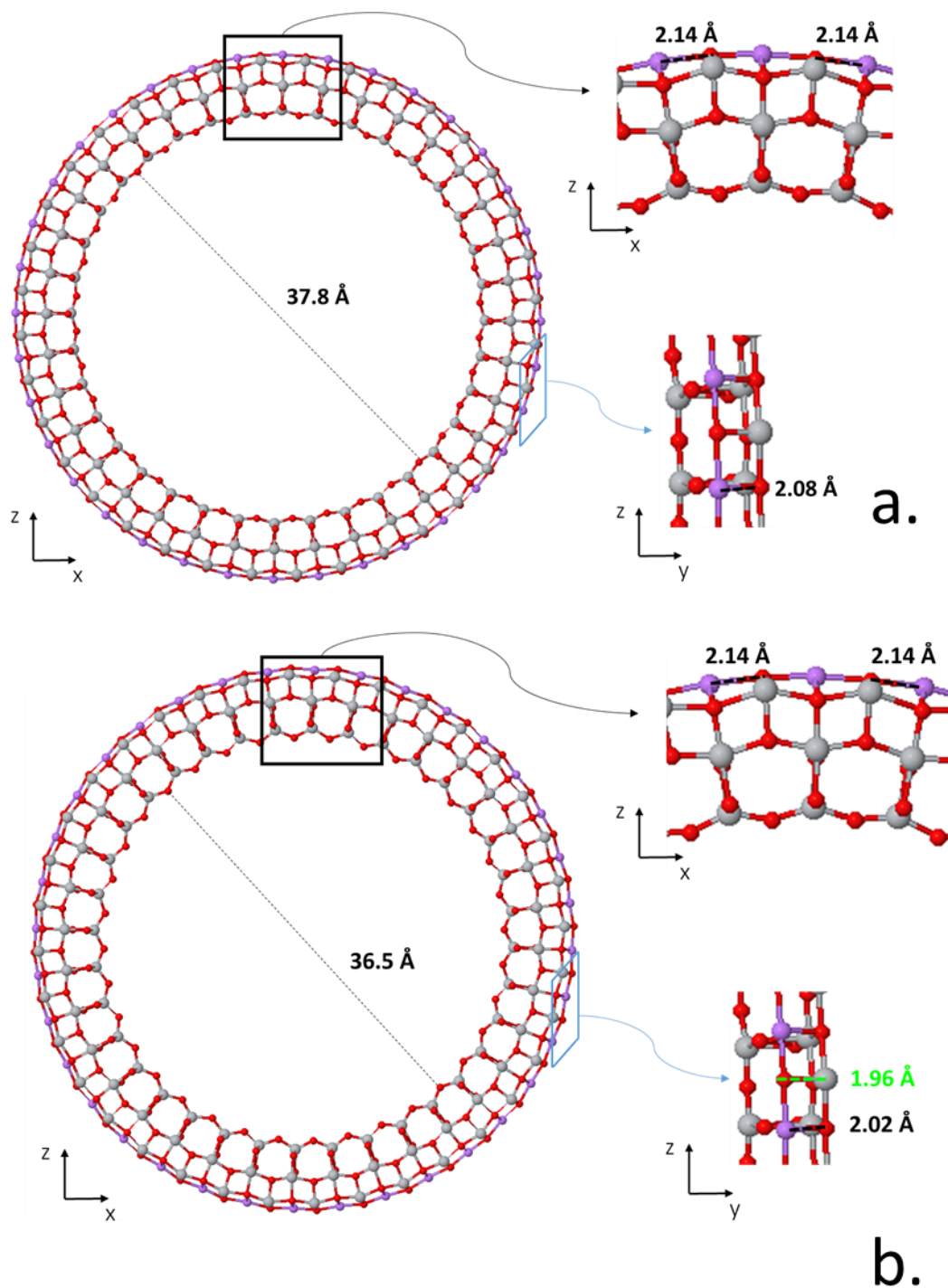


Figure 4.35: Non-optimized (a) and optimized (b) anatase (36,0) nanotubes with lithium intercalated into the external wall. The purple, red and grey spheres represent the Li, O and Ti elements, respectively.

This lithiated *nt*-S2 was built by inserting the lithium ions into the slab before rolling up the whole structure. As a result, the starting *nt*-TiO<sub>2</sub> does not contain any atomic displacement in the inner layer. However, the optimization of the lithiated nanotube does not generate atomic displacement in the inner layer neither, confirming that lithium intercalation into the external wall stabilizes the structure. The only modification concerns the Li-O and Ti-O<sub>2c</sub> bonds parallel to the *y* axis that are shorten to 2.02 Å and 1.96 Å, respectively. This modification can be explained by the Coulombic stabilization of the lithium and the reduction of the undercoordinated bond length. The latter being regularly observed in surface stabilization<sup>178</sup>.

The *nt*-S1 and the *nt*-S2 nanotubes exhibit very similar electronic structure. As a result, the comparison of the DOS and Mulliken population of these two nanotubes is not necessary. Thus, only the electronic structure of the *nt*-S1 will be detailed and discussed. The Mulliken population shows that the lithium gives 0.67 e to the lattice. This added charge is hosted by the titania atoms located on the external wall that are all reduced to Ti<sup>3+</sup>. The storage of the added charge into the *d* orbitals of the Ti<sup>3+</sup> ions depends on their position in the nanotube. The particular geometry of the nanotube leads to Ti-O bonds exhibiting many different orientations in the *xz* plane, as it was shown in Figure 4.34. Thus, there are as many Ti-O bonds parallel to the *x* axis as there are Ti-O bonds parallel to the *z* axis. As a result, the filling of the titania *d* orbitals is different for every atom.

The DOS of the titania atoms located on the external wall is shown in Figure 4.36 where the blue plot represents the total DOS of the unit cell and the green plot stands for the *d* orbitals of the titania atoms. It can be observed that the added charges give rise to a localized state in the band gap. As a result, the conductivity of the nanotube is enhanced despite the low lithium capacity of  $x = 0.33$ . This result indicates that the strain energy, by modifying the charge repartition occurring upon lithium intercalation, also influences the conductivity of the nanotubes.

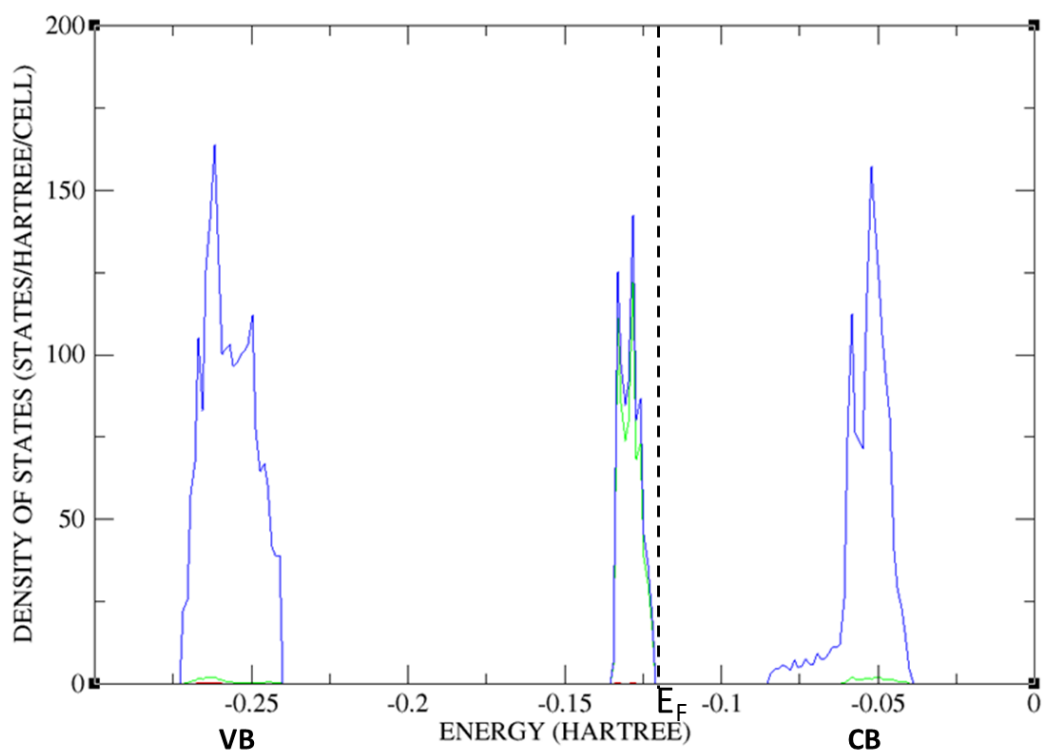


Figure 4.36: DOS of the titania atoms located on the external wall of the  $\text{Li}_{0.33}\text{TiO}_2$  anatase (36,0) nanotube. The blue and green plots are associated with the total DOS and the  $d$  orbital contributions of the Ti atoms, respectively. VB and CB represent the valence and conduction bands, respectively.

The lithium intercalation energy of both the *nt*-S1 and the *nt*-S2 nanotubes equals  $-2.42$  eV per  $\text{TiO}_2$  unit, corresponding to an intercalation voltage of 7.25 V. This very favourable intercalation energy can be explained by the absorption of the strain energy induced by the lithium intercalation. By removing the different atomic displacements present in the inner layer of the previously optimized nanotube, the lithium insertion limits the extension of the Ti-O bonds above their equilibrium values. Moreover, the reduction of the titania atoms to  $\text{Ti}^{3+}$  also contributes to the stabilization of the nanotube as the length of the  $\text{Ti}^{3+}$ -O bonds located on the external wall (that equals  $2.09 \text{ \AA}$ ) is closer to the equilibrium lengths of the  $\text{Ti}^{3+}$ -O bonds than to the  $\text{Ti}^{4+}$ -O ones. The lithium insertion into the external wall is the most favourable one reported in this thesis.

- **The octahedral intercalation sites located on the internal wall**

The lithium was then intercalated in the internal wall of the *nt-S1*. The changes in geometry induced by the lithium insertion are shown in Figure 4.37.

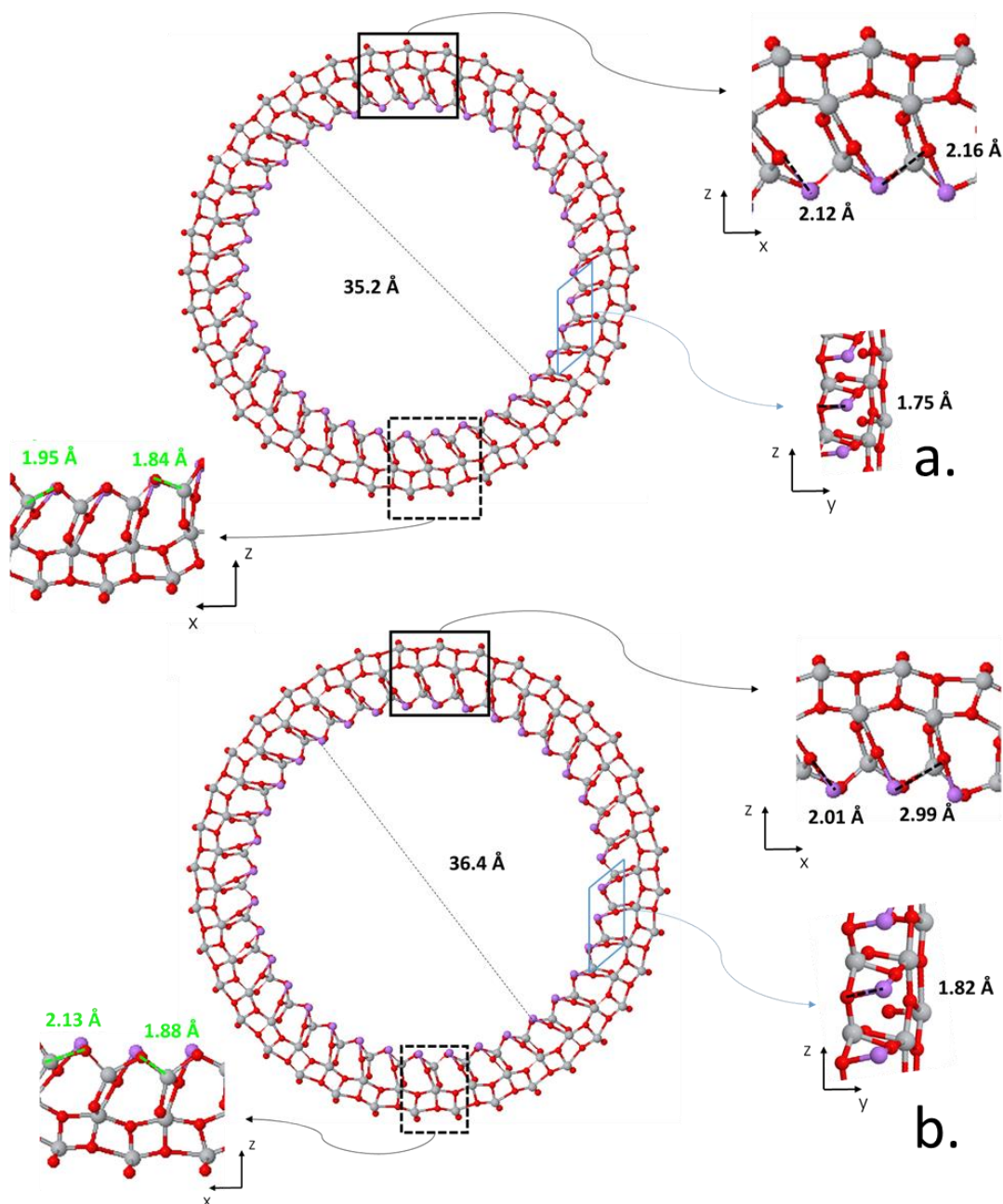


Figure 4.37: Previously optimized anatase (36,0) nanotube with lithium intercalated into the internal wall before (a) and after (b) the final geometry optimization. The Li ions are in purple while the Ti and O atoms are in grey and red, respectively. The Ti-O bond lengths are indicated in green.

The octahedral sites located in the internal wall are highly distorted by the atomic displacements present in the inner layer of the nanotube. Consequently, the Li-O bonds exhibit lengths varying between 1.75 Å and 2.16 Å, as shown in Figure 4.37a. When the final optimization is performed, the octahedral sites stay distorted and the lithium are only two-fold coordinated. This behaviour is very different from the one observed with the lithiation of the external wall, where all the atomic displacements present in the inner layer of the nanotube were released during the final optimization. Thus, the absorption of the strain energy by the lithiation of the internal wall is less consequent. The reduction of the titania atoms located on the internal wall to  $\text{Ti}^{3+}$ , combined with the Li-Li repulsion (as the lithium ions are only separated by 3 Å) limits the stabilization of the nanotube, and lead to an increase of the *nt*- $\text{TiO}_2$  diameter by 1.2 Å. As a result, all the atomic displacements that were initially present in the inner layer of the nanotube are maintained.

The lithium was then intercalated into the *nt*-S2, as it is shown in Figure 4.38, to complete the understanding of the geometry modifications induced by the lithiation of the internal wall. The octahedral sites are not distorted and the Li-O bond lengths equal 1.88 Å or 1.89 Å, as displayed in Figure 4.38a. The geometry optimization of the lithiated nanotube does not induce major geometry modifications. Both the Ti-O and the Li-O bonds are elongated, probably because of the presence of  $\text{Ti}^{3+}$  ions and the Li-Li repulsion. However, the optimization of the structure does not generate any atomic displacement in the inner layer of the nanotube. Thus, the octahedral sites are not distorted, and the Li ions are three-fold coordinated. As a result, the lithiation of the internal wall avoids atomic displacements in the inner layer and seems to absorb a part of the strain energy.

The comparison of the lithium intercalation into *nt*-S1 and *nt*-S2 nanotubes indicates that the lithiation of the internal wall participates to the stabilization of the nanotube by absorbing a part of the strain energy. However, this contribution is less consequent than the one observed with the external wall as the atomic displacements present in the inner layer of the *nt*-S1 are not released.

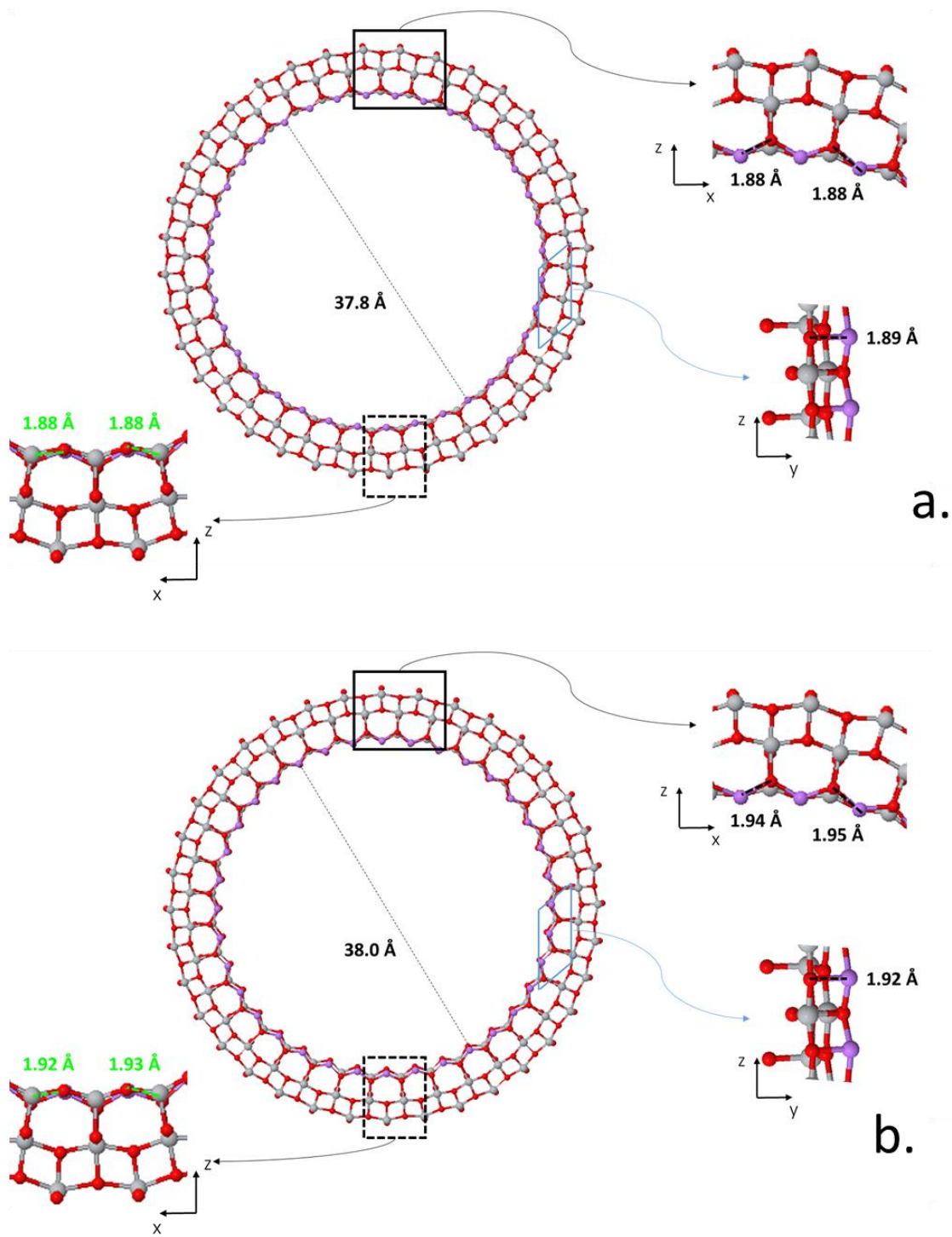


Figure 4.38: Non-optimized anatase (36,0) nanotube with lithium intercalated into the internal wall before (a) and after (b) geometry optimization. The grey, red and purple colours refer to the Ti, O and Li elements, respectively. The Ti-O bond lengths are indicated in green.

The Mulliken population of *nt*-S1 and *nt*-S2 nanotubes indicates that all the titania atoms present in the internal wall are reduced to  $\text{Ti}^{3+}$ . However, like for the lithiation of the external wall, the repartition of the added charge into the *d* orbitals is different for each  $\text{Ti}^{3+}$  ions. This is due to the multiple orientations of the Ti-O bonds.

The DOS of the  $\text{Ti}^{3+}$  ions belonging to the *nt*-S1 and *nt*-S2 previously optimized and the non-optimized nanotubes are shown in Figures 4.39 and 4.40, respectively. In both figures, the blue plot stands for the total DOS of the unit cell while the green plot corresponds to the *d* orbitals of the titania atoms. The two nanotubes do not exhibit the same electronic structure. The added charge forms a localized state in the band gap of the *nt*-S1, whereas it widens the conduction band of the *nt*-S2 without generating a splitting of the *d* orbitals. In both cases, the conductivity of the nanotubes is enhanced. These results indicate that the atomic displacements present in the inner layer of the previously optimized nanotube induces electronic repulsions between the different *d* orbitals of the  $\text{Ti}^{3+}$  ions.

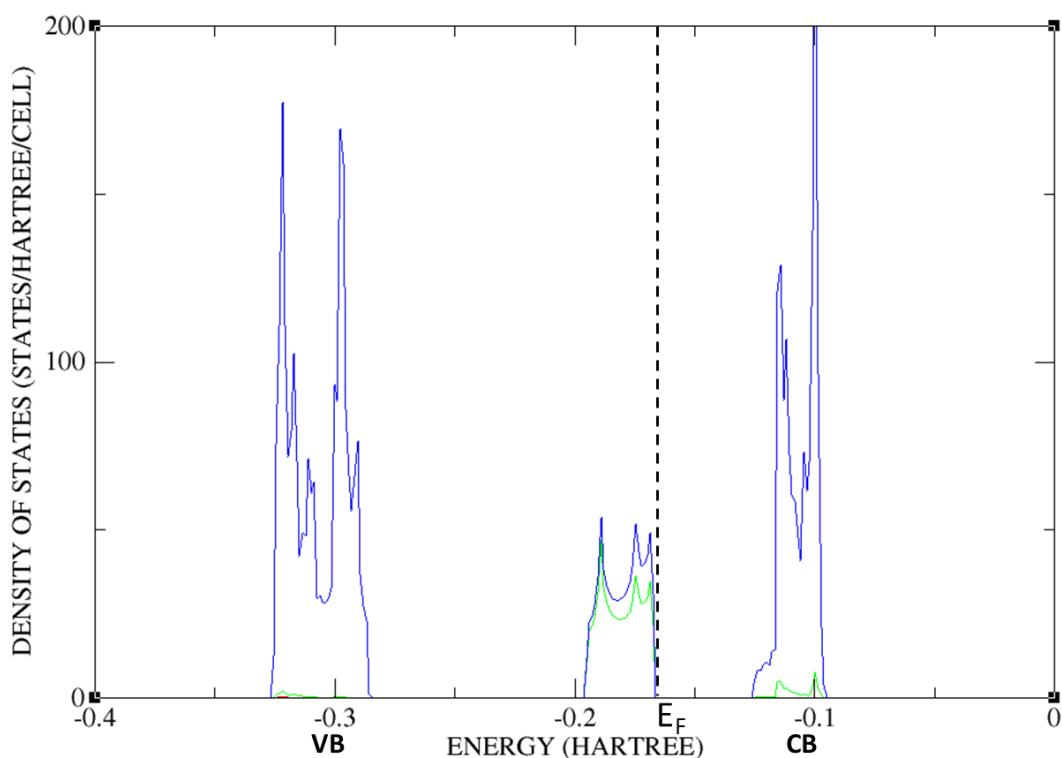


Figure 4.39: DOS of the  $\text{Ti}^{3+}$  ions of the previously optimized anatase (36,0) nanotube having its internal wall lithiated. The blue and green plots represent the total DOS and the titania *d* orbital contributions, respectively. VB represents the valence band while CB stands for the conduction band.

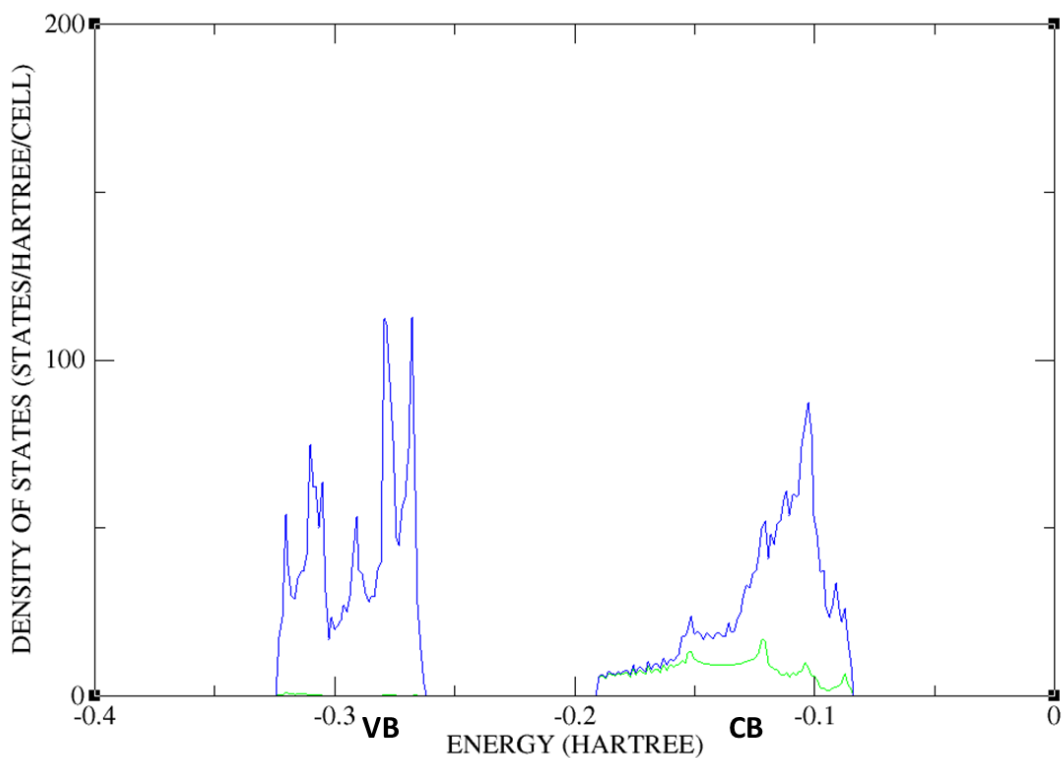


Figure 4.40: DOS of the  $\text{Ti}^{3+}$  ions of the *nt-S2* anatase (36,0) nanotube having its internal wall lithiated. The blue and green plots stand for the total DOS and the *d* orbital contribution of the Ti atoms, respectively. VB and CB represent the valence and conduction bands, respectively.

The lithium intercalation energies equal -1.31 eV and -1.09 eV for the *nt-S1* and the *nt-S2* nanotubes, respectively. The corresponding intercalation voltages equal 3.9 V and 3.3 V. In both cases the lithium insertion is favourable. The lower intercalation energy exhibited by the previously optimized nanotube can be explained by its enhanced stabilization induced by the atomic displacements in the inner layer. However, the internal wall exhibits the less favourable intercalation energies reported for the nanotube in this thesis, certainly because of the Li-Li repulsions and the presence of  $\text{Ti}^{3+}$  ions in the internal wall where the Ti-O bonds are particularly short.

- **The octahedral intercalation sites located on the central layer**

The central layer of the anatase nanotube also contains octahedral sites. The lithium ions were firstly intercalated into the *nt-S1*, as it is shown in Figure 4.41. The atomic displacements present in the inner layer of the nanotube leads to highly distorted octahedral sites exhibiting Li-O bonds having lengths varying between 1.75 Å along the nanotube axis to 2.14 Å in the *xy* plane. The lithium ions are also located 2.52 Å away from the oxygen atoms located on the external wall. The final geometry optimization does not modify the structure that remains the same as the initial one. Thus, the lithium ions stay two-fold coordinated. As a result, the lithium insertion into the central layer, like the one performed into the internal wall, does not remove the atomic displacements present in the inner layer of the nanotube. Thus, these two kinds of lithium intercalation absorb only a small part of the strain energy. As a conclusion, the lithiation of the external wall of the nanotube is the only configuration able to release the atomic displacements in the inner layer induced by the strain energy.

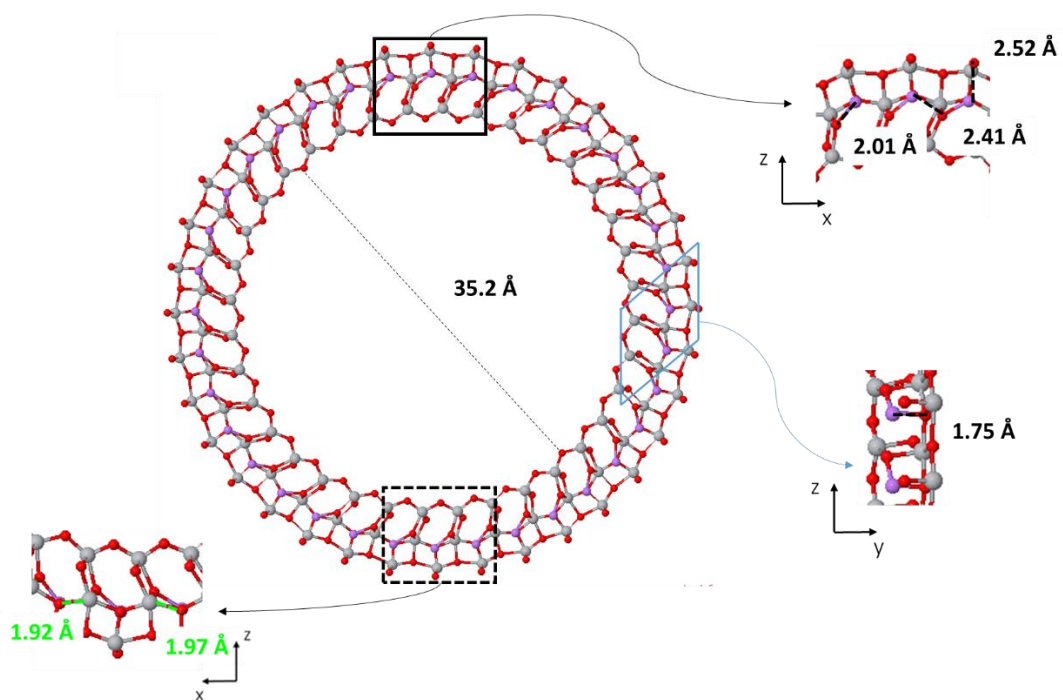


Figure 4.41: Optimized anatase (36,0) nanotube with lithium inserted into the central layer. The Li ions are in purple while the Ti and O atoms are in grey and red, respectively.

The Mulliken population indicates that added charge is shared between the titania atoms located on the central layer and the one located on the external wall. They all exhibit a different repartition of the added charge in their  $d$  orbitals because of the different orientation exhibited by the Ti-O bonds. The titania atoms located on the internal wall do not contribute to the storage of the added charge. This result indicates that the storage of extra charges is more favourable in the external wall than in the central layer.

The DOS of the titania atoms located on the central layer and on the external wall of *nt-S1* is displayed in Figure 4.42. The green plots represent the  $d$  orbitals of the titania atoms while the blue plots stand for the total DOS of the unit cell. The lithiation of the central layer forms a localized state in the band gap. Both the titania located in the central layer and in the external wall contribute to this localized state. This electronic structure highlights the electronic repulsion between the  $d$  orbitals of the different titania atoms.

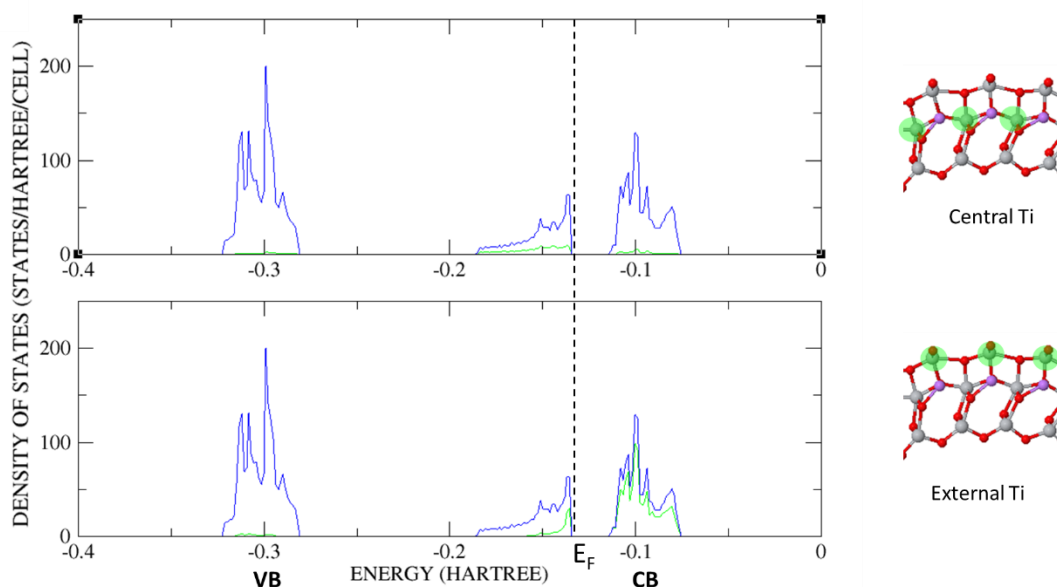


Figure 4.42: DOS of the reduced Ti ions located in the central layer and in the external wall of the previously optimized anatase (36,0) nanotube having its central layer lithiated. The total DOS is displayed in blue while the green plots represent the  $d$  orbital contributions of the selected titania atom (highlighted in green). VB and CB stand for the valence and conduction bands, respectively.

The lithium was inserted in the central layer of the *nt*-S1 with an intercalation energy of -0.28 eV, corresponding to an intercalation voltage of 0.86 V. Although the lithium insertion is still favourable, the intercalation energy is the smallest reported for the nanotube in this thesis. This weak energy can be explained by the unfavourable storage of the added charge by the titania atoms located on the central layer. Moreover, the absence of reconstruction during the geometry optimization, resulting in highly distorted octahedral sites exhibiting Li-O bond lengths far from the equilibrium value reported in Li<sub>2</sub>O<sub>2</sub>, may also contribute to the small intercalation energy.

For comparison, the lithium was also inserted into the central layer of the *nt*-S2, as it is displayed in Figure 4.43. The octahedral sites are not distorted in the *xz* plane and exhibit Li-O bond lengths included between 1.89 Å along the tube axis and 2.06 Å in the *xz* plane. The lithium ions are also located 2.38 Å away from the oxygen atoms of the external wall. The geometry optimization induces an extension of the nanotube diameter by 1 Å. The width of the nanotube is also extended as the Li-O bond parallel to the nanotube axis are also elongated from 1.89 Å to 1.92 Å. The Li-O bonds located in the *xz* plane are also modified, allowing the lithium ions to move closer to the oxygen atoms located on the external wall. As the consequence, the lithium ions are five-fold coordinated with Li-O bond lengths varying between 2.13 Å and 2.16 Å in the *xz* plane. This result highlights the major role played by the Coulombic stabilization of the lithium ions in the geometry optimization. The Li ions inserted in the central layer of the non-optimized nanotube are the only five-fold coordinated lithium inserted into a nanotube reported in this thesis. Like for the internal wall, no atomic displacement in the inner layer of the nanotube occurs during the optimization.

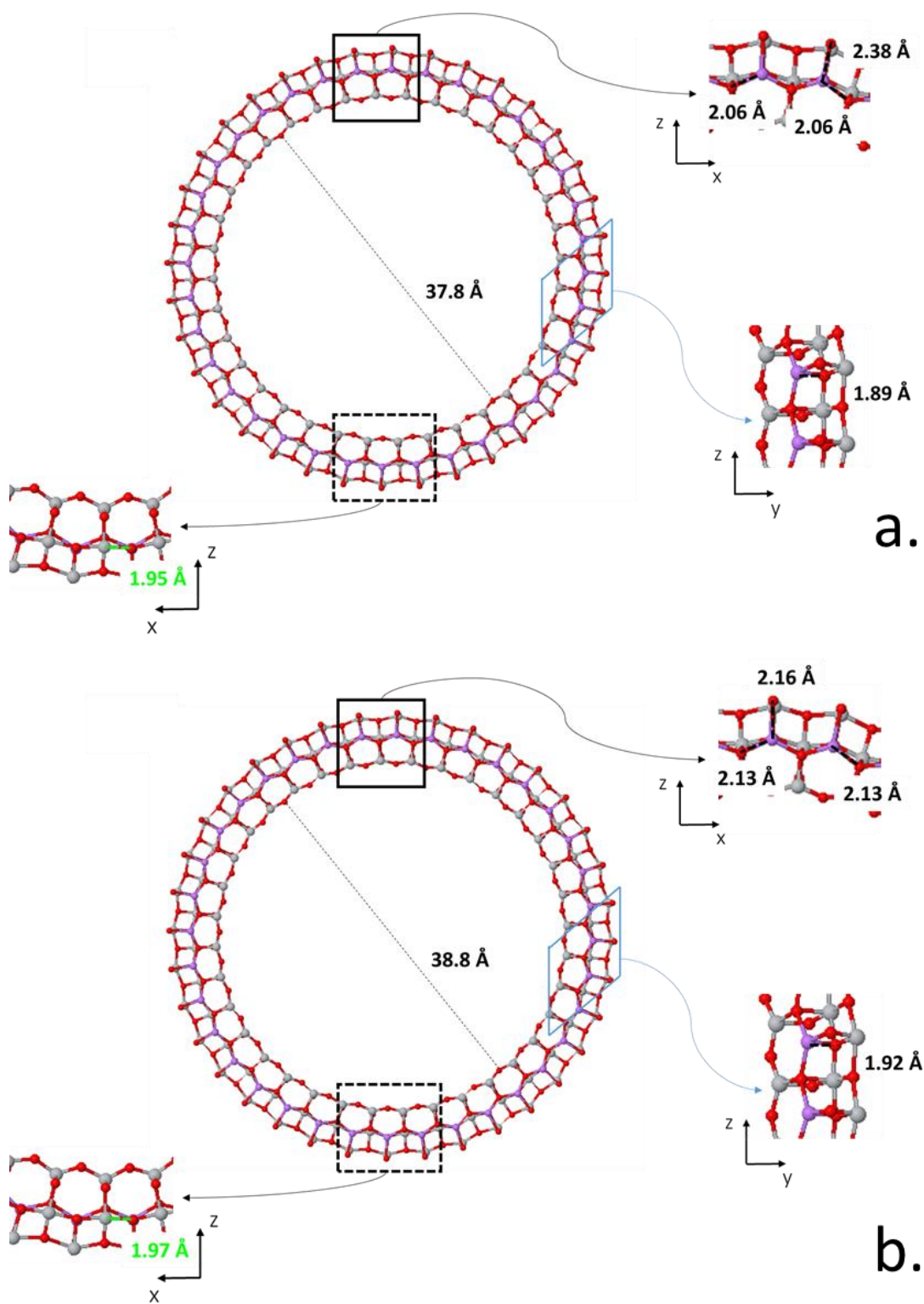


Figure 4.43: *Nt-S2* anatase (36,0) nanotube with lithium inserted into the central layer before (a) and after (b) geometry optimization. The grey, red and purple spheres represent the Ti, O and Li elements, respectively.

The Mulliken population indicates that the added charge is stored exclusively by the titania atoms located on the external wall. The titania atoms located on the central layer, that hosted a part of the added charge in the *nt*-S1, do not contribute to the storage of the added charge in the *nt*-S2. This phenomenon can be explained by the geometry of the nanotube in which the lithium ions are closer to the external wall and can be five-fold coordinated with the oxygen atoms located on this external wall. The filling of the *d* orbitals is different for each  $\text{Ti}^{3+}$  ions as it depends on the orientation of the Ti-O bonds.

The DOS of the titania atoms located on the central layer and on the external wall are displayed in Figure 4.44. The blue plot refers to total DOS of the unit cell while the green plot stands for the *d* orbitals of the titania atoms.

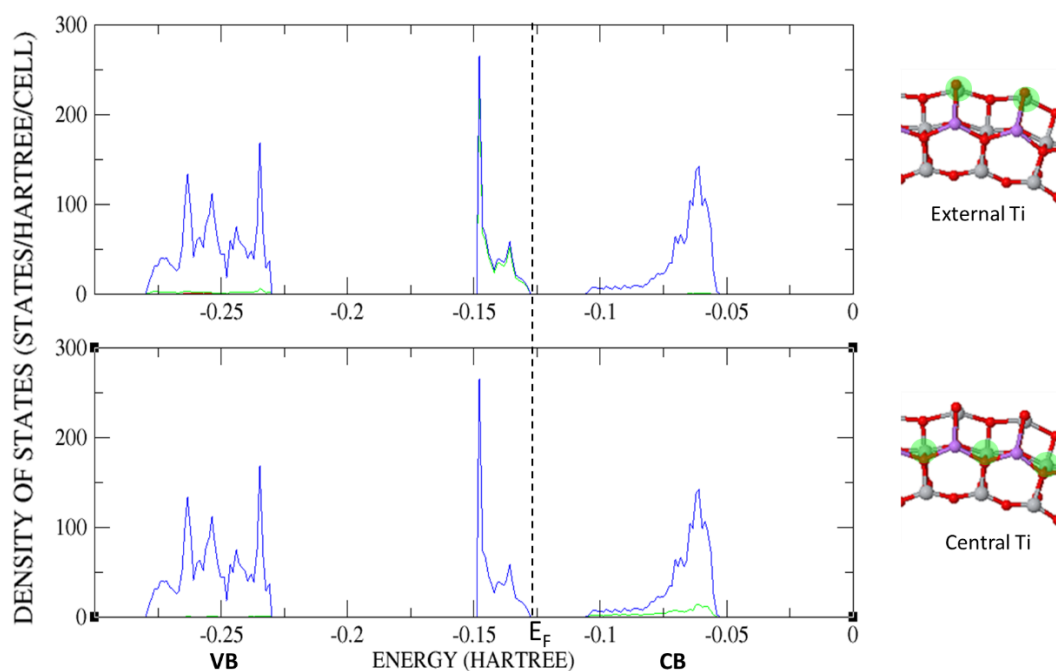


Figure 4.44: DOS of the  $\text{Ti}^{3+}$  ions located on the external wall and the central layer of the *nt*-S2 anatase (36,0) nanotube having its central layer lithiated. The blue and green plots refer to the total DOS and the Ti *d* orbital contributions, respectively. VB represents the valence band while CB stands for the conduction band.

The DOS indicates that the added charge stored in the  $d$  orbitals of the titania atoms located on the external wall forms a localized state in the band gap. Similar results were observed with the lithiation of the external wall and indicates that the strain energy favours the electronic repulsions between the different  $d$  orbitals of the  $\text{Ti}^{3+}$ . The titania atoms located on the central layer do not contribute to the localized state, despite being located closer to the lithium ions. As a result, the storage of added charges is more favourable in the external wall than inside the nanotube.

The lithium was inserted into the central layer of the  $nt$ -S2 with an intercalation energy of  $-1.37$  eV, corresponding to an intercalation voltage of  $4.1$  V. This intercalation energy is more favourable than the one reported for the  $nt$ -S1, probably because of the Li-O bond lengths that are closer to the equilibrium values reported for  $\text{Li}_2\text{O}_2$ . The lithium insertion into central layer is also more favourable than the one reported for the internal wall, certainly because of the reduction of the Li-Li repulsions.

#### **4.6.2 Intercalation with lithium capacities of $x = 0.67$ and $x = 1$**

The lithium intercalation was favourable in the slab when the two outermost surfaces were lithiated, corresponding to an intercalation ratio of  $x = 0.67$ . The same configuration for the nanotube consists of inserting lithium into both the internal and the external walls. As the lithiation of the external wall led to a release of all the atomic displacements present in the inner layer of the nanotube, the lithium was intercalated into the non-optimized  $nt$ -S2 nanotube, as shown in Figure 4.45. However, the calculations did not converge because of the unstable repartition of the added charges. The two added charges were stored by the same titania atom, reducing it to  $\text{Ti}^{2+}$ . Moreover, the titania atoms located on the external and on the internal walls were alternately reduced to  $\text{Ti}^{2+}$ , making the calculation oscillating and impossible to converge.

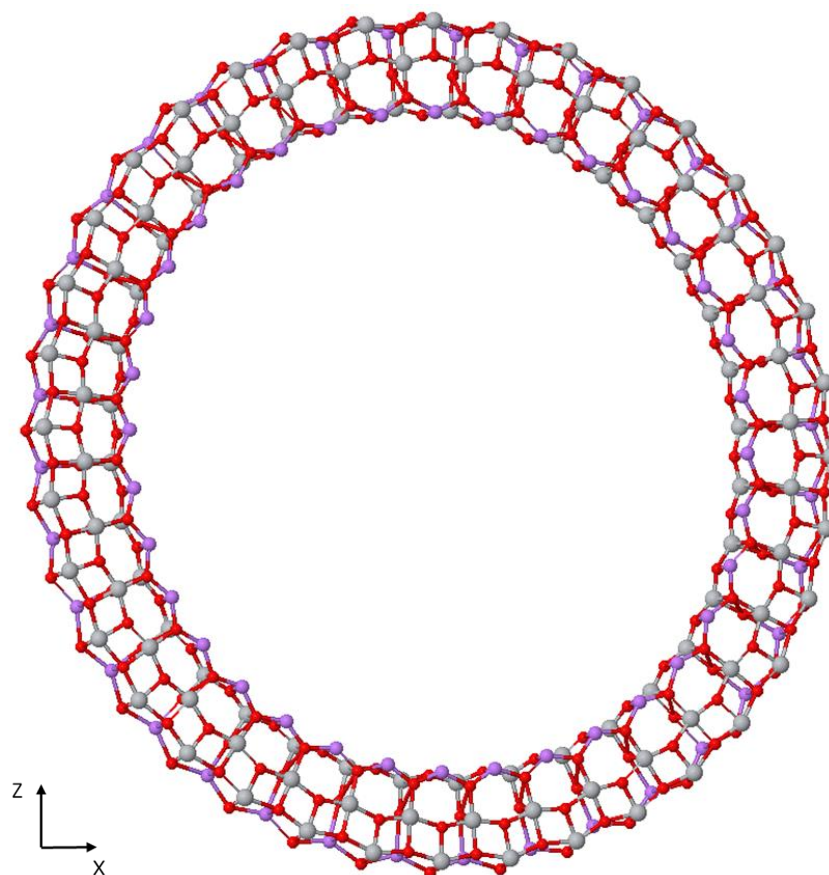


Figure 4.45: Non-optimized anatase (36,0) nanotube having both its internal and external walls lithiated. The Li ions are in purple while the Ti and O atoms are in grey and red, respectively.

Extra lithium ions were then intercalated into the central layer of the non-optimized nanotube, leading to a lithium capacity of  $x = 1$ . However, the calculation did not converge neither because of alternating reduction of the titania atoms.

### 4.6.3 Intercalation versus lithium metal plating

The lithium metal plating was not favourable at the surface of the slab. However, the lithiation of the external wall of the nanotube was particularly favourable. Moreover, the geometry of the nanotube increases the distances between the different Li ions located at the surface of the external wall, reducing the Li-Li repulsion and making their possible adsorption more favourable. Thus, lithium ions were added at the surface of the external wall of the *nt-S2*, above the fully coordinated  $O_{3c}$  atoms, as displayed in Figure 4.46.

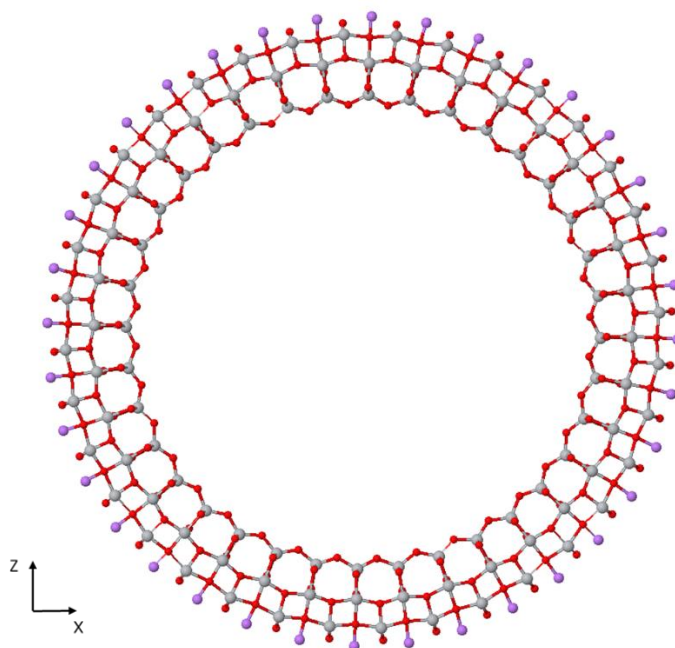


Figure 4.46: *Nt-S2* anatase (36,0) nanotube with lithium adsorbed at the surface of the external wall. The purple, red and grey spheres represent the Li, O and Ti elements, respectively.

The geometry optimization does not generate structure changes but the presence of lithium at the surface of the external wall avoids atomic displacement in the inner layer of the nanotube. The lithium adsorption is favourable as the intercalation energy equals  $-0.68$  eV per  $\text{TiO}_2$  unit, corresponding to a voltage of 2.1 V. However, this energy is weaker compared to the one reported for the lithiation of the octahedral sites located on external wall, that equals  $-2.42$  eV per  $\text{TiO}_2$  unit. It can be clearly seen from Figure 4.46 that both the octahedral sites of external wall and the adsorption sites above the fully coordinated oxygens cannot host lithium simultaneously because of the Li-Li repulsion. Thus, the lithium intercalation will primarily occur into the octahedral sites. However, the favourable adsorption above the  $\text{O}_{3c}$  atoms certainly supports the diffusion of lithium ions from the electrolyte to the intercalation sites.

Lithium ions were also added above the undercoordinated  $\text{O}_{2c}$  atoms of the external wall. However, the calculations did not converge, indicating that this kind of adsorption is not favourable. The lithium ions were not inserted at the surface of the internal wall as the short distance between the Li ions does not make their adsorption favourable.

#### 4.6.4 Intercalation voltages

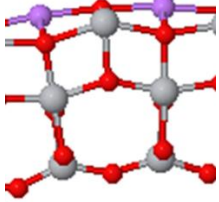
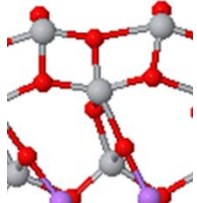
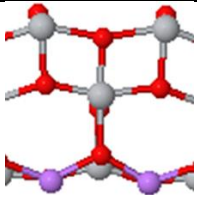
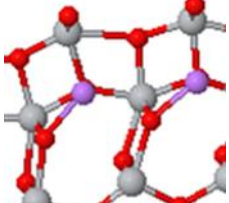
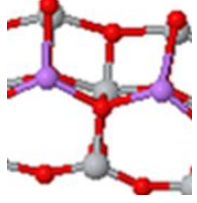
For a better understanding of the *nt*-TiO<sub>2</sub> behaviour as electrode, the lithium intercalation energies per TiO<sub>2</sub> unit and the corresponding intercalation voltages calculated for all the Li<sub>0.33</sub>TiO<sub>2</sub> nanotubes are summarized in Table 4.4 where they are compared with the bulk value. As discussed in section 4.6.2, the calculations did not converge for the nanotubes having capacities above  $x = 0.33$ .

The most favourable intercalation energy, observed when the Li ions are intercalated into the external wall, is the most negative one reported for lithium in this thesis. Thus, this intercalation is more favourable than the ones reported for anatase bulk or flat surface and highlights the reactivity of the nanotubes structure towards lithium. The corresponding voltage is particularly high and indicates that this lithiation will occur very early in the discharge process. The lithium intercalation into the external wall stabilizes the nanotube and removes the different atomic displacements in the inner layer induced by the strain energy.

The lithium intercalation into the central layer is more favourable when no atomic displacements are present in the inner layer of the nanotube. In that case, the corresponding intercalation energy is equal to -1.37 eV per TiO<sub>2</sub> unit and is more favourable than the one observed for the corresponding (001) slab that equalled -0.91 eV (as discussed in section 4.5.5). Thus, by removing the atomic displacements present in the inner layer of the nanotube, the lithiation of the external wall also supports the lithium insertion into the central layer.

Even though the lithium intercalation energies reported for the internal wall are negative, they are the less favourable reported for nanotubes in this thesis. This can be explained by the formation of short Ti<sup>3+</sup>-O bonds and the Li-Li repulsion. As a result, the corresponding intercalation voltages are relatively low, indicating that the lithiation of the internal wall will occur after the lithiation of the external wall and the central layer in the discharge process.

Table 4.4: Lithium intercalation energies and voltages for different anatase (36,0) nanotube configurations.

Li position	x (number of Li per TiO <sub>2</sub> unit)	E <sub>Li Intercalation</sub> (eV)	Intercalation voltage (V)
 <i>Nt-S1 and nt-S2</i>	0.33	-2.42	7.25
 <i>Nt-S1</i>	0.33	-1.31	3.9
 <i>Nt-S2</i>	0.33	-1.09	3.3
 <i>Nt-S1</i>	0.33	-0.28	0.86
 <i>Nt-S2</i>	0.33	-1.37	4.1
Titanate Li <sub>0.5</sub> TiO <sub>2</sub> <b>bulk</b>	0.5	-1.68	3.37

## 4.7 Conclusion

- The lithium intercalation into anatase was studied using the lithium 3s2p basis set developed by Doll et al.<sup>185</sup>.
- No favourable lithium intercalation into the tetrahedral sites was found for the bulk, slab and nanotube anatase. Consequently, only the insertions into the octahedral sites were studied in detail in this thesis and were all favourable.
- Lithium was intercalated with an energy of -1.68 eV per TiO<sub>2</sub> unit into the bulk anatase when the capacity was equal to  $x = 0.5$ . The geometry constraints do not allow any orthorhombic distortion of the lattice upon lithium intercalation, but highlight the major role played by the Coulomb stabilization of the lithium on the reorganization of the lattice. This lithiation induces the formation of a localized state in the band gap that enhances the conductivity.
- The lithium insertion into bulk anatase with a capacity of  $x = 1$  leads to a slightly distorted rock salt structure. The corresponding intercalation energy equals -1.27 eV per TiO<sub>2</sub> unit and is less favorable than the one calculated for the Li<sub>0.5</sub>TiO<sub>2</sub> bulk because of the Li-Li repulsions. The LiTiO<sub>2</sub> band gap does not contain any localized state but is 0.2 eV smaller than the TiO<sub>2</sub> bulk anatase one.
- The most favourable lithium insertions into the slab were found for capacities superior to  $x = 0.67$ , indicating that the lithiation into the anatase surface will spontaneously occur with high ratios. The intercalation energies equal -1.91 eV for the Li<sub>0.67</sub>TiO<sub>2</sub> slab and -1.86 eV for the fully lithiated LiTiO<sub>2</sub> slab. Both values are more negative, and thus more favourable, than the one calculated for the Li<sub>0.5</sub>TiO<sub>2</sub> titanate bulk.
- The lithiation of the two outermost surfaces, corresponding to the Li<sub>0.67</sub>TiO<sub>2</sub> slab, reduces the titania ions present on the surfaces to Ti<sup>3+</sup>, and induces a hybridization of their  $d_{xy}$  orbitals with the  $d$  orbitals parallel to the O<sub>3c</sub>-Ti-O<sub>3c</sub> chains. These changes of the electronic structure, combined with a higher overlap population in the Ti<sup>3+</sup>-O<sub>3c</sub> bonds than in the Ti<sup>3+</sup>-O<sub>2c</sub> ones, induces visible surface reconstruction. Thus, the lithiated outermost surfaces exhibits a mixed geometry between the LiTiO<sub>2</sub> rock salt and the Li<sub>0.5</sub>TiO<sub>2</sub> titanate structures. This lithiation of the outermost surfaces does not form a localized state in the band gap but reduces the value by 0.2 eV.

- In the fully lithiated  $\text{LiTiO}_2$  slab, the  $\text{Ti}^{3+}$  ions located on the outermost surfaces do not exhibit hybridized orbitals but store the added charge in the  $d$  orbital that is parallel to the  $\text{Ti}^{3+}\text{-O}_{3c}$  bonds. This electronic structure leads to the formation of a localized state in the band gap, resulting in a doped system with enhanced conductivity. The changes in electronic structure also affect the geometry of the surfaces by shortening the  $\text{Ti}_{5c}\text{-O}$  bonds parallel to the  $z$  axis, and thus displace the external  $\text{Ti}^{3+}$  ions inward from the surfaces. The undercoordinated oxygen atoms present on the outermost surfaces are also displaced inward as they are attracted by the Li-fulfil intercalation sites located at the centre of the slab. As a result, a rich  $\text{LiTiO}_2$  phase having a geometry close to the rock salt structure is formed at the surface of the anatase electrode for a capacity of  $x = 1$ .
- The lithiation of the nanotube with capacities superior to  $x = 0.33$  leads to the reduction of the titania ions to  $\text{Ti}^{2+}$  as the the two added charges are stored together by the same ion. However, the titania atoms located on the external and on the internal walls were alternately reduced to  $\text{Ti}^{2+}$ , avoiding the convergence of the calculations. Thus, only the capacity of  $x = 0.33$  was considered for the nanotubes in this thesis.
- On the contrary of the slab, the storage of the added charge into nanotube titania  $d$  orbitals is different for every ion as it depends of the orientations of the Ti-O bonds.
- Except for the external wall, the strain energy present in the nanotubes considerably limits the geometry reconstruction that is supporting the lithium intercalation.
- The most favourable lithium intercalation into the nanotube was found for the external wall with a corresponding intercalation energy of  $-2.42$  eV per  $\text{TiO}_2$  unit. Moreover, this lithiation stabilizes the nanotube by reducing the external titania to  $\text{Ti}^{3+}$ , leading to external Ti-O bonds having a length close to the equilibrium value reported for the  $\text{Ti}^{3+}\text{-O}$  bonds.
- The lithiation of the external wall of the previously optimized nanotube releases all the atomic displacements present in the inner layer of the  $nt\text{-TiO}_2$  and widen its diameter. These geometry changes will facilitate the lithiation of the central layer that is  $1.09$  eV per  $\text{TiO}_2$  unit more favourable when no atomic displacements are present in the inner layer.

- All the lithium intercalations into the nanotube induce the formation of a localized state in the band gap, except the one performed into the internal wall of the *nt-S2*.
- The only favourable lithium adsorption reported in this work was found above the fully coordinated oxygens located on the external wall of the nanotube.

# Chapter 5

## Sodium intercalation into anatase

### 5.1 Aims

Just like lithium, sodium ions have been successfully intercalated into anatase nanoparticles<sup>141</sup>, nanorods<sup>144</sup> or nanotubes<sup>145</sup>. However, the crystalline structures reported for the sodiated anatase differ depending on the nanoarchitecture of the electrode and the voltage applied. For example, a phase transformation into a rhombohedral layered structure was reported for the anatase nanoparticles<sup>143</sup>. On the contrary, the XRD measurements carried out on nanorods<sup>144</sup> and nanotubes<sup>145</sup> indicate that the anatase structure is retained even at 0.0 V vs. Na<sup>+</sup>/Na. However, a more recent study<sup>7</sup> using XANES analysis reported an irreversible transformation of the anatase nanotubes into amorphous ones for potentials below 0.5 V vs. Na<sup>+</sup>/Na.

The electrochemical measurements<sup>7,145</sup> carried out on the anatase *nt*-TiO<sub>2</sub> indicate that the Na ions rather adsorb at the nanotube surface than diffuse inside the *nt*-TiO<sub>2</sub>. Moreover, the XANES analysis show an irreversible phase transformation of the *nt*-TiO<sub>2</sub> surface into amorphous sodium titanate where the Ti<sup>4+</sup> ions are partially reduced to metallic Ti.

The main goal of this section is to carry out a comparative study of the sodium intercalation into the anatase bulk, slab and nanotube. No computational study of sodium intercalation into anatase surfaces or nanotubes has been carried out to the best of our knowledge. Thus, sodium is inserted into the bulk and slab with different capacities in order to better understand the formation of the amorphous phase observed for low potentials or in the surface region. Like for lithium, sodium is also inserted into the nanotube to isolate the influence of the strain energy and determine the most favourable intercalation sites present in the *nt*-TiO<sub>2</sub>. Sodium ions were also added above the slab and nanotube surfaces to check if the high surface reactivity towards sodium shown by the experimental studies can lead to a sodium metal plating.

## 5.2 Choice of Sodium basis set

Sodium intercalation was studied in this thesis following the same approach as for lithium. Thus, the first step was to determine the more appropriate sodium basis set allowing to identify the most favourable intercalation sites present in the different  $\text{TiO}_2$  systems. The basis set must be able to define both the energy of the sodium in a metallic bulk as well as an intercalated ion into a  $\text{TiO}_2$  structure. Some basis sets can fail to describe metallic bulk because of linear dependencies even though they are able to describe correctly the properties of sodium as an intercalated ionic species. When using this kind of basis sets, the metallic bulk energy is replaced by a single point calculation performed on one sodium atom. Moreover, the intercalation voltage calculated using one basis set may not be correct. As a result, the most suitable sodium basis set was determined by comparing the sodium intercalation energies and intercalation voltages obtained using different basis sets with the reference values reported in the literature. The sodium intercalation energy was calculated using the Equation 1.4 while the intercalation voltage was obtained from the Equation 1.6 (both detailed in section 1.2.6).

Three sodium basis sets<sup>184,192,193</sup> reported on the CRYSTAL website library<sup>172</sup> (8-511G<sup>192</sup>, 8-511(1d) G<sup>193</sup> and TZVP<sup>184</sup>) were tested in this thesis. Full geometry optimizations of the sodium metallic bulk were firstly performed using the three basis sets. All the calculations were carried out using the B3LYP functional, shrink factor and cut-off threshold described in chapter 2. The 8-511G<sup>192</sup> basis set failed to describe the metallic bulk because of the linear dependencies. As a result, a single point calculation was performed instead using this basis set.

The metallic sodium belongs to the same space group  $\text{Im}\bar{3}\text{m}$  ( $\text{Im-3m}$ ) as lithium, and exhibits a body centred cubic structure<sup>194</sup>. However, the sodium lattice parameter is 0.81 Å larger than lithium and equals 4.29 Å. The primitive unit cell of the sodium bulk is shown in Figure 5.1.

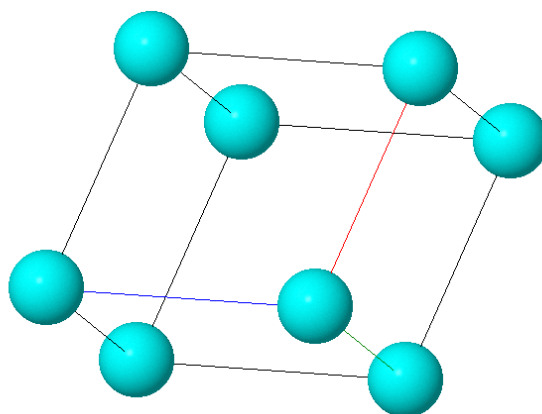


Figure 5.1: Primitive unit cell of sodium bulk.

The total energies obtained with the different basis sets are displayed in Table 5.1. The two basis sets that successfully optimized the bulk structure were the Na\_8-511(1d) G<sup>193</sup> and the Na\_TZVP<sup>184</sup> ones. They both lead to the same total energy of - 4414.330 eV.

Table 5.1: Total bulk energies or single point energy obtained with the different Na basis sets.

Basis set	Sodium bulk energy (eV)	Single point energy (eV)
Na_8-511G <sup>192</sup>		-4408.169
Na_8-511(1d) G <sup>193</sup>	-4414.330	
Na_TZVP <sup>184</sup>	-4414.330	

The different Na basis sets were then employed to calculate the sodium intercalation energy into bulk anatase, using the same TiO<sub>2</sub> bulk supercell (1 x 1 x 2) as the one used for lithium in chapter 4. This supercell allows to insert sodium every second octahedral site, corresponding to a capacity of Na<sub>0.5</sub>TiO<sub>2</sub>. The non-optimized Na<sub>0.5</sub>TiO<sub>2</sub> supercell is displayed in Figure 5.2.

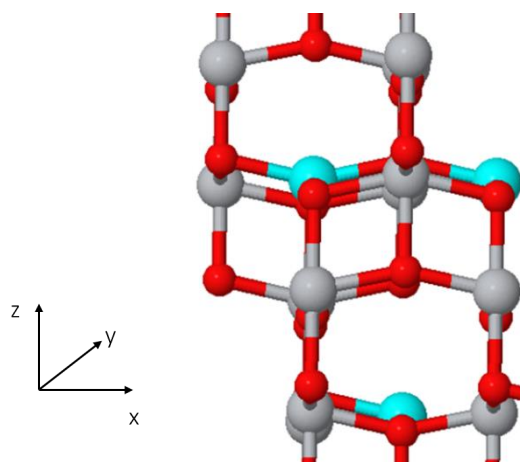


Figure 5.2: Non-optimized  $\text{Na}_{0.5}\text{TiO}_2$  supercell. The Na ions are in blue while the Ti and O atoms are in grey and red, respectively.

The  $\text{Na}_{0.5}\text{TiO}_2$  supercells were then fully optimized and the total energies of the sodiated bulks were calculated. The values obtained were combined with the sodium bulk energies reported in Table 5.1 to calculate the sodium intercalation energies and the corresponding voltages for each basis set. The results obtained are summarized in Table 5.2.

Table 5.2: Sodium intercalation energies and voltages calculated with different basis sets.

\* Note Na\_8-511G is based on single point calculation.

Basis set	Sodium intercalation energy (kJ/mol)	Sodium intercalation voltage (V)
Na_8-511G <sup>192</sup>	-879.02	18.22
Na_8-511(1d) G <sup>193</sup>	-172.13	3.57
Na_TZVP <sup>184</sup>	-183.57	3.81

The sodium redox potential equals -2.71 V and is only 0.3 V above the lithium one<sup>195</sup>. Thus, the closest intercalation voltage is obtained with the Na\_8-511(1d) G basis set. However, as the Na\_TZVP and the Na\_8-511(1d) G basis sets gave close results, their computational times were compared. It appears that the calculations performed using the Na\_8-511(1d) G basis sets are two times faster. As a result, the Na\_8-511(1d) G basis set was chosen to study the sodium intercalation into anatase in this thesis.

## 5.3 Sodium intercalation into $\text{Na}_{0.5}\text{TiO}_2$ anatase bulk

In order to gain a deeper understanding of the influence of the sodium ions on the anatase structure, the first step consists on studying the effect of sodium intercalation into a bulk anatase. This study will allow to generate a set of data from where the differences between the intercalation into a bulk and into surfaces can be studied. The  $\text{Na}_{0.5}\text{TiO}_2$  bulk will be also compared with the  $\text{Li}_{0.5}\text{TiO}_2$  one.

The previous theoretical studies<sup>25,106,149</sup> point out the unfavourable intercalation of sodium into the tetrahedral intercalation sites due to its large radius. As a result, no intercalation of Na ions into the tetrahedral sites of bulk anatase have been considered. Thus, sodium was intercalated under its reduced form (with eleven electrons) into half of the octahedral sites of the (1 x 1 x 2) anatase supercell described in the previous section. The same supercell was used to study lithium intercalation into bulk in chapter 4 and corresponds to a capacity of  $x = 0.5$ . The geometry of the sodiated anatase bulk was then fully optimized (both the lattice parameters and the atomic positions were allowed to relax). However, the number of symmetry operators was kept constant during the geometry optimization as this constraint will be later necessary for the modelling of nanotubes. Consequently, all the anisotropic modifications of the lattice, including the orthorhombic distortion, can not be observed. The bond lengths of the optimized anatase bulks before and after sodium intercalation are displayed in Figures 5.3a and 5.3b.

The Mulliken population analysis indicates the oxidation of the sodium atoms to  $\text{Na}^+$  ions, as well as the reduction of the adjacent titania ions to  $\text{Ti}^{3+}$ . The reduced  $\text{Ti}^{3+}$  ions are highlighted in green in Figure 5.3b. The sodium intercalation induces an elongation of the Ti-O bonds located in the  $xy$  plane. This elongation is more pronounced for the  $\text{Ti}^{3+}$ -O bonds than for the  $\text{Ti}^{4+}$ -O ones, that equal 2.11 Å and 2.09 Å, respectively. The bond length modifications along the  $z$  direction are also influenced by the oxidation state of the titania ions: the  $\text{Ti}^{3+}$ -O bonds are slightly elongated by 0.03 Å whereas the  $\text{Ti}^{4+}$ -O bonds are shorten to 1.90 Å.

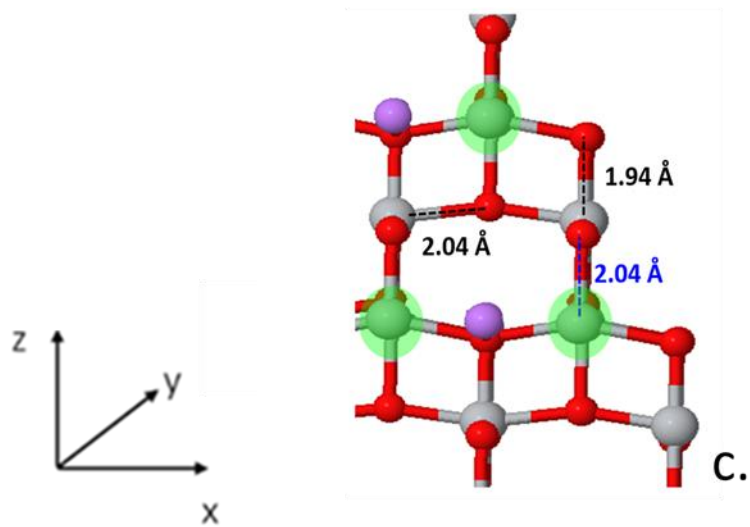
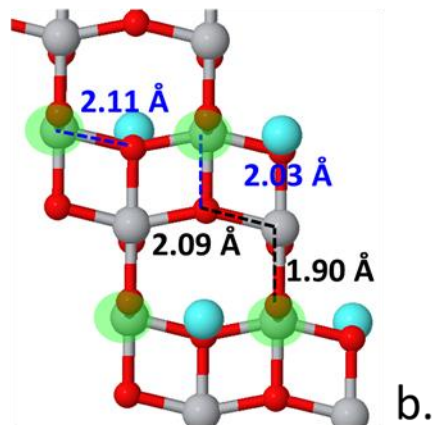
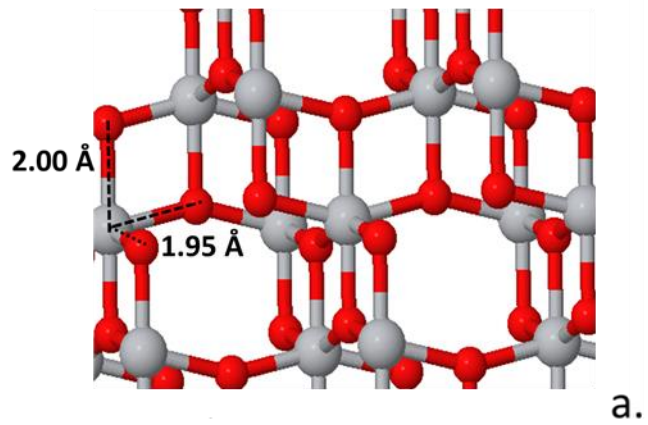


Figure 5.3: Optimized anatase  $\text{TiO}_2$  (a),  $\text{Na}_{0.5}\text{TiO}_2$  (b) and  $\text{Li}_{0.5}\text{TiO}_2$  (c) bulks. The Na and Li ions are in blue and purple, while Ti and O elements are in grey and red, respectively. The reduced  $\text{Ti}^{3+}$  ions are highlighted in green.

Similar geometry modifications were induced by lithium intercalation, as it can be observed from Figure 5.3c. However, the elongation of the Ti-O bonds located in the  $xy$  plane is more pronounced for the  $\text{Na}_{0.5}\text{TiO}_2$  bulk than for the  $\text{Li}_{0.5}\text{TiO}_2$  one. It is interesting to note that the situation is reversed for the Ti-O bonds parallel to the  $z$ -axis that are shorter when Na is intercalated. These results are in agreement with the previous study reported by Lunell et al.<sup>106</sup>.

The octahedral sites of the optimized  $\text{Na}_{0.5}\text{TiO}_2$  bulk are distorted as the oxygen atoms located in the  $xy$  plane are not all at the same height but sit above and below a central plane. The sodium ions are located in the middle of this distorted octahedral sites and are fourfold coordinated. The Na-O distances equal 2.11 Å in the equatorial plane and 2.62 Å along the  $z$ -axis, as displayed in Figure 5.4. This result disagrees with previous studies<sup>25,143,149</sup> that mentioned a displacement of the Na ion varying between 0.4 Å and 0.6 Å along the  $z$  direction, allowing the sodium to be fivefold coordinated. The absence of displacement along the  $z$  direction is explained by the fixed number of symmetry operators that avoids any anisotropic modification of the unit cell.

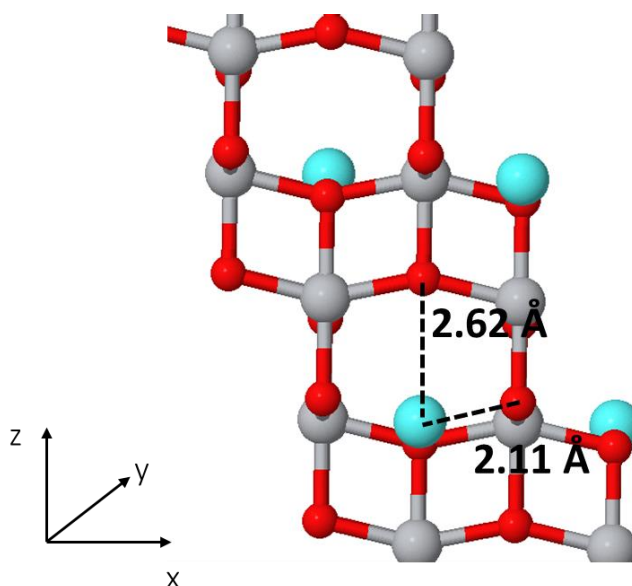


Figure 5.4: Measures of the Na-O distances for  $\text{Na}_{0.5}\text{TiO}_2$  bulk. The blue, grey and red colours represent the Na, Ti and O elements, respectively.

The Mulliken population analysis indicates that the extra charge is accommodated exclusively by the  $d_{xy}$  orbital of the adjacent titanium ion, reducing it to  $\text{Ti}^{3+}$ . Thus, there is no hybridization of the titania  $d$  orbitals, as it was already observed for the  $\text{Li}_{0.5}\text{TiO}_2$  bulk.

The partial DOS of the  $\text{Na}_{0.5}\text{TiO}_2$  bulk are shown in Figure 5.5 where the blue plot stands for the total DOS of the bulk while the red and green colors represents the  $p$  and  $d$  orbital contributions of the indicated atom, respectively. The  $s$  orbitals do not appear on the graph as they do not contribute to the band gap. The main modification induced by the sodium intercalation is a splitting of the  $d$  orbitals. The  $d_{xy}$  orbitals, that is now filled with an extra charge, form a localized state in the band gap located 0.87 eV below the conduction band edge. This phenomenon was already observed for lithium intercalation and is explained by the Mott-Hubbard theory.

The total DOS of the  $\text{Na}_{0.5}\text{TiO}_2$  and  $\text{Li}_{0.5}\text{TiO}_2$  bulks are compared in Figure 5.6 where slight differences can be observed. The gap between the localized state and the edge of the conduction band is slightly larger for the  $\text{Na}_{0.5}\text{TiO}_2$  bulk than for the  $\text{Li}_{0.5}\text{TiO}_2$  one (with 0.87 eV and 0.62 eV respectively), in agreement with previous theoretical studies<sup>148,149</sup>. The valence band of the  $\text{Na}_{0.5}\text{TiO}_2$  exhibits a smaller density than the  $\text{Li}_{0.5}\text{TiO}_2$  one.

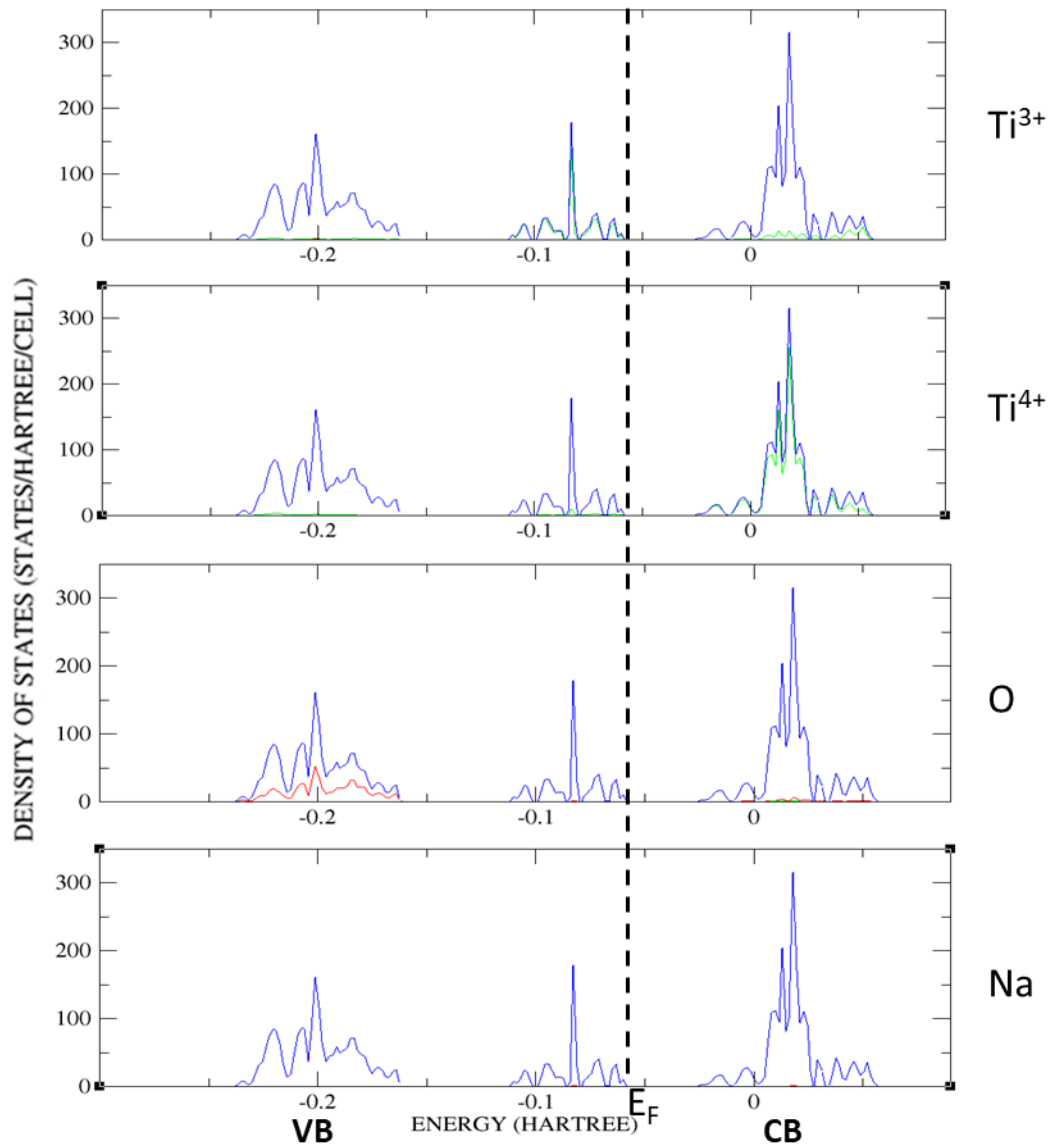


Figure 5.5: DOS of the  $\text{Na}_{0.5}\text{TiO}_2$  bulk where VB and CB indicate the positions of the valence and conduction bands. The blue plot represents the total DOS while the red and green plots stand for the  $p$  and  $d$  orbital contributions, respectively.

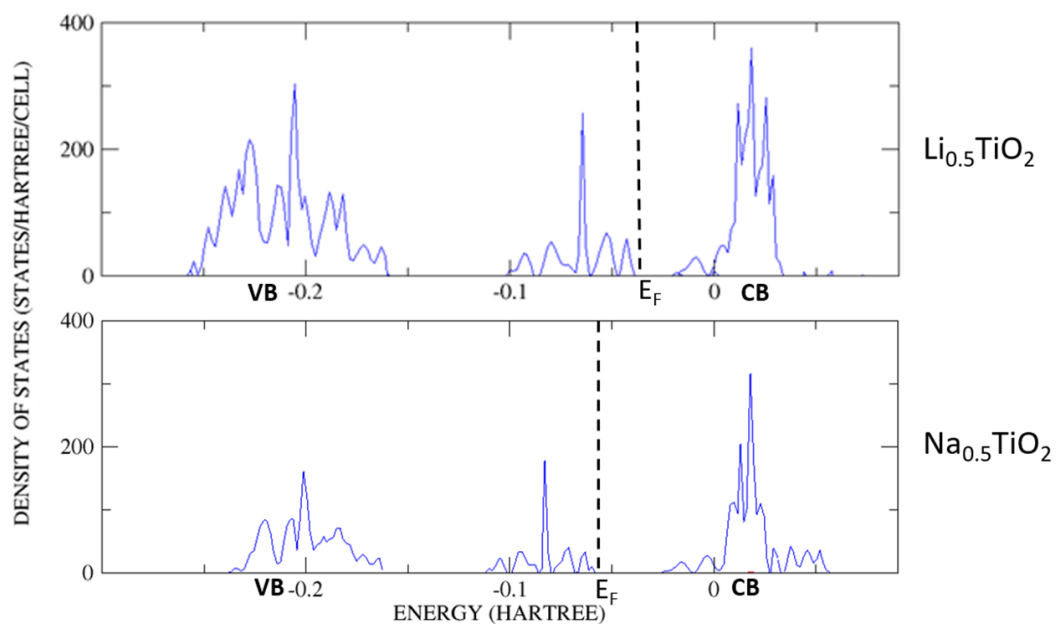


Figure 5.6: Total DOS of the  $\text{Li}_{0.5}\text{TiO}_2$  and  $\text{Na}_{0.5}\text{TiO}_2$  bulks. VB and CB stand for the valence and conduction bands, respectively.

Sodium was intercalated with an energy of  $-1.79$  eV per  $\text{TiO}_2$  unit, corresponding to an intercalation voltage of  $3.57$  V. By comparing these results with the ones obtained for lithium intercalation in chapter 4 (that was inserted with an energy of  $-1.68$  eV per  $\text{TiO}_2$  unit, associated with an intercalation voltage of  $3.37$  V), it can be noted that the sodium intercalation looks more favorable than the lithium one. This result disagrees with the previous theoretical studies<sup>25,149</sup> that reported a much more favorable intercalation for lithium ions that exhibit smaller radius. Nevertheless, as detailed in section 5.1, the intercalation energy is strongly affected by the basis set chosen to model the inserted cation, making impossible a direct comparison between the lithium and sodium intercalation energies.

## 5.4 Sodium intercalation into NaTiO<sub>2</sub> bulk anatase

The crystallographic structure of the anatase bulk containing high sodium ratio seems to be strongly influenced by the experimental conditions. For example, anatase nanoparticles undergo a phase transformation into a rhombohedral layered structure once fully sodiated while some anatase *nt*-TiO<sub>2</sub> are irreversibly transformed into amorphous ones when potentials below 0.5 V vs. Na<sup>+</sup>/Na are applied. Thus, the main goal of this section is to study the sodium intercalation at a high concentration to better understand its influence on the phase transformations.

The optimized NaTiO<sub>2</sub> bulk is shown in Figure 5.7. The insertion of 0.5 mols of additional Na ions into the anatase bulk induces a further elongation of the Ti-O bonds located in the *xy* plane that are now equal to 2.23 Å. In Na<sub>0.5</sub>TiO<sub>2</sub>, the bond distance of 2.09 Å was measured. It can be also noted that the Ti-O bonds parallel to the *z*-axis shorten to 1.97 Å compared to 2.03 Å in Na<sub>0.5</sub>TiO<sub>2</sub> and have now the same length as in the non-sodiated anatase bulk. Moreover, the Ti-O-Ti chains belonging to the *xy* plane are not flat, as it was the case for the LiTiO<sub>2</sub> bulk but have an angle of 165.1°. As a result, the sodium intercalation with a ratio of  $x = 1$  does not induce a phase transformation from anatase to a slightly distorted rock salt structure, as it was the case for lithium. The structure exhibited by the NaTiO<sub>2</sub> bulk corresponds to a “flattened” anatase one, in agreement with the experimental results<sup>144,145</sup>.

The Na ions of the NaTiO<sub>2</sub> bulk are six-fold coordinated with Na-O distances that equal 2.23 Å in the *xy* plane and 2.55 Å along the *z* direction, as detailed in Figure 5.7b. The distance separating two Na ions equals 3.16 Å and is 0.22 Å longer than the one separating two Li ions in the rock salt structure. The Li ions were also six-fold coordinated in the LiTiO<sub>2</sub> bulk with Li-O distances equal to 2.03 Å in the *xy* plane and 2.12 Å along the *z* direction.

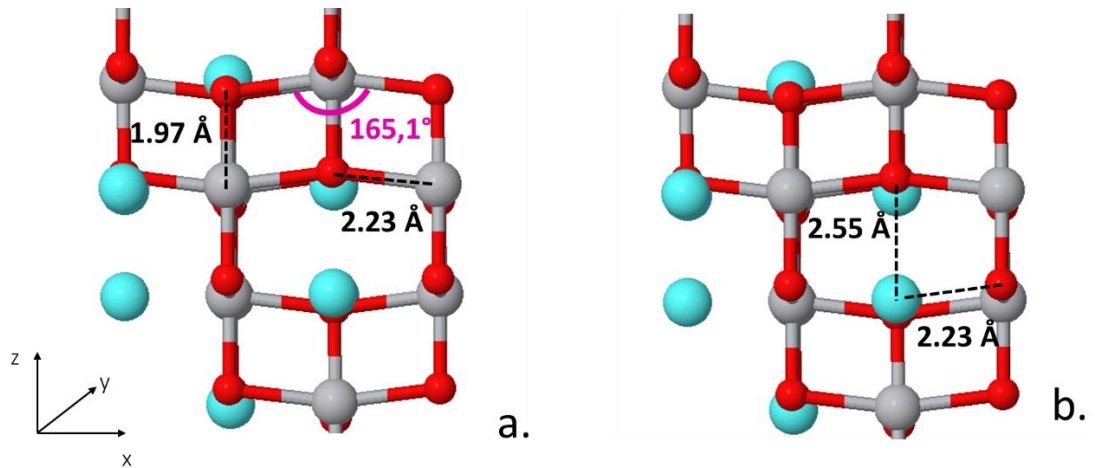


Figure 5.7: Measures of the Ti-O bond lengths and angle (a) and of the Na-O distances (b) of the optimized NaTiO<sub>2</sub> anatase bulk. The Na ions are in blue while the Ti and O atoms are in grey and red, respectively.

The Mulliken population analysis indicates the reduction of all the titania to Ti<sup>3+</sup>. However, no hybridization of the *d* orbitals is observed, instead the extra charge is stored exclusively in the *d*<sub>xy</sub> orbitals. This electronic repartition is very different from the one observed for the LiTiO<sub>2</sub> bulk where the three lowest *d*<sub>xy</sub>, *d*<sub>xz</sub> and *d*<sub>yz</sub> orbitals of the TiO<sub>2</sub> were hybridized and occupied with the extra electrons.

The partial DOS of the NaTiO<sub>2</sub> are displayed in Figure 5.8 where the blue plot stands for the total DOS of the bulk while the green and red plots represent the *d* and *p* orbitals of the indicating atom, respectively. The added charge stored in the *d*<sub>xy</sub> orbitals forms a localized state in the band gap. The main modification induced by the change of stoichiometry from Na<sub>0.5</sub>TiO<sub>2</sub> to NaTiO<sub>2</sub> concerns the conduction band that is shifted to higher energies for NaTiO<sub>2</sub>. As a result, the localized state is located 3.03 eV below the edge of the conduction band, leading to a gap between the localized state and the edge of the conduction band that is 3.5 times larger in the NaTiO<sub>2</sub> than in the Na<sub>0.5</sub>TiO<sub>2</sub>. The shift of the band gap can be explained by the electronic repulsions between the different *d* orbitals of the titania ions.

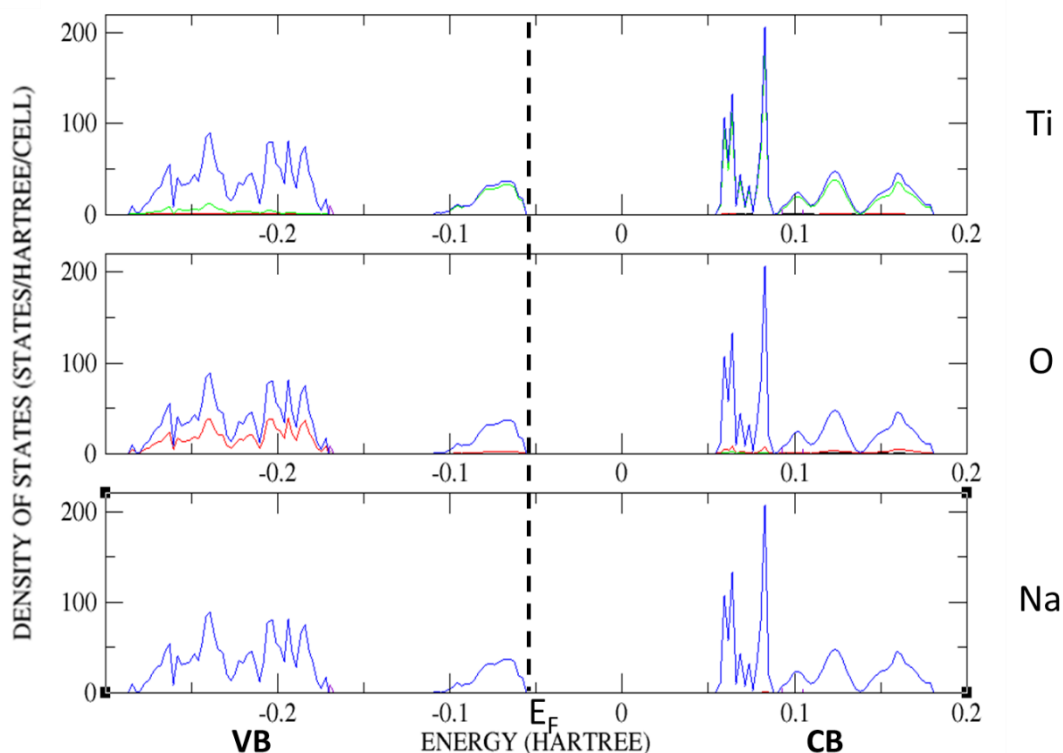


Figure 5.8: DOS of the NaTiO<sub>2</sub> bulk. The total DOS is represented in blue while the red and green plots stand for the *p* and *d* orbital contributions, respectively. VB and CB indicate the positions of the valence band and conduction bands, respectively.

The LiTiO<sub>2</sub> and NaTiO<sub>2</sub> DOS are compared in Figure 5.9. The main difference concerns the localized state that is not present in LiTiO<sub>2</sub> due to the hybridization of the *d* orbitals. Indeed, in LiTiO<sub>2</sub> there is no single occupied orbital to form a localized state in the band gap, resulting in all the extra charges being located in the conduction band.

The sodium was intercalated into NaTiO<sub>2</sub> with an intercalation energy of -2.29 eV per TiO<sub>2</sub> unit. This energy is more favorable than the one encountered for Na<sub>0.5</sub>TiO<sub>2</sub> that equalled -1.79 eV per TiO<sub>2</sub> unit. Moreover, the corresponding intercalation voltage for NaTiO<sub>2</sub> equals 2.29 V and is particularly high, indicating that high concentration of Na will be easily intercalated into TiO<sub>2</sub> anatase. These results let also suppose that some Na ions trapping can occur, explaining a part of the irreversible capacity losses observed experimentally during the first cycle<sup>145</sup>. The results observed for NaTiO<sub>2</sub> are very different from the ones observed with lithium where the intercalation into the rock salt LiTiO<sub>2</sub> was less favorable than in Li<sub>0.5</sub>TiO<sub>2</sub> titanate, and occurred at only 1.27 V.

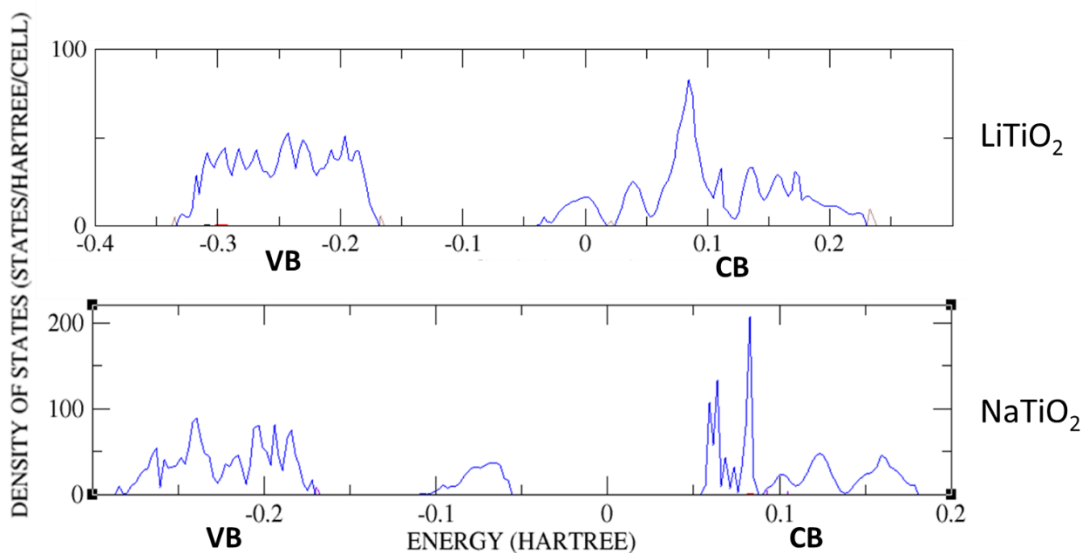


Figure 5.9 : Total DOS of the  $\text{LiTiO}_2$  and  $\text{NaTiO}_2$  bulks. VB and CB represent the valence and conduction bands, respectively.

The results obtained for the  $\text{NaTiO}_2$  bulk can provide some explanations to the different phase transformations observed experimentally. The geometry optimization confirms that the anatase structure is maintained upon high sodium ratio. However, the structural changes necessary to accommodate the Na ions are important and may lead to bonds breaking when the sodiation/desodiation cycles are repeated. Moreover, the sodium does not require low potential to be intercalated with high ratio, meaning that the “flattened”  $\text{NaTiO}_2$  anatase phase can be formed relatively soon in the discharge process. As a result, the bonds breaking can occur early in the battery life and can increase after each charge/discharge cycle. The multiplication of these bonds breaking can progressively form an amorphous structure for the *nt*- $\text{TiO}_2$ <sup>7</sup> or a reorganization of the lattice into a rhombohedral structure for the anatase nanoparticles<sup>143</sup>. Thus, the observations of the structural modifications of the anatase structure are strongly dependent on the intrinsic nature of the electrode and on the cycling conditions. Some electrodes can maintain an anatase structure whereas some others will be more brittle and undergo phase transformation. The formation of the  $\text{NaTiO}_2$  bulk at a relatively high voltage, combined with its associated bonds breaking, can also explain a part of the irreversible decrease of capacity often observed<sup>7,145</sup> after the first discharge of the anatase electrode.

## 5.5 Sodium intercalation into the slab

In section 5.4, it was concluded that a part of the irreversible capacity loss observed during the first cycle can be caused by the bonds breaking that take place in the anatase electrode. The particular reactions occurring between sodium and anatase surface mentioned in several studies<sup>7,145,146</sup> also explain the decrease of capacity observed. The electrochemical measurements carried out by Bella et al.<sup>146</sup> clearly indicate the formation of a passivating film at the surface of the electrode during the first cycle. The scanning electron microscopy images reported by Li et al.<sup>7</sup> shows the formation of flower-like structures at the top surface of the *nt*-TiO<sub>2</sub> when the potential applied equals 0.01 V vs Na/Na<sup>+</sup>. These flower-like structures were identified as Na<sub>2</sub>CO<sub>3</sub> and disappear during the charge. Gonzales et al.<sup>145</sup> mentioned a surface accommodation of the cation that is more pronounced in the Na cell than in the Li one. All these results indicate a higher reactivity of the anatase surface towards sodium than towards lithium.

The XANES analysis carried out by Li et al.<sup>7</sup> indicate a partial reduction of the Ti<sup>4+</sup> ions into Ti metal occurring in the surface region of the *nt*-TiO<sub>2</sub> electrode upon sodium intercalation. The XANES results also show an irreversible phase transformation of the *nt*-TiO<sub>2</sub> surface from an anatase structure to amorphous phases during the first cycle. This result is different from the one observed with lithium intercalation where the ions induced a phase transformation of the surfaces layers into a rock salt structure.

The main goal of this section is to gain a better understanding of the particular reactivity of the anatase surface towards sodium by studying its intercalation and adsorption at the surface of a slab. Like for lithium, these calculations will later allow to isolate the influence of the strain energy present in the *nt*-TiO<sub>2</sub> by comparing the results obtained with the nanotubes ones. The slab used to carry out the calculations is the same as in chapter 4, it consists of a 3 monolayers thick (001) oxygen terminated surface that will be later used to construct *nt*-TiO<sub>2</sub> with a negative strain energy. The sodium intercalation was studied with Na ions concentrations ranging from  $x = 0.33$  to  $x = 1$ . When the Na ions were inserted in the sites located on the outermost layers, only one side of the slab was considered as the two surfaces are symmetric.

### 5.5.1 Intercalation with sodium capacity of $x = 0.33$

The stoichiometry of  $\text{Na}_{0.33}\text{TiO}_2$  is obtained when only one sodium ion per slab primitive unit cell is inserted. As detailed in chapter 4, the anatase slab contains tetrahedral and octahedral intercalation sites that can be located in the inner or in the outermost layers. The inner tetrahedral intercalation sites exhibit very similar geometry as the bulk ones, and thus were not considered in this thesis as they are not favourable for sodium intercalation. However, the tetrahedral sites located on the outermost layers contain only two Ti atoms, and thus less Coulombic repulsions. As the anatase surface was reported to show a high reactivity towards sodium, the outermost tetrahedral sites were filled with Na ions to evaluate their eventual contributions to the sodium intercalation. The corresponding slab is displayed in Figure 5.10. However, the calculations did not converge, indicating that this kind of intercalation leads to an unstable system and is unfavourable. As a result, the tetrahedral sites do not contribute to the reactivity of the anatase surface towards sodium.

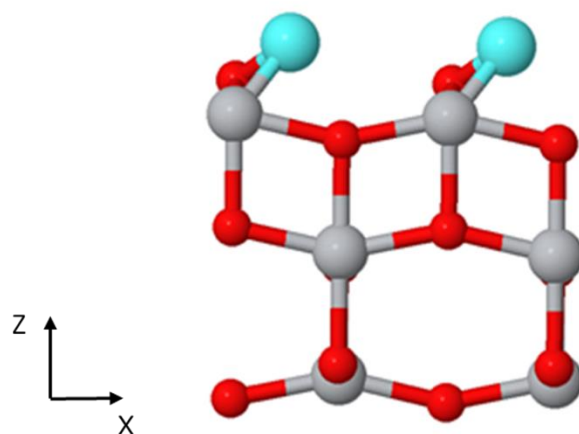


Figure 5.10: (001) anatase slab having its outermost tetrahedral sites filled with sodium. The blue, red and grey colours represent the Na, O and Ti elements, respectively.

Sodium ions were also intercalated into the octahedral sites located on one of the outermost layers. The corresponding optimized slab is shown in Figure 5.11. It can be noted that this kind of intercalation breaks the symmetry of the slab and generates a dipole moment over the slab that can influence the results obtained.

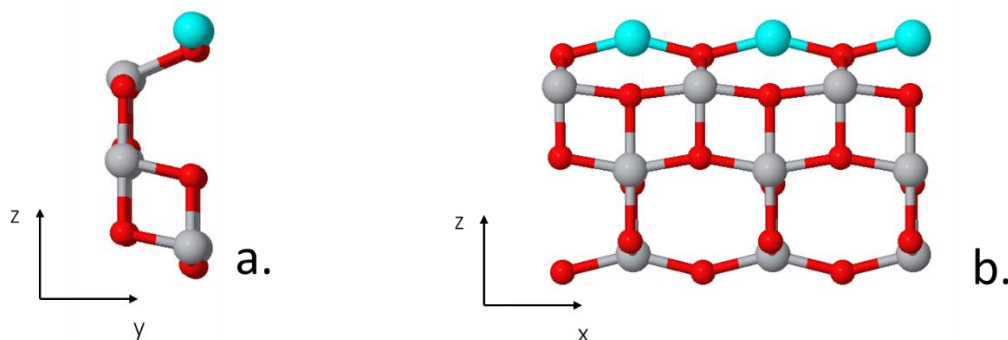


Figure 5.11: Side (a) and face (b) views of the optimized  $\text{Na}_{0.33}\text{TiO}_2$  anatase (001) slab. The blue, red and grey colours represent the Na, O and Ti elements, respectively.

The sodium intercalation does not generate major structure changes to the slab that retains an anatase structure. However, it can be observed that the sodium ions are accommodated outside the surface. This intercalation position is different from the one observed with the lithium ions that were intercalated inside the outermost surface in an attempt to reduce the dipole moment. The lithium intercalation was accompanied by a surface reconstruction that is not present when Na ions are inserted instead. The Na ions are fourfold coordinated with Na-O distances that equal  $2.00 \text{ \AA}$  and  $2.45 \text{ \AA}$  along the  $x$  and  $y$  directions, respectively.

The Mulliken population analysis indicates that all the titania atoms present on the outermost layer that contains sodium are reduced to  $\text{Ti}^{3+}$ . There is no hybridization of the titania  $d$  orbitals but the added charge is stored exclusively in the  $d_{xz}$  orbitals. The localisation of the additional charge is different from the one observed in the sodiated anatase bulks and in the corresponding lithiated slab, where the extra charges were stored exclusively in the  $d_{xy}$  orbitals. The  $d_{xy}$  orbitals are usually the first ones to be filled with the added electrons as they exhibit the lowest energy in  $\text{TiO}_2$ . This different electronic repartition points out the electronic repulsion generated by the Na ions and can be explained by their larger radius.

The corresponding DOS is displayed in Figure 5.12 where the blue plot represents the total DOS of the slab. The reduced  $\text{Ti}^{3+}$  form a localized state in the band gap and lead to a DOS similar to the ones observed for the sodiated bulk. However, this DOS is different from the one reported for the corresponding  $\text{Li}_{0.33}\text{TiO}_2$  slab that does not contain any localized state, confirming the electronic repulsion generated by the Na ions.

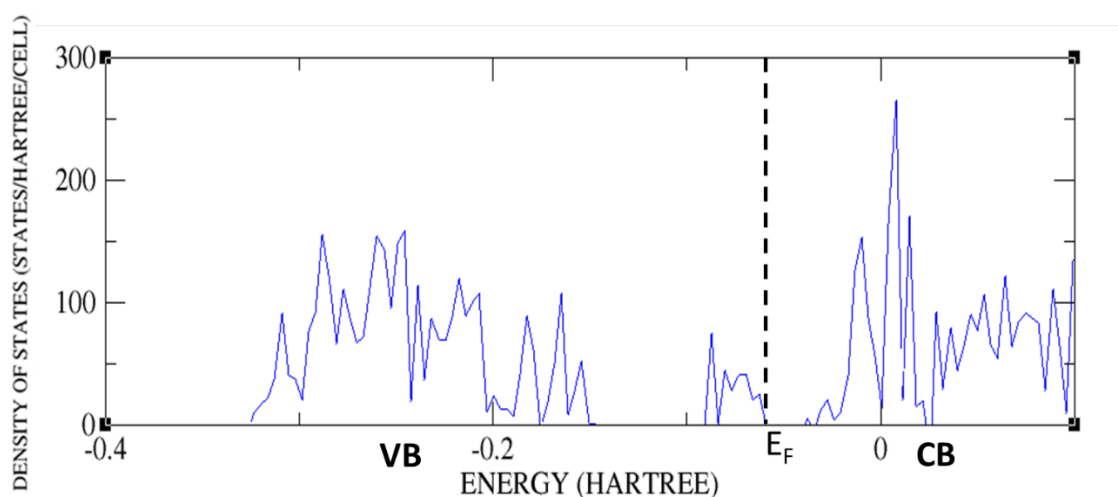


Figure 5.12: Total DOS of the optimized (001) anatase slab having Na ions intercalated in one outermost surface. VB stands for the valence band while CB represents the conduction band.

The Na ions were favourably inserted with an intercalation energy equal to  $-1.19$  eV per  $\text{TiO}_2$  unit. However, this intercalation is less favourable by  $0.59$  eV per  $\text{TiO}_2$  unit than the one found in the  $\text{Na}_{0.5}\text{TiO}_2$  bulk. Similar results were obtained with lithium and were explained by the dipole moment generated in the slab.

The Na ions were then inserted into the inner octahedral sites as it is displayed in Figure 5.13 where the Na-O distances and Ti-O bond lengths are indicated in blue and black, respectively. The sodium ions are four-fold coordinated with Na-O distances that equal  $2.06$  Å. Their insertion does not induce major structure modification except a slight elongation of the Ti-O bonds located in the  $xy$  plane whose lengths equal  $2.03$  Å and are  $0.12$  Å longer than in the non-sodiated slab. As a result, the anatase structure is retained.

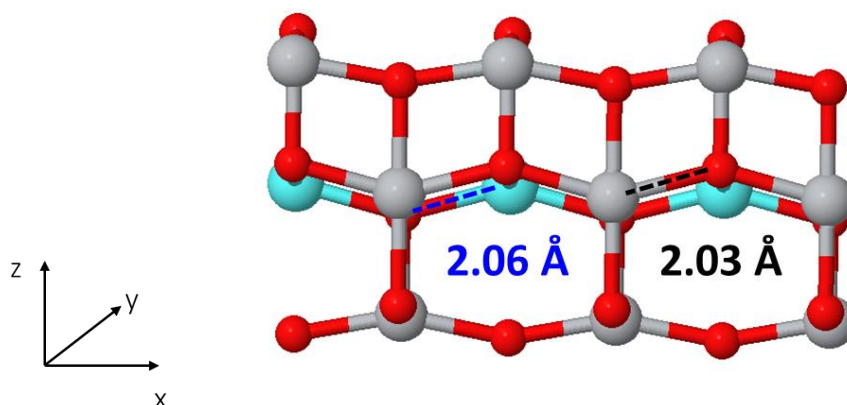


Figure 5.13: Optimized (001) anatase slab with Na ions inserted into the inner octahedral sites. The Na ions are in light blue while the Ti and O are in grey and red, respectively. The Na-O distance are indicated in blue while the Ti-O bond length is written in black.

The Mulliken population indicates that all the titania atoms located in the inner plane are reduced to  $\text{Ti}^{3+}$  and host the extra charge exclusively in their  $d_{xy}$  orbitals. There is no hybridization of the titania  $d$  orbitals. This charge repartition is the same as the one observed for bulk. The total DOS, shown in Figure 5.14, indicates the formation of a localized state in the band gap. However, the shape of this localized state is different from the one observed when one outermost surface was sodiated. Here, the localized state does not contain any sharp peak. The broader peak suggests a more delocalized state, resulting in a smaller band gap and, therefore, an enhanced conductivity.

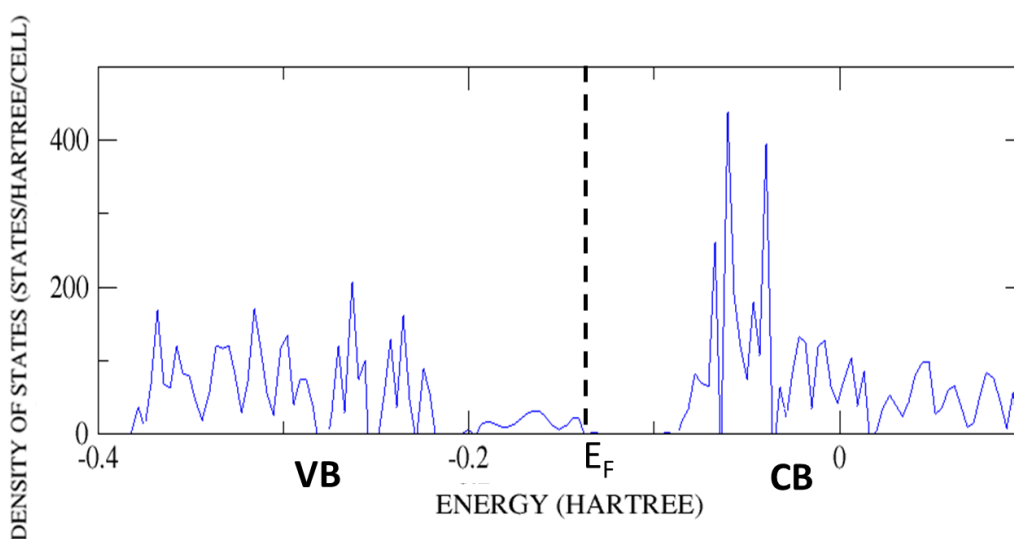


Figure 5.14: Total DOS of the optimized anatase (001) slab having the inner octahedral sites filled with sodium. VB and CB represent the valence and conduction bands, respectively.

The corresponding intercalation energy equals -0.32 eV per TiO<sub>2</sub> unit and is the less favourable reported for the sodiated slabs in this thesis. Similar results were observed for lithium intercalations and were explained by the particular structure of the slab. The inner sites are surrounded by empty octahedral sites on both outermost surfaces, whose geometry is influenced by the surface reconstruction. Thus, the geometry modifications of the inner octahedral sites, that usually allow to stabilize the sodium intercalation, are limited as it can be observed from the lengths exhibited by the Ti-O bonds located in the *xy* plane that equal 2.03 Å in the slab and 2.23 Å in the bulk.

### 5.5.2 Intercalation with sodium capacity of $x = 0.67$

The sodium ions were intercalated in both the outermost surfaces, leading to a capacity of Na<sub>0.67</sub>TiO<sub>2</sub>. This kind of intercalation is symmetric and does not generate a dipole moment in the slab. Thus, the surface reconstruction is not driven by the reduction of the dipole moment. The sodiated bulks before and after geometry optimization are displayed in Figure 5.15a and 5.15b, respectively. The optimized Li<sub>0.67</sub>TiO<sub>2</sub> slab is shown in Figure 5.15c for comparison.

The Na ions are four-fold coordinated in the centre of distorted octahedral sites, with Na-O distances varying between 2.04 and 2.33 Å. The Na-O distances are longer than the Li-O ones that equal 1.96 Å and 2.07 Å, respectively. It can be noted that the Na-O<sub>2c</sub>-Na angle equals 159.1° while the Li-O<sub>2c</sub>-Li angle is equal to 190.5°. Thus, the sodium ions are intercalated more outward the surface than the lithium ones, certainly because of their bigger radius.

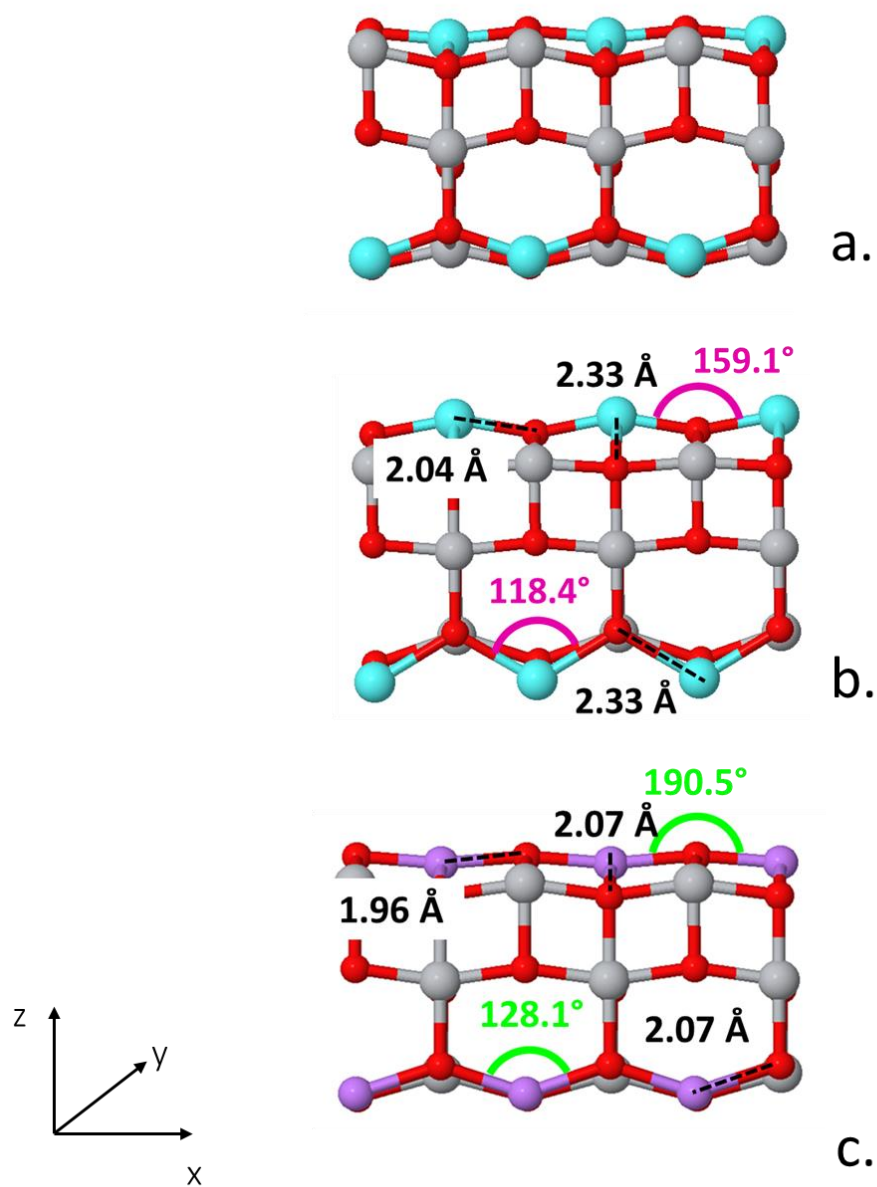


Figure 5.15: Non optimized  $\text{Na}_{0.67}\text{TiO}_2$  (a), optimized  $\text{Na}_{0.67}\text{TiO}_2$  (b) and optimized  $\text{Li}_{0.67}\text{TiO}_2$  (c) (001) slabs. The blue, purple, red and grey colours represent the Na, Li, O and Ti elements, respectively.

The Mulliken population analysis indicates that all the titania atoms located on the outermost surfaces are reduced to  $\text{Ti}^{3+}$ . The added charge is accommodated in a single  $d$  orbital and there is no hybridization. Moreover, this extra charge is stored in the  $d$  orbitals that is parallel to the  $\text{O}_{3c}\text{-Ti-O}_{3c}$  chains. As a result, the  $\text{Ti}^{3+}$  that are located at the top of the slab host the added charge in their  $d_{xz}$  orbitals whereas the ones located at the bottom accommodate this charge in their  $d_{yz}$  orbitals, as it is displayed in Figure 5.16. The electronic repartition influences the length of the Ti-O bonds located on the outermost surface: the  $\text{Ti}^{3+}\text{-O}_{3c}$  bonds are shorter than the  $\text{Ti}^{3+}\text{-O}_{2c}$  ones. Thus, the octahedral sites present in the outermost surfaces are distorted.

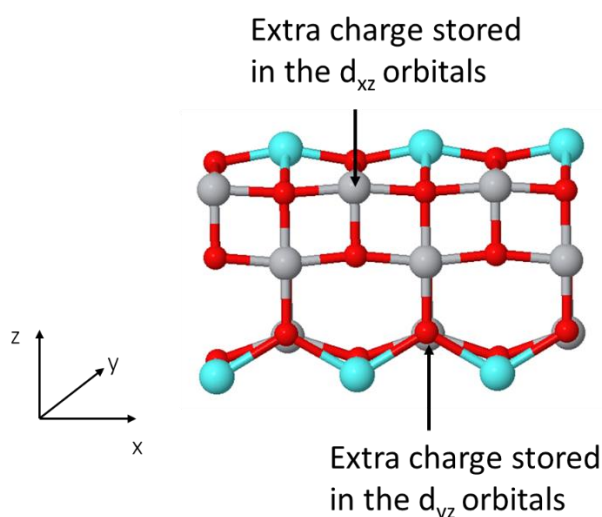


Figure 5.16: Storage of the added charges in the (001)  $\text{Na}_{0.67}\text{TiO}_2$  anatase slab. The blue, red and grey colours stand for the Na, O and Ti elements, respectively.

The electronic structure of the  $\text{Na}_{0.67}\text{TiO}_2$  slab also indicates that the  $d_{xy}$  orbitals, that are the lowest in energy in  $\text{TiO}_2$ , are not involved in accommodating the extra charge. In the  $\text{Li}_{0.67}\text{TiO}_2$  slab, the filling of the titania  $d$  orbitals were also influenced by the orientation of the  $\text{O}_{3c}\text{-Ti-O}_{3c}$  chains. The  $d_{xy}$  orbitals were not empty but hosted one part of the extra charge and were hybridized with the  $d$  orbitals parallel to the  $\text{O}_{3c}\text{-Ti-O}_{3c}$  chains. These results confirm the consequent electronic repulsion generated by the Na ions.

The total DOS of the  $\text{Na}_{0.67}\text{TiO}_2$  slab is shown in Figure 5.17. The sodium intercalation into the second outermost surface leads to a higher density of the localized state than observed when Na was intercalated in a single outermost surface (Figure 5.12). This DOS is different from the  $\text{Li}_{0.67}\text{TiO}_2$  one that does not contain any localized state because of the hybridization of the *d* orbitals.

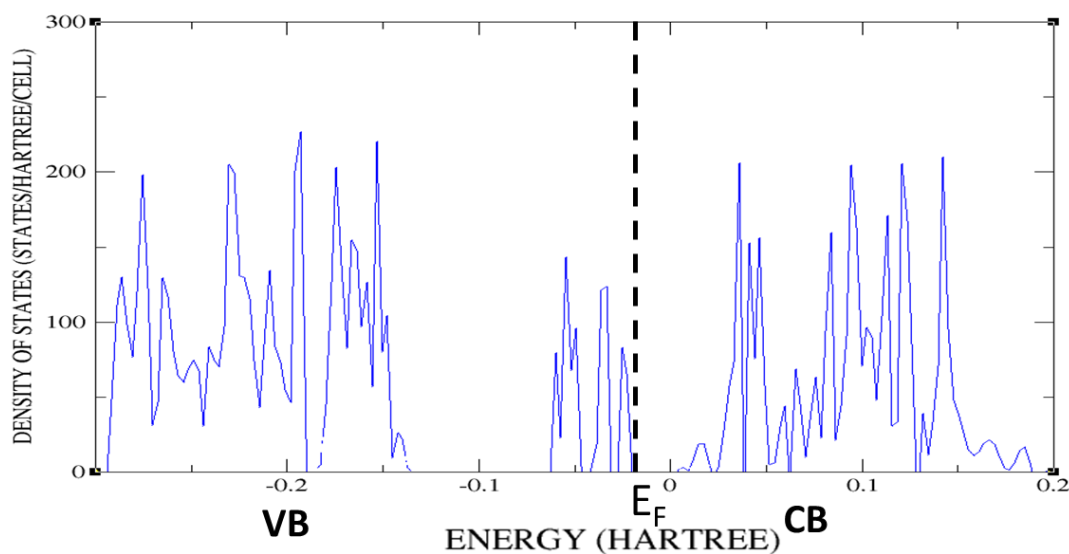


Figure 5.17: Total DOS of the  $\text{Na}_{0.67}\text{TiO}_2$  (001) anatase slab where VB and CB indicate the positions of the valence and conduction bands, respectively.

The Na ions were inserted into the  $\text{Na}_{0.67}\text{TiO}_2$  slab with an intercalation energy of -1.80 eV per  $\text{TiO}_2$  unit. This value is 0.02 eV more negative than the one calculated for the  $\text{Na}_{0.5}\text{TiO}_2$  bulk and confirms the particularly high reactivity exhibited by the  $\text{TiO}_2$  surface towards sodium.

### 5.5.3 Intercalation with sodium capacity of $x = 1$

When all the octahedral sites within the slab are filled with sodium, the corresponding capacity is  $\text{NaTiO}_2$ . The optimized slab is shown in Figure 5.18 where it can be noticed that the sodium intercalation at high ratio leads to major structure modifications driven by the electronic structure of the titanium ions. The Mulliken population analysis indicates that all the titania present in the slab are reduced to  $\text{Ti}^{3+}$  upon sodium intercalation.

The added charges are stored in single  $d$  orbitals without hybridization. The fillings of the  $d$  orbitals depend on the titania location. Thus, the  $\text{Ti}^{3+}$  ions located on the outermost surfaces host the added charge in the  $d$  orbitals that are parallel to the  $\text{O}_{3c}\text{-Ti-O}_{3c}$  chains: the  $d_{xz}$  orbitals for  $\text{Ti}^{3+}$  ions located at the top of the slab and the  $d_{yz}$  orbitals for the ones located at the bottom. The titania ions located in the inner layer store the extra charge in their  $d_{xy}$  orbitals.

The Ti-O bond lengths are displayed in Figure 5.18. It can be noted that all the Ti-O bonds located in the  $xy$  plane are elongated. Moreover, the angles of the Ti-O-Ti chains located in this plane are increased, leading to “flatter” chains. The increases in the bond length depend on the location of the bond: the Ti-O bond lengths located in the outermost surfaces increase to 2.11 Å and 2.15 Å, while the bonds located in the inner plane are all elongated to 2.13 Å. The difference in bond length associated with the outermost surfaces is explained by the filling of the  $\text{Ti}^{3+}$   $d$  orbitals that are parallel to the  $\text{O}_{3c}\text{-Ti-O}_{3c}$  chains, as discussed in section 5.5.2.

The Ti-O bonds parallel to the  $z$  direction exhibit different bond lengths. The  $\text{Ti}_{6c}\text{-O}_{3c}$  bonds are 2.06 Å long while the  $\text{Ti}_{5c}\text{-O}_{3c}$  bonds have a length of 1.92 Å. As a result, the  $\text{Ti}_{6c}\text{-O}_{3c}$  bonds are 0.14 Å longer than the  $\text{Ti}_{5c}\text{-O}_{3c}$  ones. The lengths difference is explained by the filling of the  $\text{Ti}^{3+}$   $d$  orbitals. The titania ions located in the outermost surfaces, by hosting the added charge in their  $d$  orbitals parallel to the  $\text{O}_{3c}\text{-Ti-O}_{3c}$  chains, generate short  $\text{Ti}_{5c}\text{-O}_{3c}$  bonds. At the opposite, the  $\text{Ti}^{3+}$  located in the inner layer store the added charge in their  $d_{xy}$  orbitals. This particular storage induces an electronic repulsion that will elongates the  $\text{Ti}_{6c}\text{-O}_{3c}$  bonds.

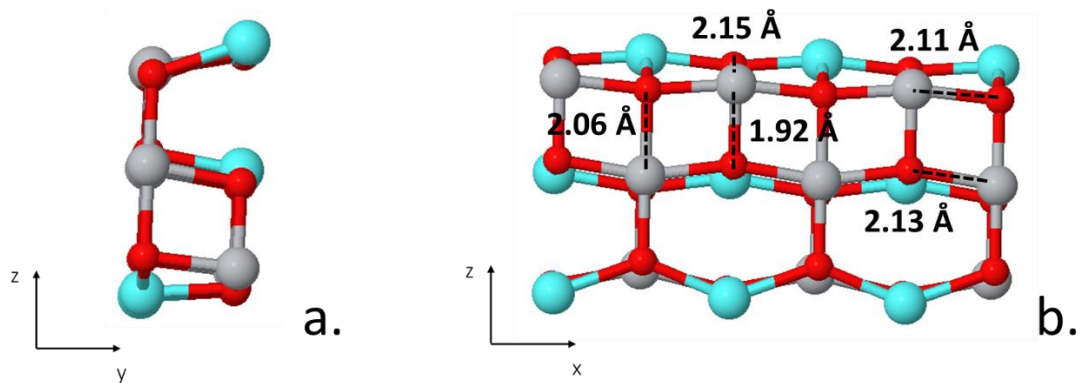


Figure 5.18: Side (a) and face (b) views of the optimized  $\text{NaTiO}_2$  (001) anatase slab. The Na ions are represented in blue while the Ti and O atoms are in grey and red, respectively.

The differences in bond length leads to inequivalent octahedral sites. The sites located in the outermost surfaces are distorted while the ones located in the central layer are symmetric. All the sodium ions are four-fold coordinated.

The total DOS of the  $\text{NaTiO}_2$  slab is displayed in Figure 5.19 where it can be noted that the reduction of all the titania to  $\text{Ti}^{3+}$  forms a localized state in the band gap exhibiting a particularly high density. This DOS is similar to the  $\text{LiTiO}_2$  one where the electronic repulsion between the different  $\text{Ti}^{3+}$   $d$  orbitals have generated a localized state, as discussed in chapter 4.

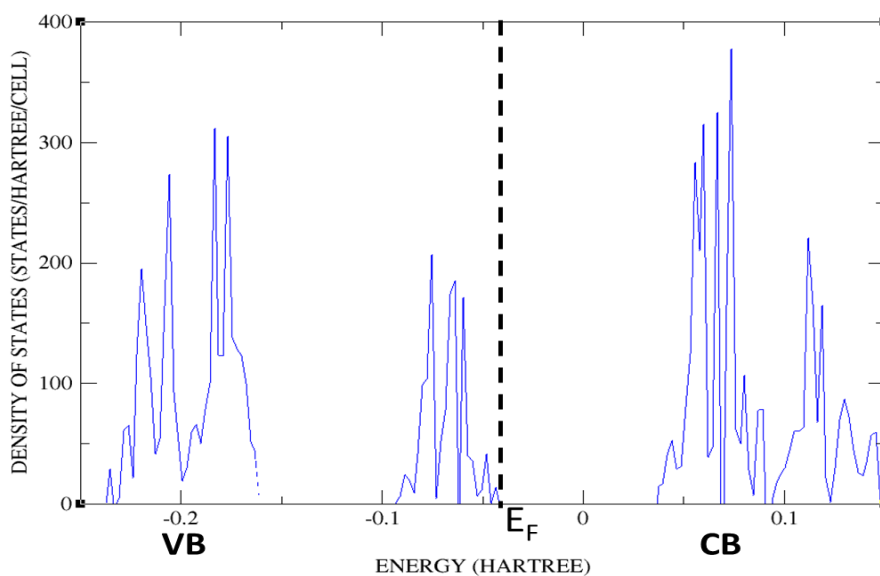


Figure 5.19: Total DOS of the optimized  $\text{NaTiO}_2$  (001) anatase slab. VB and CB stand for the valence and conduction bands, respectively.

The sodium ions were inserted into the  $\text{NaTiO}_2$  slab with an intercalation energy of  $-1.95$  eV per  $\text{TiO}_2$  unit. This value is the most favourable reported for the sodiated slab in this thesis, indicating that the Na intercalation will spontaneously occur with high ratio into the anatase surface. This intercalation is more favourable by  $0.17$  eV per  $\text{TiO}_2$  unit than the one calculated for the  $\text{Na}_{0.5}\text{TiO}_2$  bulk. However, by comparing the slab intercalation energy with the  $\text{NaTiO}_2$  bulk one, that equals  $-2.29$  eV per  $\text{TiO}_2$  unit, it can be noted that intercalation with high ratio is less favourable in the slab than in the bulk. This result can be explained by the larger radius of the Na ions that limit the surface reconstruction necessary to stabilize the structure.

To summarize this section, it can be concluded from the intercalation energy that sodium intercalation will spontaneously occur into the slab with the high ratio of  $x = 1$ . The optimized  $\text{NaTiO}_2$  and  $\text{TiO}_2$  slabs are compared in Figure 5.20 where the modification of the Ti-O bond lengths induced by the sodium insertion can be noticed. As a result, such an intercalation will inevitably be accompanied by bonds breaking, especially if the charge/discharge cycles are repeated. Thus, the anatase surface will progressively be transformed into an amorphous structure, in agreement with the XANES analysis carried out by Li et al.<sup>7</sup>.

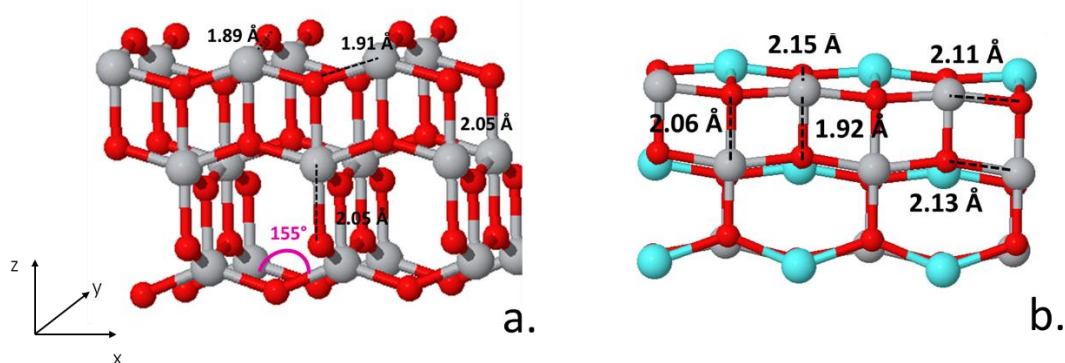
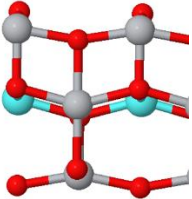
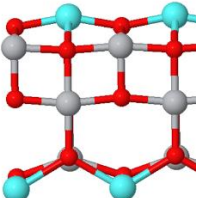
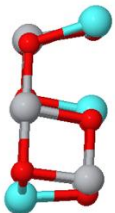


Figure 5.20: Optimized  $\text{TiO}_2$  (a) and  $\text{NaTiO}_2$  (b) (001) anatase slabs. The Na ions are in blue while the Ti and O atoms are in grey and red, respectively.

## 5.5.4 Intercalation voltages

The sodium intercalation energies per  $\text{TiO}_2$  unit, and the corresponding intercalation voltages, calculated for all the bulks and slabs of the previous sections are summarized in Table 5.3.

Table 5.3: Sodium intercalation energies and voltages for different slab and bulk configurations.

Na position	x (number of Na per $\text{TiO}_2$ unit)	$E_{\text{Li Intercalation}}$ (eV)	Intercalation voltage (V)
	0.33	-1.19	3.57
	0.33	-0.32	0.96
	0.66	-1.80	2.70
	1	-1.95	1.94
$\text{Na}_{0.5}\text{TiO}_2$ <b>bulk</b>	0.5	-1.78	3.57
$\text{NaTiO}_2$ <b>bulk</b>	1	-2.29	2.29

The comparison of the intercalation energies clearly indicates the preferable insertion with the highest ratio of  $x = 1$  for both the slab and bulk. This result is different from the ones observed with lithium where the intercalation with a capacity of  $x = 1$  were not the most favourable ones due to the Li-Li repulsions. Consequently, the reactivity of the anatase is more important towards sodium than toward lithium. As discussed in the previous section, the sodium insertion with a ratio of  $x = 1$  is less favourable in the slab than in the bulk, certainly because of the limited surface reconstruction induced by the Na ions.

The intercalation voltages were calculated versus sodium and thus correspond to a half cell made of a titania and a sodium metal electrode. They do not correspond to a full battery where the titania electrode is usually the anode. Like for the lithium intercalation voltages discussed in section 4.5.5, the lowest intercalation voltages correspond to the highest sodium capacities.

The intercalation voltages obtained for the sodiated and lithiated bulks are summarized in Table 5.4. Although a direct comparison between the results obtained for sodium and lithium is not possible due to the strong influence of the basis sets, it is interesting to note that the voltage difference between the two capacities is much smaller for sodium than for lithium. This result points out that the full intercalation will occur earlier in the discharge when Na ions are intercalated.

Table 5.4: Intercalation energies and voltages obtained for the sodiated and lithiated bulks.

<b>Bulk</b>	<b><math>E_{\text{Li Intercalation}}</math> (eV)</b>	<b>Intercalation voltage (V)</b>
Titanate $\text{Li}_{0.5}\text{TiO}_2$	-1.68	3.37
Rock salt $\text{LiTiO}_2$	-1.27	1.27
$\text{Na}_{0.5}\text{TiO}_2$	-1.78	3.57
$\text{NaTiO}_2$	-2.29	2.29

### 5.5.5 Intercalation versus sodium metal plating

As mentioned at the beginning of section 5.5, several experimental studies reported the formation of a passivating film at the surface of the electrode<sup>146</sup>, or the surface accommodation of Na ions<sup>145</sup>. Thus, Na ions were also added above the oxygen atoms located on the outermost surfaces of the slab to check if this kind of adsorption is favourable. Like for lithium, the sodium was added above both the outermost surfaces to avoid the formation of a dipole moment that will destabilize the whole slab. Na ions were successively added above the fully coordinated and undercoordinated oxygen atoms, as it is displayed in Figure 5.21.

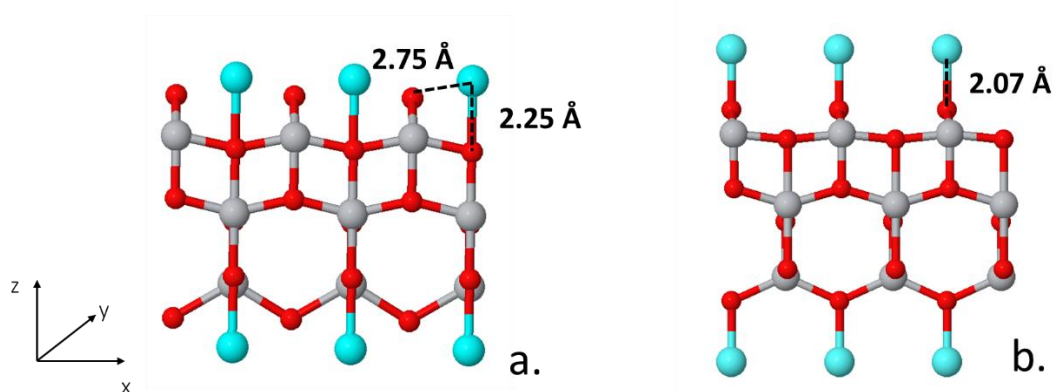


Figure 5.21: Optimized (001) anatase slabs with sodium adsorbed above the fully coordinated (a) and undercoordinated (b) surface oxygen atoms. The Na ions are in blue while the Ti and O atoms are in grey and red, respectively.

The corresponding sodium adsorption energies were calculated using the same equation as for the sodium intercalation energies (Equation 1.4) and equal  $-0.57$  eV per  $\text{TiO}_2$  unit for both the fully coordinated and undercoordinated oxygen atoms. The negative value points out the favourable sodium adsorption at the surface of  $\text{TiO}_2$  electrodes. This favourable adsorption, that was not present with lithium, confirms the experimental results previously reported<sup>145,146</sup>.

The Na ions are favourably adsorbed above the fully coordinated oxygen with a Na-O distance that equals 2.25 Å. The adsorption induces a displacement of the undercoordinated oxygen located on the outermost surfaces outward from the surface. As a result, the Na-O<sub>2c</sub> distance equals 2.75 Å. The Mulliken analysis indicates that the Na ions give 0.8e to the lattice, inducing the reduction of the titania located on the outermost surfaces to Ti<sup>3+</sup>. It can be noted that when the Na ions were intercalated into the octahedral sites located on the outermost surfaces, they gave 0.9e to the lattice. The extra charge is stored exclusively on their *d<sub>xz</sub>* orbitals without hybridization. The corresponding DOS is displayed in Figure 5.22 and shows that the Ti<sup>3+</sup> ions generates a localized state in the band gap. As a result, the adsorption of the Na ions above the fully coordinated oxygens leads to an electronic structure very similar to the one observed when sodium was intercalated into the octahedral sites located on the outermost surfaces.

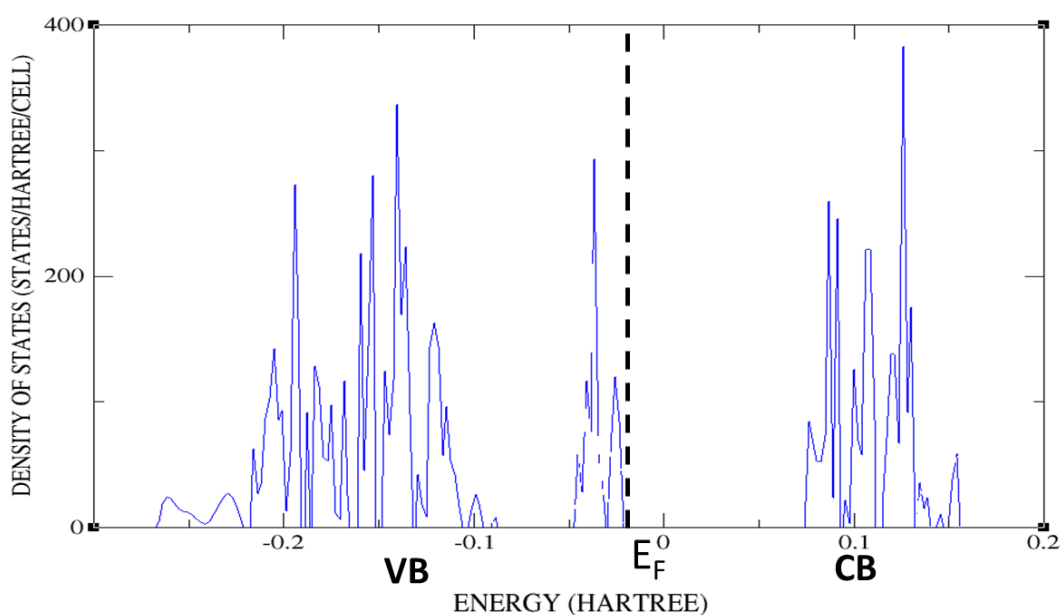


Figure 5.22: Total DOS of the anatase (001) slab having sodium adsorbed above its fully coordinated oxygen atoms. VB represents the valence band while CB stands for the conduction band.

The Na ions are also energetically stable when adsorbed above the undercoordinated oxygen atoms located in the outermost surfaces. The Na-O distances are shorter than the ones observed for the adsorption above the fully coordinated oxygens and equal 2.07 Å. The adsorption generates a slight displacement of the fully coordinated oxygen atoms located on the outermost surfaces outward from this surface. As a result, the O<sub>3c</sub>-Ti-O<sub>3c</sub> chains of the outermost surfaces are flattened. The Mulliken population indicates that the adsorbed sodium ions give 0.5e to the lattice and reduce the titanium located in the outer layers to Ti<sup>3+</sup>. The added charge induces a hybridization of the Ti<sup>3+</sup> *d* orbitals and is stored in the *d*<sub>xz</sub> and *d*<sub>yz</sub> orbitals. The corresponding total DOS is displayed in Figure 5.23 and confirms that the hybridization of the orbitals avoids the formation of a localized state in the band gap.

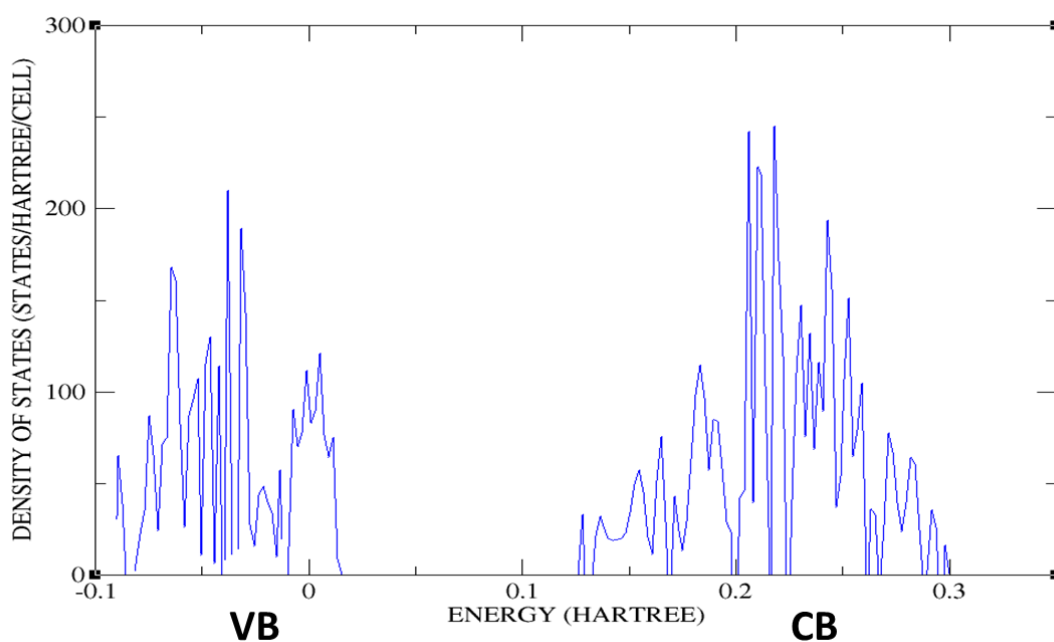


Figure 5.23: Total DOS of the anatase (001) slab having sodium adsorbed above its undercoordinated oxygen atoms. VB and CB indicate the positions of the valence and conduction bands, respectively.

To summarize this section, it can be noted that the adsorption above the undercoordinated oxygen atoms gives less charge to the lattice than the one performed above the fully coordinated oxygens. As a result, the electronic repulsions between the different  $d$  orbitals of the  $\text{Ti}^{3+}$  ions are less important, and the orbitals are hybridized. The sodium adsorption energies indicate that both the adsorptions are favourable with the same energy of  $-0.57$  eV per  $\text{TiO}_2$  unit. Thus, neither adsorption is more favourable than the other one and they will likely occur simultaneously. However, the adsorption energy of  $-0.57$  eV per  $\text{TiO}_2$  unit is relatively small compared to the sodium intercalation energy of  $-1.80$  eV per  $\text{TiO}_2$  unit reported for the  $\text{Na}_{0.67}\text{TiO}_2$  slab. Consequently, the adsorbed Na ions will spontaneously move to the octahedral intercalation sites located in the outermost surfaces. As a conclusion, the favourable sodium adsorption certainly supports its further intercalation and confirms the high surface anatase reactivity towards this element.

## 5.6 Sodium intercalation into the nanotube

Sodium intercalation into the nanotubes was studied using the same  $38 \text{ \AA}$  diameter  $nt\text{-TiO}_2$ , rolled up along the  $(n_1,0)$  direction, as for lithium. The calculations were guided by the results obtained for the corresponding slabs described in section 5.5. Thus, the intercalation into tetrahedral sites were not considered for the sodiated nanotubes. However, both the intercalation into the octahedral sites and the sodium metal plating were studied in detail with high truncation criteria.

The main differences between the non-optimized nanotube and the slab concern the Ti-O bond lengths. The rolling-up elongates the  $\text{Ti-O}_{3c}$  bonds located on the external wall while it shortens the  $\text{Ti-O}_{2c}$  bonds located on the internal wall. Sodium ions can be intercalated into the  $nt\text{-TiO}_2$  before or after the nanotube optimization. Like for lithium, when the Na ions are intercalated into the already optimized nanotube, this system is referred to as  $nt\text{-S1}$ . On the contrary, when the sodium is inserted into a non-optimized nanotube, this system is referred to as  $nt\text{-S2}$ . The optimization of the nanotube is breaking the symmetry of the Ti-O bonds located on the same wall, one becoming shorter than the other. Thus, the Na ions intercalated into the  $nt\text{-S1}$  are inserted into distorted octahedral sites.

## 5.6.1 Intercalation with sodium capacity of $x = 0.33$

The capacity of  $x = 0.33$  is reached when the sodium ions are intercalated into a single layer of the nanotube.

### 5.6.1.1 Intercalation into the external wall

The study of lithium intercalation into the external wall, carried out in chapter 4, indicates that the previous optimization of the nanotube does not influence the results obtained. Based on this result, sodium ions were inserted only into the *nt-S2* system (corresponding to sodium being inserted into the slab and secondary “rolled” into a nanotube) for computational time saving. The corresponding intercalated nanotube is shown in Figure 5.24 where it can be noticed that the Na ions are inserted outward from the surface. This Na location is similar to the one observed for the intercalation into the outermost surfaces of the slab, but also to the one reported for lithium in section 4.6.1. The geometry optimization leads to an increase of the nanotube thickness with optimized Na-O distance that equals 2.17 Å along the tube axis. In the *xz* plane, the Na-O distance equals 2.23 Å, resulting in Na ions that are four-fold coordinated. By comparing the Na-O distances observed for the external wall of the nanotube with the ones reported for the outermost surface of the slab, that equalled 2.00 Å and 2.45 Å, it can be noticed that the octahedral sites are less distorted in the nanotubes than in the outermost surfaces of the slab. The sodium intercalation does not modify the nanotube diameter. This result is different from the one observed with lithium intercalation that induced a shrink of the nanotube diameter by 1.3 Å. The difference can be explained by the bigger radius of the Na ions that elongate the Ti-O bonds located on the external wall.

The Mulliken population analysis indicates that the sodium give 0.9e to the lattice. This amount is the same as the one observed for the outermost surfaces of the slab but is higher than the one reported for lithium that gave 0.67e to the lattice. This result points out the higher reactivity of the external wall towards sodium. The sodium intercalation induces the reduction of all the titanium located on the external wall to  $\text{Ti}^{3+}$ . The added charge is stored in a single *d* orbital that is different for each  $\text{Ti}^{3+}$  as it depends on the multiple orientations of the Ti-O bonds located on the *xz* plane.

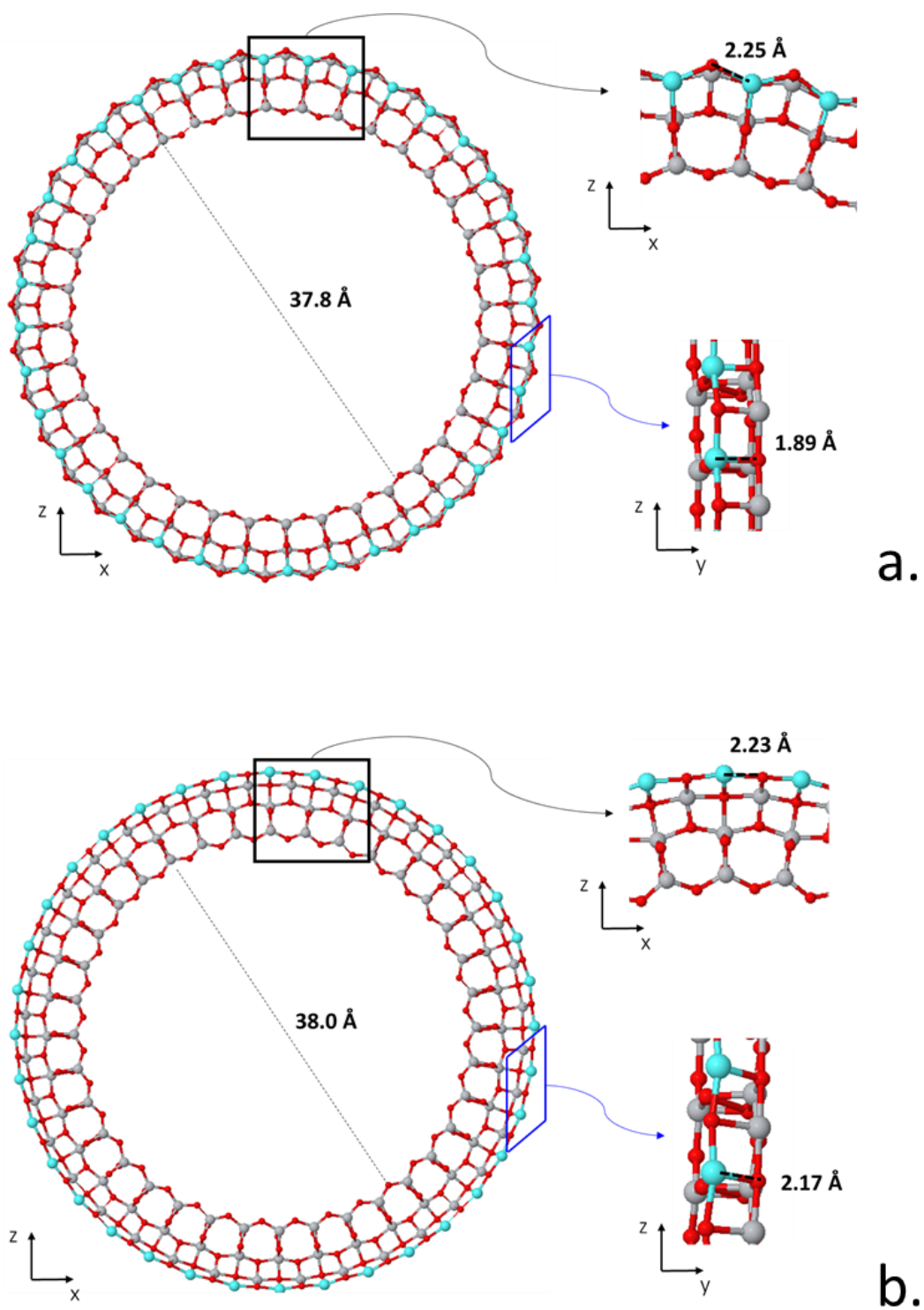


Figure 5.24: *Nt-S2* anatase (36,0) nanotube having sodium intercalated into the external wall before (a) and after (b) geometry optimization. The blue, red and grey spheres represent the Na, O and Ti elements, respectively.

The total DOS of the corresponding nanotube is displayed in Figure 5.25 where it can be observed that sodium intercalation generates a localized state in the band gap. A similar electronic structure was observed for the outermost surface of the slab or the corresponding lithium intercalation.

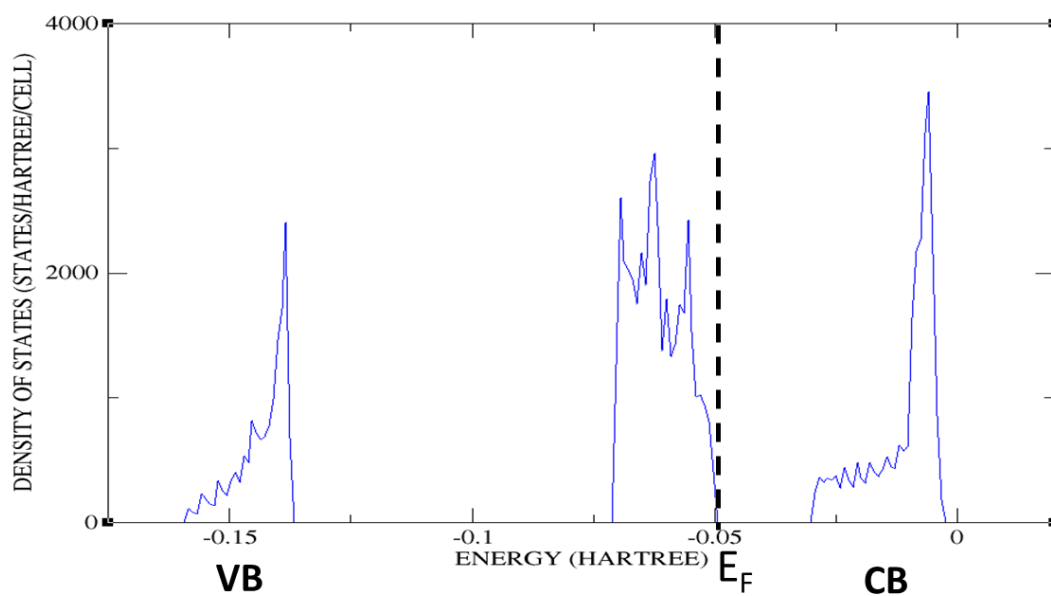


Figure 5.25: Total DOS of the anatase (36,0) nanotube having Na intercalated in its external wall. VB and CB represent the valence and conduction bands, respectively.

The Na ions were inserted with an intercalation energy equal to  $-2.27$  eV per  $\text{TiO}_2$  unit, corresponding to an intercalation voltage of  $6.8$  V. This particularly favourable intercalation energy can be explained by the geometry of the octahedral sites that are less distorted than in the slab. Moreover, the Na intercalation avoids the formation of atomic displacements in the inner layer of the nanotube, indicating that the intercalation is stabilizing the nanotube. Thus, the intercalation energy is very low as it also includes the stabilization of the nanotube induced by the sodium intercalation.

The Na insertion into the external wall is the only favourable intercalation found for sodium in this thesis. This result agrees with the lithium one where the most favourable intercalation was reported for the external wall.

### 5.6.1.2 Intercalation into the internal wall

Sodium ions were then intercalated into the internal walls of both the *nt*-S1 and *nt*-S2 nanotubes, as displayed in Figure 5.26.

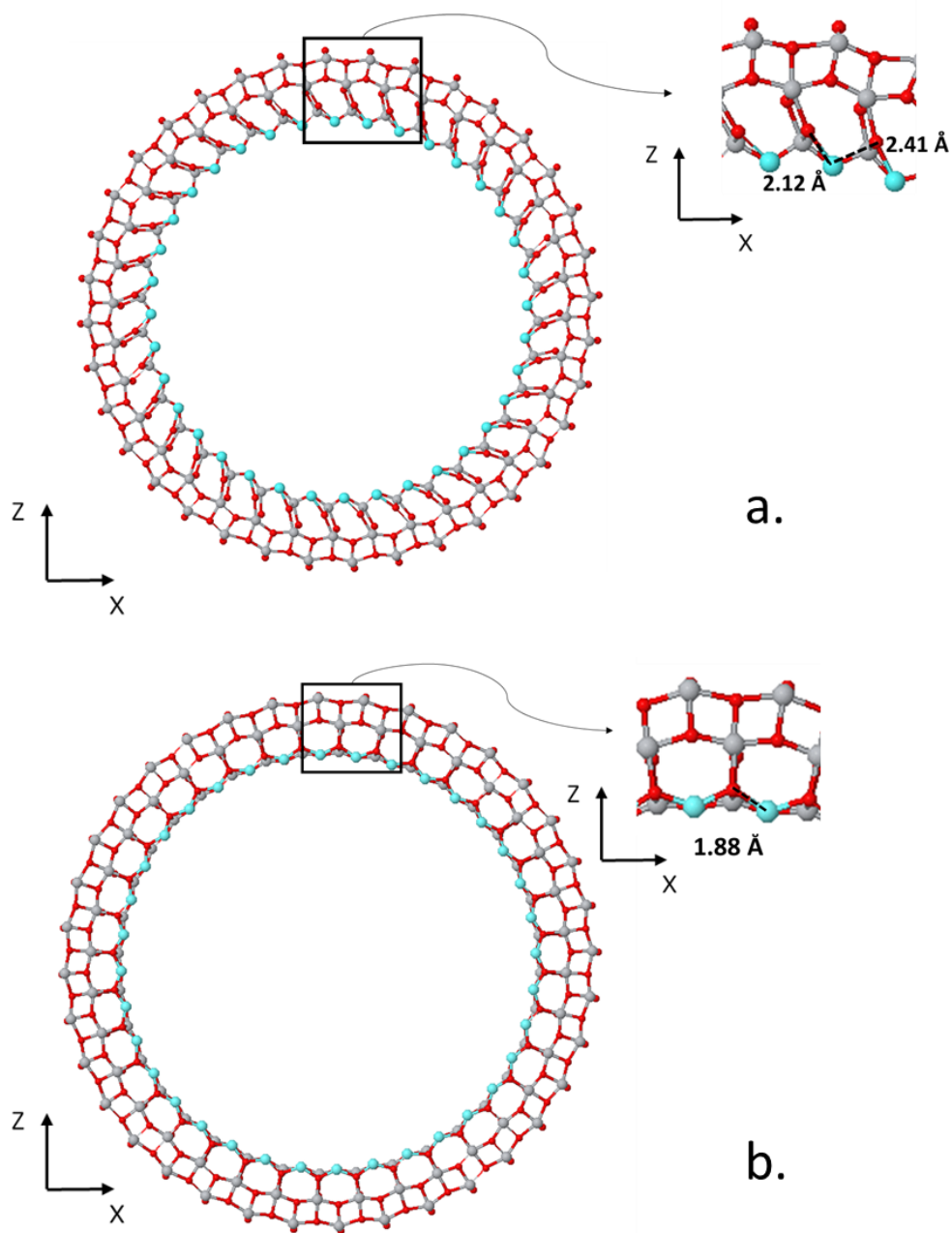


Figure 5.26: Sodium intercalation into the internal wall of *nt*-S1 (a) and *nt*-S2 (b) anatase (36,0) nanotubes. The blue, red and grey colors represent the Na, O and Ti elements, respectively.

The calculations did not converge when the Na ions were intercalated into the *nt-S2*. This may be explained by the short length exhibited by the Na-O bonds located on the internal wall, that equals 1.88 Å, resulting in a particularly unstable system.

The sodium intercalation into the *nt-S1* breaks the Ti-O bonds located in the internal wall, as shown in Figure 5.27. This result highlights the capacity of sodium intercalation to break down the structure and generate amorphous TiO<sub>2</sub> near the surface region. The associated intercalation energy is not favourable and equals 0.22 eV per TiO<sub>2</sub> unit.

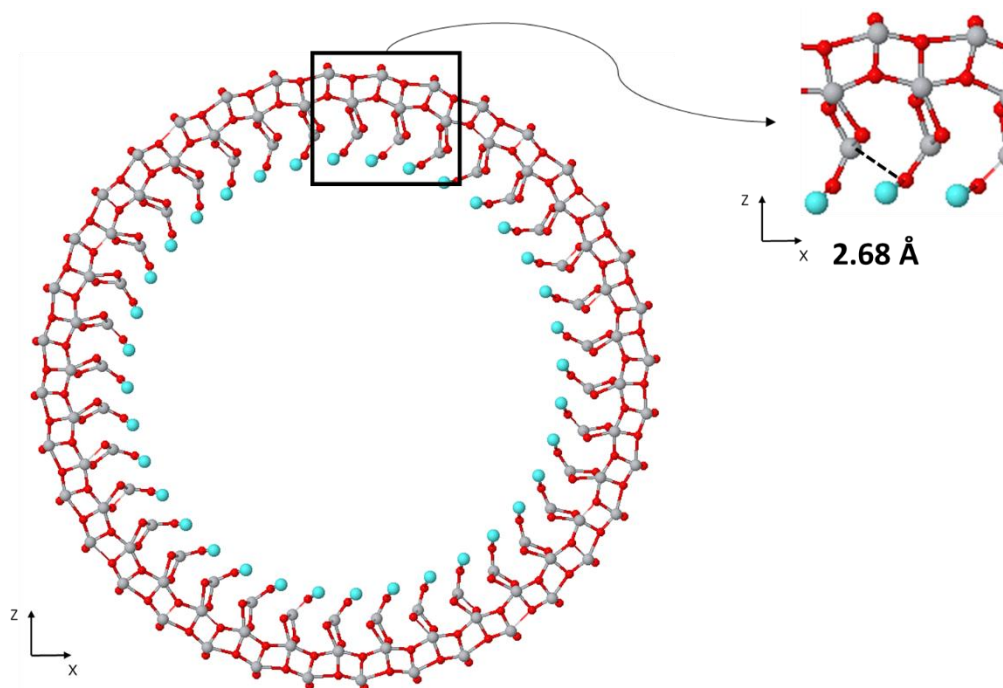


Figure 5.27: *Nt-S1* anatase (36,0) nanotube having sodium intercalated into its internal wall after geometry optimization. The Na are in blue, the O in red and the Ti in grey.

The results obtained for sodium intercalation into the internal wall are very different from the ones obtained with lithium where the intercalation was favourable and did not break any Ti-O bond.

### 5.6.2.3 Intercalation into the central layer

The octahedral sites located in the central layer of the *nt-S2* were filled with sodium ions, as shown in Figure 5.28. However, the calculation did not converge, probably because of the instability of the system. The Na ions were then inserted into the central layer of the *nt-S1*, but the calculations did not converge neither. Thus, no favourable sodium intercalation into the central layer of the nanotube are found in this thesis. These results do not agree with the lithium ones that were favourably inserted into the central layer.

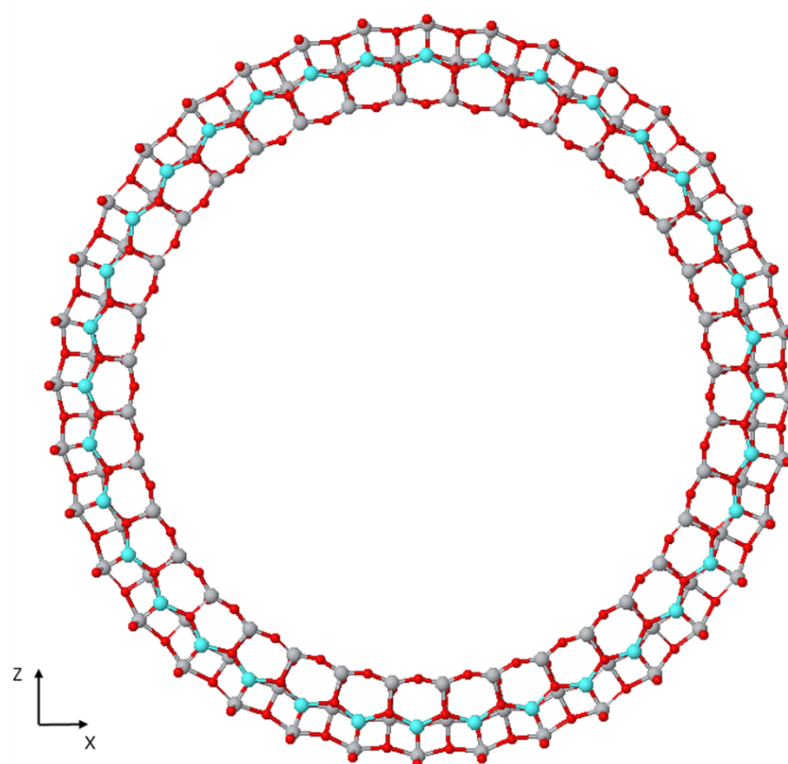


Figure 5.28: *Nt-S2* anatase (36,0) nanotube having sodium intercalated into its central layer. The Na ions are in blue while the Ti and O atoms are in grey and red, respectively.

## 5.6.2 Intercalation with sodium capacities of $x = 0.67$ and $x = 1$

The sodium ions were successfully intercalated into both the outermost surfaces of the slab, corresponding to a capacity of  $\text{Na}_{0.67}\text{TiO}_2$ . The same capacity can be obtained for the nanotube by filling both the internal and the external walls with sodium, as it is displayed in Figure 5.29. Nevertheless, the calculations did not run because of the linear dependencies of the basis sets. When lithium ions were inserted following this configuration, the calculations did not converge either because of the unstable repartition of the added charges.

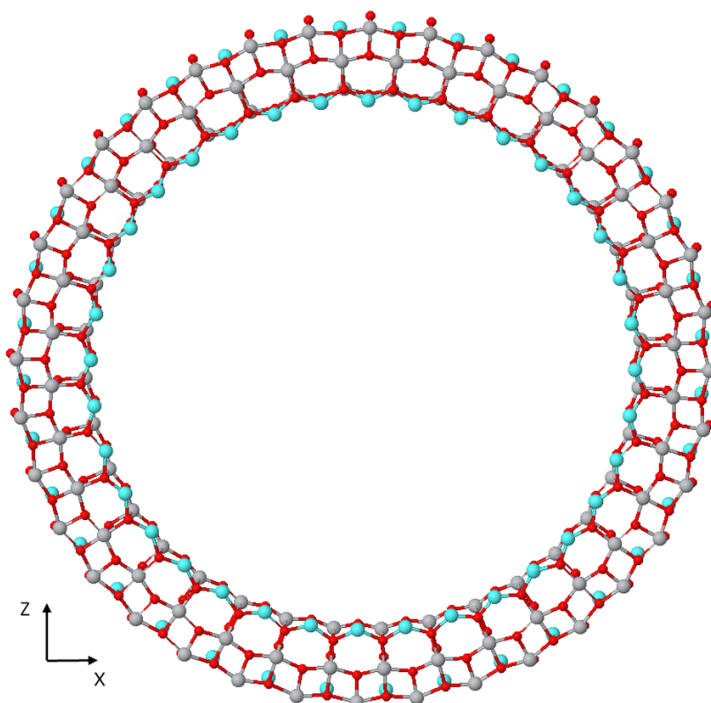


Figure 5.29: *Nt-S2* anatase (36,0) nanotube having both its internal and external walls sodiated. The blue, red and grey spheres represent the Na, O and Ti elements, respectively.

Sodium ions were then intercalated into the central layer as well as the internal and external walls to reach the capacity of  $x = 1$ , but again linear basis sets dependencies prevented the calculation to run. The calculation did not converge neither for the  $\text{LiTiO}_2$  nanotube because of the unstable repartition of the added charges. As a conclusion, the particular geometry exhibited by the anatase nanotube does not allow to perform calculations for lithium and sodium capacities superior to  $x = 0.33$ .

### 5.6.3 Intercalation versus sodium metal plating

The sodium ions were successfully adsorbed above both the undercoordinated and fully coordinated oxygen atoms located on the outermost surfaces of the slab, indicating that a sodium metal plating is favourable at the anatase (001) surface. Gonzales et al.<sup>145</sup> reported the accommodation of sodium at the surface of the nanotubes. Nevertheless, the adsorption at the surface of the internal wall cannot be studied because of the small nanotube radius that generates short and unfavourable Na-Na distances. Thus, Na ions were only added above the oxygen atoms located on the external wall.

The sodium ions were favourably adsorbed above the fully coordinated oxygens of the *Nt-S2*, as displayed in Figure 5.30. The adsorptions of Na-ions in this site do not lead to significant structural changes. Thus, no atomic displacements are observed in the inner layer of the nanotube, indicating that the sodium adsorption contributes to the nanotube stabilization.

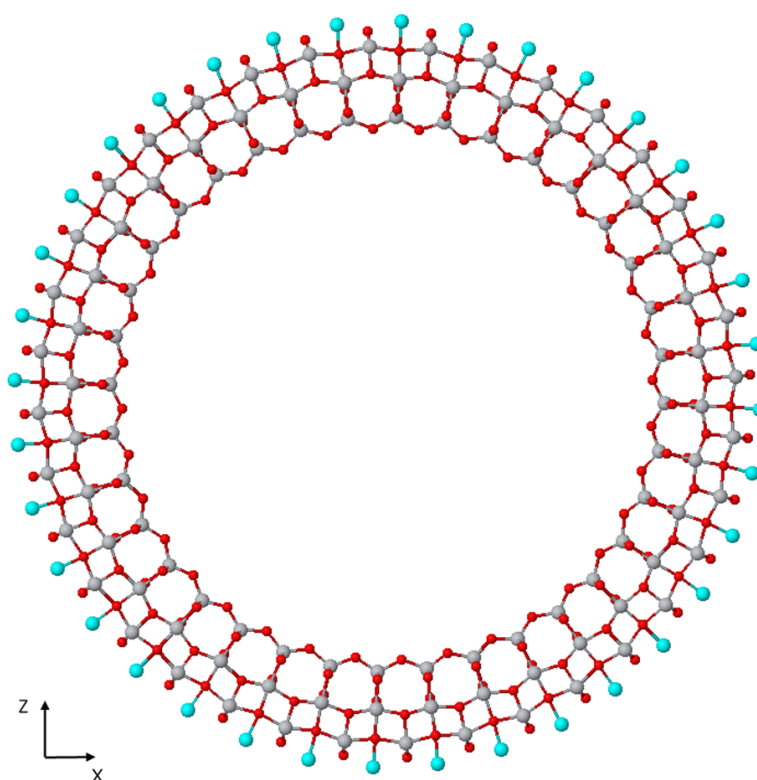


Figure 5.30: *Nt-S2* anatase (36,0) nanotube having sodium adsorbed above the fully coordinated oxygen atoms of the external wall. The blue, red and grey colors stand for the Na, O and Ti elements, respectively.

The Mulliken population analysis indicates that the sodium give 0.8e to the lattice, inducing a reduction of the titania located on the external wall to  $\text{Ti}^{3+}$ . The added charge is stored in single  $d$  orbital that is different for each  $\text{Ti}^{3+}$  because of the multiple orientation of the Ti-O bonds. The corresponding total DOS, shown in Figure 5.31, indicates that sodium adsorption induces the formation of a localized state in the band gap. A similar electronic structure was observed for the Na adsorption above the slab.

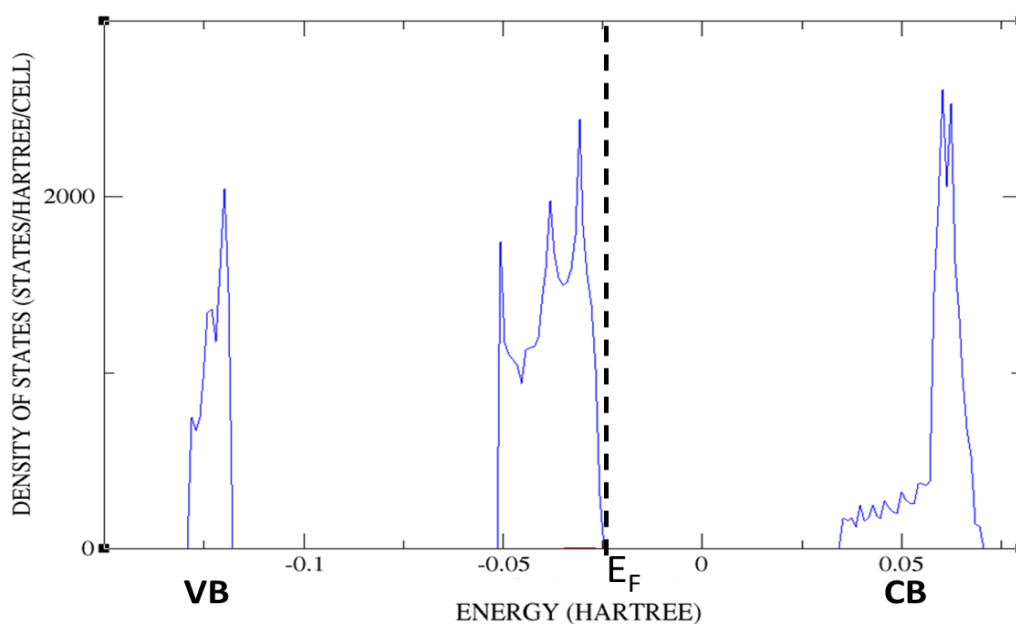


Figure 5.31: Total DOS of the *Nt-S2* anatase (36,0) nanotube having sodium adsorbed above the fully coordinated oxygen atoms located on the external wall. VB stands for the valence band while CB represents the conduction band.

The adsorption energy equals  $-0.86$  eV per  $\text{TiO}_2$  unit, corresponding to a voltage of 2.6 V. This energy is less favourable than the one reported for the sodium intercalation into the octahedral sites of the external wall that equalled  $-2.27$  eV per  $\text{TiO}_2$  unit. This difference in energies indicates that the adsorbed sodium will spontaneously move to the octahedral sites during the battery cycling. Nonetheless, the favourable Na adsorption, by reducing the external titania to  $\text{Ti}^{3+}$ , supports and speeds up the sodium diffusion from the electrolyte to the intercalation sites. Moreover, this result highlights the high reactivity of anatase surface towards sodium, in agreement with the passivating film<sup>146</sup> or sodium accommodation<sup>145</sup> reported in the experimental studies.

The calculations did not converge when the sodium ions were added above the above the undercoordinated oxygen atoms of the external wall, indicating that this kind of adsorption is not favourable. As a conclusion, only the fully coordinated oxygens contribute to the sodium adsorption at the surface of the external wall. Similar results were found for the lithium adsorption in chapter 4.

## 5.7 Conclusion

- The 8-511(1d) G basis set developed by Banarek et al<sup>193</sup> was chosen to study the sodium intercalation into anatase.
- The sodium intercalation is not favourable into any tetrahedral sites, even into the ones located on the outermost surfaces where the Coulombic repulsions are reduced.
- None of the sodium intercalations into the octahedral sites induces a hybridization of the  $\text{Ti}^{3+}$  *d* orbitals, indicating that the sodium insertion generated more electronic repulsions than the lithium one. As a result, all the sodium intercalations go along with the formation of a localized state in the band gap.
- The  $\text{Na}_{0.5}\text{TiO}_2$  and  $\text{Li}_{0.5}\text{TiO}_2$  bulks exhibit similar geometry. However, the extension of the Ti-O bonds located in the *xy* plane, as well as their shrinking along the *z* direction, are more pronounced in the  $\text{Na}_{0.5}\text{TiO}_2$  bulk.
- The most favourable sodium intercalations into bulk and slab were found with the highest capacity of  $x = 1$ . These results differ from the lithium ones (where the most favourable insertions into bulk and slab were found for capacities of  $x = 0.5$  and  $x = 0.67$ , respectively) and highlight the higher reactivity of anatase towards sodium. Moreover, these high ratio intercalations are reached for relatively high voltages, indicating that they will occur soon in the discharge process.
- The  $\text{NaTiO}_2$  bulk does not undergo a phase transformation into a tetragonal structure, like the  $\text{LiTiO}_2$  bulk, but retains its anatase structure. However, the Ti-O bond lengths are modified far above their equilibrium value, indicating that sodium intercalation can easily induce bonds breaking in the structure. This result explains how the most brittle anatase electrodes, like the anatase nanoparticles for example, can undergo phase transformations when low potentials are applied.
- The  $\text{NaTiO}_2$  slab also retains its anatase structure. However, like for the  $\text{NaTiO}_2$  bulk, the Ti-O bonds are shortened or elongated far above their equilibrium value. Thus, bonds breaking can occur easily and transform the anatase surface region into an amorphous phase, in agreement with the XANES observations. The bonds breaking occurring in the surface area also explained the further reductions of the  $\text{Ti}^{4+}$  ions into metallic Ti.

- The intercalation sites located in the outermost surfaces of the slab are more favourable than the ones located in the inner layer, highlighting the high anatase surface reactivity towards sodium.
- The sodium ions intercalated in the outermost surfaces of the slab are accommodated outward from the surface. This intercalation position differs from the lithium one where the cations were displaced inward from the surface in an attempt to reduce the dipole moment. Thus, when Na ions are intercalated into a surface, its reconstruction is guided by the electronic repulsion of the sodium and not by the reduction of the dipole moment.
- The only favourable sodium intercalation into the octahedral sites of the nanotube was found in the external wall where the Ti-O bonds exhibit the longer lengths. As a result, all the sodium intercalation into the nanotube with capacities superior to  $x = 0.33$  were not favourable.
- The sodium adsorption is favourable above all the oxygen atoms located on the outermost surfaces of the slab and above the fully coordinated oxygen atoms located in the external wall of the nanotube. However, in all cases, the adsorption energy is much smaller than the intercalation energy into the nearest octahedral sites where the adsorbed Na ions will spontaneously move. As a result, the favourable sodium adsorptions certainly support and speed up its diffusion from the electrolyte to the intercalation sites.
- The lithium adsorption was favourable only above the fully coordinated oxygen atoms present in the external wall of the nanotube. No favourable lithium adsorptions were found above the slab, highlighting the higher anatase surface reactivity towards sodium.

# Chapter 6

## Conclusions and future work

The experimental studies carried out on the anatase TiO<sub>2</sub> nanotubes point out their promising properties as a negative electrode for microbatteries. The *nt*-TiO<sub>2</sub> grown on Ti foam, and therefore having a better contact between the electrolyte and their external walls show improved capacities<sup>36</sup> while the *nt*-TiO<sub>2</sub> having no external wall do not exhibit any pseudocapacitive behaviour<sup>37</sup>. However, the fundamental processes involved in the lithium and sodium intercalations are not fully understood, holding back the improvement of the microbatteries.

The different TiO<sub>2</sub> crystalline structures and their corresponding surfaces are used in a wide variety of technological applications (e.g. batteries, heterogeneous catalysis, water splitting hydrogen generation, solar cell). Thus, they both have been extensively studied experimentally as well as computationally. A lot of studies have also been carried out about the lithium intercalation into the TiO<sub>2</sub> bulk structures. However, less articles concern its intercalation into the surfaces and only one computational study about its insertion into the nanotubes has been carried out to the best of our knowledge. Due to their recent interest, the Na-ion batteries using TiO<sub>2</sub> electrodes have not been widely studied. Thus, no theoretical study concerning the sodium intercalation into the surfaces or nanotubes has been carried out yet.

The main goal of this thesis was to gain a deeper comprehension of the anatase nanotubes as a negative electrode. By comparing the Li and Na intercalations into bulk, surfaces and nanotubes, the reactivity of the surface, as well as the influence of the strain energy can be better understood. Thus, the *nt*-TiO<sub>2</sub> architecture allowing to accommodate the highest lithium or sodium capacities can be designed.

## 6.1 Lithium intercalation into anatase

The calculations were firstly performed on the  $\text{Li}_{0.5}\text{TiO}_2$  bulk anatase using the geometry constraints necessary for the modelling of nanotubes. The number of symmetry operators was kept constant during the geometry optimization as this condition will allow afterwards to reduce the size of the nanotube unit cell below ten atoms. Thus, no anisotropic modifications, such as the orthorhombic distortion of the cell or the shift of the Li ion along the  $c$  axis can be observed. However, the most recent theoretical studies<sup>27,118</sup> indicated that the reduction of the  $\text{Ti}^{4+}$  ions to  $\text{Ti}^{3+}$  alone was not enough to induce an orthorhombic distortion of the lattice, the presence of the Li ions being necessary to stabilize the structure. These results are confirmed by the reorganization of the  $\text{Li}_{0.5}\text{TiO}_2$  lattice observed in this thesis, that seems to be driven by the Coulomb stabilization of the lithium when geometry constraints are applied. The lithium ions were also intercalated into the anatase bulk with a capacity of  $x = 1$  but the intercalation energy is less favorable than the one reported for the  $\text{Li}_{0.5}\text{TiO}_2$  bulk because of the Li-Li repulsions. The  $\text{LiTiO}_2$  bulk exhibits a distorted rock salt structure in agreement with the previous studies<sup>40,196</sup>.

The Li ions were then inserted into the (001) anatase slab, for which the most favorable lithium intercalations were found for capacities higher than  $x = 0.67$ . These results confirm the spontaneous and high ratio lithium insertion occurring into the surface and can partly explain the higher capacity observed for the nanostructured electrodes<sup>1,197</sup>. Moreover, the comparison of the lithium insertion energies between the bulk and the slab indicates a more favorable intercalation into the slab, highlighting the high reactivity of the anatase surface towards lithium. However, no lithium plating or favorable lithium intercalation into the tetrahedral sites were observed in the slab, indicating that none of these phenomena contributes to the lithium storage in thin film electrodes.

The reconstruction of the lithiated anatase surface is influenced by the lithium concentration. When only the outermost surfaces of the slab are lithiated, the reconstruction is influenced by the coordination of the surface atoms, resulting in  $\text{Ti}^{3+}\text{-O}_{3c}$  bonds shorter than the  $\text{Ti}^{3+}\text{-O}_{2c}$  ones. Consequently, the  $\text{Li}_{0.67}\text{TiO}_2$  slab exhibit a mixed geometry between the  $\text{LiTiO}_2$  rock salt and the  $\text{Li}_{0.5}\text{TiO}_2$  titanate structures.

The further lithiation of the slab induces a “flattening” of the outermost surface layers, resulting in a  $\text{LiTiO}_2$  slab exhibiting a geometry close to the rock salt structure. This later modification seems to be induced by the attraction of the undercoordinated surface oxygen atoms when Li intercalates into the centre of the slab. As a result, the gradual surface reconstructions occurring upon lithium intercalation appear to be one of the driving mechanisms for the formation of the rich  $\text{LiTiO}_2$  phase observed at the surface of the anatase electrodes in the experimental studies.

The (36, 0) anatase nanotube, chosen as a model for the nanotubular anatase electrodes in this thesis, is made of three layers: one external wall, one central layer and one internal wall. The calculations performed on this nanotube were converging only when one single layer was lithiated, corresponding to a nanotube capacity of  $x = 0.33$ . The further lithiations induced an alternating reduction of the titania ions located on the external and on the internal walls to  $\text{Ti}^{2+}$ . However, all the octahedral sites present in the same layer were filled with lithium, resulting in a fully lithiated wall with a layer capacity of  $x = 1$ . All the corresponding lithium insertion energies were negative, indicating that the lithium intercalation is favourable in all the nanotube octahedral sites. However, no favourable intercalation into the tetrahedral sites was observed despite the strain energy that expands their size in the external wall.

The most favourable intercalation sites are located on the external wall where the reduction of the external  $\text{Ti}^{4+}$  ions to  $\text{Ti}^{3+}$  results in outermost Ti-O bonds exhibiting length closer to the equilibrium value of the  $\text{Ti}^{3+}$ -O bonds than to the  $\text{Ti}^{4+}$ -O ones. Moreover, the lithium intercalation into the external wall was the only one releasing all the atomic displacements present in the inner layer of the nanotube, indicating that this insertion also plays a role in the stabilization of the nanotubular structure by absorbing the strain energy. The lithium intercalation into the central layer is five times more favourable when no atomic displacements are present in the inner layer of the nanotube. Thus, by removing the atomic displacements in the inner layer, the lithium intercalation into the external wall also promotes further lithiation of the central layer. On the contrary, the lithium insertion into the internal wall is the less favourable one and does not release the atomic displacements in the inner layer induced by the strain energy.

The comparison between the lithium intercalations into the nanotube and into the slab indicates that the lithium insertions into the external wall and the central layer of the nanotube are more favourable than the corresponding slab ones. Moreover, while no lithium metal plating was observed at the slab surface, the Li ions are favourably adsorbed above the fully coordinated oxygen atoms located on the external wall. However, the adsorption energy being significantly weaker than the intercalation energy into the adjacent octahedral sites, the adsorption does not contribute to the nanotube capacity but certainly supports the lithium diffusion from the electrolyte to the external wall. These results highlight the particularly high reactivity of the external wall but also explain why the nanotubes grown on Ti foam<sup>36</sup> exhibit better capacities than the nanotubes grown on Ti foil, because the distance between the nanotubes on the Ti foam are larger exposing more of the external walls. This leads to a better contact between the electrolyte and their external walls. On the contrary, the lithium intercalation into the internal wall of the nanotube is less favourable than the corresponding slab one because of the reduced size of the octahedral sites. This result can explain the absence of pseudocapacitive behaviour observed experimentally for the nanotubes without external wall<sup>37</sup>. As a conclusion, the high reactivity of the external wall towards lithium should encourage the design of nanotubular electrodes allowing a good contact between the electrolyte and the nanotubes external walls.

## 6.2 Sodium intercalation into anatase

The sodium ions were intercalated into the octahedral sites of the anatase bulk with capacities of  $x = 0.5$  and  $x = 1$ . Calculations were carried out using geometry constraints avoiding anisotropic modifications of the cell. As a result, no orthorhombic distortion of the lattice or shifts of the Na ions along the  $c$ -direction were observed. Both intercalations are favourable, in agreement with the literature<sup>141–143</sup>. The sodium intercalation induces an elongation of the Ti-O bonds located in the  $xy$  plane and a shortening of the ones parallel to the  $z$  direction.

The lattice modifications are more important for the  $\text{NaTiO}_2$  bulk than for the  $\text{Na}_{0.5}\text{TiO}_2$  one but in both cases the anatase structure is retained and no phase transformation into a rock salt structure is observed. As a result, the sodium intercalation into anatase does not occur via a two-phase equilibrium process, explaining why no plateau is observed experimentally in the charge/discharge potential profiles<sup>7</sup>. Moreover, the sodium intercalation energies indicate that its insertion is more favourable in the  $\text{NaTiO}_2$  bulk, where the Ti-O bonds are modified farther away from their equilibrium values, than for the  $\text{Na}_{0.5}\text{TiO}_2$  bulk. This result highlights the high reactivity of anatase towards sodium but also shows that its intercalation will occur spontaneously with high ratio into the bulk. Thus, some Na ions trapping can also occur, explaining a part of the irreversible capacity losses observed experimentally during the first cycle<sup>145</sup>. The calculations indicate that the anatase structure is retained in agreement with the experimental results carried out on electrodes made of continuous portions of anatase such as nanorods<sup>144</sup> or nanotubes<sup>145,146</sup>. However, for the smaller anatase nanoparticles embedded in a composite electrode, the structural changes can induce bonds breaking followed by a reorganization of the lattice into a rhombohedral structure or a mixture of amorphous sodium titanate, metallic titanium and sodium superoxide  $\text{NaO}_2$  as it was reported in the literature<sup>141,143</sup>.

Sodium was also intercalated into the octahedral sites of the anatase slab with capacities ranging from  $x = 0.33$  to  $x = 1$ . The intercalations were favourable and the anatase structure retained for all the sodium concentrations. The most favourable intercalation energy was found for  $x = 1$ , indicating that the Na ions will spontaneously be inserted with the highest ratio into the anatase surface. This result confirms the particularly high reactivity of anatase towards sodium previously observed in the bulk.

In all the sodiated slabs, the Na ions inserted into the outermost layers are accommodated outward from the surface, limiting the surface reconstruction that is normally stabilized by a motion of the cations inward. The Ti-O bond length elongations are also less pronounced in the  $\text{NaTiO}_2$  slab than in the corresponding bulk. As a result, the sodium intercalation energy is 0.34 eV per  $\text{TiO}_2$  unit less favourable in the  $\text{NaTiO}_2$  slab compared to the bulk.

These results propose a limited stability of the sodiated surfaces, that combined with an important stress applied on the Ti-O bonds, can progressively transform the anatase surface into the amorphous structure reported experimentally<sup>7</sup>. This is especially true when the charge/discharge cycles are repeated.

The high reactivity of the anatase surface towards sodium is also pointed out by the favourable adsorptions of the Na ions above all the oxygen atoms. These adsorptions certainly support and accelerate the sodium diffusion from the electrolyte to the octahedral sites, but also explain the formation of flower-like structures made of Na<sub>2</sub>CO<sub>3</sub> observed at the top surface of the *nt*-TiO<sub>2</sub> when low potentials are applied<sup>7</sup>.

The only favourable sodium intercalation into the nanotube was found for the octahedral sites located on the external wall and corresponds to a capacity of  $x = 0.33$ . This insertion is more favourable than all the intercalations carried out into the slab probably because of the bigger size and the less distorted geometry exhibited by the nanotube external octahedral sites. The sodium ions are also favourably adsorbed above the fully coordinated oxygens of the external wall. Thus, the last step of the sodium diffusion from the electrolyte to the intercalation sites is supported and speeded up. The geometry optimization of the former nanotubes does not generate atomic displacements in the inner layer of the *nt*-TiO<sub>2</sub>, indicating that both sodium intercalation and adsorption on the external wall contribute to the nanotube stabilization by absorbing a part of the strain energy.

The calculations carried out with sodium inserted into the internal wall converged only if the nanotube is previously optimized, and thus contains atomic displacements in the inner layer. The corresponding intercalation energy is not favourable and equals 0.22 eV per TiO<sub>2</sub> unit. However, this relatively low insertion energy suggests that the Na ions are still able to interact with the internal wall, especially when low potentials are applied. The sodium intercalation into the internal wall is accompanied by a rupture of the neighbouring Ti-O bonds, confirming the ability of the Na ions to break down the structure. This result can explain the reduction of the Ti<sup>4+</sup> ions into metallic Ti, as well as the irreversible phase transformation into amorphous TiO<sub>2</sub>, observed in the near surface regions by XANES analysis<sup>7</sup>.

The positive insertion energy reported for the internal wall also points out that the sodium intercalation associated with structural breakdowns is not going to occur spontaneously. However, as mentioned above, the relatively low insertion energy indicates that this phenomenon can occur at low potentials. This result confirms the full transformation of the anatase nanotubes into amorphous ones observed experimentally when voltage below 0.5 V vs Na/Na<sup>+</sup> are applied<sup>7</sup>. It can also explain the irreversible loss of capacities or the hasty aging of the electrode reported experimentally<sup>145</sup> for low potentials and highlights the importance of limiting the voltage applied while cycling.

The calculations performed with sodium intercalated into the octahedral sites of the nanotube central layer do not converge. The lattice modifications necessary to intercalate the large Na cations are limited by the strain energy and cannot be compensated by an intercalation outward from the surface or the rupture of the outermost Ti-O bonds as it was observed for the external and the internal walls, respectively. Moreover, the octahedral sites present in the central layer are distorted by the strain energy. As a result, the nanotube containing sodium in its central layer is particularly unstable, preventing the calculations to converge. Thus, the sodium intercalation into the nanotube is more likely to occur in its surface, confirming the electrochemical measurements<sup>145</sup> pointing out the important sodium accommodation in the *nt*-TiO<sub>2</sub> surface.

As a conclusion, the Na intercalation leads to a particularly destabilized system when occurring into the central layer, and to Ti-O bonds ruptures degrading the battery capacity when taking place into the internal wall. Thus, the most suitable Na insertion occurs into the external wall and should encourage the design of electrodes having a good contact between the *nt*-TiO<sub>2</sub> external wall and the electrolyte.

## 6.3 Comparison of the lithium and sodium insertions

By comparing the sodium and lithium intercalations into the different anatase structures, the first thing that can be noted is the important electronic repulsion generated by the Na ions. As a result, all the sodium insertions induce the formation of a localized state in the band gap induced by an absence of hybridization of the neighbouring  $\text{Ti}^{3+}$   $3d$  orbitals. The electronic repulsion generated by the Na ions also have consequences on their intercalation into the surface: the sodium ions are inserted outward from the surface and limit the surface reconstruction. Thus, the sodiated surface are particularly unstable and will progressively be transformed into an amorphous structure. This phenomenon is very different from the lithium intercalation into the surface that will induce a phase transformation into a stable  $\text{LiTiO}_2$  rock-salt structure.

The lithium and sodium intercalation energies into the different  $\text{TiO}_2$  structures and the corresponding voltages are summarized in Table 6.1. All the intercalation and adsorption energies reported for the nanotubes are the ones obtained with the *nt-S2* system, meaning that the nanotube has not been previously optimized, and thus does not contain atomic displacements in the inner layer. The more favourable sodium insertions into the bulk are in contradiction with the literature and highlight the influence of the basis set on the calculated intercalation energies. Thus, a direct comparison between the lithium and sodium insertion energies and their associated voltages is not possible. However, the higher reactivity of anatase towards sodium is shown by the spontaneous insertion of the Na ions with the highest ratio, as well as the adsorption above the slab that is favourable only for sodium.

The lithium and sodium intercalations into the bulk occur through two different mechanisms. The lithium is inserted via a two-phases equilibrium process between a Li-poor phase made of  $\text{Li}_{0.01}\text{TiO}_2$  anatase and a Li-rich phase made of  $\text{Li}_{0.5}\text{TiO}_2$  titanate. As a result, the lithium intercalation is associated with a constant electrical potential over a wide range of Li concentrations. On the contrary, the sodium insertion does not induce any phase transformation and occurs spontaneously with the highest capacity of  $x=1$ . This result explains the absence of potential plateau observed during the cycling of the sodiated electrodes.

Table 6.1: Comparison of the lithium and sodium intercalation energies and voltages in the different TiO<sub>2</sub> structures. \*NC indicates that the calculations do not converge.

TiO <sub>2</sub> structure	x	Cation position	Lithium		Sodium	
			Insertion energy (eV)	Insertion voltage (V)	Insertion energy (eV)	Insertion voltage (V)
<b>Bulk</b>	0.5	-	-1.68	3.37	-1.78	3.57
	1	-	-1.27	1.27	-2.29	2.29
<b>Slab</b>	0.33	Inner layer	-0.91	2.73	-0.32	0.96
	0.33	Outermost surface	-1.57	4.7	-1.19	3.57
	0.67	-	-1.91	2.86	-1.80	2.70
	1	-	-1.86	1.86	-1.95	1.94
	0.67	<b>Plating</b>	<b>+0.33</b>	-	-0.57	0.85
<b>Nanotube</b>	0.33	External wall	-2.42	7.25	-2.27	6.8
		Internal wall	-1.09	3.3	NC*	-
		Central layer	-1.37	4.1	NC*	-
	0.67 & 1	-	NC*	-	NC*	-
	0.33	<b>Plating</b>	-0.68	2.1	-0.86	2.6

Both lithium and sodium insertions occur spontaneously with higher capacities into the surface than into the bulk, explaining why capacities up to 200 mA.h.g<sup>-1</sup> can be reached in lithium microbatteries containing nanostructured electrodes<sup>29</sup> while the maximal theoretical capacity of lithium intercalation into the bulk equals 168 mA.h.g<sup>-1</sup>. As a result, the design of 2D or 3D anatase electrodes exhibiting large surface area should be favoured in both lithium and sodium microbatteries. Moreover, when the anatase electrodes are made of nanotubes, the space between the different *nt*-TiO<sub>2</sub> should be large enough to allow the best possible contact between the electrolyte and their external walls that are particularly reactive towards lithium and sodium.

## 6.4 Future work

The particularly high intercalation voltages calculated for the nanotubes encourage a further optimization of the lithium and sodium basis sets that should be able to describe their behaviours as cations as well as metals. The modeling of metals requires the use of diffuse functions with low coefficients allowing to reproduce a nearly uniform density. However, the use of diffuse functions increases the calculations cost by requiring an important number of integrals to be calculated in order to avoid linear dependencies. So, by keeping in mind the calculation cost required for nanotubes, it can be interesting to try to decrease the function coefficients in order to get a better model of the metal, and thus more realistic intercalation voltages.

The computational cost of first principles calculations limits the size of the nanotubes. Nonetheless, larger *nt*-TiO<sub>2</sub> can be investigated using Molecular Dynamics. Thus, lithium or sodium intercalations with capacities higher than  $x = 0.33$ , as well as their diffusions can be studied. It could be interesting to investigate how the distortion of the octahedral intercalation sites generated by the strain energy affect the cations diffusion, especially for lithium whose particularly low diffusion through the LiTiO<sub>2</sub> rock salt structure is the main factor limiting the electrodes capacities<sup>103</sup>. The study of sodium intercalation into larger nanotubes can allow to gain a deeper understanding of the formation of the amorphous phase observed experimentally at the nanotubes surface<sup>7</sup>. Furthermore, the Molecular Dynamics methods can be useful to study the amorphous TiO<sub>2</sub> nanotubes that are also used as electrodes in lithium and sodium microbatteries<sup>1,140</sup>.

The TiO<sub>2</sub> nanotubes are grown by an anodization process into an electrolyte containing fluorine ions. The first *nt*-TiO<sub>2</sub> to be formed are amorphous and can then be transformed into anatase ones by annealing. The X-ray photoelectron spectroscopy (XPS) measurements indicate the presence of fluorine species in both the amorphous (up to about 5 wt%) and the anatase (less than 1 wt%) nanotubes<sup>198</sup>. These results encourage further investigations on the possible consequences that this fluorine presence can generate on the electrochemical properties of the *nt*-TiO<sub>2</sub>.

Sn-doped nanotubes can be fabricated by anodization of co-sputtered Ti-Sn thin films. These doped *nt*-TiO<sub>2</sub> exhibit an amorphous structure and have been used in lithium microbatteries where they show better capacities than the corresponding non-doped TiO<sub>2</sub> nanotubes<sup>199</sup>. Moreover, the annealing of the Sn-doped nanotubes induces a phase transformation into rutile accompanied by a further enhancement of the capacities and lithium diffusion<sup>199</sup>. This behaviour towards lithium is very different from the rutile TiO<sub>2</sub> bulk where the lithium intercalation at room temperature is negligible due to poor Li diffusion<sup>189</sup>. Thus, theoretical studies of the Sn-doped TiO<sub>2</sub> structures can help to better understand the mechanisms induced by the tin doping, but also to complete the comprehension of the nanotubular electrodes behaviour towards cation intercalation and diffusion.

# Appendix A

## Titanium basis set

```
222 6
HAYWSC
0 1 4 8. 1.
  16.6627995 0.00528827652 -0.00247236521
  3.82352098 0.348881529 -0.490787025
  3.76734787 0.2 0.5
  1.33437747 -0.846874184 0.047543445
0 1 1 2. 1.
  0.7725692 1.0 1.0
0 1 1 0. 1.
  0.4369296 1.0 1.0
0 3 3 2. 1.
  21.429541 0.0880789808
  6.08722431 0.417373956
  2.07945196 1.0
0 3 1 0. 1.
  0.8310327 1.0
0 3 1 0. 1.
  0.3562744 1.0
```

Figure A.1: Hay-Wadt ECP basis set chosen for titanium atom<sup>173</sup>

# References

- (1) Ortiz, G. F.; Hanzu, I.; Djenizian, T.; Lavela, P.; Tirado, J. L.; Knauth, P. Alternative Li-Ion Battery Electrode Based on Self-Organized Titania Nanotubes. *Chem. Mat.* **2009**, *21* (1), 63–67. <https://doi.org/10.1021/cm801670u>.
- (2) Ellis, B. L.; Knauth, P.; Djenizian, T. Three-Dimensional Self-Supported Metal Oxides for Advanced Energy Storage. *Adv. Mater.* **2014**, *26* (21), 3368–3397. <https://doi.org/10.1002/adma.201306126>.
- (3) Ortiz, G. F.; Hanzu, I.; Knauth, P.; Lavela, P.; Tirado, J. L.; Djenizian, T. TiO<sub>2</sub> Nanotubes Manufactured by Anodization of Ti Thin Films for On-Chip Li-Ion 2D Microbatteries. *Electrochim. Acta* **2009**, *54* (17), 4262–4268. <https://doi.org/10.1016/j.electacta.2009.02.085>.
- (4) Kyeremateng, N. A.; Dumur, F.; Knauth, P.; Pecquenard, B.; Djenizian, T. Electropolymerization of Copolymer Electrolyte into Titania Nanotube Electrodes for High-Performance 3D Microbatteries. *Electrochem. Commun.* **2011**, *13* (8), 894–897. <https://doi.org/10.1016/j.elecom.2011.03.026>.
- (5) Dovesi, R.; Orlando, R.; Erba, A.; Zicovich-Wilson, C. M.; Civalieri, B.; Casassa, S.; Maschio, L.; Ferrabone, M.; De La Pierre, M.; D'Arco, P.; Noel, Y.; Causa, M.; Rerat, M.; Kirtman, B. CRYSTAL14: A Program for the Ab Initio Investigation of Crystalline Solids. *Int. J. Quantum Chem.* **2014**, *114* (19), 1287–1317. <https://doi.org/10.1002/qua.24658>.
- (6) Noel, Y.; D'Arco, P.; Demichelis, R.; Zicovich-Wilson, C. M.; Dovesi, R. On the Use of Symmetry in the Ab Initio Quantum Mechanical Simulation of Nanotubes and Related Materials. *Journal of Computational Chemistry* *31* (4), 855–862. <https://doi.org/10.1002/jcc.21370>.
- (7) Li, J.; Liu, J.; Sun, Q.; Banis, M. N.; Sun, X.; Sham, T.-K. Tracking the Effect of Sodium Insertion/Extraction in Amorphous and Anatase TiO<sub>2</sub> Nanotubes <https://pubs.acs.org/doi/full/10.1021/acs.jpcc.7b01106> (accessed 2019 -10 -23). <https://doi.org/10.1021/acs.jpcc.7b01106>.

- (8) Omar, N.; Daowd, M.; Van den Bossche, P.; Hegazy, O.; Smekens, J.; Coosemans, T.; Van Mierlo, J. Rechargeable Energy Storage Systems for Plug-in Hybrid Electric Vehicles—Assessment of Electrical Characteristics. *Energies* **2012**, *5*, 2952–2988. <https://doi.org/10.3390/en5082952>.
- (9) Armand, M.; Tarascon, J.-M. Building Better Batteries. *Nature* **2008**, *451* (7179), 652–657. <https://doi.org/10.1038/451652a>.
- (10) Whittingham, M. Electrical Energy-Storage and Intercalation Chemistry. *Science* **1976**, *192* (4244), 1126–1127. <https://doi.org/10.1126/science.192.4244.1126>.
- (11) Yoshimatsu, I.; Hirai, T.; Yamaki, J. Lithium Electrode Morphology During Cycling in Lithium Cells. *J. Electrochem. Soc.* **1988**, *135* (10), 2422–2427. <https://doi.org/10.1149/1.2095351>.
- (12) Tarascon, J. M.; Armand, M. Issues and Challenges Facing Rechargeable Lithium Batteries. *Nature* **2001**, *414* (6861), 359–367. <https://doi.org/10.1038/35104644>.
- (13) Mauger, A.; Armand, M.; Julien, C. M.; Zaghbi, K. Challenges and Issues Facing Lithium Metal for Solid-State Rechargeable Batteries. *Journal of Power Sources* **2017**, *353*, 333–342. <https://doi.org/10.1016/j.jpowsour.2017.04.018>.
- (14) Megahed, S.; Scrosati, B. Lithium-Ion Rechargeable Batteries. *J. Power Sources* **1994**, *51* (1–2), 79–104. [https://doi.org/10.1016/0378-7753\(94\)01956-8](https://doi.org/10.1016/0378-7753(94)01956-8).
- (15) Bhatt, M. D.; O’Dwyer, C. Recent Progress in Theoretical and Computational Investigations of Li-Ion Battery Materials and Electrolytes. *Phys. Chem. Chem. Phys.* **2015**, *17* (7), 4799–4844. <https://doi.org/10.1039/C4CP05552G>.
- (16) Nishi, Y. Lithium Ion Secondary Batteries; Past 10 Years and the Future. *J. Power Sources* **2001**, *100* (1–2), 101–106. [https://doi.org/10.1016/S0378-7753\(01\)00887-4](https://doi.org/10.1016/S0378-7753(01)00887-4).
- (17) Bruce, P. G.; Scrosati, B.; Tarascon, J.-M. Nanomaterials for Rechargeable Lithium Batteries. *Angew. Chem.-Int. Edit.* **2008**, *47* (16), 2930–2946. <https://doi.org/10.1002/anie.200702505>.

- (18) Djenizian, T.; Hanzu, I.; Knauth, P. Nanostructured Negative Electrodes Based on Titania for Li-Ion Microbatteries. *J. Mater. Chem.* **2011**, *21* (27), 9925–9937. <https://doi.org/10.1039/c0jm04205f>.
- (19) Macklin, W.; Neat, R. Performance of Titanium Dioxide-Based Cathodes in a Lithium Polymer Electrolyte Cell. *Solid State Ion.* **1992**, *53*, 694–700. [https://doi.org/10.1016/0167-2738\(92\)90449-Y](https://doi.org/10.1016/0167-2738(92)90449-Y).
- (20) Zwilling, V.; Darque-Ceretti, E.; Boutry-Forveille, A.; David, D.; Perrin, M. Y.; Aucouturier, M. Structure and Physicochemistry of Anodic Oxide Films on Titanium and TA6V Alloy. *Surf. Interface Anal.* **1999**, *27* (7), 629–637. [https://doi.org/10.1002/\(SICI\)1096-9918\(199907\)27:7<629::AID-SIA551>3.0.CO;2-0](https://doi.org/10.1002/(SICI)1096-9918(199907)27:7<629::AID-SIA551>3.0.CO;2-0).
- (21) Armstrong, A. R.; Armstrong, G.; Canales, J.; Garcia, R.; Bruce, P. G. Lithium-Ion Intercalation into TiO<sub>2</sub>-B Nanowires. *Adv. Mater.* **2005**, *17* (7), 862–+. <https://doi.org/10.1002/adma.200400795>.
- (22) Fang, D.; Huang, K.; Liu, S.; Li, Z. Electrochemical Properties of Ordered TiO<sub>2</sub> Nanotube Loaded with Ag Nano-Particles for Lithium Anode Material. *J. Alloy. Compd.* **2008**, *464* (1–2), L5–L9. <https://doi.org/10.1016/j.jallcom.2007.09.141>.
- (23) Varghese, O. K.; Gong, D. W.; Paulose, M.; Grimes, C. A.; Dickey, E. C. Crystallization and High-Temperature Structural Stability of Titanium Oxide Nanotube Arrays. *J. Mater. Res.* **2003**, *18* (1), 156–165. <https://doi.org/10.1557/JMR.2003.0022>.
- (24) Huang, S.; Kavan, L.; Exnar, I.; Gratzel, M. Rocking Chair Lithium Battery Based on Nanocrystalline TiO<sub>2</sub> (Anatase). *J. Electrochem. Soc.* **1995**, *142* (9), L142–L144. <https://doi.org/10.1149/1.2048726>.
- (25) Dawson, J. A.; Robertson, J. Improved Calculation of Li and Na Intercalation Properties in Anatase, Rutile, and TiO<sub>2</sub>(B). *J. Phys. Chem. C* **2016**, *120* (40), 22910–22917. <https://doi.org/10.1021/acs.jpcc.6b08842>.

- (26) Koudriachova, M. V.; de Leeuw, S. W.; Harrison, N. M. Orthorhombic Distortion on Li Intercalation in Anatase. *Phys. Rev. B* **2004**, *69* (5), 054106. <https://doi.org/10.1103/PhysRevB.69.054106>.
- (27) Kavan, L.; Gratzel, M.; Rathousky, J.; Zukal, A. Nanocrystalline TiO<sub>2</sub> (Anatase) Electrodes: Surface Morphology, Adsorption, and Electrochemical Properties. *J. Electrochem. Soc.* **1996**, *143* (2), 394–400. <https://doi.org/10.1149/1.1836455>.
- (28) Ding, S.; Chen, J. S.; Luan, D.; Boey, F. Y. C.; Madhavi, S.; Lou, X. W. (David). Graphene-Supported Anatase TiO<sub>2</sub> Nanosheets for Fast Lithium Storage. *Chem. Commun.* **2011**, *47* (20), 5780–5782. <https://doi.org/10.1039/C1CC10687B>.
- (29) Xu, J.; Jia, C.; Cao, B.; Zhang, W. F. Electrochemical Properties of Anatase TiO<sub>2</sub> Nanotubes as an Anode Material for Lithium-Ion Batteries. *Electrochimica Acta* **2007**, *52* (28), 8044–8047. <https://doi.org/10.1016/j.electacta.2007.06.077>.
- (30) Lindstrom, H.; Sodergren, S.; Solbrand, A.; Rensmo, H.; Hjelm, J.; Hagfeldt, A.; Lindquist, S. E. Li<sup>+</sup> Ion Insertion in TiO<sub>2</sub> (Anatase) .2. Voltammetry on Nanoporous Films. *J. Phys. Chem. B* **1997**, *101* (39), 7717–7722. <https://doi.org/10.1021/jp970490q>.
- (31) Zhu, K.; Wang, Q.; Kim, J.-H.; Pesaran, A. A.; Frank, A. J. Pseudocapacitive Lithium-Ion Storage in Oriented Anatase TiO<sub>2</sub> Nanotube Arrays. *J. Phys. Chem. C* **2012**, *116* (22), 11895–11899. <https://doi.org/10.1021/jp301884x>.
- (32) Zhang, H.; Li, G. R.; An, L. P.; Yan, T. Y.; Gao, X. P.; Zhu, H. Y. Electrochemical Lithium Storage of Titanate and Titania Nanotubes and Nanorods. *J. Phys. Chem. C* **2007**, *111* (16), 6143–6148. <https://doi.org/10.1021/jp0702595>.
- (33) Plylahan, N.; Demoulin, A.; Lebouin, C.; Knauth, P.; Djenizian, T. Mechanism Study of Li<sup>+</sup> Insertion into Titania Nanotubes. *RSC Adv.* **2015**, *5* (36), 28474–28477. <https://doi.org/10.1039/c5ra03759j>.
- (34) Wagemaker, M.; Lutzenkirchen-Hecht, D.; van Well, A. A.; Frahm, R. Atomic and Electronic Bulk versus Surface Structure: Lithium Intercalation in Anatase

- TiO<sub>2</sub>. *J. Phys. Chem. B* **2004**, *108* (33), 12456–12464. <https://doi.org/10.1021/jp048567f>.
- (35) Wagemaker, M.; Borghols, W. J. H.; Mulder, F. M. Large Impact of Particle Size on Insertion Reactions. A Case for Anatase Li<sub>x</sub>TiO<sub>2</sub>. *J. Am. Chem. Soc.* **2007**, *129* (14), 4323–4327. <https://doi.org/10.1021/ja067733p>.
- (36) Bi, Z.; Paranthaman, M. P.; Menchhofer, P. A.; Dehoff, R. R.; Bridges, C. A.; Chi, M.; Guo, B.; Sun, X.-G.; Dai, S. Self-Organized Amorphous TiO<sub>2</sub> Nanotube Arrays on Porous Ti Foam for Rechargeable Lithium and Sodium Ion Batteries. *J. Power Sources* **2013**, *222*, 461–466. <https://doi.org/10.1016/j.jpowsour.2012.09.019>.
- (37) Wei, W.; Oltean, G.; Tai, C.-W.; Edstrom, K.; Bjorefors, F.; Nyholm, L. High Energy and Power Density TiO<sub>2</sub> Nanotube Electrodes for 3D Li-Ion Microbatteries. *J. Mater. Chem. A* **2013**, *1* (28), 8160–8169. <https://doi.org/10.1039/c3ta11273j>.
- (38) Mackrodt, W. C. First Principles Hartree-Fock Description of Lithium Insertion in Oxides I. The End Members TiO<sub>2</sub> and LiTiO<sub>2</sub> of the System Li<sub>x</sub>TiO<sub>2</sub>. *J. Solid State Chem.* **1999**, *142* (2), 428–439. <https://doi.org/10.1006/jssc.1998.8058>.
- (39) Laskova, B.; Frank, O.; Zikalova, M.; Bousa, M.; Dracinsky, M.; Kavan, L. Lithium Insertion into Titanium Dioxide (Anatase): A Raman Study with O-16/18 and Li-6/7 Isotope Labeling. *Chem. Mat.* **2013**, *25* (18), 3710–3717. <https://doi.org/10.1021/cm402056j>.
- (40) Tielens, F.; Calatayud, M.; Beltran, A.; Minot, C.; Andres, J. Lithium Insertion and Mobility in the TiO<sub>2</sub>-Anatase/Titanate Structure: A Periodic DFT Study. *J. Electroanal. Chem.* **2005**, *581* (2), 216–223. <https://doi.org/10.1016/j.jelechem.2005.04.009>.
- (41) Nuspl, G.; Yoshizawa, K.; Yamabe, T. Lithium Intercalation in TiO<sub>2</sub> Modifications. *J. Mater. Chem.* **1997**, *7* (12), 2529–2536. <https://doi.org/10.1039/A703935B>.

- (42) Asahi, R.; Morikawa, T.; Ohwaki, T.; Aoki, K.; Taga, Y. Visible-Light Photocatalysis in Nitrogen-Doped Titanium Oxides. *Science* **2001**, *293* (5528), 269–271. <https://doi.org/10.1126/science.1061051>.
- (43) Sanjines, R.; Tang, H.; Berger, H.; Gozzo, F.; Margaritondo, G.; Levy, F. Electronic-Structure of Anatase TiO<sub>2</sub> Oxide. *J. Appl. Phys.* **1994**, *75* (6), 2945–2951.
- (44) Stashans, A. Theoretical Study of Lithium Intercalation in Rutile and Anatase. *Phys. Rev. B* **1996**, *53* (1), 159–170. <https://doi.org/10.1103/PhysRevB.53.159>.
- (45) Hebenstreit, W.; Ruzycki, N.; Herman, G. S.; Gao, Y.; Diebold, U. Scanning Tunneling Microscopy Investigation of the TiO<sub>2</sub> Anatase (101) Surface. *Phys. Rev. B* **2000**, *62* (24), R16334–R16336.
- (46) Labat, F.; Baranek, P.; Adamo, C. Structural and Electronic Properties of Selected Rutile and Anatase TiO<sub>2</sub> Surfaces: An Ab Initio Investigation. *Journal of Chemical Theory and Computation* **2008**, *4* (2), 341–352. <https://doi.org/10.1021/ct700221w>.
- (47) Hart, J. N.; Parker, S. C.; Lapkin, A. A. Energy Minimization of Single-Walled Titanium Oxide Nanotubes. *ACS Nano* **2009**, *3* (11), 3401–3412. <https://doi.org/10.1021/nn900723f>.
- (48) Ferrari, A. M.; Szieberth, D.; Noel, Y. DFT Modeling of Anatase Nanotubes. *J. Mater. Chem.* **2011**, *21* (12), 4568–4580. <https://doi.org/10.1039/c0jm03257c>.
- (49) Ortega, Y.; Hevia, D. F.; Oviedo, J.; San-Miguel, M. A. A DFT Study of the Stoichiometric and Reduced Anatase (001) Surfaces. *Applied Surface Science* **2014**, *294*, 42–48. <https://doi.org/10.1016/j.apsusc.2013.12.105>.
- (50) De Angelis, F.; Di Valentin, C.; Fantacci, S.; Vittadini, A.; Selloni, A. Theoretical Studies on Anatase and Less Common TiO<sub>2</sub> Phases: Bulk, Surfaces, and Nanomaterials. *Chem. Rev.* **2014**, *114* (19), 9708–9753. <https://doi.org/10.1021/cr500055q>.

- (51) Araujo-Lopez, E.; Alcala Varilla, L.; Seriani, N.; Montoya, J. A. TiO<sub>2</sub> Anatase's Bulk and (001) Surface, Structural and Electronic Properties: A DFT Study on the Importance of Hubbard and van Der Waals Contributions. *Surf. Sci.* **2016**, *653*, 187–196. <https://doi.org/10.1016/j.susc.2016.07.003>.
- (52) Vittadini, A.; Casarin, M. Ab Initio Modeling of TiO(2) Nanosheets. *Theor. Chem. Acc.* **2008**, *120* (4–6), 551–556. <https://doi.org/10.1007/s00214-008-0425-8>.
- (53) Mino, L.; Ferrari, A. M.; Lacivita, V.; Spoto, G.; Bordiga, S.; Zecchina, A. CO Adsorption on Anatase Nanocrystals: A Combined Experimental and Periodic DFT Study. *J. Phys. Chem. C* **2011**, *115* (15), 7694–7700. <https://doi.org/10.1021/jp2017049>.
- (54) Zhao, Z.; Li, Z.; Zou, Z. Surface Properties and Electronic Structure of Low-Index Stoichiometric Anatase TiO<sub>2</sub> Surfaces. *J. Phys.: Condens. Matter* **2010**, *22* (17), 175008. <https://doi.org/10.1088/0953-8984/22/17/175008>.
- (55) Scaranto, J.; Giorgianni, S. A DFT Study of CO Adsorbed on Clean and Hydroxylated Anatase TiO<sub>2</sub> (001) Surfaces. *Molecular Physics* **2009**, *107* (19), 1997–2003. <https://doi.org/10.1080/00268970903084961>.
- (56) Calatayud, M.; Minot, C. Effect of Relaxation on Structure and Reactivity of Anatase (100) and (001) Surfaces. *Surf. Sci.* **2004**, *552* (1–3), 169–179. <https://doi.org/10.1016/j.susc.2004.01.036>.
- (57) Iijima, S. Helical Microtubules of Graphitic Carbon. *Nature* **1991**, *354* (6348), 56–58. <https://doi.org/10.1038/354056a0>.
- (58) Tenne, R.; Margulis, L.; Genut, M.; Hodes, G. Polyhedral and Cylindrical Structures of Tungsten Disulfide. *Nature* **1992**, *360* (6403), 444–446. <https://doi.org/10.1038/360444a0>.
- (59) Remškar, M. Inorganic Nanotubes. *Adv. Mater.* **2004**, *16* (17), 1497–1504. <https://doi.org/10.1002/adma.200306428>.

- (60) Hoyer, P. Formation of a Titanium Dioxide Nanotube Array. *Langmuir* **1996**, *12* (6), 1411–1413. <https://doi.org/10.1021/la9507803>.
- (61) Kasuga, T.; Hiramatsu, M.; Hoson, A.; Sekino, T.; Niihara, K. Formation of Titanium Oxide Nanotube. *Langmuir* **1998**, *14* (12), 3160–3163. <https://doi.org/10.1021/la9713816>.
- (62) Roy, P.; Berger, S.; Schmuki, P. TiO<sub>2</sub> Nanotubes: Synthesis and Applications. *Angew. Chem. Int. Ed.* **2011**, *50* (13), 2904–2939. <https://doi.org/10.1002/anie.201001374>.
- (63) Hossain, F. M.; Evteev, A. V.; Belova, I. V.; Nowotny, J.; Murch, G. E. Structural, Electronic and Optical Properties of Titania Nanotubes. *Adv. Appl. Ceram.* **2012**, *111* (1–2), 72–93. <https://doi.org/10.1179/1743676111Y.0000000063>.
- (64) White, C.; Robertson, D.; Mintmire, J. Helical and Rotational Symmetries of Nanoscale Graphitic Tubules. *Phys. Rev. B* **1993**, *47* (9), 5485–5488. <https://doi.org/10.1103/PhysRevB.47.5485>.
- (65) Charlier, J.-C.; Blase, X.; Roche, S. Electronic and Transport Properties of Nanotubes. *Rev. Mod. Phys.* **2007**, *79* (2), 677–732. <https://doi.org/10.1103/RevModPhys.79.677>.
- (66) Rubio, A.; Corkill, J. L.; Cohen, M. L. Theory of Graphitic Boron Nitride Nanotubes. *Phys. Rev. B* **1994**, *49* (7), 5081–5084. <https://doi.org/10.1103/PhysRevB.49.5081>.
- (67) Ivanovskaya, V. V.; Enyashin, A. N.; Ivanovskii, A. L. Electronic Structure of Single-Walled TiO<sub>2</sub> and VO<sub>2</sub> Nanotubes. *Mendeleev Communications* **2003**, *13* (1), 5–7. <https://doi.org/10.1070/MC2003v013n01ABEH001686>.
- (68) Ferrari, A. M.; Lessio, M.; Szieberth, D.; Maschio, L. On the Stability of Dtitanate Nanotubes: A Density Functional Theory Study. *J. Phys. Chem. C* **2010**, *114* (49), 21219–21225. <https://doi.org/10.1021/jp1079185>.

- (69) Chen, Q.; Du, G. H.; Zhang, S.; Peng, L. M. The Structure of Trititanate Nanotubes. *Acta Crystallogr. Sect. B-Struct. Sci.* **2002**, *58*, 587–593. <https://doi.org/10.1107/S0108768102009084>.
- (70) Enyashin, A. N.; Seifert, G. Structure, Stability and Electronic Properties of TiO<sub>2</sub> Nanostructures. *phys. stat. sol. (b)* **2005**, *242* (7), 1361–1370. <https://doi.org/10.1002/pssb.200540026>.
- (71) Szieberth, D.; Ferrari, A. M.; Noel, Y.; Ferrabone, M. Ab Initio Modeling of TiO<sub>2</sub> Nanotubes. *Nanoscale* **2010**, *2* (1), 81–89. <https://doi.org/10.1039/b9nr00214f>.
- (72) He, T.; Zhao, M.; Zhang, X.; Zhang, H.; Wang, Z.; Xi, Z.; Liu, X.; Yan, S.; Xia, Y.; Mei, L. Layered Titanium Oxide Nanosheet and Ultrathin Nanotubes: A First-Principles Prediction. *J. Phys. Chem. C* **2009**, *113* (31), 13610–13615. <https://doi.org/10.1021/jp9032244>.
- (73) Meng, Q.; Wang, J.; Xie, Q.; Li, X. Nanotubes from Rutile TiO<sub>2</sub> (110) Sheets: Formation and Properties. *J. Phys. Chem. C* **2010**, *114* (20), 9251–9256. <https://doi.org/10.1021/jp100389f>.
- (74) Mowbray, D. J.; Martinez, J. I.; García Lastra, J. M.; Thygesen, K. S.; Jacobsen, K. W. Stability and Electronic Properties of TiO<sub>2</sub> Nanostructures With and Without B and N Doping. *J. Phys. Chem. C* **2009**, *113* (28), 12301–12308. <https://doi.org/10.1021/jp904672p>.
- (75) Evarestov, R. A.; Bandura, A. V.; Losev, M. V.; Piskunov, S.; Zhukovskii, Yu. F. Titania Nanotubes Modeled from 3- and 6-Layered (1 0 1) Anatase Sheets: Line Group Symmetry and Comparative Ab Initio LCAO Calculations. *Physica E: Low-dimensional Systems and Nanostructures* **2010**, *43* (1), 266–278. <https://doi.org/10.1016/j.physe.2010.07.068>.
- (76) Evarestov, R. A.; Zhukovskii, Yu. F.; Bandura, A. V.; Piskunov, S.; Losev, M. V. Symmetry and Models of Double-Wall BN and TiO<sub>2</sub> Nanotubes with Hexagonal Morphology. *J. Phys. Chem. C* **2011**, *115* (29), 14067–14076. <https://doi.org/10.1021/jp2027737>.

- (77) Lisovski, O.; Piskunov, S.; Zhukovskii, Y. F.; Bocharov, D. Quantum Chemical Simulations of Titanium Dioxide Nanotubes Used for Photocatalytic Water Splitting. *J. Surf. Investig.* **2017**, *11* (1), 78–86. <https://doi.org/10.1134/S1027451016050335>.
- (78) Zhang, H.-Y.; Dong, S.-L. First Principles Study of Single Wall TiO<sub>2</sub> Nanotubes Rolled by Anatase Monolayers. *Chinese Physics Letters* **2013**, *30* (4), 043102. <https://doi.org/10.1088/0256-307X/30/4/043102>.
- (79) Meng, Q.; Guan, Z.; Huang, J.; Li, Q.; Yang, J. Electronic and Optical Properties of TiO<sub>2</sub> Nanotubes and Arrays: A First-Principles Study. *Phys. Chem. Chem. Phys.* **2014**, *16* (23), 11519–11526. <https://doi.org/10.1039/c4cp01077a>.
- (80) Hossain, F. M.; Evteev, A. V.; Belova, I. V.; Nowotny, J.; Murch, G. E. Electronic and Optical Properties of Anatase TiO<sub>2</sub> Nanotubes. *Computational Materials Science* **2010**, *48* (4), 854–858. <https://doi.org/10.1016/j.commatsci.2010.04.007>.
- (81) Bandura, A. V.; Evarestov, R. A. From Anatase (101) Surface to TiO<sub>2</sub> Nanotubes: Rolling Procedure and First Principles LCAO Calculations. *Surf. Sci.* **2009**, *603* (18), L117–L120. <https://doi.org/10.1016/j.susc.2009.07.041>.
- (82) Liu, Z.; Zhang, Q.; Qin, L.-C. Reduction in the Electronic Band Gap of Titanium Oxide Nanotubes. *Solid State Communications* **2007**, *141* (3), 168–171. <https://doi.org/10.1016/j.ssc.2006.09.055>.
- (83) Lin, F.; Zhou, G.; Li, Z.; Li, J.; Wu, J.; Duan, W. Molecular and Atomic Adsorption of Hydrogen on Nanotubes: An Ab Initio Study. *Chemical Physics Letters* **2009**, *475* (1–3), 82–85. <https://doi.org/10.1016/j.cplett.2009.05.018>.
- (84) Evarestov, R. A.; Bandura, A. B.; Losev, M. V. Symmetry and Stability of Nanotubes Based on Titanium Dioxide. *Russ. J. Gen. Chem.* **2010**, *80* (6), 1152–1167. <https://doi.org/10.1134/S1070363210060198>.
- (85) Pan, X.; Cai, Q.; Chen, W.; Zhuang, G.; Li, X.; Wang, J. A DFT Study of Gas Molecules Adsorption on the Anatase (0 0 1) Nanotube Arrays. *Computational*

- (86) Ferrari, A. M.; Szieberth, D.; Zicovich-Wilson, C. M.; Demichelis, R. Anatase(001) 3 ML Nanotubes, The First TiO<sub>2</sub> Nanotube With Negative Strain Energies: A DFT Prediction. *J. Phys. Chem. Lett.* **2010**, *1* (19), 2854–2857. <https://doi.org/10.1021/jz101184f>.
- (87) Alvarez-Ramirez, F.; Ruiz-Morales, Y. Ab Initio Molecular Dynamics Calculations of the Phase Transformation Mechanism for the Formation of TiO<sub>2</sub> Titanate-Type Nanosheets from Anatase. *Chem. Mat.* **2007**, *19* (12), 2947–2959. <https://doi.org/10.1021/cm062162l>.
- (88) Casarin, M.; Vittadini, A.; Selloni, A. First Principles Study of Hydrated/Hydroxylated TiO<sub>2</sub> Nanolayers: From Isolated Sheets to Stacks and Tubes. *ACS Nano* **2009**, *3* (2), 317–324. <https://doi.org/10.1021/nn800608n>.
- (89) Zhao, M.; Xia, Y.; Mei, L. Energetic Minimum Structures of Imogolite Nanotubes: A First-Principles Prediction. *J. Phys. Chem. C* **2009**, *113* (33), 14834–14837. <https://doi.org/10.1021/jp9056169>.
- (90) Zhang, S.; Peng, L.-M.; Chen, Q.; Du, G. H.; Dawson, G.; Zhou, W. Z. Formation Mechanism of  $\text{H}_2\text{T}_3\text{O}_7$  Nanotubes. *Phys. Rev. Lett.* **2003**, *91* (25), 256103. <https://doi.org/10.1103/PhysRevLett.91.256103>.
- (91) Lisovski, O.; Piskunov, S.; Zhukovskii, Y. F.; Ozolins, J. Ab Initio Modeling of Sulphur Doped TiO<sub>2</sub> Nanotubular Photocatalyst for Water-Splitting Hydrogen Generation. In *International Conference on Functional Materials and Nanotechnologies (fm&nt2012)*; Iop Publishing Ltd: Bristol, 2012; Vol. 38.
- (92) Mogilevsky, G.; Chen, Q.; Kulkarni, H.; Kleinhammes, A.; Mullins, W. M.; Wu, Y. Layered Nanostructures of Delaminated Anatase: Nanosheets and Nanotubes. *J. Phys. Chem. C* **2008**, *112* (9), 3239–3246. <https://doi.org/10.1021/jp076899p>.

- (93) Saponjic, Z. V.; Dimitrijevic, N. M.; Tiede, D. M.; Goshe, A. J.; Zuo, X.; Chen, L. X.; Barnard, A. S.; Zapol, P.; Curtiss, L.; Rajh, T. Shaping Nanometer-Scale Architecture Through Surface Chemistry. *Advanced Materials* **17** (8), 965–971. <https://doi.org/10.1002/adma.200401041>.
- (94) Piskunov, S.; Lisovski, O.; Begens, J.; Bocharov, D.; Zhukovskii, Y. F.; Wessel, M.; Spohr, E. C-, N-, S-, and Fe-Doped TiO<sub>2</sub> and SrTiO<sub>3</sub> Nanotubes for Visible-Light-Driven Photocatalytic Water Splitting: Prediction from First Principles. *J. Phys. Chem. C* **2015**, *119* (32), 18686–18696. <https://doi.org/10.1021/acs.jpcc.5b03691>.
- (95) Zhukovskii, Y. F.; Piskunov, S.; Begens, J.; Kazeroovskis, J.; Lisovski, O. First-Principles Calculations of Point Defects in Inorganic Nanotubes. *Phys. Status Solidi B-Basic Solid State Phys.* **2013**, *250* (4), 793–800. <https://doi.org/10.1002/pssb.201200817>.
- (96) Chesnokov, A.; Lisovski, O.; Bocharov, D.; Piskunov, S.; Zhukovskii, Y. F.; Michael Wessel; Spohr, E. Ab Initio Simulations on N and S Co-Doped Titania Nanotubes for Photocatalytic Applications. *Phys. Scr.* **2015**, *90* (9), 094013. <https://doi.org/10.1088/0031-8949/90/9/094013>.
- (97) Murphy, D.; Cava, R.; Zahurak, S.; Santoro, A. Ternary LixTiO<sub>2</sub> Phases from Insertion Reactions. *Solid State Ion.* **1983**, *9–10* (DEC), 413–417. [https://doi.org/10.1016/0167-2738\(83\)90268-0](https://doi.org/10.1016/0167-2738(83)90268-0).
- (98) Cava, R.; Murphy, D.; Zahurak, S.; Santoro, A.; Roth, R. The Crystal-Structures of the Lithium-Inserted Metal-Oxides Li<sub>0.5</sub>TiO<sub>2</sub> Anatase, Li<sub>2</sub>O<sub>4</sub> Spinel, and Li<sub>2</sub>Ti<sub>2</sub>O<sub>4</sub>. *J. Solid State Chem.* **1984**, *53* (1), 64–75. [https://doi.org/10.1016/0022-4596\(84\)90228-7](https://doi.org/10.1016/0022-4596(84)90228-7).
- (99) Wagemaker, M.; van de Krol, R.; Kentgens, A. P. M.; van Well, A. A.; Mulder, F. M. Two Phase Morphology Limits Lithium Diffusion in TiO<sub>2</sub> (Anatase): A <sup>7</sup>Li MAS NMR Study. *J. Am. Chem. Soc.* **2001**, *123* (46), 11454–11461. <https://doi.org/10.1021/ja0161148>.
- (100) Legrain, F.; Malyi, O.; Manzhos, S. Insertion Energetics of Lithium, Sodium, and Magnesium in Crystalline and Amorphous Titanium Dioxide: A

Comparative First-Principles Study. *Journal of Power Sources* **2015**, 278, 197–202. <https://doi.org/10.1016/j.jpowsour.2014.12.058>.

- (101) Armstrong, A. R.; Arrouvel, C.; Gentili, V.; Parker, S. C.; Islam, M. S.; Bruce, P. G. Lithium Coordination Sites in  $\text{Li}_x\text{TiO}_2(\text{B})$ : A Structural and Computational Study. *Chem. Mat.* **2010**, 22 (23), 6426–6432. <https://doi.org/10.1021/cm102589x>.
- (102) Koudriachova, M. V.; Harrison, N. M.; de Leeuw, S. W. Effect of Diffusion on Lithium Intercalation in Titanium Dioxide. *Phys. Rev. Lett.* **2001**, 86 (7), 1275–1278. <https://doi.org/10.1103/PhysRevLett.86.1275>.
- (103) Belak, A. A.; Wang, Y.; Van der Ven, A. Kinetics of Anatase Electrodes: The Role of Ordering, Anisotropy, and Shape Memory Effects. *Chem. Mat.* **2012**, 24 (15), 2894–2898. <https://doi.org/10.1021/cm300881t>.
- (104) Morgan, B. J.; Watson, G. W. GGA+U Description of Lithium Intercalation into Anatase  $\text{TiO}_2$ . *Phys. Rev. B* **2010**, 82 (14), 144119. <https://doi.org/10.1103/PhysRevB.82.144119>.
- (105) Wagemaker, M.; Kearley, G. J.; van Well, A. A.; Mutka, H.; Mulder, F. M. Multiple Li Positions inside Oxygen Octahedra in Lithiated  $\text{TiO}_2$  Anatase. *J. Am. Chem. Soc.* **2003**, 125 (3), 840–848. <https://doi.org/10.1021/ja028165q>.
- (106) Lunell, S.; Stashans, A.; Ojamäe, L.; Lindström, H.; Hagfeldt, A. Li and Na Diffusion in  $\text{TiO}_2$  from Quantum Chemical Theory versus Electrochemical Experiment. *J. Am. Chem. Soc.* **1997**, 119 (31), 7374–7380. <https://doi.org/10.1021/ja9708629>.
- (107) Olson, C. L.; Nelson, J.; Islam, M. S. Defect Chemistry, Surface Structures, and Lithium Insertion in Anatase  $\text{TiO}_2$ . *J. Phys. Chem. B* **2006**, 110 (20), 9995–10001. <https://doi.org/10.1021/jp057261l>.
- (108) Kerisit, S.; Rosso, K. M.; Yang, Z.; Liu, J. Dynamics of Coupled Lithium/Electron Diffusion in  $\text{TiO}_2$  Polymorphs. *J. Phys. Chem. C* **2009**, 113 (49), 20998–21007. <https://doi.org/10.1021/jp9064517>.

- (109) Arrouvel, C.; Peixoto, T. C.; Valerio, M. E. G.; Parker, S. C. Lithium Migration at Low Concentration in TiO<sub>2</sub> Polymorphs. *Comput. Theor. Chem.* **2015**, *1072*, 43–51. <https://doi.org/10.1016/j.comptc.2015.09.002>.
- (110) Dawson, J. A.; Robertson, J. Improved Calculation of Li and Na Intercalation Properties in Anatase, Rutile, and TiO<sub>2</sub>(B). *J. Phys. Chem. C* **2016**, *120* (40), 22910–22917. <https://doi.org/10.1021/acs.jpcc.6b08842>.
- (111) van de Krol, R.; Goossens, A.; Meulenkamp, E. A. In Situ X-Ray Diffraction of Lithium Intercalation in Nanostructured and Thin Film Anatase TiO<sub>2</sub>. *J. Electrochem. Soc.* **1999**, *146* (9), 3150–3154. <https://doi.org/10.1149/1.1392447>.
- (112) Henningsson, A.; Rensmo, H.; Sandell, A.; Siegbahn, H.; Södergren, S.; Lindström, H.; Hagfeldt, A. Electronic Structure of Electrochemically Li-Inserted TiO<sub>2</sub> Studied with Synchrotron Radiation Electron Spectroscopies. *Journal of Chemical Physics* **2003**, *118* (12), 5607.
- (113) Wagemaker, M.; Kentgens, A. P. M.; Mulder, F. M. Equilibrium Lithium Transport between Nanocrystalline Phases in Intercalated TiO<sub>2</sub> Anatase. *Nature* **2002**, *418* (6896), 397–399. <https://doi.org/10.1038/nature00901>.
- (114) Arrouvel, C.; Parker, S. C.; Islam, M. S. Lithium Insertion and Transport in the TiO<sub>2</sub>-B Anode Material: A Computational Study. *Chem. Mat.* **2009**, *21* (20), 4778–4783. <https://doi.org/10.1021/cm900373u>.
- (115) Braithwaite, J. S.; Richard, C.; Catlow, A.; Harding, J. H.; Gale, J. D. A Theoretical Study of Lithium Intercalation into V<sub>6</sub>O<sub>13</sub> - a Combined Classical, Quantum Mechanical Approach. *Phys. Chem. Chem. Phys.* **2001**, *3* (18), 4052–4059.
- (116) Koudriachova, M. V.; Harrison, N. M.; de Leeuw, S. W. Open Circuit Voltage Profile for Li-Intercalation in Rutile and Anatase from First Principles. *Solid State Ion.* **2002**, *152*, 189–194. [https://doi.org/10.1016/S0167-2738\(02\)00299-0](https://doi.org/10.1016/S0167-2738(02)00299-0).

- (117) Mei, Y.; Huang, Y.; Hu, X. Nanostructured Ti-Based Anode Materials for Na-Ion Batteries. *J. Mater. Chem. A* **2016**, *4* (31), 12001–12013. <https://doi.org/10.1039/C6TA04611H>.
- (118) Morgan, B. J.; Watson, G. W. Role of Lithium Ordering in the  $\text{Li}_x\text{TiO}_2$  Anatase  $\rightarrow$  Titanate Phase Transition. *J. Phys. Chem. Lett.* **2011**, *2* (14), 1657–1661. <https://doi.org/10.1021/jz200718e>.
- (119) Smirnov, M.; Baddour-Hadjean, R. Li Intercalation in  $\text{TiO}_2$  Anatase: Raman Spectroscopy and Lattice Dynamic Studies. *J. Chem. Phys.* **2004**, *121* (5), 2348–2355. <https://doi.org/10.1063/1.1767993>.
- (120) Baddour-Hadjean, R.; Bach, S.; Smirnov, M.; Pereira-Ramos, J. P. Raman Investigation of the Structural Changes in Anatase  $\text{Li}_x\text{TiO}_2$  upon Electrochemical Lithium Insertion. *J. Raman Spectrosc.* **2004**, *35* (7), 577–585. <https://doi.org/10.1002/jrs.1200>.
- (121) van de Krol, R.; Goossens, A.; Meulenkamp, E. A. Electrical and Optical Properties of  $\text{TiO}_2$  in Accumulation and of Lithium Titanate  $\text{Li}_{0.5}\text{TiO}_2$ . *J. Appl. Phys.* **2001**, *90* (5), 2235–2242. <https://doi.org/10.1063/1.1388165>.
- (122) Sodergren, S.; Siegbahn, H.; Rensmo, H.; Lindstrom, H.; Hagfeldt, A.; Lindquist, S. E. Lithium Intercalation in Nanoporous Anatase  $\text{TiO}_2$  Studied with XPS. *J. Phys. Chem. B* **1997**, *101* (16), 3087–3090. <https://doi.org/10.1021/jp9639399>.
- (123) Wagemaker, M.; Lützenkirchen-Hecht, D.; Keil, P.; van Well, A. A.; Frahm, R. Quasi-in-Situ Reflection Mode XANES at the Ti K-Edge of Lithium Intercalated  $\text{TiO}_2$  Rutile and Anatase. *Physica B: Condensed Matter* **2003**, *336* (1–2), 118–123. [https://doi.org/10.1016/S0921-4526\(03\)00279-5](https://doi.org/10.1016/S0921-4526(03)00279-5).
- (124) Koudriachova, M. V.; Harrison, N. M. Li Sites and Phase Stability in  $\text{TiO}_2$ -Anatase and Zr-Doped  $\text{TiO}_2$ -Anatase. *J. Mater. Chem.* **2006**, *16* (20), 1973–1977. <https://doi.org/10.1039/B600794P>.

- (125) Fergus, J. W. Recent Developments in Cathode Materials for Lithium Ion Batteries. *Journal of Power Sources* **2010**, *195* (4), 939–954. <https://doi.org/10.1016/j.jpowsour.2009.08.089>.
- (126) Wagemaker, M.; van Well, A. A.; Kearley, G. J.; Mulder, F. M. The Life and Times of Lithium in Anatase TiO<sub>2</sub>. *Solid State Ion.* **2004**, *175* (1–4), 191–193. <https://doi.org/10.1016/j.ssi.2003.11.030>.
- (127) Legrain, F.; Malyi, O.; Manzhos, S. Insertion Energetics of Lithium, Sodium, and Magnesium in Crystalline and Amorphous Titanium Dioxide: A Comparative First-Principles Study. *J. Power Sources* **2015**, *278*, 197–202. <https://doi.org/10.1016/j.jpowsour.2014.12.058>.
- (128) Richter, J. H.; Henningsson, A.; Karlsson, P. G.; Andersson, M. P.; Uvdal, P.; Siegbahn, H.; Sandell, A. Electronic Structure of Lithium-Doped Anatase TiO<sub>2</sub> Prepared in Ultrahigh Vacuum. *Phys. Rev. B* **2005**, *71* (23), 235418. <https://doi.org/10.1103/PhysRevB.71.235418>.
- (129) Ebina, T.; Iwasaki, T.; Onodera, Y.; Hayashi, H.; Nagase, T.; Chatterjee, A.; Chiba, K. Ab Initio Study on the Topological Li Insertion in Titanium Oxide. *Journal of Power Sources* **1999**, *81*, 393–396. [https://doi.org/10.1016/S0378-7753\(99\)00192-5](https://doi.org/10.1016/S0378-7753(99)00192-5).
- (130) Kavan, L.; Grätzel, M.; Gilbert, S. E.; Klemenz, C.; Scheel, H. J. Electrochemical and Photoelectrochemical Investigation of Single-Crystal Anatase. *J. Am. Chem. Soc.* **1996**, *118* (28), 6716–6723. <https://doi.org/10.1021/ja954172l>.
- (131) Zachachristiansen, B.; West, K.; Jacobsen, T.; Atlung, S. Lithium Insertion in Different TiO<sub>2</sub> Modifications. *Solid State Ion.* **1988**, *28*, 1176–1182. [https://doi.org/10.1016/0167-2738\(88\)90352-9](https://doi.org/10.1016/0167-2738(88)90352-9).
- (132) Whittingham, M.; Dines, M. Normal-Butyllithium - Effective, General Cathode Screening Agent. *J. Electrochem. Soc.* **1977**, *124* (9), 1387–1388. <https://doi.org/10.1149/1.2133659>.

- (133) Macklin, W.; Neat, R. Performance of Titanium Dioxide-Based Cathodes in a Lithium Polymer Electrolyte Cell. *Solid State Ion.* **1992**, *53*, 694–700. [https://doi.org/10.1016/0167-2738\(92\)90449-Y](https://doi.org/10.1016/0167-2738(92)90449-Y).
- (134) Bresser, D.; Paillard, E.; Binetti, E.; Krueger, S.; Striccoli, M.; Winter, M.; Passerini, S. Percolating Networks of TiO<sub>2</sub> Nanorods and Carbon for High Power Lithium Insertion Electrodes. *J. Power Sources* **2012**, *206*, 301–309. <https://doi.org/10.1016/j.jpowsour.2011.12.051>.
- (135) Borghols, W. J. H.; Lutzenkirchen-Hecht, D.; Haake, U.; van Eck, E. R. H.; Mulder, F. M.; Wagemaker, M. The Electronic Structure and Ionic Diffusion of Nanoscale LiTiO(2) Anatase. *Phys. Chem. Chem. Phys.* **2009**, *11* (27), 5742–5748. <https://doi.org/10.1039/b823142g>.
- (136) Lafont, U.; Carta, D.; Mountjoy, G.; Chadwick, A. V.; Kelder, E. M. In Situ Structural Changes upon Electrochemical Lithium Insertion in Nanosized Anatase TiO<sub>2</sub>. *J. Phys. Chem. C* **2010**, *114* (2), 1372–1378. <https://doi.org/10.1021/jp908786t>.
- (137) Koudriachova, M. V. Mechanism of Lithium Intercalation in Titanates. *J. Solid State Electrochem.* **2010**, *14* (4), 549–553. <https://doi.org/10.1007/s10008-008-0654-8>.
- (138) Liang, K.; Chen, X.; Guo, Z.; Hou, T.; Zhang, X.; Li, Y. Lithium Intercalation and Diffusion in TiO<sub>2</sub> Nanotubes: A First-Principles Investigation. *Physical Chemistry Chemical Physics* **2016**, *18* (35), 24370–24376. <https://doi.org/10.1039/C6CP03830A>.
- (139) Guo, S.; Yi, J.; Sun, Y.; Zhou, H. Recent Advances in Titanium-Based Electrode Materials for Stationary Sodium-Ion Batteries. *Energy Environ. Sci.* **2016**, *9* (10), 2978–3006. <https://doi.org/10.1039/c6ee01807f>.
- (140) Xiong, H.; Slater, M. D.; Balasubramanian, M.; Johnson, C. S.; Rajh, T. Amorphous TiO<sub>2</sub> Nanotube Anode for Rechargeable Sodium Ion Batteries. *J. Phys. Chem. Lett.* **2011**, *2* (20), 2560–2565. <https://doi.org/10.1021/jz2012066>.

- (141) Wu, L.; Buchholz, D.; Bresser, D.; Chagas, L. G.; Passerini, S. Anatase TiO<sub>2</sub> Nanoparticles for High Power Sodium-Ion Anodes. *J. Power Sources* **2014**, *251*, 379–385. <https://doi.org/10.1016/j.jpowsour.2013.11.083>.
- (142) Ding, C.; Nohira, T.; Hagiwara, R. A New Sodiation-Desodiation Mechanism of the Titania-Based Negative Electrode for Sodium-Ion Batteries. *Phys. Chem. Chem. Phys.* **2016**, *18* (44), 30770–30776. <https://doi.org/10.1039/c6cp05944a>.
- (143) Li, W.; Fukunishi, M.; Morgan, B. J.; Borkiewicz, O. J.; Chapman, K. W.; Pralong, V.; Maignan, A.; Lebedev, O. I.; Ma, J.; Groult, H.; Komaba, S.; Damboumet, D. A Reversible Phase Transition for Sodium Insertion in Anatase TiO<sub>2</sub>. *Chem. Mat.* **2017**, *29* (4), 1836–1844. <https://doi.org/10.1021/acs.chemmater.7b00098>.
- (144) Kim, K.-T.; Ali, G.; Chung, K. Y.; Yoon, C. S.; Yashiro, H.; Sun, Y.-K.; Lu, J.; Amine, K.; Myung, S.-T. Anatase Titania Nanorods as an Intercalation Anode Material for Rechargeable Sodium Batteries. *Nano Lett.* **2014**, *14* (2), 416–422. <https://doi.org/10.1021/nl402747x>.
- (145) Gonzalez, J. R.; Alcantara, R.; Nacimiento, F.; Ortiz, G. F.; Tirado, J. L. Microstructure of the Epitaxial Film of Anatase Nanotubes Obtained at High Voltage and the Mechanism of Its Electrochemical Reaction with Sodium. *Crystengcomm* **2014**, *16* (21), 4602–4609. <https://doi.org/10.1039/c4ce00272e>.
- (146) Bella, F.; Muñoz-García, A. B.; Meligrana, G.; Lamberti, A.; Destro, M.; Pavone, M.; Gerbaldi, C. Unveiling the Controversial Mechanism of Reversible Na Storage in TiO<sub>2</sub> Nanotube Arrays: Amorphous versus Anatase TiO<sub>2</sub>. *Nano Res.* **2017**, *10* (8), 2891–2903. <https://doi.org/10.1007/s12274-017-1656-6>.
- (147) Koudriachova, M. V.; de Leeuw, S. W.; Harrison, N. M. Orthorhombic Distortion on Li Intercalation in Anatase. *Phys. Rev. B* **2004**, *69* (5), 054106. <https://doi.org/10.1103/PhysRevB.69.054106>.
- (148) Kordatos, A.; Kelaidis, N.; Chroneos, A. Migration of Sodium and Lithium Interstitials in Anatase TiO<sub>2</sub>. *Solid State Ionics* **2018**, *315*, 40–43. <https://doi.org/10.1016/j.ssi.2017.12.003>.

- (149) Legrain, F.; Malyi, O.; Manzhos, S. Insertion Energetics of Lithium, Sodium, and Magnesium in Crystalline and Amorphous Titanium Dioxide: A Comparative First-Principles Study. *Journal of Power Sources* **2015**, *278*, 197–202. <https://doi.org/10.1016/j.jpowsour.2014.12.058>.
- (150) Hinchliffe, A. *Molecular Modelling for Beginners*; Wiley, 2003.
- (151) Tang, Y. H.; Zhang, H. P. Theoretical Understanding of Bio-Interfaces/Bio-Surfaces by Simulation: A Mini Review. *Biosurface and Biotribology* **2016**, *2* (4), 151–161. <https://doi.org/10.1016/j.bsbt.2016.11.003>.
- (152) Jensen, F. *Introduction to Computational Chemistry*; Wiley, 2007.
- (153) Sutcliffe, B. The Decoupling of Electronic and Nuclear Motions in the Isolated Molecule Schrodinger Hamiltonian. *Advances in Chemical Physics, Vol 114* **2000**, *114*, 1–121. <https://doi.org/10.1002/9780470141731.ch1>.
- (154) Hohenberg, P.; Kohn, W. Inhomogeneous Electron Gas. *Phys. Rev.* **1964**, *136* (3B), B864–B871. <https://doi.org/10.1103/PhysRev.136.B864>.
- (155) Canepa, P. Phd Thesis, University of kent, 2012.
- (156) Kohn, W.; Sham, L. J. Self-Consistent Equations Including Exchange and Correlation Effects. *Phys. Rev.* **1965**, *140* (4A), A1133–A1138. <https://doi.org/10.1103/PhysRev.140.A1133>.
- (157) Alfredsson, M. Phd Thesis, UppsalaUniversity, 1999.
- (158) Kohn, W.; Becke, A. D.; Parr, R. G. Density Functional Theory of Electronic Structure. *J. Phys. Chem.* **1996**, *100* (31), 12974–12980. <https://doi.org/10.1021/jp960669l>.
- (159) Becke, A. Density-Functional Exchange-Energy Approximation with Correct Asymptotic-Behavior. *Phys. Rev. A* **1988**, *38* (6), 3098–3100. <https://doi.org/10.1103/PhysRevA.38.3098>.

- (160) Lee, C.; Yang, W.; Parr, R. Development of the Colle-Salvetti Correlation-Energy Formula into a Functional of the Electron-Density. *Phys. Rev. B* **1988**, *37* (2), 785–789. <https://doi.org/10.1103/PhysRevB.37.785>.
- (161) Perdew, J. P.; Burke, K.; Ernzerhof, M. Generalized Gradient Approximation Made Simple. *Phys. Rev. Lett.* **1996**, *77* (18), 3865–3868. <https://doi.org/10.1103/PhysRevLett.77.3865>.
- (162) Woods, M. PhD Thesis, University of kent, 2016.
- (163) Becke, A. Density-Functional Thermochemistry .3. the Role of Exact Exchange. *J. Chem. Phys.* **1993**, *98* (7), 5648–5652. <https://doi.org/10.1063/1.464913>.
- (164) Adamo, C.; Barone, V. Toward Reliable Density Functional Methods without Adjustable Parameters: The PBE0 Model. *The Journal of Chemical Physics* **1999**, *110* (13), 6158–6170. <https://doi.org/10.1063/1.478522>.
- (165) Labat, F.; Baranek, P.; Domain, C.; Minot, C.; Adamo, C. Density Functional Theory Analysis of the Structural and Electronic Properties of TiO<sub>2</sub> Rutile and Anatase Polytypes: Performances of Different Exchange-Correlation Functionals. *J. Chem. Phys.* **2007**, *126* (15), 154703. <https://doi.org/10.1063/1.2717168>.
- (166) Szabo, A.; Ostlund, N. S. *Modern Quantum Chemistry : Introduction to Advanced Electronic Structure Theory*; Dover publications, 1996.
- (167) Payne, M.; Teter, M.; Allan, D.; Arias, T.; Joannopoulos, J. Iterative Minimization Techniques for Abinitio Total-Energy Calculations - Molecular-Dynamics and Conjugate Gradients. *Rev. Mod. Phys.* **1992**, *64* (4), 1045–1097. <https://doi.org/10.1103/RevModPhys.64.1045>.
- (168) Monkhorst, H.; Pack, J. Special Points for Brillouin-Zone Integrations. *Phys. Rev. B* **1976**, *13* (12), 5188–5192. <https://doi.org/10.1103/PhysRevB.13.5188>.

- (169) Gilat, G.; Raubenheimer, L. J. Accurate Numerical Method for Calculating Frequency-Distribution Functions in Solids. *Phys. Rev.* **1966**, *144* (2), 390–395. <https://doi.org/10.1103/PhysRev.144.390>.
- (170) Gilat, G. Analysis of Methods for Calculating Spectral Properties in Solids. *Journal of Computational Physics* **1972**, *10* (3), 432–465. [https://doi.org/10.1016/0021-9991\(72\)90046-0](https://doi.org/10.1016/0021-9991(72)90046-0).
- (171) Hay, P.; Wadt, W. Abinitio Effective Core Potentials for Molecular Calculations - Potentials for the Transition-Metal Atoms Sc to Hg. *J. Chem. Phys.* **1985**, *82* (1), 270–283. <https://doi.org/10.1063/1.448799>.
- (172) R. Dovesi, R. Orlando, B. Civalleri, C. Roetti, V. R. Saunders, and C. M. Zicovich-Wilson,; Z. Kristallogr. **220**, 571 (2005). <http://www.crystal.unito.it/basis-sets.php> (accessed 2019 -09 -01).
- (173) Piskunov, S.; Heifets, E.; Eglitis, R. I.; Borstel, G. Bulk Properties and Electronic Structure of SrTiO<sub>3</sub>, BaTiO<sub>3</sub>, PbTiO<sub>3</sub> Perovskites: An Ab Initio HF/DFT Study. *Comput. Mater. Sci.* **2004**, *29* (2), 165–178. <https://doi.org/10.1016/j.commatsci.2003.08.036>.
- (174) Scaranto, J.; Giorgianni, S. A DFT Study of CO Adsorbed on Clean and Hydroxylated Anatase TiO<sub>2</sub> (001) Surfaces. *Mol. Phys.* **2009**, *107* (19), 1997–2003. <https://doi.org/10.1080/00268970903084961>.
- (175) Cora, F. The Performance of Hybrid Density Functionals in Solid State Chemistry: The Case of BaTiO<sub>3</sub>. *Mol. Phys.* **2005**, *103* (18), 2483–2496. <https://doi.org/10.1080/00268970500179651>.
- (176) Kurtz, R.; Henrich, V. Surface Electronic-Structure of Corundum Transition-Metal Oxides - Ti<sub>2</sub>O<sub>3</sub>. *Phys. Rev. B* **1982**, *25* (6), 3563–3571. <https://doi.org/10.1103/PhysRevB.25.3563>.
- (177) Ortega, Y.; Hevia, D. F.; Oviedo, J.; San-Miguel, M. A. A DFT Study of the Stoichiometric and Reduced Anatase (001) Surfaces. *Applied Surface Science* **2014**, *294*, 42–48. <https://doi.org/10.1016/j.apsusc.2013.12.105>.

- (178) Vittadini, A.; Casarin, M. Ab Initio Modeling of TiO<sub>2</sub> Nanosheets. *Theor Chem Account* **2008**, *120* (4), 551–556. <https://doi.org/10.1007/s00214-008-0425-8>.
- (179) Mino, L.; Spoto, G.; Bordiga, S.; Zecchina, A. Particles Morphology and Surface Properties As Investigated by HRTEM, FTIR, and Periodic DFT Calculations: From Pyrogenic TiO<sub>2</sub> (P25) to Nanoanatase. *J. Phys. Chem. C* **2012**, *116* (32), 17008–17018. <https://doi.org/10.1021/jp303942h>.
- (180) Zhao, Z.; Li, Z.; Zou, Z. Surface Properties and Electronic Structure of Low-Index Stoichiometric Anatase TiO<sub>2</sub> surfaces. *J. Phys.: Condens. Matter* **2010**, *22* (17), 175008. <https://doi.org/10.1088/0953-8984/22/17/175008>.
- (181) Piskunov, S.; Lisovski, O.; Begens, J.; Bocharov, D.; Zhukovskii, Y. F.; Wessel, M.; Spohr, E. C-, N-, S-, and Fe-Doped TiO<sub>2</sub> and SrTiO<sub>3</sub> Nanotubes for Visible-Light-Driven Photocatalytic Water Splitting: Prediction from First Principles. *J. Phys. Chem. C* **2015**, *119* (32), 18686–18696. <https://doi.org/10.1021/acs.jpcc.5b03691>.
- (182) Dovesi, R.; Ferrero, E.; Pisani, C.; Roetti, C. Abinitio Study of the Electron Momentum Distribution of Metallic Lithium. *Z. Phys. B-Condens. Mat.* **1983**, *51* (3), 195–203. <https://doi.org/10.1007/BF01307674>.
- (183) Ojamae, L.; Hermansson, K.; Pisani, C.; Causa, M.; Roetti, C. Structural, Vibrational and Electronic-Properties of a Crystalline Hydrate from Ab-Initio Periodic Hartree-Fock Calculations. *Acta Crystallogr. Sect. B-Struct. Sci. Cryst. Eng. Mat.* **1994**, *50*, 268–279. <https://doi.org/10.1107/S0108768193010390>.
- (184) Peintinger, M. F.; Oliveira, D. V.; Bredow, T. Consistent Gaussian Basis Sets of Triple-Zeta Valence with Polarization Quality for Solid-State Calculations. *J. Comput. Chem.* **2013**, *34* (6), 451–459. <https://doi.org/10.1002/jcc.23153>.
- (185) Doll, K.; Harrison, N. M.; Saunders, V. R. A Density Functional Study of Lithium Bulk and Surfaces. *J. Phys.: Condens. Matter* **1999**, *11* (26), 5007–5019. <https://doi.org/10.1088/0953-8984/11/26/305>.

- (186) Anderson, M.; Swenson, C. Experimental Equations of State for Cesium and Lithium Metals to 20-Kbar and the High-Pressure Behavior of the Alkali-Metals. *Phys. Rev. B* **1985**, *31* (2), 668–680. <https://doi.org/10.1103/PhysRevB.31.668>.
- (187) Djenizian, T.; Hanzu, I.; Knauth, P. Nanostructured Negative Electrodes Based on Titania for Li-Ion Microbatteries. *J. Mater. Chem.* **2011**, *21* (27), 9925–9937. <https://doi.org/10.1039/c0jm04205f>.
- (188) van de Krol, R.; Goossens, A.; Meulenkamp, E. A. Electrical and Optical Properties of TiO<sub>2</sub> in Accumulation and of Lithium Titanate Li<sub>0.5</sub>TiO<sub>2</sub>. *J. Appl. Phys.* **2001**, *90* (5), 2235–2242. <https://doi.org/10.1063/1.1388165>.
- (189) Koudriachova, M. V. Effect of Diffusion on Lithium Intercalation in Titanium Dioxide. *Phys. Rev. Lett.* **2001**, *86* (7), 1275–1278. <https://doi.org/10.1103/PhysRevLett.86.1275>.
- (190) Mackrodt, W. C. First Principles Hartree-Fock Description of Lithium Insertion in Oxides I. The End Members TiO<sub>2</sub> and LiTiO<sub>2</sub> of the System Li<sub>x</sub>TiO<sub>2</sub>. *J. Solid State Chem.* **1999**, *142* (2), 428–439. <https://doi.org/10.1006/jssc.1998.8058>.
- (191) Wagemaker, M.; Lützenkirchen-Hecht, D.; Keil, P.; van Well, A. A.; Frahm, R. Quasi-in-Situ Reflection Mode XANES at the Ti K-Edge of Lithium Intercalated TiO<sub>2</sub> Rutile and Anatase. *Physica B: Condensed Matter* **2003**, *336* (1–2), 118–123. [https://doi.org/10.1016/S0921-4526\(03\)00279-5](https://doi.org/10.1016/S0921-4526(03)00279-5).
- (192) Dovesi, R.; Roetti, C.; Freyriafova, C.; Prencipe, M.; Saunders, V. On the Elastic Properties of Lithium, Sodium and Potassium Oxide - an Abinitio Study. *Chem. Phys.* **1991**, *156* (1), 11–19. [https://doi.org/10.1016/0301-0104\(91\)87032-Q](https://doi.org/10.1016/0301-0104(91)87032-Q).
- (193) Sophia, G.; Banarek, P.; Sarrazin, C.; Rerat, M.; Dovesi, R. Systematic Influence of Atomic Substitution on the Phase Diagram of ABO<sub>3</sub> Ferroelectric Perovskites. 2014.

- (194) Chichagov, A. V.; Varlamov, D. A.; Dilanyan, R. A.; Dokina, T. N.; Drozhzhina, N. A.; Samokhvalova, O. L.; Ushakovskaya, T. V. MINCRYST: A Crystallographic Database for Minerals, Local and Network (WWW) Versions. *Crystallogr. Rep.* **2001**, *46* (5), 876–879. <https://doi.org/10.1134/1.1405882>.
- (195) Guo, S.; Yi, J.; Sun, Y.; Zhou, H. Recent Advances in Titanium-Based Electrode Materials for Stationary Sodium-Ion Batteries. *Energy Environ. Sci.* **2016**, *9* (10), 2978–3006. <https://doi.org/10.1039/C6EE01807F>.
- (196) Koudriachova, M. V.; Harrison, N. M.; de Leeuw, S. W. Effect of Diffusion on Lithium Intercalation in Titanium Dioxide. *Phys. Rev. Lett.* **2001**, *86* (7), 1275–1278. <https://doi.org/10.1103/PhysRevLett.86.1275>.
- (197) Bresser, D.; Paillard, E.; Binetti, E.; Krueger, S.; Striccoli, M.; Winter, M.; Passerini, S. Percolating Networks of TiO<sub>2</sub> Nanorods and Carbon for High Power Lithium Insertion Electrodes. *J. Power Sources* **2012**, *206*, 301–309. <https://doi.org/10.1016/j.jpowsour.2011.12.051>.
- (198) Macak, J. M.; Aldabergerova, S.; Ghicov, A.; Schmuki, P. Smooth Anodic TiO<sub>2</sub> Nanotubes: Annealing and Structure. *physica status solidi (a)* **2006**, *203* (10), R67–R69. <https://doi.org/10.1002/pssa.200622214>.
- (199) Kyeremateng, N. A.; Vacandio, F.; Sougrati, M.-T.; Martinez, H.; Jumas, J.-C.; Knauth, P.; Djenizian, T. Effect of Sn-Doping on the Electrochemical Behaviour of TiO<sub>2</sub> Nanotubes as Potential Negative Electrode Materials for 3D Li-Ion Micro Batteries. *J. Power Sources* **2013**, *224*, 269–277. <https://doi.org/10.1016/j.jpowsour.2012.09.104>.